Investigating the role of FGL2 in tumour progression and surgical stress-induced immunosuppression

Kristianne Galpin

A thesis submitted in partial fulfillment of the requirements for the
Doctorate in Philosophy degree in Cellular and Molecular Medicine

Department of Cellular and Molecular Medicine University of Ottawa
Ottawa, Ontario, Canada

Contributions

Manuscripts

1. **Galpin KJC**, Rodriguez GM, Maranda V, Cook DP, Macdonald EA, Zhao S, McCloskey CW, Chruscinski A, Levy GA, Barbara C. Vanderhyden BC. FGL2 promotes tumour growth by attenuating infiltration of activated anti-tumour dendritic, natural killer, and T cells. *Submitted to OncoImmunology*.
2. Rodriguez GM*, **Galpin KJC***, Cook DP, Yakubovich E, Maranda V, Macdonald EA, Wilson-Sanchez J, Thomas AL, Burdette JE, Vanderhyden BC. The Tumour Immune Profile of Murine Ovarian Cancer Models: An Essential Tool for Ovarian Cancer Immunotherapy Research. *Cancer Research Communications*. June 2022; 2 (6): 417–433. doi: 10.1158/2767-9764.CRC-22-0017. *authors contributed equally
3. Mehdi S, Macdonald E, **Galpin K**, Landry DA, Rodriguez G, Vanderhyden B, Bachvarov D. LY75 Suppression in Mesenchymal Epithelial Ovarian Cancer Cells Generates a Stable Hybrid EOC Cellular Phenotype, Associated with Enhanced Tumour Initiation, Spreading and Resistance to Treatment in Orthotopic Xenograft Mouse Model. I*nternational Journal of Molecular Sciences* 2020 Jul 15;21(14):4992. doi: 10.3390/ijms21144992. PMID: 32679765.
4. **Galpin KJC,** Cook DP, Salemi LM, Urowitz S, Williams C, Bell JC, Brundage MD, Vanderhyden BC. The Canadian Cancer Research Conference 2019. *Current Oncology*. 2020 Apr;27(2):e226-e230. doi: 10.3747/co.27.6245. Epub 2020 May 1. PMID: 32489273.
5. McCloskey CW, Rodriguez GM, **Galpin KJC**, Vanderhyden BC. Ovarian Cancer Immunotherapy: Preclinical Models and Emerging Therapeutics. *Cancers*. 2018 Jul 26;10(8):244. doi: 10.3390/cancers10080244. PMID: 30049987.
6. Rodriguez GM, **Galpin KJC**, McCloskey CW, Vanderhyden BC. The Tumour Microenvironment of Epithelial Ovarian Cancer and Its Influence on Response to Immunotherapy. *Cancers*. 2018 Jul 24;10(8):242. doi: 10.3390/cancers10080242. PMID: 30042343.

Students under supervision of Kristianne Galpin

1. Juliette Wilson-Sanchez: assisted with ID8 and STOSE tumour immunohistochemistry in Figures 9-12 and 14-16.

Other lab members

- Dr. Galaxia Rodriguez:
    - Performed flow cytometry analysis of Figure 5A, B
    - Irradiated cells for immunogenicity experiments shown in Figure 5E, F
    - Collaborated with intrabursal surgeries, processing/collecting tissue samples for flow cytometry, and performed flow cytometry analysis for Figures 7-21
    - Provided technical assistance for flow cytometry Figures 26-30, Figures 32-37, Figure 41, Figures 44-45, and Figure 48.
- Dr. Galaxia Rodriguez and Vincent Maranda: purified oncolytic virus used in Figure 38 and performed oncolytic virus treatment.

- Dr. David Cook: compiled, processed, and analyzed all single-cell RNA-sequencing data shown in Figures 2-4, Figures 21- 24, Figure 39, Figure 40, and Figure 46.
- Edward Yakubovich: generated differential gene expression/gene sets for ID8/STOSE and M0/M1/M2 profiles for Figures 2-4 and Figure 21.
- Elizabeth Macdonald: processed and cataloged human ovarian cancer ascites samples used in this study
- Vincent Maranda, Elizabeth Macdonald, and Humaira Murshed: provided technical assistance with *in vivo* experiments and collecting mouse tissues for flow cytometry
- Dr. Shan Zhao: performed ID8 - intraperitoneal experiment shown in Figure 26D and x-gal staining of lung metastases shown in Figure 41C

Contributions by collaborators

- Dr. Christiano T. De Souza (OHRI): performed all intravenous injections and surgeries (laparotomy/nephrectomy) for the surgical stress experiments.
- Dr. Leonard Angka and Dr. Marisa Market: collected peripheral blood mononuclear cells for single cell RNA-sequencing for Figure 39, Figure 40, and Figure 46.
- Dr. Marisa Market: collected human plasma samples at baseline and POD1 for use in Figure 39A
- Dr. Angela Cheung, Chisom Okwor, Alicia Storey and Danielle Dewar-Darch (OHRI): facilitated access to ascites from non-cancer patients.
- Dr. Gary Levy and Dr. Andrzej Chruscinski (UHN, University of Toronto): Provided α-FGL2 antibodies and *Fgl2*$^{-/-}$ mice.

Funding

- CIHR Doctoral Research Award to Kristianne Galpin
- Cancer Research Society to Dr. Barbara Vanderhyden
- Ovarian Cancer Canada/OvCAN through funding provided by Health Canada to Drs. Barbara Vanderhyden, Gary Levy and Andrzej Chruscinski
- Joan Sealy Trust for Cancer Research to Drs. Barbara Vanderhyden and Rebecca Auer

Thesis advisory committee members

- Dr. Ben Tsang
- Dr. Carolina Ilkow
- Dr. Michele Ardolino

Abstract

Fibrinogen-like protein 2 (FGL2) expression is associated with tumour progression and poor survival in a number of different cancers. In these cancers, FGL2 promotes tumour progression via an immunosuppression-mediated mechanism or by promoting angiogenesis. Querying single-cell RNA sequencing (scRNA-seq) human cancer data shows FGL2 is produced by immune and stromal cells in the tumour microenvironment (TME), while cancer cells have minimal expression of FGL2. We therefore studied the role of FGL2 produced by cells in the TME in tumour progression in two models of cancer in which the role of FGL2 has not been previously studied: epithelial ovarian cancer (EOC) and melanoma.

EOC is the most lethal gynecologic cancer with an imperative need for new treatments. Before testing novel immunotherapies, we first characterized the TME of six syngeneic ovarian cancer models. ID8-*p53*$^{-/-}$ and ID8-C3 tumours were most highly infiltrated by T cells, whereas STOSE and MOE-PTEN/KRAS tumours were primarily infiltrated by tumour associated macrophages and were unique in MHC class I and II expression. This panel of well-defined murine EOC models can serve as a valuable resource for studies that aim to test immunotherapies.

We next studied the role of FGL2 in tumour progression in melanoma and ovarian cancer models. Using wild-type and FGL2 knockout mice, we found that absence of FGL2 led to a more activated TME, including activated dendritic cells (DCs - CD86+, CD40+) and T cells (CD25+, TIGIT+), as well as demonstrating for the first time that the absence of FGL2 led to more activated Natural Killer (NK) cells (DNAM-1, NKG2D) in the TME. The absence of FGL2 prolonged survival in the B16F10 model of melanoma, and synergized with oncolytic virus to prolong survival in the ID8-*p53*$^{-/-}$*Brca2*$^{-/-}$ model of ovarian cancer.

Surgery is a common first-line treatment for many different cancers, including EOC and melanoma. Surgical stress can cause increased metastasis through expansion of myeloid-derived suppressor cells (MDSCs) and NK/T cell dysfunction. We found that FGL2 levels were increased in human and mouse plasma following surgery and were associated with fewer activated NK cells and DCs, suggesting a major role for FGL2 in immunosuppression following surgical stress. In mouse models, the absence of/blocking FGL2 prevented increased lung metastasis caused by surgical stress, suggesting a potential new opportunity to treat in the post-operative window to improve patient outcomes.

Table of Contents

List of Tables

List of Figures

List of Abbreviations

°C	Degrees Celsius
aa	amino acid
ACK	Ammonium-Chloride-Potassium
ARG1	Arginase-1
BRCA	Breast cancer gene (1/2)
CAF	Cancer associated fibroblast
ccRCC	Clear cell renal cell carcinoma
CRC	Colorectal carcinoma
CSCC	Cutaneous squamous cell carcinoma
CTLA-4	Cytotoxic T-lymphocyte-associated antigen-4
DAB	Diaminobenzidine
DAMPs	Damage-associated molecular patterns
DC	Dendritic cell
DMEM	Dulbecco's Modified Eagle Medium
DNAM	DNAX accessory molecule, CD226
EDTA	Edetate calcium disodium
EGF	Epidermal growth factor
EOC	Epithelial ovarian cancer
FFPE	Formalin-fixed paraffin-embedded
FGL2	Fibrinogen like protein 2
GBM	Glioblastoma multiforme
HBV	Hepatitis B virus
HCC	Hepatocellular carcinoma
HGSOC	High grade serous ovarian cancer
HR	Homologous recombination
i.b.	Intrabursal
ICI	Immune checkpoint inhibitor
IF	Immunofluorescence
IFN-γ	Interferon gamma
IHC	Immunohistochemistry
IL	Interleukin
i.p.	Intraperitoneal
i.v.	Intravenous
L	Length
LAG3	Lymphocyte-activation gene 3
LCMV	Murine lymphocytic choriomeningitis virus clone 13
LPS	Lipopolysaccharide
M2	Macrophage 2
MDSC	Myeloid derived suppressor cell
mFGL2	Membrane-bound FGL2
MHV-3	Murine hepatitis virus
MOE	Murine oviductal epithelium
NK	Natural killer
NSCLC	Non-small cell lung cancer
OHRI	Ottawa Hospital Research Institute

OS	Overall survival
OSE	Ovarian surface epithelium
OV	Oncolytic virus
PARPi	Poly(ADP-ribose) polymerase inhibitors
PBMC	Peripheral blood mononuclear cell
PBS	Phosphate buffered saline
PD-1	Programed cell death protein 1
PD-L1	Programmed death ligand 1
PFA	Paraformaldehyde
PGE2	Prostaglandins
PMN	Polymorphonuclear neutrophils
PRRs	Pattern recognition receptors
PW	Peritoneal wash
qPCR	Quantitative reverse transcription-polymerase chain reaction
RT	Room temperature
s.c.	Subcutaneous
sFGL2	Soluble FGL2
TAA	Tumour associated antigen
TAM	Tumour associated macrophage
TCGA	The Cancer Genome Atlas
TGF-β	Transforming growth factor beta
TIGIT	T cell immunoreceptor with Ig and ITIM domains
TIM-3	T cell immunoglobulin and mucin domain-containing protein 3
Th	T helper
TMB	Tumour mutational burden
TME	Tumour microenvironment
TNF-α	Tumour necrosis factor alpha
Tregs	Regulatory T cells
T-VEC	Talimogene laherparepvec
rFGL2	Recombinant FGL2
VEGF	Vascular endothelial growth factor
VSV	Vesicular stomatitis virus
W	Width
WT	Wild type

Acknowledgements

First, I'd like to acknowledge my supervisor Dr. Barbara Vanderhyden for giving me the opportunity to be in her lab. I'm grateful that I was given so many wonderful opportunities to learn so many new techniques, to mentor students, present my work at conferences, and to share my work in publications. Her encouragement and passion for science is unmatched and in combination with her critical eye has helped me be a better scientist. I'm always in awe of her ability to juggle knowledge of dozens of different projects going on in the lab, including three of my own, and is always ready to jump in with guidance and enthusiasm. I am so very thankful for all the ways I've grown both as a scientist and as a person over the past five years, thanks to Barb and the incredible group of people she's brought together in the lab and on the floor.

I can't thank Dr. Galaxia Rodriguez enough for her guidance from day 1 of my PhD, her patience for teaching me her expertise in flow cytometry and immunology is something I'm very grateful for. I'd like to give credit to Dr. Shan Zhao and Dr. Curtis McCloskey who not only made the steep learning curve during my first year of PhD a lot of fun, but who also were the ones who got the FGL2 project off the ground and left it in my (capable?) hands. I would not have gotten very far without Elizabeth Macdonald who patiently taught me how to work with mice, and then kept a steady stream of FGL2 knockout mice for me throughout my PhD. Thank you to all the members of the Vanderhyden lab that have come and gone over the years, eagerly sharing techniques and advice and makes the lab experience such a positive one.

Many thanks to the members of the Ardolino lab, particularly Dr. Marie Marotel and Dr. Shaad Hasim, for providing me with protocols and lending me reagents when my project unexpectedly brought me into the world of NK cells. Thanks as well to the members of the Auer lab for their help and collaboration on the surgical stress project. Particularly to Christiano Tanese de Souza for performing all the i.v. injections and surgeries for this project, as well as for his enthusiasm and encouragement. Thanks to Dr. Leonard Angka and Marisa Market for letting me use their data/samples to complement my findings.

Last but not least, I can't thank my family enough for supporting me and cheering me on through my graduate studies. I'm glad you all can use my stories about mouse mishaps to entertain at social gatherings. Especially thank you to Stephanie for being by my side through all the lows that accompany research and for making all the highs that much sweeter.

Chapter 1: Introduction

1.1. Fibrinogen-like protein 2 (FGL2)

Cancer is a leading cause of death in Canada. Immunosuppressive mechanisms in the TME allows the tumour to escape targeted elimination by the immune system and contribute to this high mortality rate. FGL2, also known as fibroleukin, is an important new player in mediating immunosuppression and is upregulated in a number of different cancers with correlation to poor prognosis (Qin et al., 2014; Tang et al., 2017; Wang et al., 2016; Yan et al., 2015). FGL2 was originally identified in 1987 in mice (pT49 cDNA) as a cytotoxic T-lymphocytic specific gene, sharing 36% homology to fibrinogen beta and gamma subunits (Koyama et al., 1987). The human form, which shares 80% homology to the mouse FGL2 and 25% homology to fibrinogen, was identified in 1995 to be constitutively expressed in both CD4 and CD8 T cells (Rüegg and Pytela, 1995). It was originally described as a novel mouse (Parr et al., 1995) and human prothrombinase (Levy et al., 2000) after hepatitis viral infection induced expression of FGL2 in macrophages. FGL2 is expressed in macrophages (Marsden et al., 2003; Ning et al., 2005; Yang et al., 2013), T cells (notably regulatory T cells (Tregs) and TIGIT+ Tregs) (Joller et al., 2014; Liu et al., 2008; Marazzi et al., 1998; Shalev et al., 2008, 2009), endothelial cells (Cho et al., 2018; Ding et al., 1998; Liu et al., 2003), cancer associated fibroblasts (CAFs) (Zhu et al., 2017), natural killer (NK) cells (Bezman et al., 2012; Yu et al., 2021), innate lymphoid cells 2 (Ghaedi et al., 2019), dendritic cells (DCs) (Yang et al., 2013), and polymorphonuclear neutrophils (PMN) (Zhou et al., 2019).

The FGL2 protein can be found in either a secreted form (sFGL2) (Marazzi et al., 1998) or a membrane-bound form (mFGL2) (Levy et al., 2000). The membrane-bound form is typically expressed on macrophages and endothelial cells (Ding et al., 1998), and has pro-coagulation activity, directly cleaving prothrombin to thrombin (Levy et al., 2000; Yuwaraj et al., 2001). The secreted form of the protein has immunomodulatory functions (Rüegg and Pytela, 1995; Shalev et al., 2008). FGL2 is 439 amino acids (aa) long with a hydrophobic transmembrane domain (aa1-26) in the N-terminus, followed by an α-helical (coiled-coiled domain) which is responsible for the thrombinase activity, and fibrinogen-related domain in the C-terminus (aa200-430) which is responsible for binding to the Fcγ receptors and the immunosuppressive functions (Liu et al., 2013; Yuwaraj et al., 2001). In its native form, FGL2 exists as an oligomer, where FGL2 monomers dimerize and subsequently assemble into a tetrameric complex, joined by disulphide bonds formed by cysteine residues at aa positions 94, 97, 184 and 187 in the α-helical domain. While oligomeric FGL2 has greater affinity for the Fcγ receptors compared to the monomeric form, the monomeric FGL2 has greater immunosuppressive activity, demonstrated by inhibiting T cell proliferation in response to alloantigen (Liu et al., 2013). The serine residue at aa89 (Ser89-Xaa-Xaa-Lys) in mouse FGL2 is responsible for prothrombinase functions of FGL2 (Chan et al., 2002), whereas in human FGL2 a similar motif is found near aa91 (Li et al., 2014).

While it is known that sFGL2 is spontaneously secreted (Marazzi et al., 1998), how sFGL2 becomes secreted is not yet well established, but it should be noted that both mFGL2 and sFGL2 are derived from the same transcript. FGL2 has a putative signal peptidase site aa23, thus cleavage at this site may release sFGL2 from the membrane (Olson et al., 2004). In a mouse model of sepsis, sFGL2 increased while mFGL2 expression in monocytes/macrophages decreased by 6 hours after induction of sepsis, suggesting that while sFGL2 and mFGL2 are expressed together, there may be some control of sFGL2 secretion (Zhou et al., 2019). Furthermore, in this model, they demonstrated that miR-466l increased both sFGL2 and mFGL2 expression in monocytes/macrophages, while treatment with ADAM10 and ADAM17 metalloproteinase inhibitors reduced sFGL2 secretion and increased mFGL2 expression, suggesting ADAM17 is capable of cleaving sFGL2 (Zhou et al., 2019). Generally, studies investigating the role of FGL2 in various disease systems differentiate between the forms only by the functional assays used to answer the research questions. For example, an ELISA on plasma/cell supernatant suggests sFGL2 while immunofluorescence suggests mFGL2.

FGL2 expression in human tissues and murine models can be induced by interferon gamma (IFN-γ) and tumour necrosis factor alpha (TNF-α) (Chan et al., 2003; Marazzi et al., 1998; Rüegg and Pytela, 1995), miR-466l (Zhou et al., 2019), virus infection [murine hepatitis virus (MHV-3), hepatitis c virus (El-Mesery et al., 2017; Foerster et al., 2010), hepatitis B virus (HBV) (Marsden et al., 2003; Van Tong et al., 2018), severe acute respiratory syndrome-associated coronavirus (Han et al., 2008a), murine lymphocytic choriomeningitis virus clone 13 (LCMV) (Luft et al., 2018)], as well as parasitic infection (Fu et al., 2020; Wang et al., 2015). It is also induced by other inflammatory conditions such as colitis (Bartczak et al., 2017; Li et al., 2020; Lin et al., 2017; Zhu et al., 2018), autoimmune hepatitis (Ai et al., 2018), myocarditis (Zheng et al., 2018), sepsis (Zhou et al., 2019), and pancreatitis (Ye et al., 2017). sFGL2 production is reduced in *IL-1R1*$^{-/-}$ mice in response to MHV-3 infection (Guo et al., 2015a) while sFGL2 production is greater in *PD-1*$^{-/-}$ mice in response to inflammatory cytokines (IFN-γ,TNF-α) produced during intracerebral hemorrhage (Yuan et al., 2016). Signalling pathways involved in activation of FGL2 transcription include: MAPK (ERK/JNK) activation of transcription factor c-Ets-2 (Han et al., 2008b), C/EBP (Han et al., 2008a), IFN-γ induction of STAT1 signalling activation of Sp1/Sp3 and GAS/PU.1 (Liu et al., 2006), and transcription factors Oct-1, and Ets-1 (Liu et al., 2003).

1.1.1 mFGL2 as a prothrombinase

mFGL2 was initially characterized as a membrane-bound prothrombinase protein in macrophages and endothelial cells (Ding et al., 1997, 1998). mFGL2 induction in endothelial cells and macrophages has been extensively studied in response to viral infection in mice with fibrin deposition, immune cell infiltration, and necrosis leading to organ damage in liver (HBV and MHV-3; (Ding et al., 1997, 1998; Levy et al., 2000; Marsden et al., 2003; Zhu et al., 2005)) or lungs (severe acute respiratory syndrome-associated coronavirus; Han et al., 2008a). mFGL2 has also been studied extensively in xeno- and allo-transplantation, where mFGL2 contributes to vascular thrombosis, fibrin deposition, and immune cell infiltration, ultimately leading to rejection of the graft (Ghanekar et al., 2004; Mendicino et al., 2005; Ning et al., 2005). mFGL2 expression in maternal decidua and fetal trophoblasts has also been associated with spontaneous abortion in mice (Clark et al., 1999, 1999, 2001). Several antibodies targeting and blocking the prothrombinase function of FGL2 have been developed (Li et al., 1992, 2014). Collectively, the prothrombinase function of mFGL2 has been attributed to fibrosis and poor outcomes in numerous conditions including viral infection and organ transplantation, however knocking out FGL2 or blocking its function with antibodies have improved outcomes in mouse and rat transplant models (Mendicino et al., 2005; Ning et al., 2005).

1.1.2. sFGL2 as an immunomodulatory cytokine

sFGL2-mediated immunosuppression is involved in numerous immunoregulatory processes as shown in viral (El-Mesery et al., 2017; Foerster et al., 2010; Van Tong et al., 2018) and parasitic infections (Fu et al., 2020; Wang et al., 2015), promoting allo/xenograft tolerance (Bartczak et al., 2016; Liu et al., 2008; Pan et al., 2018; Zhao et al., 2014), and restricting progression of autoimmune diseases such as glomerulonephritis (Shalev et al., 2008), hepatitis (Ai et al., 2018), myocarditis (Zheng et al., 2018), and arthritis (Melnyk et al., 2011). It also has protective roles in inflammatory conditions such as myocardial infarction (Zacchigna et al., 2018), sepsis (Zhou et al., 2019), and colitis (Bartczak et al., 2017; Li et al., 2020; Lin et al., 2017; Zhu et al., 2018). sFGL2 acts directly on immune cells to promote immunosuppression and there is additional evidence showing an association between elevated sFGL2 and the presence of immunosuppressive immune cell populations, i.e. indirect effects of sFGL2 (**Figure 1**).

sFGL2 acts via its receptors FcγRIIB and FcγRIII expressed on the surface of macrophages and DCs (both FcγRIIB and FcγRIII) as well as B cells (FcγRIIB only) (Shalev et al., 2008). sFGL2 leads to downregulation of MHC-II expression and co-stimulatory molecules (CD86, CD83, CD80, and CD40) on DCs and macrophages, and upregulation of tolerogenic molecules such as CD31 on DCs (Liu et al., 2008; Shalev et al., 2008; Yang et al., 2019). In a subset of Batf3-dependent migratory DCs, sFGL2 blocks GM-CSF induction of CD103 expression, preventing CD8+ T cell activation (Yan et al., 2019). sFGL2 binding to FcγRIIB on macrophages suppressed MCP-1 expression through JNK activation, leading to reduced recruitment of IFN-γ producing NK and NKT cells (Fu et al., 2020). sFGL2 also directly induces B cell apoptosis upon binding to the FcγRllB receptor (Liu et al., 2008; Shalev et al., 2008).

There has been increasing evidence in several disease systems that an abundance of sFGL2 promotes M2 macrophage polarization, with M2 macrophages being immunosuppressive or anti-inflammatory (Latha et al., 2019; Pan et al., 2018; Yan et al., 2015; Zhu et al., 2018). sFGL2 polarizes activated macrophages to an M2 phenotype with more CD206+ expression and interleukin-10 (IL-10) and TNF-β secretion, but lower TNF-α and IL-12 secretion, through attenuation of p65/pSTAT1/ IkKb signalling (Pan et al., 2018). Hou et al. have confirmed the direct effect of sFGL2 binding FcγRllB receptors to promote M2 macrophage polarization, including increased CD206 expression, secretion of transforming growth factor beta (TGF-β) and IL-10, and expression of immunosuppressive genes such as Arginase-1 (*ARG1*) (Hou et al., 2021). Conversely, FGL2 deletion has been associated with M2 polarization in intrauterine inflammation (Zhan et al., 2021) and renal fibrosis (Wu et al., 2020), where treatment with recombinant FGL2 (rFGL2) improved outcomes in mice (Wu et al., 2020). Furthermore, there has been some evidence that reduced mFGL2 is associated with greater M2 macrophage infiltration in coronary microvascular obstruction (Li et al., 2018). The role of FGL2 in M2 macrophage polarization is clearly context dependent.

Notably, CD25+ FOXP3+ Tregs have high expression of FGL2 (Liu et al., 2008; Marazzi et al., 1998, 1998; Shalev et al., 2008, 2009), suggesting that FGL2 is a Treg effector gene by suppressing T effector cell proliferation via DCs and macrophages (Chan et al., 2003; Liu et al., 2008; Shalev et al., 2008). Indeed *Fgl2*$^{-/-}$ mice have impaired Treg function (Shalev et al., 2008) while overexpression of sFGL2 (*Fgl2*^{Tg} mice) renders Tregs more effective at suppressing effector T cell poliferation *in vitro* (Bartczak et al., 2017). A subset of FOXP3+ Tregs express TIGIT (T cell immunoreceptor with Ig and ITIM domains), which upregulates expression of FGL2 upon activation, selectively suppressing the pro-inflammatory T helper 1 (Th1) and Th17, but not Th2, responses (Ai et al., 2018; Joller et al., 2014). Furthermore, sFGL2 may target T cells directly; a subset of CD8+ T cells have been shown to express FcγRIIB and binding of sFGL2 causes their apoptosis (Morris et al., 2020) or suppresses their proliferation (Ai et al., 2018). Another study suggests that FGL2 can directly bind to the FcγRllB receptor on T follicular helper cells inducing *Prdm1* and immune checkpoint molecules (TIGIT, programed cell death protein 1 (PD-1), T cell immunoglobulin and mucin domain-containing protein 3 - TIM3, and lymphocyte-activation gene 3-LAG3), directly and indirectly inhibiting B cell class switching recombination (Sungnak et al., 2020). These studies show that sFGL2 can target many different immune cell types, promoting immunosuppression via multiple mechanisms (**Figure 1**).

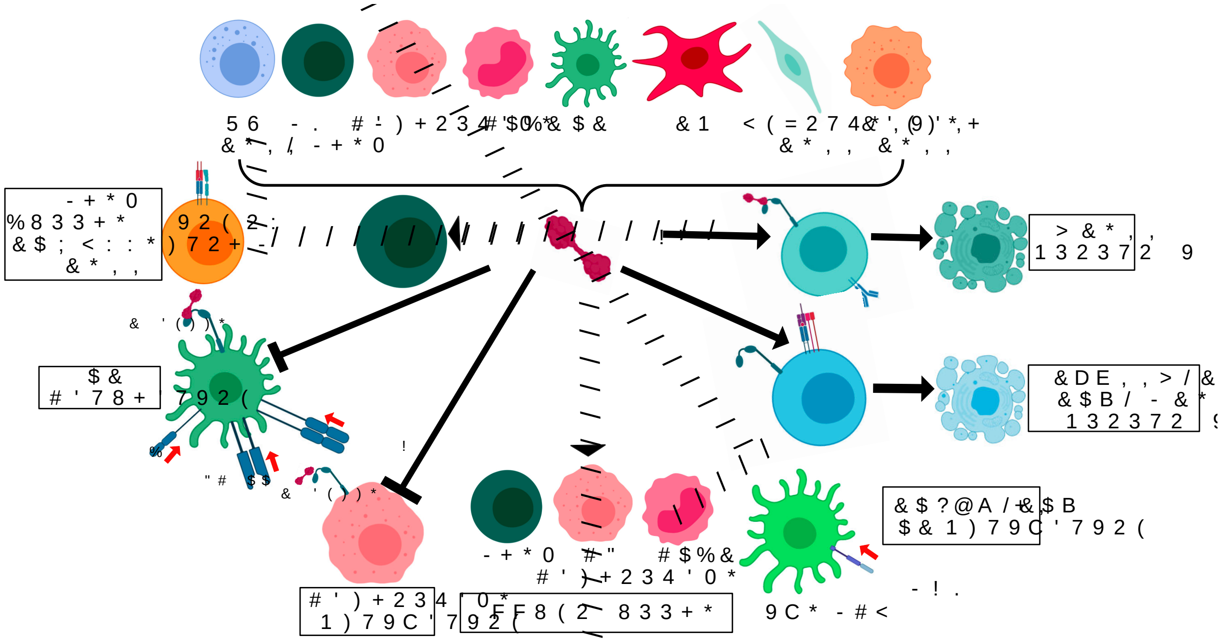

Figure 1. Immunosuppressive functions of sFGL2. FGL2 is expressed in macrophages, T cells (notably Tregs/TIGIT+ Tregs), endothelial cells, cancer associated fibroblasts (CAFs), Natural Killer (NK) cells, Dendritic Cells (DCs), and myeloid-derived suppressor cells (MDSCs). sFGL2 acts directly (solid line) to suppress DC maturation (CD80, CD86, MHC-II downregulation) and macrophage activation. Further contributing to immunosuppression, sFGL2 can directly induce B cell and FCγRllB+CD44^{hi} CD8+ T cell apoptosis. sFGL2 is associated (dotted line) with enhanced Treg suppression of effector T cells, suppression of CD103+CD8α+ DC activation, and with populations of immunosuppressive immune cell populations (Tregs, M2 macrophages, and MDSCs).

1.1.3. sFGL2 and inflammatory conditions

sFGL2 has been commonly studied in responses to transplant tolerance, inflammatory bowel disease, and other autoimmune/inflammatory conditions, where it is primarily associated with immunosuppressive immune cell functions and populations. In allograft models, elevated sFGL2 contributes to tolerance (Pan et al., 2018; Urbanellis et al., 2015; Xie et al., 2012). Administering sFGL2 can prevent tissue rejection (Bartczak et al., 2016; Bézie et al., 2015; Liu et al., 2008; Pan et al., 2018) while blocking FGL2 can induce rejection (Urbanellis et al., 2015). In experimental transplant models, elevated FGL2 leads to more suppressive Tregs (Bartczak et al., 2016) and is associated with immunosuppressive immune cell populations such as M2 macrophages (Pan et al., 2018), CD8+CD45Rlow Tregs (Zhang et al., 2021), tolerogenic CD8+ T cells (Li et al., 2010), and regulatory B cells (Bézie et al., 2015), which prolong survival time through alleviating acute rejection. The extensive research in *in vivo* transplant models, demonstrating the immunosuppressive power of sFGL2 to protect against transplant rejection, is being applied to human transplant science. Using FGL2 as a biomarker in human transplants, specifically patients with an *FGL2/IFNG* expression ratio greater than 1, identified those with optimal transplant tolerance such that 57% of could be safely removed from immunosuppressive treatments and their potential side effects without rejection of the graft (Chruscinski et al., 2021).

Elevated sFGL2 is considered as a biomarker of inflammatory bowel disease (Bartczak et al., 2017; Li et al., 2020; Lin et al., 2017; Zhu et al., 2018) where knocking out FGL2 in experimental mouse models leads to more severe colitis due to impaired anti-inflammatory functions in the absence of FGL2 (Li et al., 2020; Zhu et al., 2018). Experimental induction of inflammatory colitis elevated sFGL2 and reduced TNF-α, IL-6 and IL-1β expression (Li et al., 2020). Knocking out FGL2 increased inflammation and thus severity of the disease through increased expression of TNF-α, IL-1β and IL-17a, decreased expression of IL-10 (Zhu et al., 2018), more M1 macrophages, and greater activation of DCs (MHC-II, CD80, CD86 and CD40) (Li et al., 2020). Furthermore, knockout of FGL2 in immune cells led to increased tumour nodules in colitis-associated cancer (Zhu et al., 2018). Elevated sFGL2 levels are associated with autoimmune hepatitis and experimental autoimmune hepatitis in mice and are thought to limit disease progression by Treg-mediated suppression of CD8+ T cell proliferation and function (Ai et al., 2018). Similarly, *Fgl2*$^{-/-}$ mice develop autoimmune glomerulonephritis (Shalev et al., 2008) due to impaired Treg function while others suggest that *Fgl2*$^{-/-}$ mice develop systemic autoimmune disease similar to Lupus due to impaired regulation of autoantibodies by B cells (Sungnak et al., 2020). Overall, elevated sFGL2 in inflammatory conditions (transplants, inflammatory bowel disease, autoimmune disease) has protective effects by promoting immunosuppression through multiple immune cell types.

1.1.4. FGL2 and cancer

FGL2 is elevated, at the mRNA and protein levels, in the tumours of a number of different malignancies (**Appendix 1**) such as non-small cell lung cancer (NSCLC) (Zhu et al., 2017), colorectal carcinoma (CRC) (Liu et al., 2019; Qin et al., 2014), clear cell renal cell carcinoma (ccRCC) (Tang et al., 2017), cutaneous squamous cell carcinoma (CSCC) (Zeng et al., 2022), glioblastoma multiforme (GBM) (Latha et al., 2019; Yan et al., 2015, 2019), hepatocellular carcinoma (HCC) (Liu et al., 2021, 2012; Sun et al., 2014; Van Tong et al., 2018; Wang et al., 2016; Yang et al., 2019), and prostate cancer (Rabizadeh et al., 2015). Specifically, high levels of FGL2 in tumours is correlated with poor overall survival in GBM (Latha et al., 2019; Yan et al., 2015, 2019), CRC (Qin et al., 2014), ccRCC (Tang et al., 2017), and esophageal cancer (Yuan et al., 2020b), suggesting that FGL2 may be an effective therapeutic target. However, several studies have also reported a correlation between elevated FGL2 and better outcomes in lung cancer (Yuan et al., 2020a), breast cancer (Feng et al., 2020), gastric cancer (Cao et al., 2021), and gastrointestinal stromal tumours (Pulkka et al., 2022), indicating complex, context-specific roles for FGL2 in cancer.

mFGL2 was shown to accelerate tumour progression by promoting tumourigenesis and angiogenesis in liver (Liu et al., 2012; Su et al., 2008), prostate (Rabizadeh et al., 2015), and renal (Tang et al., 2017) cancer, as well as CSCC (Zeng et al., 2022) while sFGL2 is believed to enable tumour growth by promoting an immunosuppressive environment. Previous studies in other disease systems have demonstrated the numerous immunomodulatory roles of FGL2 as described above (**Figure 1**), including inhibiting DC and macrophage maturation, mediating Treg suppression of Th1/Th17 responses, and polarizing M2 macrophages. In data from a human GBM database (Song et al., 2020; Yan et al., 2015), *FGL2* mRNA levels were positively correlated with the abundance of transcripts for immune checkpoints *PD-L1/2, PD-1,* and *LAG3*, as well as immunosuppressive cytokines *IL-10* and *TGFβ1*. In The Cancer Genome Atlas (TCGA) data from NSCLC patients, FGL2 mRNA levels correlated with expression of CAF markers (*FAP*, *PDGFRα*) and MDSC markers (*CD33*, *IL-10*, *CD14*), suggesting FGL2 enhances immunosuppression to promote tumour progression (Zhu et al., 2017).

In GBM, FGL2 was thought to be expressed in the cancer cells (Latha et al., 2019; Yan et al., 2015, 2019) and more highly expressed in high grade gliomas compared to low grade, suggesting FGL2 may be involved in the malignant transformation of glioblastoma (Latha et al., 2019). FGL2 was later shown to act on macrophages, inducing CXCL7, which promotes glioma stem cell migration and differentiation (Yan et al., 2021). Additionally, subcutaneous glioma and brain tumour models in mice expressing high levels of FGL2 led to an increase in expression of PD-1 expressing immune cells and an increase in the percentage of tumour infiltrating Tregs (CD39+FOXP3+), MDSCs (Gr1+CD11b+), and M2 macrophages (F4/80+CD206+) (Yan et al., 2015). This study also provided the first example of using an α-FGL2 antibody for the treatment of cancer (Yan et al., 2015), although it had been used in other disease systems to attenuate immunosuppression (Luft et al., 2018; Ning et al., 2005; Shalev et al., 2009). Therapeutic use of α-FGL2 reduced PD-1 expression and decreased the percentage of Tregs, MDSCs and M2 macrophages in an FcγRIIB dependent manner (Yan et al., 2015). This novel immune therapy led to increased survival (Latha et al., 2019; Yan et al., 2015), by relieving immunosuppression mediated by FGL2 that the tumour uses to escape the immune system. Further studies showed that knocking out FGL2 in the tumours slowed tumour progression, through enhanced migratory CD103+ DCs capable of cross-presenting antigen and activating CD8+ T cells (Yan et al., 2019). In that study, sFGL2 blocked GM-GSF activation of CD103+ expression through inhibition of JAK/STAT and TRAF6 signalling pathways. GBM patients with decreased *FGL2* levels and increased *GM-CSF* levels, as identified in the TCGA (mRNA) expression data, had a longer median overall survival (Yan et al., 2019).

In all these studies the assumption was that FGL2 was expressed by the cancer cells, and in mechanistic studies cancer cells were engineered to express FGL2. However, FGL2 is also expressed in immune/stromal cells in the TME rather than cancer cells, and has similarly been shown to promote immunosuppression in the TME and tumour progression (Li et al., 2019; Yang et al., 2019; Zhu et al., 2017). *Klrg1+Areg*+ Tregs, which develop at late stages of tumour progression in a genetic mouse model of lung adenocarcinoma, were characterized by *Fgl2* gene expression and PD-1 and ST2 (suppression of tumorigenicity 2) protein expression, strengthening the association between FGL2 and highly immunosuppressive immune cell populations (Li et al., 2019). In a mouse model of subcutaneous Lewis Lung Carcinoma (LLC), subcutaneous tumours were generated in *Fgl2* knockout (*Fgl2*$^{-/-}$) mice where tumour progression was slower, compared to wild-type mice, due to decreased CXCL12 recruitment of MDSCs to the tumour and impaired activation of CAFs (Zhu et al., 2017). In syngeneic subcutaneous and orthotopic models of HCC, *Fgl2*$^{-/-}$ or α-FGL2 treated mice had reduced tumour growth with greater proportions of activated CD8+, CD4+ T cells, and DCs, and fewer Tregs in tumours. *In vitro,* sFGL2 inhibited AKT and p38 signalling, preventing DC maturation, as shown by lower levels of MHC-II+, CD40, CD80, CD86, CD83 on CD11c+ cells (DCs) (Yang et al., 2019). Therefore, it is thought that sFGL2 prevents HCC clearance by inhibiting DC maturation and activation of CD4+ and CD8+ T cells.

In several cancer models, overexpressed FGL2 in the cancer cells (GBM) and FGL2 expression in the immune and stromal cells of the TME (LLC and HCC) leads to accelerated tumour progression and poor survival. Furthermore, sFGL2 directly targets DCs, suppressing their ability to activate T cells, and is associated with the presence of tumour infiltrating immunosuppressive immune cell populations (MDSCs, Tregs, M2 macrophages). Knocking out FGL2 or blocking FGL2 (α-FGL2), increases survival by relieving this immunosuppression in these models. While elevated immunosuppressive FGL2 is beneficial in inflammatory conditions, increased immunosuppression in the context of cancer allows for a more permissive environment for cancer cells to evade the immune system and proliferate unchecked. This thesis will focus on two cancer models, in which the role of FGL2 has not previously been studied, to investigate the contribution of FGL2 to tumour progression and immunosuppression. Given our laboratory's expertise in ovarian cancer, we first focused on the role of FGL2 in ovarian cancer progression and then expanded our study to use the B16F10 model to investigate the role of FGL2 in melanoma tumour progression. In addition to expanding our knowledge of FGL2 and cancer, these models provided the opportunity to compare and contrast the role of immunomodulatory FGL2 in two cancer types, one which generally does not respond to immunotherapy in the clinic (ovarian cancer) to one that does (melanoma).

1.2. Epithelial ovarian cancer (EOC)

Ovarian cancer is the fifth most common cause of cancer-related deaths among Canadian women, and the most lethal gynecological cancer (Canadian Cancer Society, 2019a). More than 90% of ovarian cancers are of epithelial origin, while sex-cord, stromal tumours, and tumours of germline origin make up the other 10%. EOC has five main histological subtypes: endometrioid (10%), clear cell (10%), mucinous (3%), low-grade serous (<5%) and high-grade serous (HGSOC, 70%). HGSOC is the most common and lethal subtype, often diagnosed at late stages (III and IV) where it has metastasized throughout the peritoneal cavity and the 5-year overall survival (OS) is less than 40% (Canadian Cancer Society, 2019a).

Standard treatment for EOC involves platinum-based chemotherapy and cytoreductive surgical debulking. However, as many as 85% of patients will relapse and many patients become resistant to first-line chemotherapy. There are limited options and poor outcomes associated with second line chemotherapy treatment of relapsed disease (Berek and Hacker, 2015; Foley et al., 2013). In recent years several targeted treatment options have been developed for the treatment of EOC only two types that have been approved in Canada: the anti-angiogenic bevacizumab and poly(ADP-ribose) polymerase (PARP) inhibitors (PARPi,) (Banerjee and Kaye, 2013; Cortez et al., 2018). PARPi such as Olaparib has been approved by the FDA and Health Canada for the treatment of EOC with germline mutations in the breast cancer gene 1/2 (*BRCA1/2)* (Konecny and Kristeleit, 2016). Alterations in other homologous recombination (HR) proteins result in approximately 50% of HGSOC cases having defects in HR or BRCA-like phenotypes which would potentially make half of all HGSOC cases responsive to PARPi (Cancer Genome Atlas Research Network, 2011). Bevacizumab is a monoclonal antibody against vascular endothelial growth factor (VEGF), a pro-angiogenic factor, and was the first first-line treatment approved by the FDA in decades (Burger et al., 2011; Tewari et al., 2019).

Immunotherapy in ovarian cancer has examined the use of peptide vaccines, transfer of immune cells (T cells, DCs, NK cells), or monoclonal antibody treatment (reviewed in McCloskey et al., 2018; Rodriguez et al., 2018) with varying success. In clinical trials to treat ovarian cancer, immune checkpoint inhibitors (ICIs) have had limited success; inhibitors of cytotoxic T-lymphocyte-associated antigen 4 (CTLA-4), PD-1, and programed death ligand 1 (PD-L1) had response rates of 5–20% (Guo et al., 2015b; Hamanishi et al., 2015, 2016a). In spite of recent developments, OS has not improved in recent decades, largely due to lack of early screening methods, lack of early presenting symptoms, heterogeneity of disease, and the available treatments only work for a small percentage of patients (Cortez et al., 2018). There remains a pressing need to develop novel treatment strategies, including immunotherapy, for the treatment of EOC and HGSOC in particular.

1.3. Melanoma

Melanoma is the seventh most common type of cancer diagnosis in Canada and the 5-year survival rate is approximately 88% when diagnosed at early stages (Canadian Cancer Society, 2019b, 2019c). However, when melanoma has metastasized to either local or distant locations, survival drops to approximately 50% when diagnosed at stage III and down to 20% at stage IV (Canadian Cancer Society, 2019c). Surgery is considered the first-line treatment for most melanoma, and when diagnosed at advanced stages, surgery is often combined with targeted therapies (BRAF and MEK inhibitors), immunotherapy (ICIs, oncolytic viruses - OVs), chemotherapy, or radiation (Curti and Faries, 2021; Tanda et al., 2020). While BRAF and MEK inhibitors have significantly improved survival, resistance does occur, and BRAF is only mutated in around 50% of melanoma (Tanda et al., 2020). Similarly, ICIs have improved overall survival for advanced melanoma to approximately 50%, and although remarkable, a large percentage of people remain resistant or acquire resistance to ICI treatment (Carlino et al., 2021). There is a continued need to develop novel immunotherapeutic treatments for advanced melanoma, and to expand the combination strategies currently used in the clinic.

1.4. Immunotherapy

1.4.1. The tumour microenvironment

Through a process called immunoediting, tumours acquire immune tolerance to neoantigens or tumour-associated antigens (TAA) (Mittal et al., 2014; Schreiber et al., 2011). Initially, the local innate and adaptive immune response targets the cancer cells and can reduce the growth of the tumour. However, the tumour may escape the immune response due to cancer cell evolution, immunosuppression, and exhaustion of the anti-tumour response (Mittal et al., 2014; Schreiber et al., 2011).

In “hot” or immunologically active tumours, the TME is highly infiltrated by tumour infiltrating leukocytes (TILs), DCs and macrophages, NK cells, CD4+ and CD8+ T cells, as well as B cells, capable of generating anti-tumoural responses (Chen and Mellman, 2017; Rodriguez et al., 2018; Zhang et al., 2022). The presence of TILs in tumours from ovarian cancer patients correlates with increased overall survival (Santoiemma and Powell, 2015; Santoiemma et al., 2016; Zhang et al., 2003); specifically a higher ratio of CD8+ T cells to Tregs (CD4+ CD25+ FOXP3+)

is associated with improved survival (Curiel et al., 2004; Preston et al., 2013; Sato et al., 2005). Similarly, TIL infiltration, both density of infiltration and localization of infiltration, is a strong prognostic factor in melanoma prognosis (Lee et al., 2016; Schatton et al., 2014; Thomas et al., 2013).

"Cold" or immunologically silent tumours have few or excluded TILs, loss of MHC-I expression or other components of the antigen presentation machinery, are associated with poor survival (Callahan et al., 2008; Matsushita et al., 2003), and may not respond as well to immunotherapy (Kreuzinger et al., 2017; Kroeger et al., 2016; Lo et al., 2017; Zhang et al., 2003). "Cold" tumours may also be more infiltrated by highly suppressive immune cells, including MDSCs (Yang et al., 2006), M2 macrophages (Hagemann et al., 2006; Lan et al., 2013), and Tregs (Curiel et al., 2004). They may also have upregulated PD-1 on immune cells, and PD-L1 on cancer cells (Kreuzinger et al., 2017), further suppressing anti-tumoural responses. Given that patients with greater T cell infiltration in both melanoma and ovarian cancer have better outcomes, immunotherapy designed to specifically promote immune cell infiltration to the tumour and/or relieve immunosuppression, i.e. to turn a "cold" tumour "hot", may improve survival.

1.4.2 Developing immunotherapy for treatment of EOC and melanoma

Recent advances in immunotherapy have included the use of ICIs, which are monoclonal antibodies against immune checkpoint ligands, to relieve T cell dysfunction in the immunosuppressive TME. Positive response to ICIs has been associated with neoantigen burden (McGranahan et al., 2016; Van Allen et al., 2015); however, ovarian cancers possess low/intermediate levels of neoantigen load/mutation burden which presents additional challenges when developing immunotherapies for the treatment of ovarian cancer (Alexandrov et al., 2013;

Chalmers et al., 2017; Martin et al., 2016). While melanoma has one of the highest levels of neoantigen load/mutation burden (Alexandrov et al., 2013; Chalmers et al., 2017), it is only one factor in the complex TME which predicts response to immunotherapy, with many people still resistant to treatment (Carlino et al., 2021).

Checkpoint inhibitors have been shown to synergize with OVs in mouse models to improve anti-tumour responses and increase survival (Bommareddy et al., 2018; Dummer et al., 2017; Ribas et al., 2017; Swart et al., 2016). OVs selectively replicate in tumour cells, due to defects in anti-viral interferon signalling pathways, triggering direct oncolysis of tumour cells as well as the release of TAAs for presentation to T cells, thereby inducing immunogenic cell death and stimulating immune cell infiltration (Lichty et al., 2014). Talimogene laherparepvec (T-VEC), an oncolytic herpes simplex virus, is the only OV approved by the FDA for treatment of melanoma (Rehman et al., 2016). There are several OVs, including vaccinia (NCT02759588), measles (NCT00408590, NCT02364713), vesicular stomatitis virus (VSV, NCT03120624), and T-VEC (NCT03663712), that are currently in clinical trials for multiple malignancies, including ovarian cancer, although there is no approved OV treatment for ovarian cancer to date. Low or variable response rates to current immunotherapies highlight the increasing need to improve current treatments, search for novel therapeutics or novel combination strategies, and personalize treatments.

1.4.3. Immunotherapy to relieve surgical stress induced immunosuppression

Standard of care for treatment of ovarian cancer includes surgical debulking procedures where complete cytoreduction is a strong prognostic factor (Berek and Hacker, 2015; du Bois et al., 2009; Eisenkop et al., 2003; Li et al., 2012). Similarly, the first-line treatment of melanoma is surgical resection, where complete resection can lead to better prognosis (Curti and Faries, 2021; Faries et al., 2015; Sosman et al., 2011). However, in spite of the benefits of surgery, surgical stress-induced immunosuppression in the post-operative period can lead to enhanced metastatic disease in the case of incomplete resection (Bakos et al., 2018; Coffey et al., 2003; Glasner et al., 2010; Tsuchiya et al., 2003; Tyzzer, 1913).

Tissue injury is marked by an initial pro-inflammatory phase, followed by a second phase which is anti-inflammatory or immunosuppressive in order to restore the normal physiologic balance (Alazawi et al., 2016; Angka et al., 2017; Fullerton and Gilroy, 2016). Damage-associated molecular patterns (DAMPs) released by the host in response to surgery, leads to monocyte recruitment. Pattern recognition receptors (PRRs) on monocytes are activated by DAMPs to secrete pro-inflammatory cytokines such as IL-6 and TNF-α. After this initial pro-inflammatory phase, an immunosuppressive phase is triggered, characterized by anti-inflammatory cytokines (IL-10, TGF-β, and IL-6), prostaglandins (PGE2), and NK cell dysfunction (dampened cytotoxicity and impaired IFN-γ production) (Alazawi et al., 2016; Angka et al., 2017; Fullerton and Gilroy, 2016).

Myeloid-derived suppressor cells (MDSCs) are expanded following surgical stress and are a key player in mediating post-operative NK cell and T cell dysfunction (Lu et al., 2020; Mundy-Bosse et al., 2011; Tai et al., 2018; Urakawa et al., 2019; Wang et al., 2017). There is some indication that surgical stress can also cause declines in populations of both immature and mature DCs in peripheral blood mononuclear cells (PBMCs), although whether this contributes to metastasis has not been as extensively characterized (Brivio et al., 2000; De et al., 2003). While markers have been suggested to identify monocytic (M)-MDSCs (Human: CD33+CD14+HLA-DR-/Low, Mouse: CD11b+ Ly6C+ Ly6G-) and PMN-MDSCs (Human: CD33+CD14-CD15+, Mouse: CD11b+Ly6G+Ly6CLow), their characterization is defined by their suppressive properties on NK and T cells through mediators such as IL-10, TGF-β, and ARG1 (Bergenfelz and Leandersson, 2020; Makarenkova et al., 2006). While MDSC-mediated immunosuppression works to resolve inflammation, it may have negative effects on patients undergoing surgery for malignant tumours (Urakawa et al., 2019). The pro-metastatic mediators and immunoregulatory effectors associated with surgical stress contribute to an environment that allows the remaining cancer cells to evade the immune system and form metastatic tumours (Bergenfelz and Leandersson, 2020; Makarenkova et al., 2006). Indeed, in B16F10 melanoma and 4T1 breast cancer mouse models of surgical stress, mice that received surgery also had increased MDSCs in the spleen, dysfunctional NK cells, and increased metastases (Goldfarb et al., 2011; Tai et al., 2013, 2018). Immunotherapies such as OVs, ICIs, recombinant IL-2, and cellular vaccines have been proposed as perioperative treatment to reduce immunosuppression in the post-operative window (Alkayyal et al., 2017; Bakos et al., 2018; Brivio et al., 2006; Market et al., 2018).

Similarly, in the case of non-sterile tissue injury such as sepsis, pathogen-associated molecular pattern proteins (PAMPs) bind PRRs to activate monocytes and induce MDSCs (Alazawi et al., 2016). In a recent paper, plasma FGL2 was reported to be elevated in both sepsis patients and in a mouse model of sepsis (Zhou et al., 2019). In mice, sepsis induced expansion of PMNs (CD11b+Ly6G+) and monocytes (CD11b+Ly6G-) and FGL2 cleavage by the metalloproteinases ADAM17 and ADAM10 to increase sFGL2 plasma levels (Zhou et al., 2019). In a negative feedback loop, FGL2 then bound to FcγRIIB receptors triggering PMN apoptosis and regulating monocyte efferocytosis, self-limiting the inflammatory response (Zhou et al., 2019). In this model, knocking out FGL2 resulted in a greater pro-inflammatory response and poorer outcomes, whereas supplementing mice with rFGL2 had protective effects (Zhou et al., 2019).

Drawing on parallels between inflammation due to tissue injury from sepsis and surgical stress, we hypothesized that if FGL2 plays a role in resolving the pro-inflammatory response to sepsis, it would similarly play a role in immunosuppression during surgical stress. In that context, FGL2's involvement in post-operative immunosuppression may also lead to increased metastases following surgery.

1.5. Testing immunotherapy in syngeneic models

Immunocompetent mouse models are critical to understand efficacy of new therapies and mechanisms of resistance. Response to immunotherapy in transplantable syngeneic models correlates with MHC-I expression, while the composition of tumour infiltrating immune cells is based on intrinsic (MHC-I, mutation burden, transplant location) and extrinsic characteristics (eg. strain) (Lechner et al., 2013; Mosely et al., 2017; Yu et al., 2018). For example, high MHC-I expression predicts greater response to immunotherapies, such as ICIs, while tumours with low MHC-I expression respond poorly to immunotherapies (Lechner et al., 2013; Yu et al., 2018). Profiling the TME of syngeneic models will help researchers select models to perform immunotherapy studies and may guide patient stratification to maximize efficacy of treatment.

Although the B16F10 model of melanoma is considered a poorly immunogenic and poorly infiltrated tumour (Lechner et al., 2013; Yu et al., 2018) and does not have mutations commonly found in human melanoma such as *BRAF* (Couto et al., 2019), it has been used extensively for *in vivo* pre-clinical testing of immunotherapy, including ICIs (Chen et al., 2015; van Elsas et al., 1999; Spranger et al., 2014), OVs (Bridle et al., 2010; Ricca et al., 2018), or infected cell vaccines (Lemay et al., 2012). This model does not respond well to monotherapies, and has been further used to test combination immunotherapies which can prolong survival in B16F10 bearing mice (Bridle et al., 2010; Chen et al., 2015).

1.5.1. Testing immunotherapy in syngeneic models of ovarian cancer

Roby et al. generated the commonly used syngeneic ID8 model of murine ovarian cancer in 2000 (Roby et al., 2000) through spontaneous transformation by serial passaging of mouse ovarian surface epithelial (OSE) primary cells from C57BL/6 mice. Immunotherapies, including OVs (Gil et al., 2014; Nounamo et al., 2017; Thomas et al., 2016) and ICIs (Guo et al., 2014, 2015b; Wei et al., 2013), have been primarily tested using both parental and modified ID8 cells (reviewed in McCloskey et al., 2018). We (Rodriguez et al., 2022) and others have shown that the ID8 model is poorly immunogenic (Duraiswamy et al., 2013; Martin et al., 2016; van Vloten et al., 2019). Although some studies have demonstrated prolonged survival with immunotherapy over untreated groups (Gil et al., 2014; Nounamo et al., 2017), re-challenging of ID8 tumours is unlikely to show protection to due to a lack of generation of an anti-tumour memory response, the presence of which is a hallmark of successful immunotherapy discovery and development (Galluzzi et al., 2018). Our lab generated a spontaneously transformed cell line, STOSE, derived from the OSE of FVB/N mice (McCloskey et al., 2014) which has also been used to study OVs (Thomas et al., 2016).

While the ID8 model has been invaluable for pre-clinical testing of immunotherapies, other syngeneic models have since been developed in order to more accurately and extensively model HGSOC. Analysis of HGSOC tumours in data from The TCGA suggests that the tumour suppressor gene *TP53* is mutated in 96% of all cases and genetic alterations in *BRCA1/2* genes occur in approximately 30% of tumours (Cancer Genome Atlas Research Network, 2011). Dr. Iain McNeish generated ID8 derivatives with CRISPR/Cas9 deletions in genes relevant to HGSOC including ID8-*Trp53*$^{-/-}$, ID8-*Trp53*$^{-/-}$; *BRCA1*$^{-/-}$, and ID8-*Trp53*$^{-/-}$; *BRCA2*$^{-/-}$ (Walton et al., 2016, 2017).

Cell lines originating from the OSE model only a fraction of HGSOC, as the majority of cases are thought to originate from the fallopian tube epithelium (Coscia et al., 2016; Ducie et al., 2017; Lawrenson et al., 2019). While tumours resulting from STOSE and ID8 cells histologically resemble HGSOC (McCloskey et al., 2014; Roby et al., 2000), their origins from the OSE model only a fraction of HGSOC. To model HGSOC from the fallopian tube, our lab generated a mouse oviductal epithelial (MOE) cell line (Alwosaibai et al., 2017), which Dr. Joanna Burdette's lab subsequently rendered tumourigenic by modifying PI3K/RAS signaling, which is altered in 45% of HGSOC cases (Cancer Genome Atlas Research Network, 2011). Modifications included knockdown of *Pten* (MOE-$Pten^{shRNA}$) alone or in combination with a common gain-of-function mutation (Arg273His) in *Trp53* (MOE-$Pten^{shRNA}$:$Trp53^{R273H}$), or with an activating mutation in *Kras* (MOE-$Pten^{shRNA}Kras^{G12V}$ (Eddie et al., 2015; Endsley et al., 2015).

1.6. Project Rationale and Objectives

High FGL2 expression is associated with more rapid tumour progression and poor survival in a number of different cancers. In these cancers, sFGL2 promotes tumour progression via an immunosuppression-mediated mechanism as an effector of Tregs, attenuating T and DC activation, and mFGL2 accelerates tumour progression by promoting angiogenesis. In both the glioma and hepatocellular models, blocking sFGL2 with an immunotherapeutic antibody significantly prolonged survival. Targeting sFGL2 and attenuating the immunosuppressive TME may reveal a new therapeutic target for the treatment of ovarian cancer. From the literature it is evident that the majority of immunotherapy research for ovarian cancer pre-clinical testing is performed in immunodeficient mice with human cell lines which fails to model the complexities of the immune cells in the TME or with a single syngeneic model, the ID8 cell line, which fails to model either the diversity or heterogeneity of the cancer cells in human disease. Therefore, in order to test a novel immunotherapy (α-FGL2) we **first characterized available syngeneic ovarian cancer models to better understand the variations in the TME and the potential response to immunotherapy.** Furthermore, **we hypothesized that FGL2 expression promotes an immunosuppressive environment that is associated with accelerated tumour progression and poor survival in ovarian cancer and melanoma. Thus, targeting FGL2 to relieve immunosuppression in the TME in combination with activation of specific anti-tumour responses will be a novel therapeutic strategy in treatment of ovarian cancer and melanoma.** Surgical stress can cause increased metastasis through immunosuppression in the post-operative window. Given that surgery is the first line of treatment for many cancers, **we hypothesized that the immunosuppressive functions of FGL2 contribute to the post-operative immunosuppression, and that the deletion or blocking of FGL2 would reduce surgical stress-induced metastasis in an experimental model system.**

Objectives:

1. To define the TME of orthotopic tumours, ascites, and spleens of advanced-stage tumour-bearing mice of syngeneic models originating from both OSE and MOE and bearing clinically relevant mutations.
2. To determine the role of FGL2 in tumour progression of ovarian cancer and melanoma.
3. To determine the efficacy of a novel immunotherapy (α-FGL2) for treatment of ovarian cancer and melanoma in syngeneic models.
4. To investigate the contribution of FGL2 to surgical stress-induced immunosuppression.

Chapter 2. Materials and methods

2.1. Cells and cell lines

Unmodified (wild type, WT) ID8 cells were provided by Kathy Roby (Roby et al., 2000). ID8-*Trp53*$^{-/-}$ F3 (ID8-*p53*$^{-/-}$), ID8-*Trp53*$^{-/-}$*Brca1*$^{-/-}$ and ID8-*Trp53*$^{-/-}$*Brca2*$^{-/-}$, generated by CRISPR-Cas9 mediated knockout, and ID8-C3 (CRISPR control) were generously provided by Dr. Iain McNeish (Imperial College London; Walton et al., 2016, 2017), and maintained in Dulbecco's Modified Eagle Medium (DMEM, Corning) + 4% fetal bovine serum (FBS, Hyclone) and 0.01 mg/mL insulin-transferrin-sodium-selenite solution (ITSS; Roche) as previously described (Walton et al., 2016, 2017). STOSE cells were generated in our lab and maintained in α-MEM (minimal essential media) + 4% FBS and ITSS and 2μg/ml epithelial growth factor (EGF, R&D) as previously reported (McCloskey et al., 2014). MOE-*Pten*^{shRNA} (MOE-PTEN), MOE-*Pten*^{shRNA}:*Trp53*^{R273H} (MOE-PTEN/p53), and MOE-*Pten*^{shRNA}*Kras*^{G12V} (MOE-PTEN/KRAS) were generously provided by Dr. Joanna Burdette (University of Illinois, Chicago) and maintained as previously described (Eddie et al., 2015; Endsley et al., 2015). B16F10 (Overwijk and Restifo, 2001) and B16F10lacZ (Kirstein et al., 2009) cells were maintained in DMEM+10% FBS and were provided by Dr. Rebecca Auer (Ottawa Hospital Research Institute, OHRI). YAC-1 cells (Kiessling et al., 1975, provided by Dr. Michele Ardolino, OHRI) were maintained in RPMI (Corning) + 10% FBS, 1% penicillin/streptomycin, and 10mM HEPES. Mycoplasma testing was performed prior to animal experiments. Cells were incubated at 37°C with 5% carbon dioxide.

NK cells were isolated from splenocytes using EasySep™ Mouse NK Cell Isolation Kit (StemCell Technologies) and MDSCs were isolated from bone marrow using the EasySep™ Mouse MDSC (CD11b+Gr1+) Isolation Kit (StemCell Technologies) according to manufacturer's instructions. NK cells and MDSCs were maintained in complete leukocyte media (RPMI + 10%

FBS, 1% penicillin/streptomycin, 10mM HEPES, and 55µM 2-mercaptoethanol) with or without 4µg/mL recombinant FGL2 in PBS (rFGL2, R&D systems). MDSCs incubated with 1 µg/ml LPS were used as a positive control for CD155 induction (Kamran et al., 2013). Cells were incubated at 37°C with 5% carbon dioxide.

IFN-γ treatment: Cell lines were seeded in 6-well tissue culture plates (Corning) and treated with 500 pg/mL murine IFN-γ (PeproTech) for 24 hours.

Degranulation/Intracellular IFN-γ (Alter et al., 2004): Wells of flat-bottomed plates (Thermo Fisher Scientific) were coated with 5µg of α-NKR-P1C (clone PK136, BD Biosciences) in 100µL phosphate-buffered saline (PBS) overnight. The following day plates were washed 3x with PBS and 1x10^6 splenocytes per well were stimulated for 5 hours in RPMI + 5% FBS in the presence of 1:1000 Golgi Stop (BD BD Biosciences), 1000 IU/mL of recombinant murine IL-2 (BioLegend), and α-CD107a-AF647 (0.025 µg/well, BioLegend), with or without 4µg/mL recombinant FGL2 in PBS (rFGL2, R&D systems). Some cells were stimulated as above with the addition of 400nM Phorbol myristate acetate (PMA, Sigma-Aldrich) and 3.35µM ionomycin (Sigma-Aldrich).

Cytotoxicity: NK cells were isolated as above. 5x10^3 YAC-1 target cells were stained with CP450 (eBioscience) and cultured with isolated NK cells (effector) at indicated ratios for 4 hours in complete leukocyte media, with or without 4µg/mL recombinant FGL2 in PBS (rFGL2, R&D systems). Cells were then stained with ethidium homodimer [EthD, Invitrogen] prior to flow cytometric analysis.

2.2. Mouse models and *in vivo* studies

Animal experiments were carried out using protocols approved by the Animal Care Committee at the University of Ottawa and conforming to the standards defined by the Canadian Council on Animal Care. FVB/N mice (for STOSE and MOE cell lines) were acquired from Charles River and C57BL/6 mice (for ID8 and derivatives) were purchased from The Jackson Laboratory. C57BL/6 (*Fgl2*$^{\mathrm{WT}}$) mice were bred with mice purchased from The Jackson Laboratory. *Fgl2* knockout (*Fgl2*$^{-/-}$) mice, a complete knockout of *Fgl2* and therefore both lacking mFGL2 and sFGL2, were generated by Dr. Gary Levy (Marsden et al., 2003) and were generously provided for these experiments. For all experiments, unless otherwise specified, mice were 8-10 weeks of age, age-matched between *Fgl2*^{WT} and *Fgl2*$^{-/-}$.

For intraperitoneal (i.p.) injections mice received either $25x10^4$ of B16F10 melanoma cells or $5x10^6$ ovarian cancer cells (ID8-WT, ID8-C3, ID8-*p53*$^{-/-}$, ID8-*p53*$^{-/-}$*Brca2*$^{-/-}$*,* STOSE, MOE-PTEN, MOE-PTEN/p53, or MOE-PTEN/KRAS) in 100µl PBS. In an orthotopic intrabursal (i.b) model of ovarian cancer $1.5\ x10^5$ cells (ID8-WT, ID8-C3, ID8-*p53*$^{-/-}$, ID8-*p53*$^{-/-}$*Brca2*$^{-/-}$*,* STOSE, MOE-PTEN, MOE-PTEN/p53, or MOE-PTEN/KRAS) were injected under the ovarian bursa in 2µl PBS as previously described (McCloskey et al., 2014). For subcutaneous (s.c.) injection of B16F10 melanoma cells, $2x10^5$ cells were injected in 100µl PBS into the flank. Subcutaneous tumours were measured using calipers approximately every two days and tumour volume was calculated using the formula width x width x length, where width (W) is the shortest diameter and length (L) is the longer. In all cases mice were assessed for survival until humane endpoint, primarily abdominal distension for mice with ovarian tumours or for mice with s.c. tumours endpoint was reached when the tumour measured 20mm in any direction or the tumour was bleeding/necrotic. Otherwise tumours (primary and metastases) and spleens were collected and processed for flow cytometry at the indicated timepoints.

Characterization of syngeneic ovarian cancer models: As the mice developing i.b. tumours neared humane endpoint (4-5 days before anticipated endpoint), primary tumours, abdominal metastases, spleens, and ascites were collected for flow cytometry, immunohistochemistry (frozen and fixed), immunofluorescence, qPCR, and single-cell RNA sequencing analysis. *In vivo* experiments were performed with the selected cell lines able to form a primary tumour of sufficient size for flow cytometry analysis. The *Brca* mutants were excluded from the *in vivo* study as they had already undergone characterization of immune cell infiltration (Walton et al., 2016).

Immunogenicity: Cells were released from adherent cultures using trypsin (0.05% trypsin, 0.53 mM EDTA), washed 2x with PBS, counted to assess viability, and $5x10^6$ cells/mouse were injected i.p. Tumours were allowed to establish over a period of two weeks. At that time, a second set of cells were released from adherent cultures and irradiated at 100 Gy (ID8) or 60 Gy (STOSE and MOE cell lines), washed 2x, and then $5x10^6$ cells/mouse (or PBS as control) were injected i.p. Mice were monitored for survival until a humane endpoint.

Surgical stress: Female C57BL/6 mice at 15-19 weeks of age (approximately 27g) were used for all experiments. B16F10 or B16F10lacZ cells ($3x10^5$) were injected intravenously (i.v.) immediately prior to induction of surgical stress by abdominal laparotomy and partial nephrectomy as previously described (Seth et al., 2013; Tai et al., 2013). Lungs from B16F10lacZ tumour-bearing mice were collected 3 days after cancer cell inoculation, stained with X-gal as described previously (Kirstein et al., 2009), and visible metastases were counted using a stereomicroscope. In some experiments, lungs from B16F10 tumour-bearing mice were collected at 12-14 days after surgery and metastases on both faces of all 5 lobes of the lungs were quantified using a dissecting microscope. Lungs were snap frozen in liquid nitrogen to subsequently collect RNA and assess expression of melanoma-associated genes.

NK depletion: To deplete NK cells, 200μg α-NKR-P1C (clone PK136, Leinco Technologies) or IgG control antibody (Leinco Technologies) was injected i.p. on days –1 and –2 prior to tumour inoculation, followed by once per week depletions. NK depletion was verified by flow cytometry of spleens at endpoint.

FGL2 antibody treatment: To block FGL2, the monoclonal α-FGL2 (6H12) and the polyclonal α-FGL2 were generously produced and provided by Dr. Gary Levy. The mouse IgG_1 isotype control (clone HKSP) for monoclonal α-FGL2 (6H12) was purchased from Leinco Technologies. A polyclonal IgG control was purified from rabbit serum using Protein A Columns (Thermo Scientific™). For all experiments, 150μg/mouse of the monoclonal α-FGL2 (6H12) or 100μg/mouse of the polyclonal α-FGL2 or their appropriate IgG control was injected in 100μL PBS i.p. For B16F10 s.c. tumour-bearing mice, treatment began on day 3 after tumour inoculation followed by treatment on day 5 and 7 and then twice per week (day 10, 14, 17). For STOSE i.p. tumour-bearing mice, beginning 31 days post i.p. injection, mice received one daily α-FGL2

(6H12, monoclonal) injection for 7 days. For surgical stress experiments, mice were treated with a control IgG antibody or an α-FGL2 (polyclonal) antibody 3 days prior and 3 days post-surgery, as well as on the day of surgery.

Oncolytic virus treatment : VSV-M51-GFP is a recombinant virus with a deletion of methionine 51 in the M protein and encoding GFP (Stojdl et al., 2003). The virus was kindly provided by Dr. John Bell and Dr. David Stojdl (OHRI). The virus was propagated on Vero cells, purified by-ultracentrifugation, and quantified by standard plaque assay, as previously described (Tumilasci et al., 2008). Mice received a total of 3 doses of 1×10^8 pfu VSV-M51- GFP oncolytic virus by i.p. injection in 100µL PBS on days 7, 10, and 13 post-tumour cell injection.

2.3. Flow cytometry

When present, ascites fluid was collected from mice. In other cases, peritoneal wash (PW) was collected following an i.p. injection of 5mL PBS-EDTA (edetate calcium disodium) 1mM for 5 minutes with abdominal massage. Ascites or PW were filtered through a 70µm filter to generate a single-cell suspension of peritoneal cells. Single cell suspensions of spleens were derived by mechanical disruption in PBS+ 2% fetal bovine serum (FBS). Tumours (maximum 1g) were cut into tiny pieces using a razor blade in 2.5 mL of digestion solution following the manufacturer's protocol using the mouse Tumour Dissociation Kit (Miltenyi) and a gentleMACS™ Octo Dissociator with heaters (protocol tumour 37ºC_m_TDK_1). Following the dissociation protocol, the suspension was filtered, and remaining tumour pieces were further disrupted using a syringe plunger on a 70µm filter in order to generate a single-cell suspension. All samples underwent blood cell lysis with ACK (Ammonium-Chloride-Potassium) lysing buffer (VWR). Cells were counted to assess viability (Trypan-blue exclusion) prior to staining. Cells were stained for viability (BD Biosciences Fixable Viability Stain, BV510) at 1:500 per 30x10^6 cells for 15 minutes at room temperature (RT). Fc-blocking antibody (CD16/CD32 - clone 2.4G, Mouse BD Fc Block™, BD Biosciences) was incubated with samples at 3.33µl or 6.67µl for every 20 x10^6 cells from the spleen or the tumours/ascites, respectively, for 5 minutes prior to extracellular staining carried out at RT for 20 minutes. Samples were washed with PBS + 2% FBS and resuspended in 1% PFA and stored overnight at 4°C until analyzed by flow cytometry the following day. Where samples were not stained with BV510 fixable viability stain, such as the case with YAC-1/NK co-culture experiments, cells were stained with ethidium homodimer (PI, Invitrogen) to differentiate live/dead cells prior to flow cytometric analysis and were analyzed on the same day. Data were analyzed by FlowJo software (v10.7.2, TreeStar).

For intracellular staining, we used the Foxp3/Transcription Factor Staining Buffer Set (eBioscience™), following the manufacturer's instructions. Briefly, samples were incubated for 45 minutes at RT with fixation/permeabilization working solution (ebioscience) and then washed twice with 1X Permeabilization Buffer (ebioscience). Anti-IFN-γ, anti-CD206, or anti-ARG1, intracellular antibodies were diluted in the Permeabilization Buffer and incubated with samples for 40 minutes in the dark at RT. Samples were then washed with 1X permeabilization buffer, resuspended in 1% PFA, and stored overnight at 4°C until analyzed by flow cytometry the following day. Data were analyzed by FlowJo software (v10.7.2, TreeStar).

Antibodies for flow cytometric analysis: Anti-CD45 (clone 30-F1), anti-CD3e (clone 145-2C11), anti-CD4 (clone GK1.5), anti-CD8a (clone 53-6.7), anti-CD49b (clone DX5), anti-NKR-P1C (NK1.1, clone PK136), anti-CD25 (clone PC61), anti-TIGIT (clone 1G9), anti-LAG3 (clone C9B7W), anti-CD11b (clone M1/70), anti-Ly6C/Ly6G (Gr1, clone R86-8C5), anti-Ly6C (clone

Al-21), anti-Ly6G (clone 1A8), CD11c (clone HL3), anti-MHC-II (clone M5/114), anti-F4/80 (clone, T45-2342), and anti-CD86 (clone GL1), and anti-CD40 (clone 3/23) were purchased from BD Biosciences. Anti-DNAM-1 (Clone TX42.1), anti-CD155 (clone TX56), anti-PD1 (clone 29F.1A12), anti-CD206 (clone C068C2), anti-CD31 (clone 390), and anti-CD16/CD32 (clone 93) were purchased from BioLegend. Anti-ARG1 (clone A1exF5) was purchased from eBioscience™.

2.4. Immunohistochemistry (IHC) and Immunofluorescence (IF)

For IHC, 5µm sections of formalin-fixed paraffin-embedded (FFPE) tissue were deparaffinized in xylenes and an alcohol gradient, and pressurized antigen retrieval was performed in a citrate buffer (antigen unmasking solution pH 6.0, Dako). Endogenous peroxidase activity was blocked using a 10-minute incubation in 3% hydrogen peroxide. Following PBS washes, sections were blocked for non-specific staining with a protein block (Dako) for 1 hour at RT. Immunostaining was performed in antibody diluent (Dako) using antibodies and conditions listed in **Table 1**. Species appropriate horseradish peroxidase–conjugated secondary antibodies (Vector) were then added for 1 hour at RT. Sections were developed with 0.2% diaminobenzidine (DAB)/0.001% hydrogen peroxide solution (DAB, Sigma, D8001) for 5 minutes followed by counterstaining with hematoxylin (RT for 1 minute). Sections were then rehydrated in an alcohol gradient and xylenes and mounted with Permount (Thermo Fisher Scientific). Images were acquired using the Zeiss AxioScan Z1 (20X objective). Quantification was performed using ImageProPremier (cells/mm^2) and Orbit Image Analysis (percent positive pixels %).

IF experiments were done using 7µm sections of tissue snap frozen in Tissue-Tek O.C.T. compound. Sections stored at -80°C were brought to RT and fixed using ice-cold methanol (MHC-I, ab15681), ice-cold acetone (MHC-I, ab15680), or 2% PFA (CK8+18/MHC-II) for 20 minutes.

Tissue sections were washed 2x with PBS and blocked in 10% goat serum in PBS (+ 0.01% Triton-100 for CK8+18/MHC-II) for 1 hour at RT. Primary antibodies (**Table 1**), followed by secondary antibodies of the appropriate species (Invitrogen), were diluted in 10% goat serum in PBS. Slides were mounted with Immu-Mount (Thermo Fisher Scientific), cured overnight, and visualized on the AxioSkop 2 MOT (Zeiss) microscope (40X objective).

Table 1. Primary antibodies used for IHC and IF staining

Marker	Clone	Catalog	Application	Primary Antibody		Secondary Antibody
				Incubation Time	Dilution	
CD3	CD3-12	Abcam (ab11089)	IHC (FFPE)	1 hr, RT	1:500	Rat
CD4	EPR19514	Abcam (ab183685)	IHC (FFPE)	1 hr, RT	1:500	Rabbit
CD8α	EPR20305	Abcam (ab209775)	IHC (FFPE)	1 hr, RT	1:500	Rabbit
MHC Class II (I-A/I-E)	M5/114.15.2	ThermoFisher (14-5321-82)	IHC (FFPE) IF (Frozen)	O/N, 4°C	1:250	Rat
FOXP3	FJK-16s	eBioscience (14-5773-82)	IHC (FFPE)	O/N, 4°C	1:500	Rat
CD11b	EPR1344	Abcam (ab133357)	IHC (FFPE)	1hr, RT	1:10 000	Rabbit
MHC-I (d,b)	ER-HR-52	Abcam (ab15681)	IF (Frozen)	O/N, 4°C	1:100	Rat
MHC-I (q)	EPRMP42	Abcam (ab15680)	IF (Frozen)	O/N, 4°C	1:100	Rat
PD-L1	D5V3B	Cell Signalling (64988S)	IHC (FFPE)	O/N, 4°C	1:100	Rabbit
CD31	Polyclonal	Abcam (ab28364)	IHC (FFPE)	2 hr, RT	1:50	Rabbit
FGL2	Polyclonal	LsBio (LS-C293889)	IHC (FFPE)	O/N, 4°C	1:500	Rabbit
Cytokeratin 8+18	EP1628Y	Abcam(ab53280)	IF (Frozen)	O/N, 4°C	1:250	Rabbit

2.5. Quantitative reverse transcription-polymerase chain reaction (qPCR)

For RNA extracted from cells, cells were released from adherent cultures using trypsin (0.05% trypsin, 0.53 mM EDTA) and washed with PBS before lysis. RNA was extracted according to the manufacturer's instructions with the Illustra RNAspin Mini Kit (GE Healthcare). RNA was then quantified and quality assessed using a NanoDrop 3300 Spectrometer (Thermofisher) and cDNA was prepared with iScript Reverse Transcription Supermix (Bio-Rad), using 1μg of RNA. Relative gene expression was determined by qPCR SYBR Green Supermix (Bio-Rad) and the Applied Biosystems 7500 Fast Real-Time PCR system to quantify gene expression using primers (Invitrogen) specific to the genes of interest (**Table 2**). Gene expression was calculated as fold increase over untreated cells and normalized to the housekeeping genes *Ppia* and *36B4*.

For RNA extracted from lungs, all 5 lobes of the lungs were homogenized in RLT Plus Lysis buffer (Qiagen) using a rotor-stator homogenizer. RNA was extracted according to manufacturer's instructions with the RNeasy Plus Mini Kit (Qiagen). RNA was then quantified, and cDNA was prepared with iScript Reverse Transcription Supermix (Bio-Rad), using 1μg of RNA. Relative gene expression using primers (Invitrogen) specific to the genes of interest (**Table 2**) was subsequently determined by qPCR using the SsoAdvanced Universal SYBR Green Supermix (Bio-Rad) on an Applied Biosystems 7500 Fast Real-Time PCR instrument. Gene expression of *TRP2* and *GP100* was calculated as fold increase over expression in B16F10 cells, normalized to the housekeeping genes *36B4* and *Ppia*.

Table 2: Primer Sequences

Target	Gene ID	Sequence (5’→ 3’)	
		Forward	Reverse
H2K (d,b)	NM_001001892.2	AGACACAGAAAGCCAAGGG	CACTTCACAGCCAGAGATCAC
H2D (d,b)	NM_010380.3	GGGAAACACAGAAAGCCAAG	AAGTCACAGCCAGACATCTG
H2K (q)	P14428	ACGACACTGAGTTGGTGCGCTTCGAC	ACTCTGCTCATTGTCCTTGGCGATCT
H2D (q)	MF352193.1	GATCACGCAGATCGCCAAGGACAAT	CCGTCGTATGCGTACTGCTCGTACCC
PD-L1	NM_021893.3	TTGCTACGGGCGTTTACTATC	TCCCGTTCTACAGGGAATCT
GP100	NM_021882.5	AGCACCTGGAACCACATCTA	CCAGAGGGCGTTTGTGTAGT
TRP2	AF111107.1	TTAGGTCCAGGACGCCCC	CTGTGC CACGTGACAAAGGC
Ppia	NM_008907.2	AGGGTGGTGACTTTACACGC	GATGCCAGGACCTGTATGCT
Fgl2	NM_008013	GGATGGCAAGTGTTCCAAGT	CCATGGTCTCCATGTCACAG
36B4	NP_031501.1	TGACATCGTCTTTAAACCCCG	TGTCTGCTCCCACAATGAAG

2.6. Enzyme Linked Immunoassay (ELISA)

Murine plasma from ovarian tumour-bearing mice, collected from blood acquired by cardiac puncture into heparin coated capillary tubes (Microvette CB 300 Lh, Sarstedt), or ascites fluid were centrifuged at 2000 x g for 15 minutes. Additionally, murine plasma was collected via cardiac puncture from mice 24 (POD1) or 72 hours (POD3) post-surgery and from those that did not receive surgery. Human ascites supernatants were acquired from the Ottawa Ovarian Cancer Tissue Bank (Ottawa, Canada) with Research Ethics Board approval (Protocol 1999540-01H and 20210799-01H) and informed consent and was frozen at -80°C until assay. Human plasma was collected with The Ottawa Hospital Research Ethics Board approval (Protocol 20160732-01H) from whole blood of healthy donors (n=3) and surgical patients (n=10) prior to surgery (baseline) and on post-operative day 1 (POD1) (Market, 2020). Supernatant was frozen at -80°C until assay.

For mouse and human FGL2 ELISA (BioLegend), ascites and plasma samples were diluted 1:10 and assayed according to manufacturer's instructions.

2.7. LEGENDplex*TM* Bead-Based Immunoassay

Plasma was acquired from blood collected by cardiac puncture into heparin-coated capillary tubes (Microvette CB 300 Lh, Sarstedt). Ascites fluid was collected from mice, centrifuged at 2000 rpm for 15 minutes, and supernatant was frozen at -80°C until assay. Ascites supernatant and plasma samples were diluted 1:2 in assay buffer and assayed according to the manufacturer's protocol for the LEGENDplex™ Mouse Cytokine Release Syndrome Panel (13-plex) Multi-Analyte Flow Assay Kit (BioLegend). Human ascites samples were diluted 1:2 in Assay Buffer and assayed according to manufacturer's protocol for serum/plasma samples with 3 multiplex bead-based assays: LEGENDplex™ Human Cytokine Panel 2 (13-plex), Human Proinflammatory Chemokine Panel (13-plex), Human Inflammation Panel 1 (13-plex) (BioLegend). Samples were acquired in duplicate the same day of staining, on a BD LSR Fortessa™ flow cytometer and analyzed using LEGENDplex Quognit software (Biolegend).

2.8. Single-cell RNA sequencing (scRNA-seq)

ID8 and STOSE tumours (Rodriguez et al., 2022):

scRNA-seq sample preparation: Single cell suspensions were obtained as described above (under Flow Cytometry). Dead cells were removed from the single-cell suspension using the microbead-based Dead Cell Removal Kit (Miltenyi Biotec) according to the manufacturer's protocol. Briefly, $<10^7$ cells were centrifuged at 300xg for 10 minutes and resuspended in 100μl of Dead Cell

Removal MicroBeads. After 15 minutes of incubation at RT, the sample was passed through MACS MS columns (Miltenyi Biotec) and washed, collecting the flow-through of unlabelled live cells. After removal each sample had >80% viable cells.

scRNA-seq library preparation and sequencing: Single-cell suspensions were processed using the 10x Genomics Single Cell 3' RNA-seq kit (v3), loaded to target a yield of 10,000 cells per sample. Cell cDNA libraries were prepared according to the manufacturer's protocol and libraries were assessed using the Fragment Analyzer (Agilent). Libraries were sequenced using the high-output 75 cycle kit on the NextSeq500 (Illumina) achieving approximately 20,000-25,000 reads per cell. For the STOSE tumour sample, we detected a median of 10,321 UMI counts per cell and a median of 3,076 genes. For the ID8 sample, we detected a median of 7,216 UMI counts per cell and a median of 2,517 genes.

Processing of raw sequencing reads: Raw sequencing reads were processed using CellRanger v3.0.2 and the mm10 build of the mouse genome. Default settings were used for both libraries.

Data quality control and processing: Quality control was performed independently on each sample and all main processing steps were performed with *Seurat* v3.0.2(Hao et al., 2021). UMI count matrices from CellRanger were loaded into R and cells with fewer than 200 detected genes were removed. Cells with a high percentage (>25%) of mitochondria-associated transcripts were also removed. The expression values were then normalized with standard library size scaling and log transformation. The top 3000 variable genes were detected using the variance-stabilization transformation (vst) selection method in Seurat. Expression values were scaled, and cell cycle scores and the percentage of mitochondrial reads were regressed out. Principal component analysis was then performed on the data prior to integrating the two tumour samples using the R package *Harmony.* The integrated embedding was then used to cluster cells

(FindNeighbors dims=1:40, FindClusters resolution=0.3) and to a UMAP embedding of the data was generated (dims=1:40). Differential gene expression was conducted by using the ‘subset’ function in Seurat to subset relevant populations of comparison followed by applying the ‘FindMarkers’ function in Seurat using a MAST test comparing ID8 and STOSE tumour subpopulations against each other. Myeloid and lymphocyte populations were identified using an unsupervised reference-based method (Zilionis et al., 2019) while cancer cells (*Krt14, Krt19, Msln, Amhr2*), fibroblasts (*Col1a1, Col1a2*), and endothelial cells (*Pecam, Flt1*) were identified using the indicated markers. Raw sequencing files and processed scRNA-seq data are available at the NCBI GEO accession GSE183368.

ID8/STOSE Cancer cell identity: Projective non-negative matrix factorization 'scPNMF' package (Jablonski et al., 2015) was applied to either the ID8 or STOSE cancer cell populations, and then filtered out non-unique amplitude matrix genes to generate a gene-set comprising the identity of either ID8 or STOSE cancer cells (**Appendix 2**). Gene-sets were validated by scoring every cancer cell in either ID8 or STOSE variants to show enrichment respective to the gene-set and the cancer cells used to generate it.

ID8/STOSE Macrophages: A previously published microarray dataset by Jablonski, et al. (2015) (Jablonski et al., 2015) that identified either M0, M1, or M2 polarized macrophages was leveraged to generate unique gene-sets for each macrophage subpopulation (**Appendix 3**). Standard normalization and scaling methodology was applied to the raw matrix, followed by filtering out genes undetected by the microarray, and then a series of t-tests corrected with FDR against the log2FC difference means was used to generate a gene-set of 306 unique M0 genes, 459 unique M1 genes, and 478 M2 genes. The macrophage population was subset from either ID8 or STOSE sequenced tumours and scored to validate the specificity and accuracy of these gene sets by enrichment.

Human tumours:

scRNA-seq datasets (ovarian cancer (Geistlinger et al., 2020; Qian et al., 2020), melanoma (Jerby-Arnon et al., 2018) , lung (Lambrechts et al., 2018; Qian et al., 2020), breast (Bassez et al., 2021; Qian et al., 2020), and colorectal (Lee et al., 2020; Qian et al., 2020)) were previously compiled and processed (Cook and Vanderhyden, 2022). Analysis scripts are available at https://github.com/dpcook/emp_programs/blob/main/tumour_preprocessing.Rmd.

Human PBMCs:

scRNA-seq datasets were previously compiled and processed from paired cryopreserved PBMC samples from patients at baseline and POD1 (n=6). Samples were collected with Research Ethics Board approval (Protocol 20160732-01H) for the PERIOP-02 clinical trial (NCT02987296) (Market, 2020).

2.9. Statistical analysis

All graphs were prepared in Prism 9.0 or using R (ggplot2, pheatmap, Seurat). Statistical analyses were performed with Prism 9.0 (GraphPad Software Inc.). Student's *t* test was used to compare two groups and one-way analysis of variance (ANOVA) followed by Tukey's multiple comparisons test was used to compare more than two groups. Significance of survival data depicted in Kaplan–Meier plots survival plots were calculated by Log-rank (Mantel-Cox) tests. Results were considered statistically significant at $p \leq 0.05$ (*$p \leq 0.05$; **$p < 0.01$; ***$p < 0.001$; ****$p < 0.0001$). Data are presented as the means ± SD or SEM, as indicated.

Chapter 3: Results

3.1. Characterizing the tumour immune profile of murine syngeneic ovarian cancer models

These results are published in Cancer Research Communications 1 June 2022; 2 (6): 417–433. https://doi.org/10.1158/2767-9764.CRC-22-0017.

The tumour immune profile of murine ovarian cancer models: an essential tool for ovarian cancer immunotherapy research

Galaxia M. Rodriguez[1,2,†], Kristianne J.C. Galpin[1,2,†], David P. Cook[1,2], Edward Yakubovich[1,2], Vincent Maranda[1,2], Elizabeth A. Macdonald[1,2], Juliette Wilson-Sanchez[1,2], Anjali L. Thomas[1,2], Joanna E. Burdette[3], Barbara C. Vanderhyden[1,2,*]

[1]Cancer Therapeutic Program, Ottawa Hospital Research Institute, 501 Smyth Road, Ottawa, Ontario Canada, K1H 8L6.

[2]Department of Cellular and Molecular Medicine, University of Ottawa, 451 Smyth Road, Ottawa, Ontario, Canada, K1H 8M5.

[3]Department of Pharmaceutical Sciences, College of Pharmacy, University of Illinois at Chicago, 900 S. Ashland Ave, Chicago, IL 60607.

[†]These authors contributed equally to this work.

Running title: Tumour immune composition of murine models of ovarian cancer.

*Corresponding author: Barbara Vanderhyden

Cancer Therapeutics Program, Ottawa Hospital Research Institute,
501 Smyth Road, Ottawa, ON, Canada, K1H 8L6.

Phone: 613-737-7700 ext. 70330; Email: bvanderhyden@ohri.ca

Conflicts of Interest

The authors declare no potential conflicts of interest.

Keywords: ovarian cancer, tumour infiltrating immune cells, cold versus hot tumours, tumour mutational burden, immunogenicity.

3.1.1. OSE-derived STOSE tumours express MHC-I and are preferentially infiltrated by M2 tumour-associated macrophages

To fully elucidate the tumour immune composition of syngeneic models, we first assessed how models of similar origins but different strains compare. Orthotopic tumours from OSE-derived ID8-WT from C57BL/6 mice (Roby et al., 2000) and STOSE from FVB/N mice (McCloskey et al., 2014) were collected close to endpoint and pooled for scRNA-seq analysis. Clustering (**Figure 2A**) identified 5 major populations, including cancer, endothelial cells, fibroblasts, and myeloid and lymphocytic immune cells. Although both ID8 and STOSE cancer cells originated from the OSE, and both result in tumours that express markers of HGSOC such as WT1, overall they displayed distinct transcriptional profiles (**Figures 2B and 3A**, **Appendix 2**); e.g. *Amhr2*, *Star*, and *Sox9* were preferentially expressed in ID8-WT and *Ccl2*, *Il33*, and *Col1a3* were expressed in STOSE (**Figure 3B**). There were few cells captured in the lymphoid compartment (including T, NK, and B cells) which prevented further analysis. The myeloid compartment of the two models were distinct (**Figure 2C**). We generated signatures of M0/M1/M2 phenotypes and found that STOSE tumours were enriched with M2 tumour associated macrophages (TAMs) [F13a1 (Wang et al., 2021), Fabp5 (Hao et al., 2018), S100a4 and Arg1(Jablonski et al., 2015)] (**Figure 4, Appendix 3**) (Jablonski et al., 2015). The immunogenicity of the cancer cells was explored by analyzing MHC-I, -II, and PD-L1 transcripts. H2-K1 and H2-D1 expression (MHC-I) was very low in ID8 cells but was more evident in immune and endothelial cell clusters (**Figure 2D**). In contrast, STOSE tumours had strong MHC-I expression in most cellular components, including cancer cells. Some ID8 cancer cells expressed low amounts of H2-Ab1 (MHC-II), but in STOSE tumours, it was attributed only to the immune population. Cd274 (PD-L1) was poorly expressed in the cancer cells and immune populations of both tumour types.

Taken together, the scRNA-seq analysis suggests that STOSE tumours are preferentially infiltrated by immunosuppressive M2 TAM. Although the ID8 and STOSE share the same cellular origin, they have very different MHC-I expression profiles, indicating different capabilities to present tumour associated antigens (TAAs). These differences focused our attention on the immunogenicity and immune infiltration in the syngeneic models.

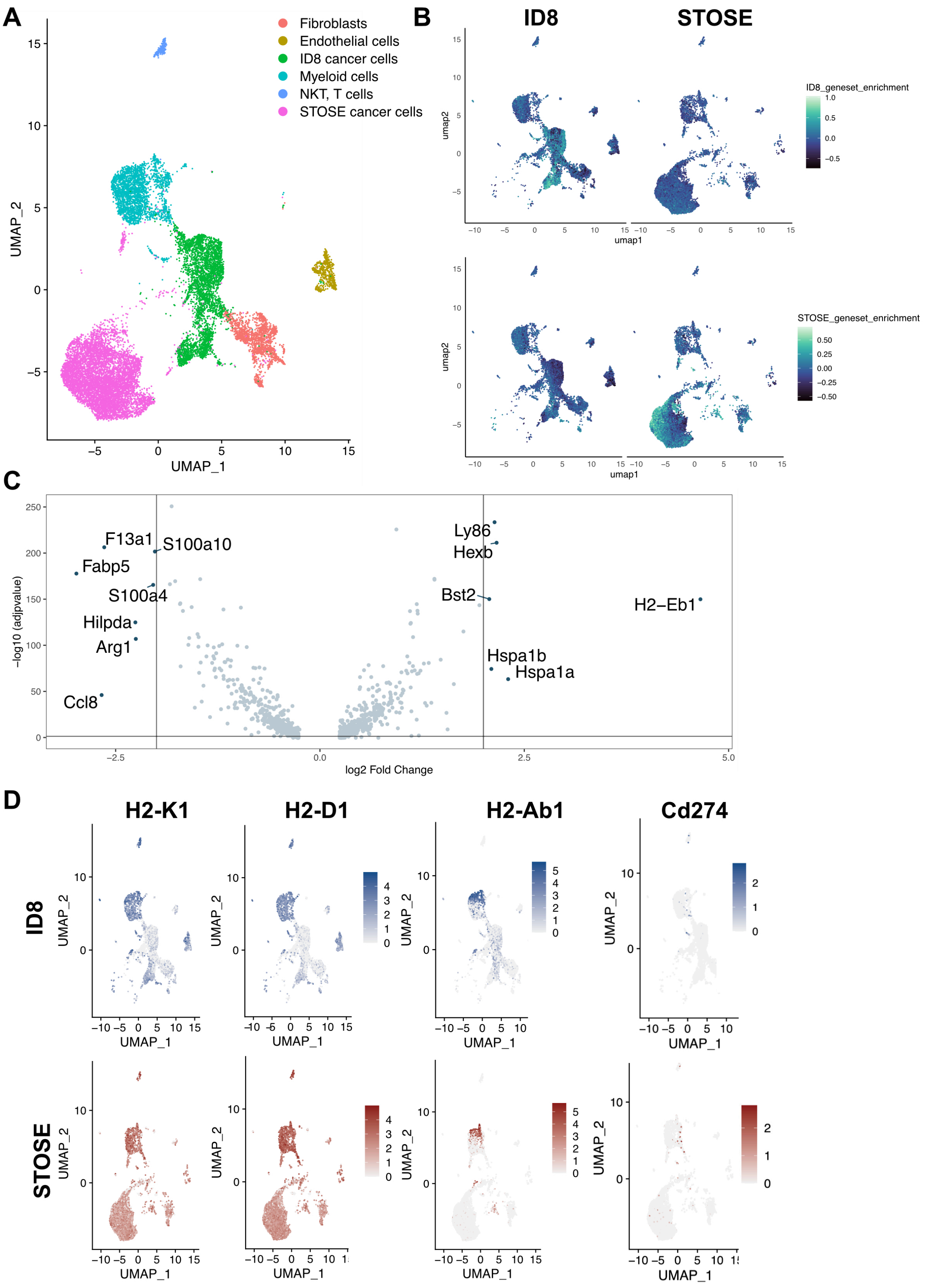
A
Fibroblasts
Endothelial cells
ID8 cancer cells
Myeloid cells
NKT, T cells
STOSE cancer cells
UMAP_1
UMAP_2
B
ID8
STOSE
ID8_geneset_enrichment
STOSE_geneset_enrichment
umap1
umap2
C
F13a1
S100a10
Fabp5
S100a4
Hilpda
Arg1
Ccl8
Ly86
Hexb
Bst2
H2−Eb1
Hspa1b
Hspa1a
−log10 (adjpvalue)
log2 Fold Change
D
H2-K1
H2-D1
H2-Ab1
Cd274
ID8
STOSE
UMAP_1
UMAP_2

Figure 2: Single-cell RNA sequencing reveals high heterogeneity among STOSE and ID8 cancer cells. (A) Single-cell RNA sequencing UMAP figures depicting cell clusters found in orthotopic ID8-WT (left) and STOSE (right) tumours at endpoint. Tumours were integrated into a gene expression matrix containing expression values of 17853 cells and 20091 genes, using Seurat. (B) UMAP plot showing enrichment of individual cancer cells for gene-sets generated for ID8 and STOSE cancer cell identity (Appendix 2). (C) Volcano plot showing the most differentially expressed genes (DGEs) between myeloid cell populations of orthotopic ID8-WT (left) and STOSE-WT (right) tumours beyond log2 fold-change threshold of 2. DGEs calculated using MAST test comparing ID8 and STOSE myeloid cells head-to-head. (D) UMAPs representing expression of MHC-I haplotypes *H2-K1* and *H2-D1*, MHC-II haplotype *H2-Ab1*, and *Cd274* in ID8-WT and STOSE orthotopic tumours. Heatmap displays the level of expression in each cell type cluster (as identified in A) in ID8-WT (blue) and STOSE (red) samples.

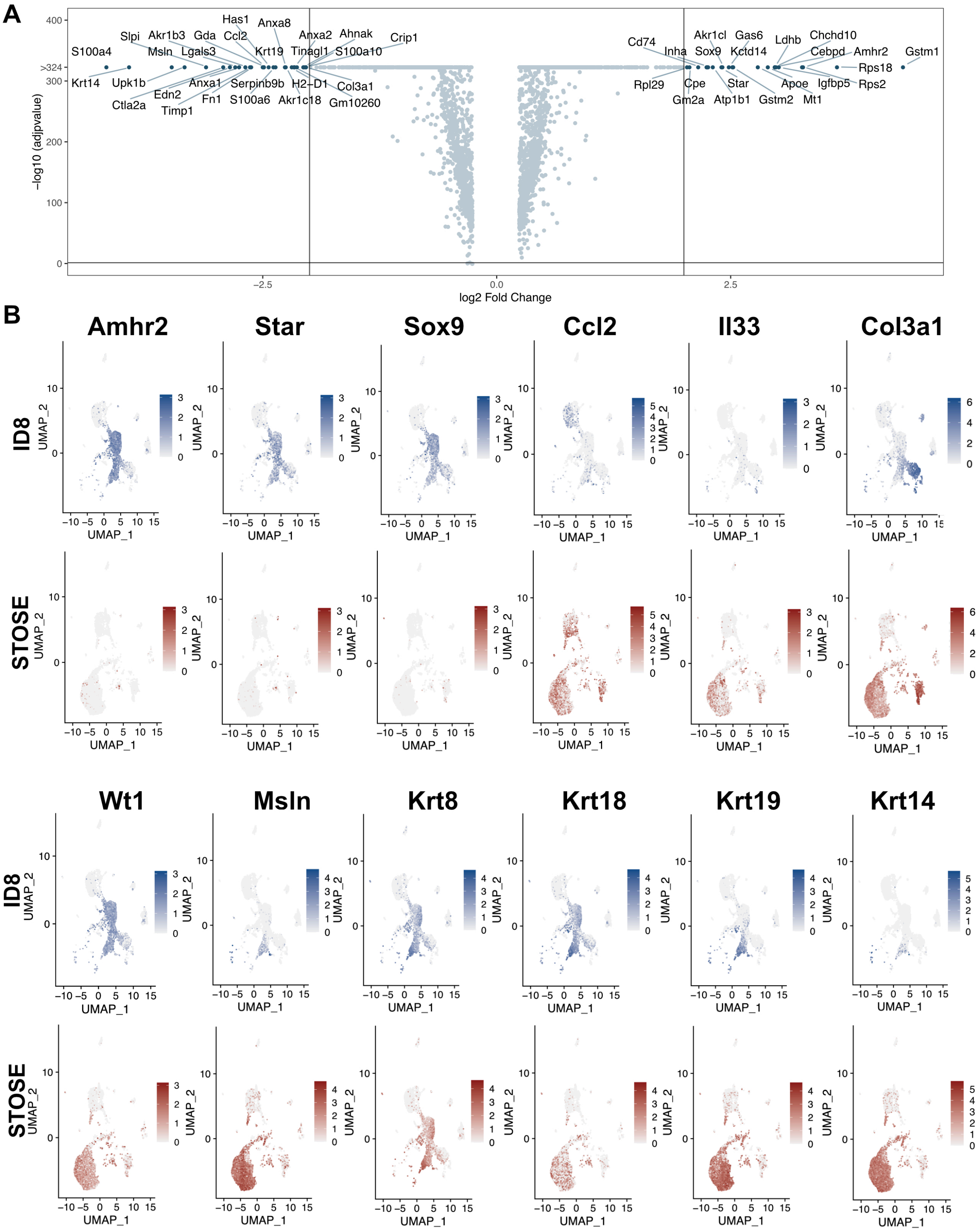
A
400
>324
300
200
100
0
−log10 (adjpvalue)
−2.5
0.0
2.5
log2 Fold Change
S100a4
Krt14
Slpi
Upk1b
Ctla2a
Akr1b3
Msln
Edn2
Timp1
Gda
Lgals3
Anxa1
Fn1
Has1
Ccl2
Serpinb9b
S100a6
Anxa8
Krt19
Akr1c18
Anxa2
Tinagl1
H2−D1
Ahnak
S100a10
Col3a1
Gm10260
Crip1
Cd74
Rpl29
Inha
Gm2a
Akr1cl
Sox9
Cpe
Atp1b1
Gas6
Kctd14
Star
Gstm2
Ldhb
Apoe
Mt1
Chchd10
Cebpd
Igfbp5
Amhr2
Rps18
Rps2
Gstm1
B
Amhr2
Star
Sox9
Ccl2
Il33
Col3a1
ID8
STOSE
Wt1
Msln
Krt8
Krt18
Krt19
Krt14
UMAP_1
UMAP_2
−10 −5 0 5 10 15

Figure 3: Differential gene expression in ID8 and STOSE tumours. (A) Volcano plot showing the most differentially expressed genes (DGEs) between cancer cell populations of orthotopic ID8-WT (left) and STOSE-WT (right) tumours beyond log2 fold-change threshold of 2. DGEs calculated using MAST test comparing ID8 and STOSE cancer cells. P-values were assigned a lower bound of p=1e-324. (B) UMAPs showing expression of *Amhr2, Star, Sox9, Il33, Ccl2, Col1a3, Wt1, Msln, Krt8, Krt18, Krt19, Krt14* in ID8-WT (upper panels) and STOSE (lower panels) orthotopic tumours. Heatmap displays the level of expression in cell types in ID8-WT (blue) and STOSE (red) samples.

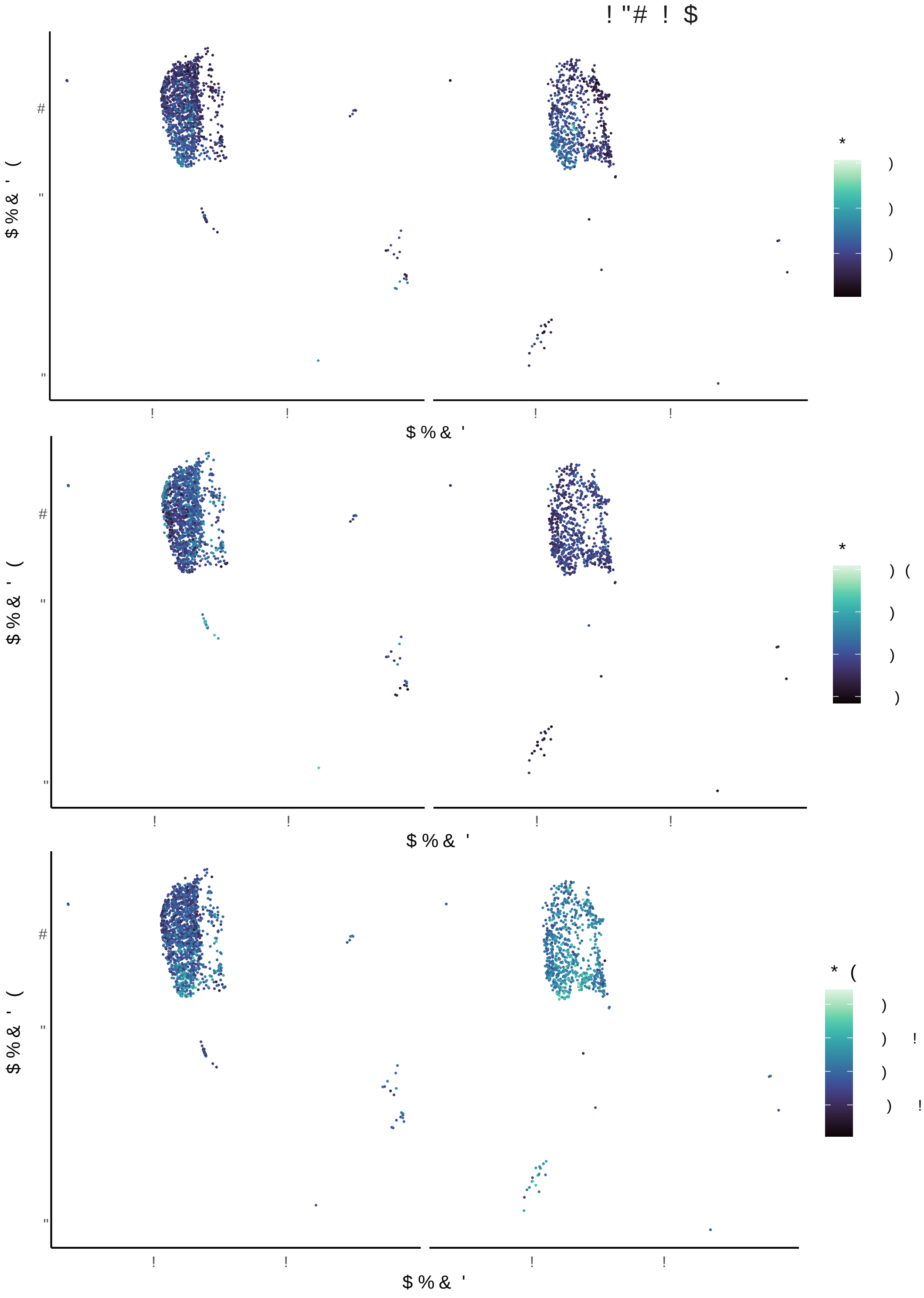

Figure 4: M2 Macrophages are enriched in STOSE tumours. UMAP plot showing enrichment of macrophages for gene-sets (Appendix 3) generated for M0, M1, M2 polarization.

3.1.2. ID8 models have lost MHC class I expression and do not confer anti-tumoural protection when administered as a cellular vaccine

Tumour antigen presentation is essential to activate adaptive immune responses which are fundamental for anti-tumoural immunity. The striking differences in MHC expression in ID8 and STOSE cancer cells prompted us to further investigate the immunogenicity of the syngeneic models. First, we screened 9 EOC cell lines, including those of oviductal origin (Eddie et al., 2015) bearing *Trp53* mutation, *PTEN* suppression, and constitutive KRAS activation, and ID8-derived cell lines (Walton et al., 2016). Using flow cytometry, all ID8-derived cell lines displayed very low levels of MHC-I, MHC-II and PD-L1 expression (**Figure 5A-B**, upper panel), while those sharing the FVB/N background maintained strong MHC-I expression regardless of their genotype or tissue of origin (**Figure 5C-D**, upper panel). To determine if the low MHC-I expression in ID8 cells was reversible, they were treated with IFN-γ for 24h. As shown in **Figure 5A-B** (lower panels), IFN-γ treatment enhanced MHC-I, PD-L1 and to a lesser extent MHC-II expression in ID8 derivatives, with ID8-$p53^{-/-}Brca1^{-/-}$ cells displaying the highest induction of PD-L1. IFN-γ also increased expression of these molecules in the FVB/N cell lines (**Figure 5C-D**, lower panels), with MOE-PTEN/p53 showing the strongest induction of MHC-I expression. PD-L1 levels were most responsive to treatment in STOSE and MOE-PTEN/p53 cells. FVB/N-derived cell lines expressed 5-fold higher levels of PD-L1 compared to C57BL/6 models. qPCR analysis confirmed that transcript levels were consistent with protein levels (**Figure 6)**, suggesting that the lost MHC-I expression in the ID8-derived cell lines is reversible and may be an immune evasion mechanism exploited by these cells.

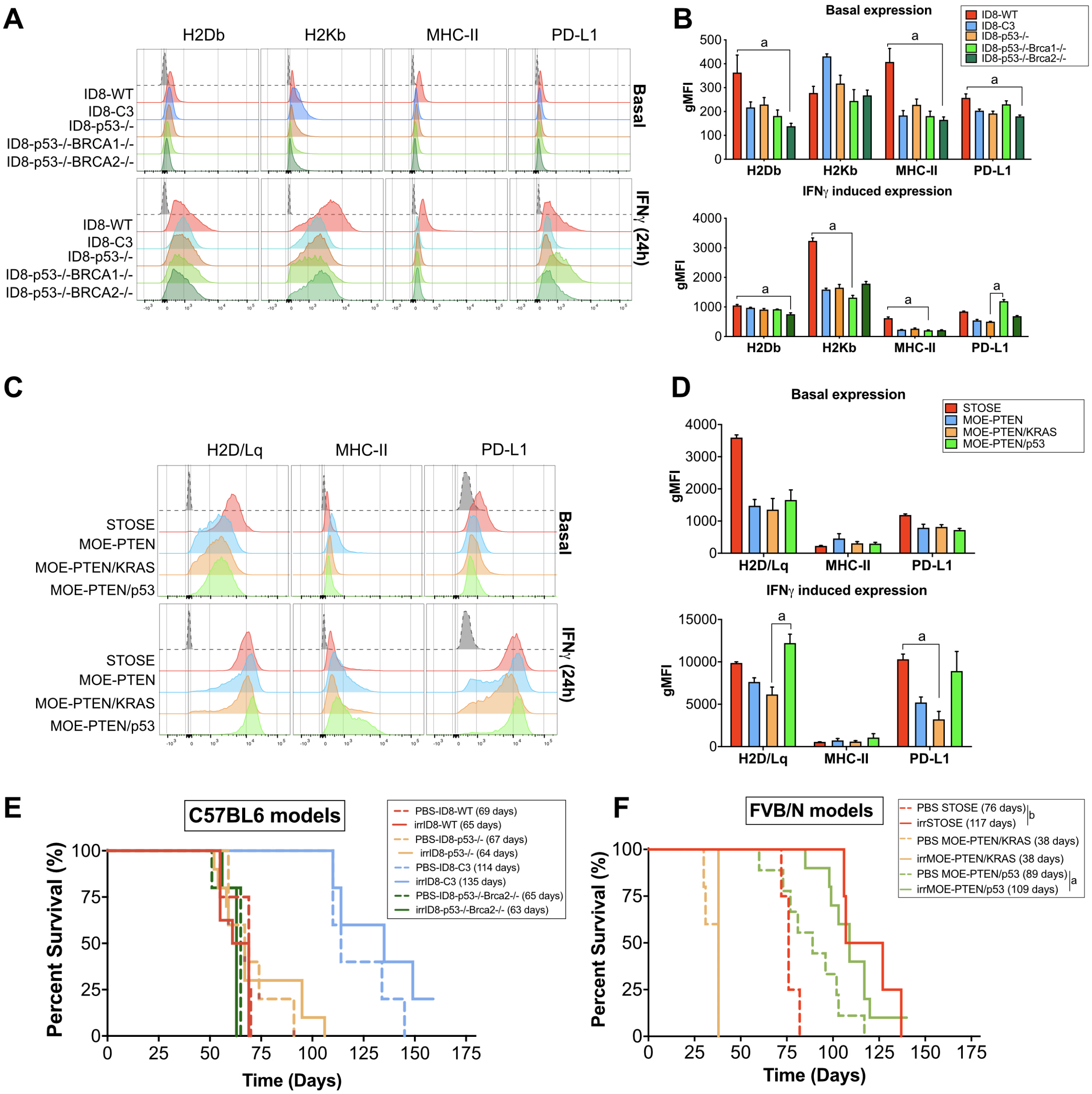

A
H2Db
H2Kb
MHC-II
PD-L1
ID8-WT
ID8-C3
ID8-p53-/-
ID8-p53-/-BRCA1-/-
ID8-p53-/-BRCA2-/-
Basal
IFNγ (24h)
B
Basal expression
ID8-WT
ID8-C3
ID8-p53-/-
ID8-p53-/-Brca1-/-
ID8-p53-/-Brca2-/-
gMFI
a
H2Db
H2Kb
MHC-II
PD-L1
IFNγ induced expression
C
H2D/Lq
MHC-II
PD-L1
STOSE
MOE-PTEN
MOE-PTEN/KRAS
MOE-PTEN/p53
Basal
IFNγ (24h)
D
Basal expression
STOSE
MOE-PTEN
MOE-PTEN/KRAS
MOE-PTEN/p53
gMFI
IFNγ induced expression
a
E
C57BL6 models
PBS-ID8-WT (69 days)
irrID8-WT (65 days)
PBS-ID8-p53-/- (67 days)
irrID8-p53-/- (64 days)
PBS-ID8-C3 (114 days)
irrID8-C3 (135 days)
PBS-ID8-p53-/-Brca2-/- (65 days)
irrID8-p53-/-Brca2-/- (63 days)
Percent Survival (%)
Time (Days)
F
FVB/N models
PBS STOSE (76 days)
irrSTOSE (117 days)
b
PBS MOE-PTEN/KRAS (38 days)
irrMOE-PTEN/KRAS (38 days)
PBS MOE-PTEN/p53 (89 days)
irrMOE-PTEN/p53 (109 days)
a
Percent Survival (%)
Time (Days)

Figure 5: Ovarian cancer cell lines originating from FVB/N mice are more immunogenic. (A-D) *In vitro* expression of MHC-I, MHC-II and PD-L1 on ID8 and its derivative cell lines. Flow cytometry on single, viable cells. Fluorescence minus one (FMOs) are depicted in grey. (A) Histograms represent the mean fluorescence intensity (MFI) of each marker at basal levels (upper panels) and after IFN-γ treatment for 24h (lower panels). (B) IFN-γ induction for the proteins of interest was quantified and depicted as geoMFI (n=3). Significance was determined by Kruskal-Wallis test, a: $p<0.05$. (C) Histograms showing basal expression of MHC-I haplotypes, MHC-II and PD-L1 on STOSE and MOE cell lines, which are further induced by IFN-γ treatment. gMFI quantification shown in (D). (E) Survival Kaplan-Meier plots of ovarian tumour-bearing mice from C57BL/6 strain and treated with syngeneic cellular vaccines. 5×10^6 cancer cells were irradiated (100 Gy) and injected IP two weeks after injection of the same number of viable cells. PBS was injected as a control. Curves represent mice as follows: n=5 PBS for each model, n=8 ID8-WT, n=5 ID8-C3, n=10 ID8-*p53*$^{-/-}$, and n=5 ID8-*p53-/-Brca2*$^{-/-}$. (F) Survival Kaplan-Meier plots of FVB/N-derived ovarian cancer cell lines, treated with syngeneic cellular vaccines (irradiated at 60 Gy) as in E. Curves represent mice as follows: n=4-10 PBS for each model, n=4 STOSE, n=4 MOE-PTEN/KRAS, n=10 MOE-PTEN/P53. Log-rank (Mantel-Cox) a: $p<0.05$, b: $p<0.01$.

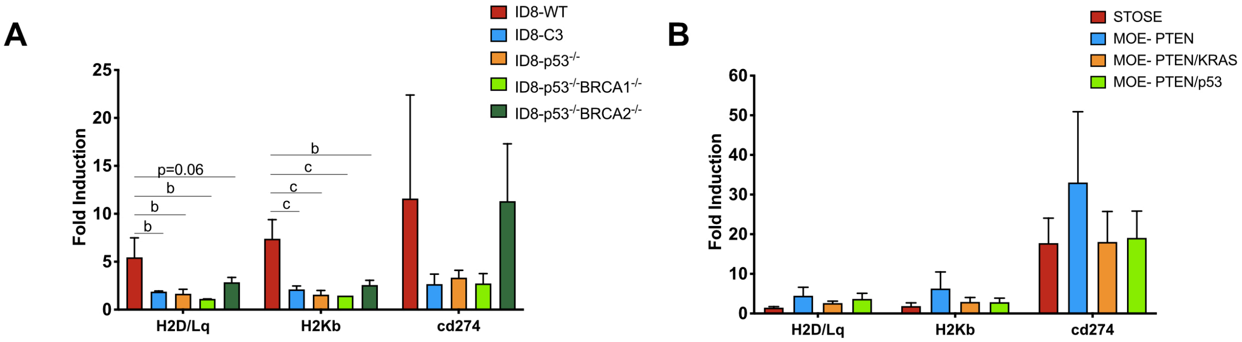

Figure 6: Expression of MHC-I and PD-L1 in various ovarian cancer cell lines. H2K, H2D, and CD274 expression under IFNγ treatment for (A) C57BL/6 and (B) FVB/N-derived cell lines. Fold induction was determined by RT-qPCR for each cell line relative to untreated samples and normalized to the housekeeping gene *Rplp0*. Cells were treated with 500 pg/mL IFNγ for 24 hours. n=3 independent replicates. Significance was determined by one-way ANOVA with Tukey's post-test, b: $p<0.01$; c: $p<0.001$.

To test the immunogenicity of the syngeneic models *in vivo*, mice were injected IP with viable cells and 14 days later, received lethally irradiated cells IP. Mice injected with irradiated ID8 derivatives reached endpoint at a similar time as control mice (**Figure 5E**), corroborating the poor immunogenicity of these cell lines. Conversely, inoculation of irradiated STOSE and MOE-PTEN/p53 significantly increased median survival of tumour-bearing mice compared to the control groups (**Figure 5F**). Despite the fact that all the cell lines could significantly increase MHC-I, MHC-II, and PD-L1 expression under IFN-γ treatment, only the STOSE and MOE-PTEN/p53 were immunogenic, evident by the increased survival of tumour-bearing mice when the cells were administered as a cellular vaccine.

3.1.3. STOSE and MOE-PTEN/KRAS orthotopic tumours are preferentially infiltrated by myeloid-like immune cells

To further characterize the syngeneic models, orthotopic tumours were generated by injecting $0.15x10^6$ cells under the ovarian bursa. Each cell line resulted in mice reaching median survival in a time frame that was similar to that observed when cells were injected at a higher number ($5x10^6$ cells) into the peritoneal cavity (**Table 3**). MOE-PTEN and MOE-PTEN/p53 were the exceptions, with lower frequencies of orthotopic tumour development (6% and 15%, respectively) even after 300 days. Comparing mouse, spleen, and tumour masses (**Figure 7**), we observed STOSE and MOE-PTEN/KRAS cells tended to generate larger orthotopic tumours (**Figure 7C**), while ID8-derived models generated more extensive peritoneal disease (**Figure 7D**) and ID8-WT mice had higher ascites accumulation (**Figure 7E**). STOSE and MOE-PTEN/KRAS models progressed quickly in the last week before humane endpoint, developing extensive peritoneal metastasis and ~4mL of ascites. Histologically, tumours consisted of very dense epithelioid cells and increased nuclear atypia, with the STOSE model having frequent association with adipocytes (**Figure 7F**). MOE-PTEN/KRAS tumours consistently contained multiple small areas of necrosis (**Figure 7G**).

Table 3: Tumour development characteristics of murine orthotopic ovarian cancer models[a]

					Orthotopic tumour burden at time of collection[c]				
Strain	**Tumour model**	**Median survival IP tumours[b] (days)**	**Median survival IB tumours (days)**	**IB take rate (%)**	**Time of collection (days)**	**IB tumour (g)**	**Ascites (ml)**	**Peritoneal metastasis (g)**	**IB tumours (%)**
FVB/N	STOSE	76	74 (63-84)	14/14 (100%)	64	0.55 ± 0.26	3.5 ± 2.8	0.1 ± 0.06	13/14 (92%)
	MOE-PTEN^{shRNA} KRAS^{G12V}	34	44 (40-48)	15/15 (100%)	42	0.79 ± 0.38	1.15 ± 1.9	0.18 (6/14)	11/14 (78%)
	MOE-PTEN^{shRNA}	126	NA	1/15 (6%)	NA	NA	NA	NA	1/15 (6%)
	MOE-PTEN^{shRNA} P53^{R273H}	96	127 (120-129)	6/40 (15%)	120	0.11 ± 0.08	3.0 ± 2.8	0.34 ± 0.46 (5/6)	6/40 (15%)
C57BL/6	ID8-WT	67	65 (57-72)	18/18 (100%)	64	0.13 ± 0.09	7.35 ± 4.5	0.52 ± 0.25	15/18 (83%)
	ID8-C3 (CRISPR control)	114	115 (108-121)	4/4 (100%)	110	0.12 ± 0.06	0.75 ± 1.5	0.18 ± 0.16	9/10 (90%)
	ID8-Tp53-/- F3	66	62 (53-70)	14/14 (100%)	54	0.13 ± 0.03	6.87 ± 1.4	0.32 ± 0.05	9/10 (90%)

[a] 8-10 week old female mice were injected in the ovarian bursa with 0.15x106 cells to trigger orthotopic tumour development. For phenotyping, tumours, spleens and ascites were collected to characterize their immune composition by flow cytometry, IHC, and single cell sequencing technology.

[b] 5x106 cells are administered IP.

[c] Time of collection was 4-5 days before theoretic median endpoint.

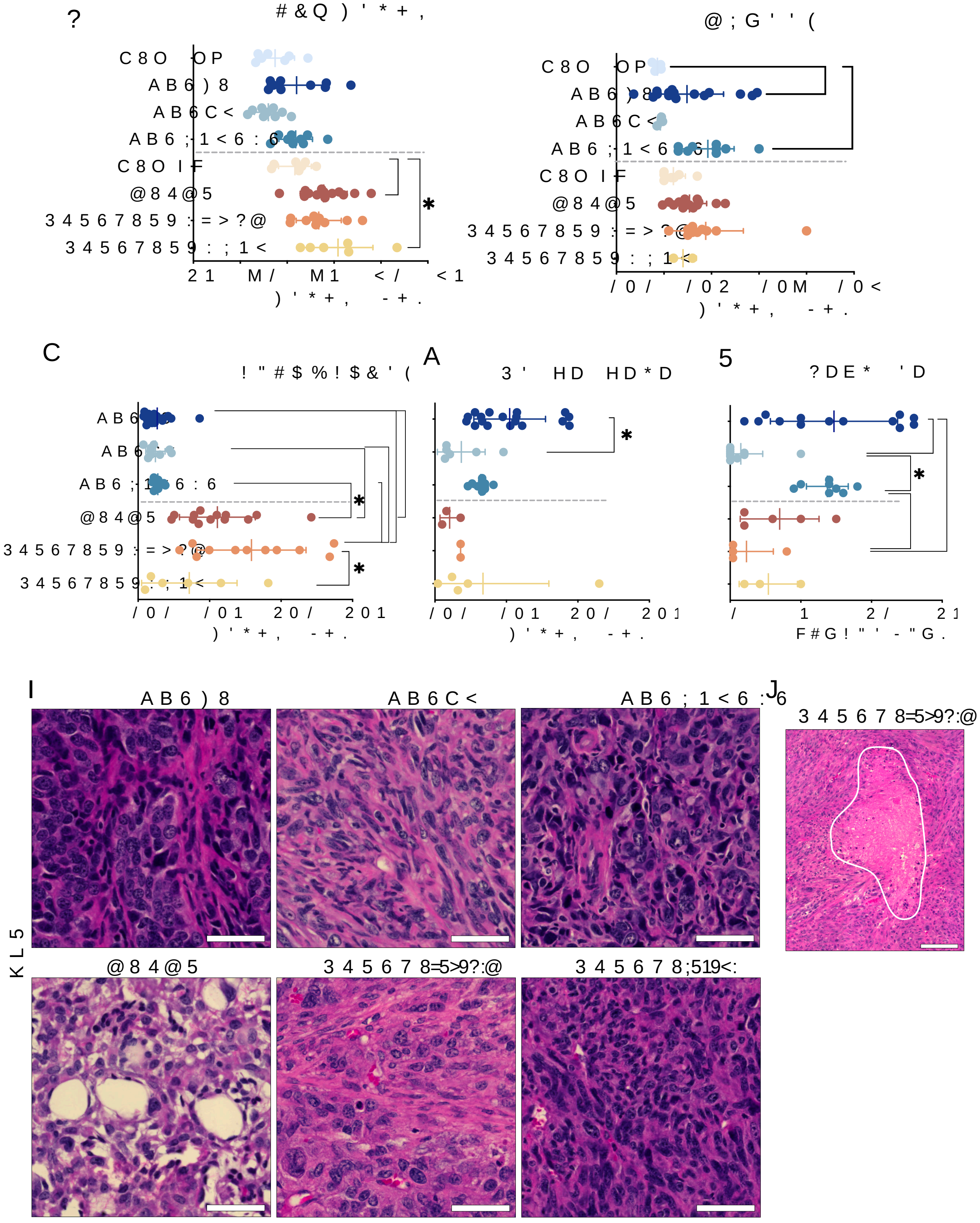
?
& Q) ' * + ,
@ ; G ' ' (
C
! " # $ % ! $ & ' (
A
3 ' HD HD * D
5
? D E * ' D
I
J
K L 5
*

Figure 7: Tumour phenotype of various murine ovarian cancer models. Mice were euthanized 4-5 days before reaching humane endpoint and the mass of (A) mice and (B) spleen weights, (C) primary tumours, and (D) metastases, as well as (E) ascites volume were collected and recorded. Each dot represents an individual sample. Mean values with SD are shown for each tumour model. Statistical significance was determined using one-way ANOVA with Tukey's multiple comparison test, a: $p<0.05$; b: $p<0.01$; and c: $p<0.001$. (F) Representative histological sections of hematoxylin and eosin staining displaying overall characteristics of the tumour niche of each orthotopic tumour. Images are representative of ID8-WT (n=9), ID8-C3 (n=6), ID8-*p53*$^{-/-}$ (n=9), STOSE (n=12), MOE-PTEN/KRAS (n=6), MOE-PTEN/p53 (n=6) tumours. Scale bars = 50µm. (G) Representative image of MOE-PTEN/KRAS tumour with hematoxylin and eosin staining with a region of necrosis outlined. Scale bars = 200µm.

To compare the immune cell composition, orthotopic tumours were analyzed by flow cytometry following the gating strategy shown in **Figure 8** and, in parallel, by IHC staining. We performed a conventional screen for T cells, MDSCs, TAMs, monocytes, and DCs (**Figure 9**), as well as additional markers to assess their potential functional phenotype. Data were normalized for each main population and summarized in a heatmap with unsupervised hierarchical clustering (**Figure 9A**)**.** The data cluster samples from each model together, highlighting the distinct TME of each model. Overall, MOE-PTEN/KRAS and STOSE are more infiltrated by myeloid populations, while the ID8-*p53*$^{-/-}$ and ID8-C3 tumours are more infiltrated by T cells (**Figure 9B**). Notably, the ID8-C3 (CRISPR control) is not equivalent to the ID8-WT.

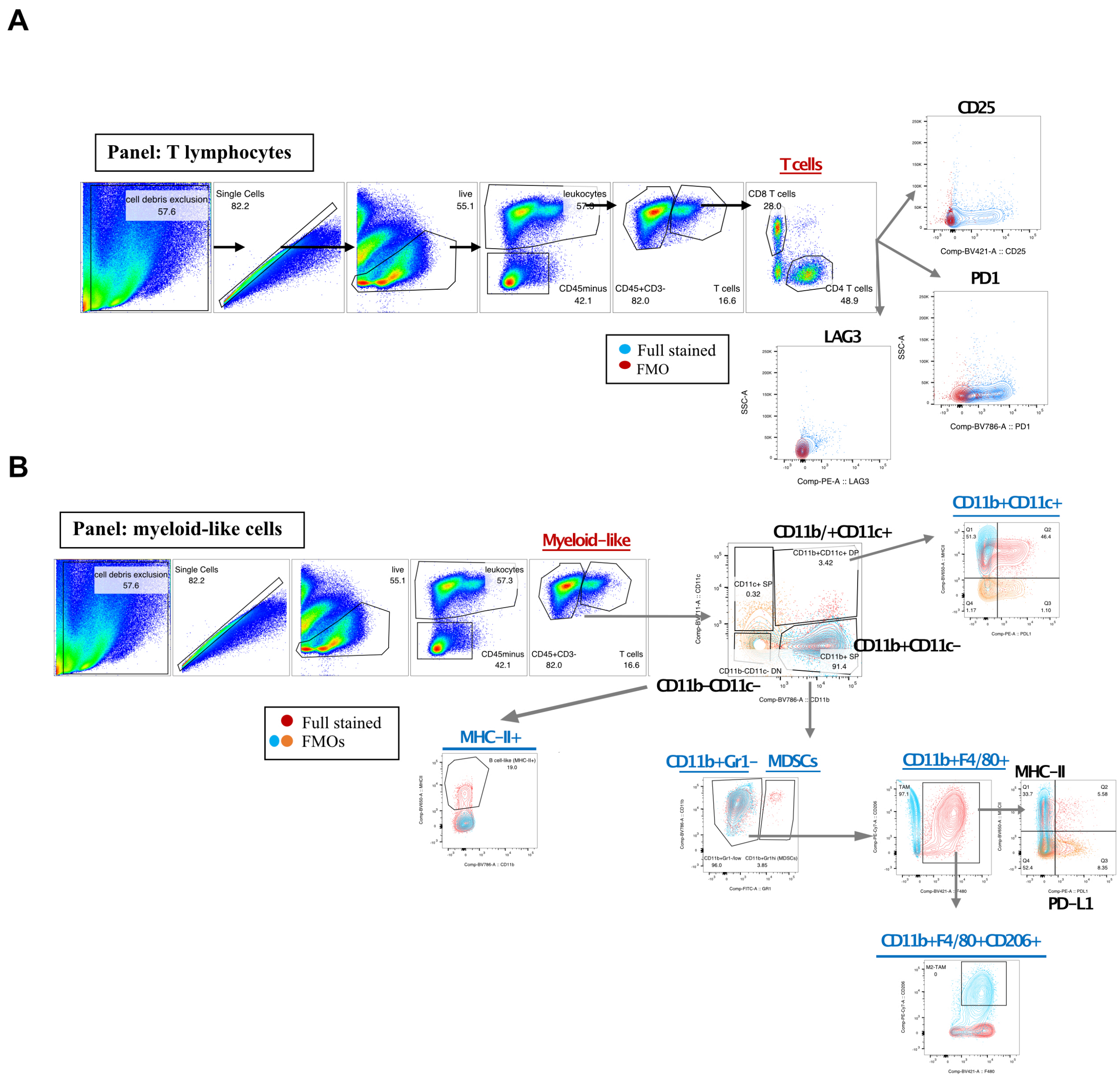

Figure 8: Gating strategy for analysis of flow cytometry data. Orthotopic murine tumours, spleens and peritoneal fluid were collected near the endpoint and processed to be analyzed by flow cytometry or IHC. (A) Gating strategy used to analyze the flow cytometry data as follows: cell debris exclusion, singlet, live/dead exclusion, leukocytes (CD45+), CD3- (myeloid-like), CD3+ (T cells). Other markers included in the T cell panel were CD4, CD8, PD1, LAG3 and CD25. (B) In the "myeloid-like" panel, the following markers were used to further identify other immune subsets: CD11b, CD11c, Gr1, MHC-II-, PD-L1, F4/80, and CD206. CD11c+ includes lymphoid-lineage DCs; CD11b+CD11c+ myeloid-lineage DCs. The subset CD11b+CD11c- was further gated for Gr1 high/low expression to discriminate between MDSCs (CD11b+Gr1+) and CD11b+Gr1-/low cell types (monocytes, macrophages). Further gating in the CD11b+Gr1- subpopulation allowed for the identification of TAMs (CD11b+F4/80+) and CD206+ TAMs (M2-like macrophages) within the same population. Contour plots representative of fluorescence minus one (FMOs) for each analyzed marker.

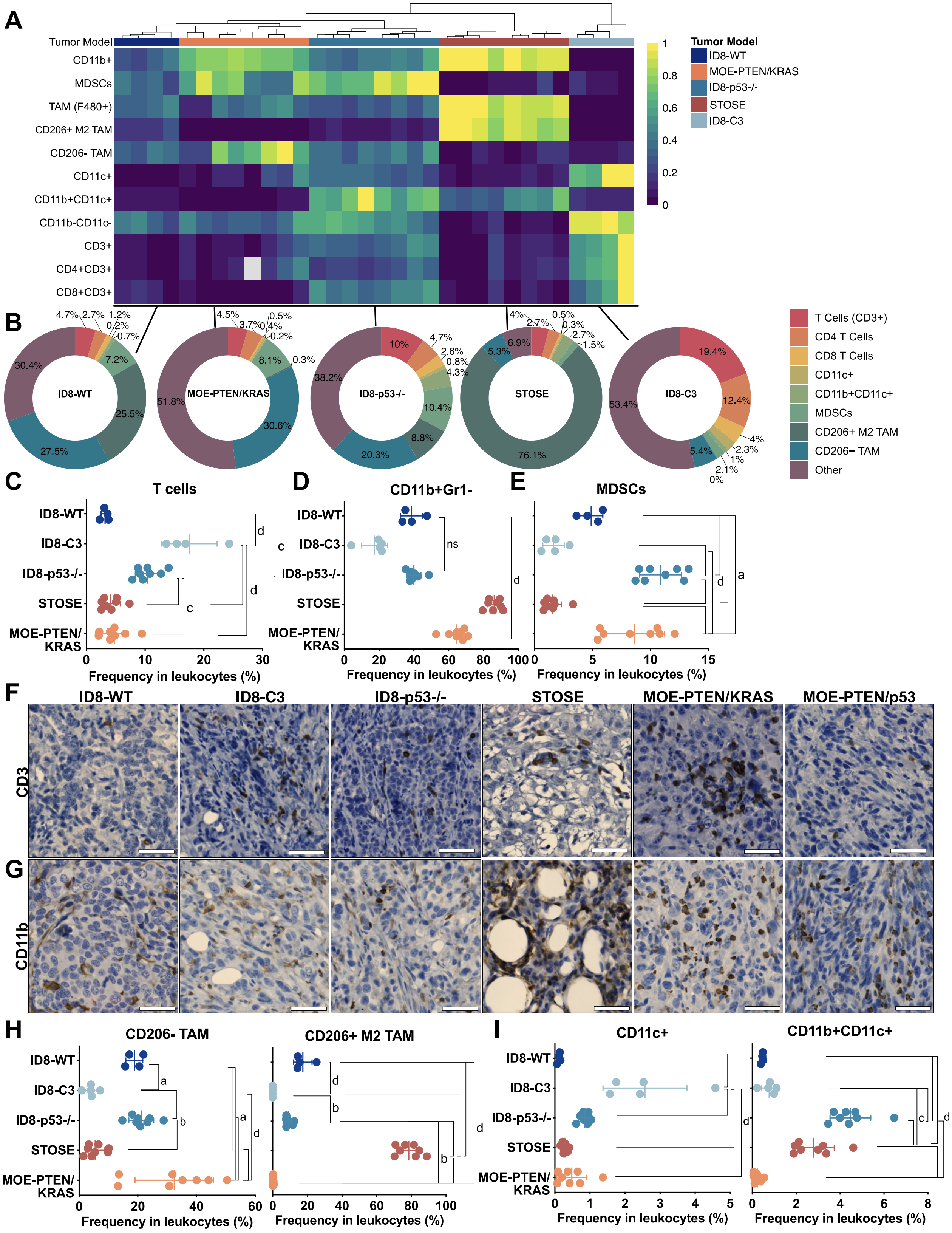
A
Tumor Model
CD11b+
MDSCs
TAM (F480+)
CD206+ M2 TAM
CD206- TAM
CD11c+
CD11b+CD11c+
CD11b-CD11c-
CD3+
CD4+CD3+
CD8+CD3+
1
0.8
0.6
0.4
0.2
0
Tumor Model
ID8-WT
MOE-PTEN/KRAS
ID8-p53-/-
STOSE
ID8-C3
B
ID8-WT
4.7% 2.7% 1.2% 0.2% 0.7% 7.2% 25.5% 27.5% 30.4%
MOE-PTEN/KRAS
4.5% 3.7% 0.4% 0.5% 0.2% 0.3% 8.1% 30.6% 51.8%
ID8-p53-/-
10% 4.7% 2.6% 0.8% 4.3% 10.4% 8.8% 20.3% 38.2%
STOSE
4% 2.7% 0.5% 0.3% 2.7% 1.5% 76.1% 5.3% 6.9%
ID8-C3
19.4% 12.4% 4% 2.3% 1% 2.1% 0% 5.4% 53.4%
T Cells (CD3+)
CD4 T Cells
CD8 T Cells
CD11c+
CD11b+CD11c+
MDSCs
CD206+ M2 TAM
CD206− TAM
Other
C
T cells
ID8-WT
ID8-C3
ID8-p53-/-
STOSE
MOE-PTEN/KRAS
d
c
d
c
0
10
20
30
Frequency in leukocytes (%)
D
CD11b+Gr1-
ID8-WT
ID8-C3
ID8-p53-/-
STOSE
MOE-PTEN/KRAS
ns
d
0
20
40
60
80
100
Frequency in leukocytes (%)
E
MDSCs
d
a
0
5
10
15
Frequency in leukocytes (%)
F
ID8-WT
ID8-C3
ID8-p53-/-
STOSE
MOE-PTEN/KRAS
MOE-PTEN/p53
CD3
G
CD11b
H
CD206- TAM
ID8-WT
ID8-C3
ID8-p53-/-
STOSE
MOE-PTEN/KRAS
a
b
a
d
0
20
40
60
Frequency in leukocytes (%)
CD206+ M2 TAM
d
b
d
b
0
20
40
60
80
100
Frequency in leukocytes (%)
I
CD11c+
ID8-WT
ID8-C3
ID8-p53-/-
STOSE
MOE-PTEN/KRAS
d
0
1
2
3
4
5
Frequency in leukocytes (%)
CD11b+CD11c+
c
d
0
2
4
6
8
Frequency in leukocytes (%)

Figure 9: ID8-C3 and ID8-p53$^{-/-}$ tumours recruit more T cells, while STOSE and MOE-PTEN/KRAS are more infiltrated by TAMs. (A) Heatmap depicts normalized relative frequency of all the studied immune cell populations for all tumour models, determined by flow cytometry. White square is an omitted outlier sample. (B) Pie charts showing relative distribution of main immune cell populations within each tumour type based on frequency (%) in CD45+ cell population. Other includes CD11b-CD11c- and CD11b+F480- populations. (C) Percentage of CD3+ cells in leukocytes found in orthotopic tumour models as assessed by flow cytometry. Total frequency among leukocytes of CD11b+Gr1- (D) and MDSCs (E). (F) Immunohistochemical detection of CD3+ cells in tumours showing CD3 stained clusters in MOE-PTEN/KRAS samples. See Figure 10A-C for quantification of cells/mm^2 and cluster representation at a lower magnification. (G) Representative images showing CD11b+ cells for all tumour models. Sections were counterstained with hematoxylin (blue) and positive cells (brown) were stained with DAB. Scale bars = 50μm. See Figure 11B for quantification of cells/mm^2. (H) Frequencies of CD206- TAMs and CD206+ M2 TAMs as well as (I) CD11b-CD11c+ and CD11b+CD11c+ DCs as determined by flow cytometry. For flow cytometry analysis, cell frequencies were determined by discriminating doublets, dead cells, and CD3+/- cells (see Figure 8). Each dot represents an orthotopic tumour. Mean values with SD are shown. Significance was determined by one-way ANOVA with Tukey's post-test comparing all models, ns: not significant; a: $p<0.05$, b: $p<0.01$; c: $p<0.001$; d: $p<0.0001$.

ID8-WT tumours possess the "coldest/immune desert" profile with very poor T cell recruitment, while ID8-*p53*$^{-/-}$ and ID8-C3 tumours have the highest frequencies of T cells (>10% of all leukocytes) (**Figure 9C**). Quantification of these cells by IHC supported the findings by flow cytometry and scRNA-seq, with ID8-WT and STOSE tumours being poorly infiltrated by CD3+ cells (**Figures 9F** and **10A**), despite the fact that the STOSE model was able to confer anti-tumoural protection when administered as a cellular vaccine (**Figure 5F**). Due to frequent rejection of tumours in the orthotopic MOE-PTEN/p53 model, the TME was only evaluated by IHC, which revealed CD3+ cells in similar abundance as in MOE-PTEN/KRAS tumours, with slightly higher CD3+ cells/mm^2 compared to STOSE (**Figures 9F** and **10A**). Interestingly, while CD3+ cells were randomly distributed in most tumours, they formed distinct clusters or areas with intense staining in MOE-PTEN/KRAS tumours (**Figures 9F** and **10B**), although necrotic areas were largely devoid of T cells. Quantification of CD3+ staining in primary vs. metastatic lesions revealed that ID8-WT metastases had proportionally more CD3+ cells, while metastases from STOSE tumours had fewer CD3+ cells (**Figure 10C**).

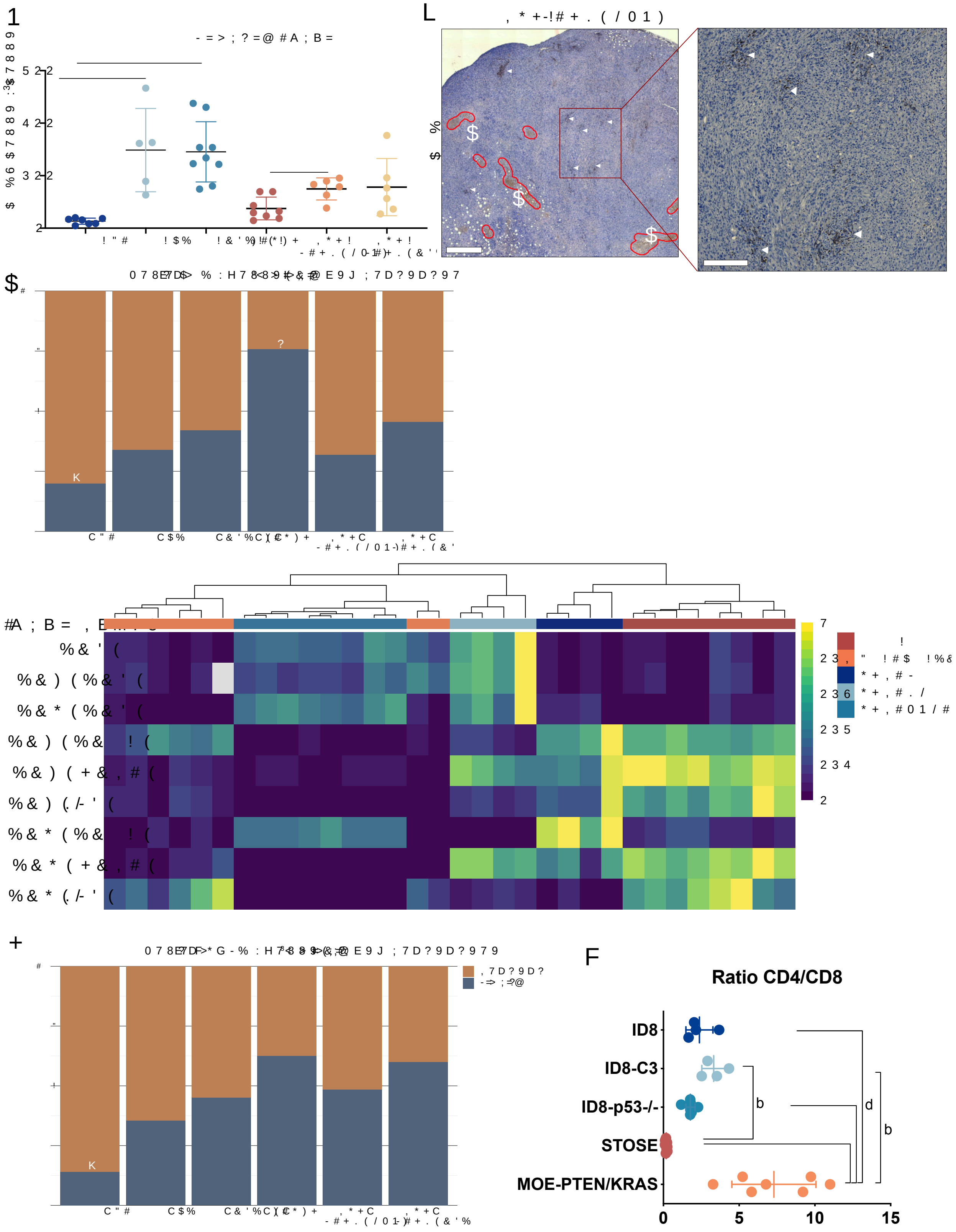
F
Ratio CD4/CD8
ID8
ID8-C3
ID8-p53-/-
STOSE
MOE-PTEN/KRAS
0
5
10
15
b
d
b

Figure 10: Abundance of T cells in the TME of syngeneic ovarian cancer models. (A) Quantification of CD3+ cells by IHC. Cell counts (number of cells/mm^2) were quantified using ImagePro Premier. Each dot represents a single tumour sample as follows: ID8-WT (n=8), ID8-C3 (n=6), ID8-*p53-/-* (n=9), STOSE (n=8), MOE-PTEN/KRAS (n=6), MOE-PTEN/p53 (n=6). Mean values with SD are shown for each tumour model. Significance was determined by one-way ANOVA within C57BL/6 or FVB/N models with Tukey's post-test or a two-tailed Student's t-test (comparing ID8 and STOSE), a: p<0.05; b: p<0.01; c: p<0.001. (B) Representative images of IHC for CD3 staining of MOE-PTEN/KRAS tumour sample revealing CD3 clusters. Scale bars = 1mm (left panel) and 200µm (right panel). White arrowheads in left panel indicating clusters of CD3+ cells are further magnified in the right panel. Asterisks (*) indicate outlined necrotic areas deprived of cells with non-specific staining. (C) Relative abundance of CD3+ cells in primary vs. metastatic tumours. Metastatic tumours were stained and quantified as with primary tumours. ID8-WT (n=9), ID8-C3 (n=6), ID8-$p53^{-/-}$ (n=10), STOSE (n=6), MOE-PTEN/KRAS (n=3), MOE-PTEN/p53 (n=5). Significance was determined by Student's t-test, a<0.05, b<0.01. (D)Heatmap depicting normalized relative frequencies of T cell subsets as determined by flow cytometry for all tumour models. White square is an omitted outlier sample. (E) Relative abundance of FOXP3+ cells in primary vs. metastatic tumours. Metastatic tumours were stained and quantified as with primary tumours presented in 2E. Data representative of ID8-WT (n=10), ID8-C3 (n=5), ID8-$p53^{-/-}$ (n=9), STOSE (n=7), MOE-PTEN/KRAS (n=3), MOE-PTEN/p53 (n=5) samples. Significance was determined by Student's t-test, b<0.01. (F) Ratio of CD4/CD8 T cells. Each dot represents a single sample derived from the supernatant of ascites from tumour-bearing mice. Mean values with SD are shown for each tumour model. Significance was determined by one-way ANOVA with Tukey's post-test comparing all models, b: p<0.01; d: p<0.0001.

Detailed analyses of the myeloid-like populations are summarized in **Figures 9A, 9B** and **11A.** Further analysis of the CD11b+ population with Gr1 co-expression identified MDSCs (CD11b+Gr1^{hi}), a heterogeneous population of polymorphonuclear MDSCs (PMN-MDSC) and CD11b+Gr$^{-/low}$ cells including monocytes, macrophages, and DCs (Bronte et al., 2016). MOE-PTEN/KRAS and STOSE were the most infiltrated by CD11b+ cells (CD11b+CD11c-Gr1^{low}) representing more than 75% of all leukocytes (**Figure 9D**) and in STOSE tumours almost 1,000 cells/mm^2 (**Figures 9G** and **11B-C**). Although the frequency of CD11b+ cells was high by flow in MOE-PTEN/KRAS, IHC quantification showed similar abundance of CD11b+ cells to ID8 models, likely due to large areas of necrotic tissue with few immune cells present (**Figure 7G**). No difference was observed in the prevalence of CD11b+ cells in primary tumours vs. metastases (**Figure 11B**). MDSCs were dominant in ID8-*p53*$^{-/-}$ and MOE-PTEN/KRAS, and to a lesser extent in ID8-WT (>10%, ~7%, and <5% among all leukocytes) (**Figure 9E**).

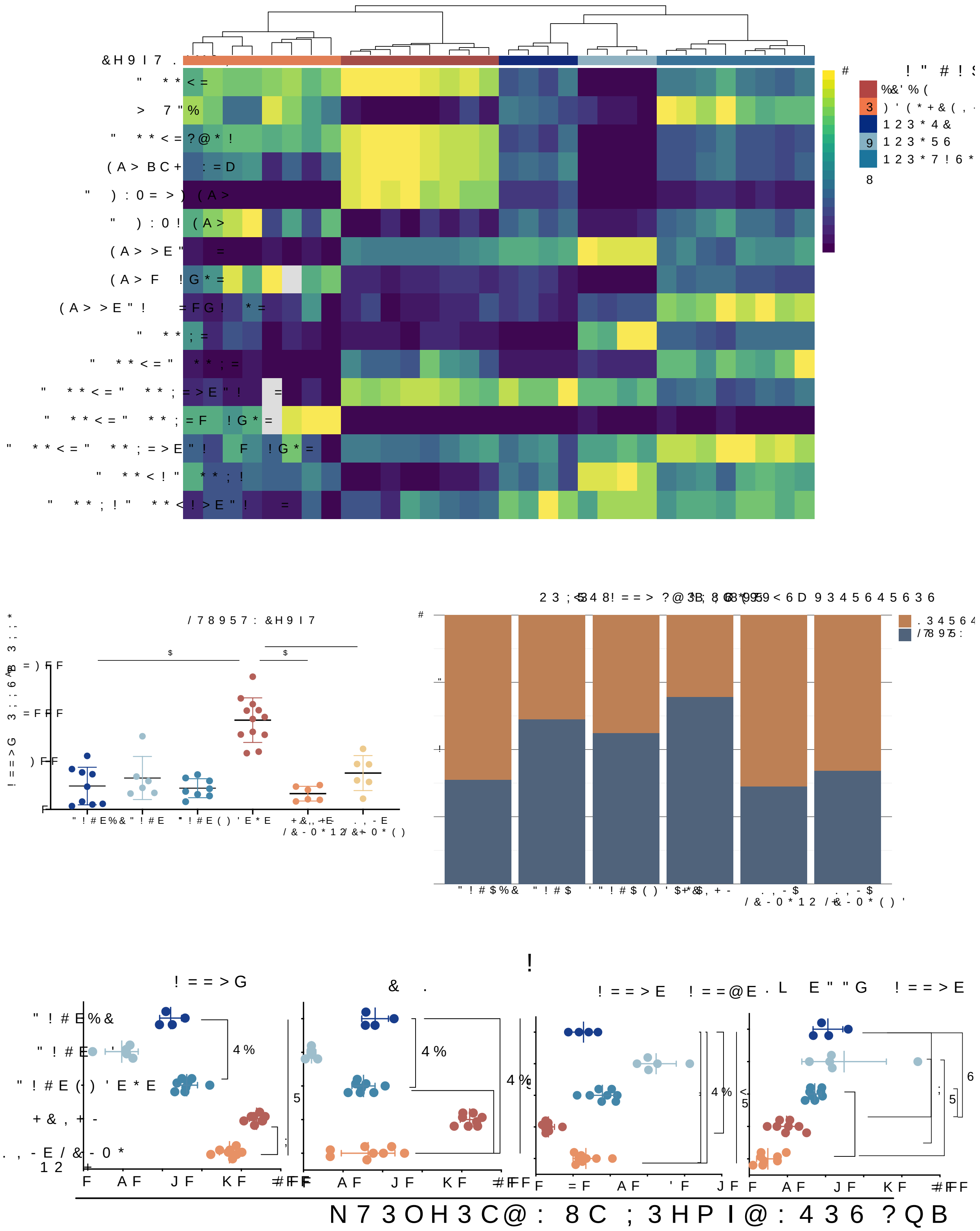

Figure 11: Abundance of myeloid-like cells in the TME of various syngeneic ovarian cancer models. (A) Heatmap depicting normalized relative frequency of the myeloid-like compartment for all tumour models, determined by flow cytometry. White squares are omitted outlier samples. (B) Cell counts (number of cells/mm^2) were quantified using ImagePro Premier. Each dot represents a single tumour sample as follows: ID8-WT (n=9), ID8-C3 (n=6), ID8-*p53-/-* (n=8), STOSE (n=12), MOE-PTEN/KRAS(n=6), and MOE-PTEN/p53 (n=6). Relative abundance of CD11b+ cells in primary vs. metastatic tumours as determined by immunohistochemistry. Metastatic tumours were stained and quantified as with primary tumours. ID8-WT (n=10), ID8-C3 (n=5), ID8-*p53-/-* (n=9), STOSE (n=6), MOE-PTEN/KRAS (n=3), MOE-PTEN/p53 (n=5). No significant difference was found by Student's t-test. (C-E) Total frequencies in leukocytes of total (C) F480+ TAMs and (D) CD11b-CD11c- cells with a MHC-II+ fraction. Each dot represents an orthotopic tumour. Mean values with SD are shown. Significance was determined by one-way ANOVA with Tukey's post-test comparing all models, a: $p<0.05$, b: $p<0.01$; c: $p<0.001$; d: $p<0.0001$.

Analysis of the CD11b+ population with TAM markers, showed that STOSE tumours were the most infiltrated by M2 CD206+ F4/80+ TAM (80% of all leukocytes) constituting the majority of immune cells in these tumours (**Figure 9B**) and confirming scRNA-seq findings (**Figures 2C** and **4**). In contrast, MOE-PTEN/KRAS tumours were infiltrated predominantly by CD206- TAM (**Figures 9B** and **9H**). As previously shown by Walton *et al.* (2016), ID8-*p53*$^{-/-}$ contained more TAMs (CD11b+CD11c-F4/80+) compared to ID8-C3 tumours (**Figures 9H** and **11C**). Interestingly, ID8-C3 differed from all other models by the infiltration of myeloid-like cells composed mainly of CD11b-CD11c+ (**Figure 9B, I),** which could represent subsets of DCs (Yu et al., 2016) and CD11b-CD11c- (**Figure 11D**) (~3 and ~40%, respectively, of all leukocytes). All the other tumours contained less than 1% CD11c+ cells. Lastly, ID8-*p53*$^{-/-}$ and STOSE were significantly infiltrated by CD11b+CD11c+ cells, which includes conventional DC2s (cDC2) that are mainly recognized by the induction of CD4+ T cell immunity in cancer (Wculek et al., 2020) (**Figure 9I**). Taken together these findings suggest that STOSE and MOE-PTEN/KRAS tumours are preferentially infiltrated by CD11b+ myeloid-like immune cells while most of the ID8-derived models possess greater capability to recruit T cells.

3.1.4. STOSE tumours contain T cells displaying high expression of exhaustion markers

To investigate the T cell compartment, we examined the activation/exhaustion markers CD25, PD-1, and LAG3 on CD4 and CD8 T subsets (**Figure 10D**) by flow cytometry, and FOXP3+ expression by IHC, suggestive of Tregs. ID8-C3 tumours contained the highest frequencies of CD4+ T cells (~10% of all tumour infiltrating leukocytes) (**Figure 12A**). CD4+ T cells from ID8-*p53*$^{-/-}$ tumours displayed very poor expression of CD25, PD1 and LAG3 compared to all other models (**Figure 12B**), while STOSE and ID8-WT, the most poorly infiltrated by T cells, expressed more CD25, PD-1, and LAG3. ID8-C3 and ID8-*p53*$^{-/-}$ tumours contained more FOXP3+ cells/mm^2 compared to ID8-WT (**Figure 12C**), corresponding to trends seen for CD3 infiltration. Considerable variability was found in the FOXP3+ populations in the two MOE models, largely due to the presence of necrotic areas with few immune cells (**Figure 7G**). When comparing primary to metastatic tumours, ID8-WT metastatic tumours had a higher abundance of FOXP3+ cells (**Figure 10E**).

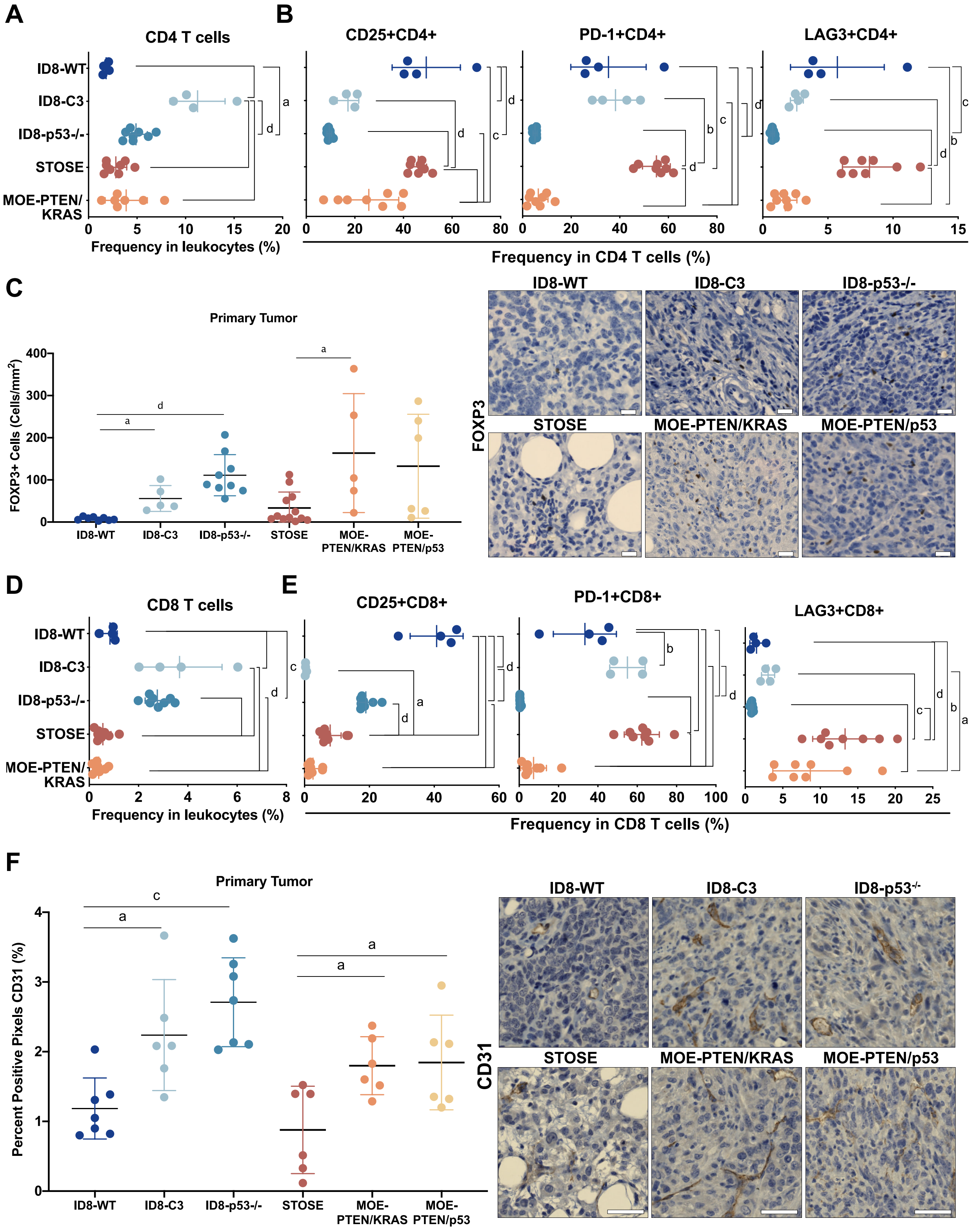
A
CD4 T cells
ID8-WT
ID8-C3
ID8-p53-/-
STOSE
MOE-PTEN/KRAS
Frequency in leukocytes (%)
B
CD25+CD4+
PD-1+CD4+
LAG3+CD4+
Frequency in CD4 T cells (%)
C
Primary Tumor
FOXP3+ Cells (Cells/mm²)
ID8-WT
ID8-C3
ID8-p53-/-
STOSE
MOE-PTEN/KRAS
MOE-PTEN/p53
FOXP3
D
CD8 T cells
Frequency in leukocytes (%)
E
CD25+CD8+
PD-1+CD8+
LAG3+CD8+
Frequency in CD8 T cells (%)
F
Primary Tumor
Percent Positive Pixels CD31 (%)
ID8-WT
ID8-C3
ID8-p53-/-
STOSE
MOE-PTEN/KRAS
MOE-PTEN/p53
CD31

Figure 12: STOSE tumours have greater frequency of CD4 and CD8 T cells expressing exhaustion markers. Flow cytometry analysis showing the frequencies of (A) CD4+ expressing cells and (B) CD25, PD1 and LAG3 expression among CD4+ T cells. (C) Images representative of FOXP3+ staining in ID8-WT (n=8), ID8-C3 (n=6), ID8-*p53*$^{-/-}$ (n=9), STOSE (n=12), MOE-PTEN/KRAS (n=6), and MOE-PTEN/p53 (n=6) samples. Cell counts (plotted as number of cells/mm^2) were quantified using ImagePro Premier. (D-E) Flow cytometry analysis showing the frequencies of (D) CD8+ T cells among leukocytes in each tumour model and (E) CD25, PD1 and LAG3 expression among CD8+ T cells. For flow cytometry analysis, cell frequencies were determined by discriminating doublets, dead cells, CD45-, and CD3+ cells (see Figure 8). Each dot represents an orthotopic tumour. Mean values with SD are shown. Significance was determined by one-way ANOVA with Tukey's post-test comparing all models, a: $p<0.05$, b: $p<0.01$; c: $p<0.001$; d: $p<0.0001$. (F) Quantification (left panel) and immunohistochemical detection of endothelial cells by CD31 staining (right panel) in all tumour models. Data was quantified using Orbit Image analysis (% positive area). Each dot represents an orthotopic tumour. Mean values with SD are shown. Scale bars = 20µm (FOXP3) and 50µm (CD31). For IHC, sections were counterstained with hematoxylin (blue) and positive cells (brown) with DAB. Mean values with SD are shown. Significance was determined by one-way ANOVA within C57BL/6 or FVB/N models with Tukey's post-test or a two-tailed Student's t-test (comparing ID8 and STOSE), a: $p<0.05$, d: $p<0.0001$.

CD8+ T cells comprised more than 2% of the leukocytic population only in the ID8-C3 and ID8-*p53*$^{-/-}$ models (**Figure 12D**). Remarkably, the model containing the highest CD4/CD8 T cell ratio was MOE-PTEN/KRAS with ~7 CD4+ T cells for each CD8+ T cell, unveiling a potential shift to CD4 Th2 response as an immune evasion mechanism (**Figure 10F**). ID8-WT tumours contained the highest frequency of CD25+CD8+ T cells (>40% among all CD8+ T cells) and PD-1+CD8+ T cells (**Figure 12E**). ID8-C3 tumours also possessed high frequencies of PD1+CD8+ T cells. Interestingly, CD8+ T cells in ID8-*p53*$^{-/-}$ tumours expressed CD25 but not exhaustion markers, PD-1 and LAG3. STOSE and MOE-PTEN/KRAS had fewer CD25+CD8+ T cells and more LAG3+CD8+ T cells (>10%), while STOSE tumours contained the highest frequency of PD-1+ CD8+ T cells (~60%).

To determine if tumour vasculature might be associated with differences in immune cell infiltration, we stained for CD31 by IHC and found less CD31+ area in ID8-WT and STOSE tumours compared to the other models (**Figure 12F**), which interestingly corresponded to tumours most poorly infiltrated by T cells (**Figures 9C** and **10A**). Conversely, ID8-C3, ID8-*p53*$^{-/-}$*,* MOE-PTEN/KRAS, and MOE-PTEN/p53 tumours displayed more CD31+ area, allowing for potentially more immune infiltration and corresponding to greater numbers of CD3+ cells/mm^2 (**Figure 10A**).

Collectively, our findings suggest that ID8-WT and STOSE tumours, having the lowest CD31 expression, were the most poorly infiltrated by T cells, these having higher expression of activation/exhaustion markers which may indicate a more impaired phenotype. Moreover, ID8-*p53*$^{-/-}$ and MOE-PTEN/KRAS tumours contained more FOXP3+ cells, potentially Tregs, but only the MOE-PTEN/KRAS model had a higher ratio of CD4/CD8, ~25% CD25+CD4+ T cells (potentially including Tregs) and low CD25+ and PD1+ expression on CD8+ T cells which suggests a lack of T cell activation in the TME.

3.1.5. Stromal cells of MOE tumours express high levels of MHC-II

Given that TAA presentation and response to immunotherapy are closely linked to MHC and PD-L1 expression (Galluzzi et al., 2018; Garrido and Aptsiauri, 2019), we next characterized their expression in tumours. By IF, we found ID8-derived orthotopic tumours expressed very low levels of MHC-I, similar to the cell lines *in vitro*, while STOSE and MOE-derived tumours maintained their positivity *in vivo* (**Figure 13**). Interestingly, comparable MHC-I expression was observed in the metastatic lesions for each tumour model (**Figure 13**). Staining for MHC-II by IHC showed ID8-*p53*$^{-/-}$ and ID8-C3 tumours had more MHC-II+ area compared to ID8-WT, while STOSE and MOE models displayed higher MHC-II+ area that was most abundant in MOE-PTEN/KRAS and MOE-PTEN/p53 tumours (~10% and ~25% positive area, respectively) (**Figure 14A**). As observed with CD3 staining (**Figure 10B**), MHC-II staining was found in clusters (**Figure 15A**) in MOE-PTEN/KRAS sections, displaying characteristics typical of immune cell clusters. Interestingly, metastases from ID8-WT tumours had higher MHC-II+ area compared to their primary tumours, while all other models were roughly equivalent between primary and metastatic lesions (**Figure 15B**). To further explore the strong MHC-II expression found in the MOE models, double IF staining for MHC-II and CK8+18 was performed. A lack of co-staining of MHC-II with epithelial cancer cells (**Figure 14B**) raised the question of the main source of MHC-II. Flow cytometry analysis showed a low frequency of MHC-II positive immune cells in the myeloid compartment (**Figure 14C-D**), and low levels of expression (**Figure 15C**) relative to the other models. Using serial sections, MHC-II staining was shown to be in excess of the staining for CD11b, suggesting that CD11b- cells also express MHC-II (**Figure 15D**). Therefore, the high expression of MHC-II in the TME of MOE models appears to be primarily associated with stromal components other than immune cells.

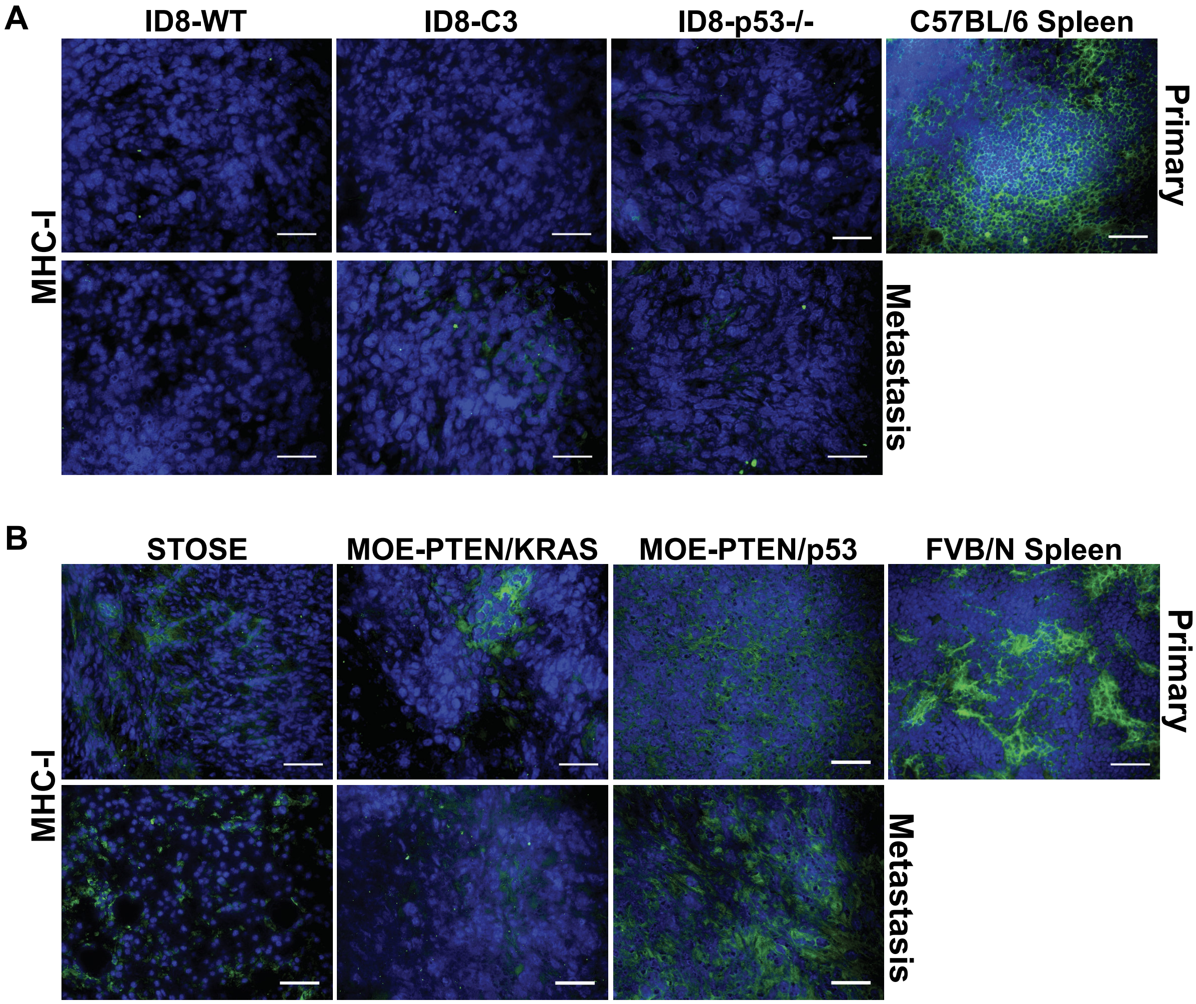

Figure 13: Primary and metastatic tumours from ID8-derived cancer cells do not express MHC-I *in vivo*, while STOSE and MOE models do. (A) Immunofluorescence depicting MHC-I (green) and nuclei (Hoechst) on primary (upper panels) and metastatic (lower panels) tumours showing little to no expression of MHC-I. C57BL/6 spleen was used as a positive control. Images are representative of n=3 primary/metastasis for each model. Scale bars = 50µm. (B) Primary and metastatic tumours derived from the FVB/N models retained MHC-I expression (green) as shown by immunofluorescence. Scale bars = 50µm.

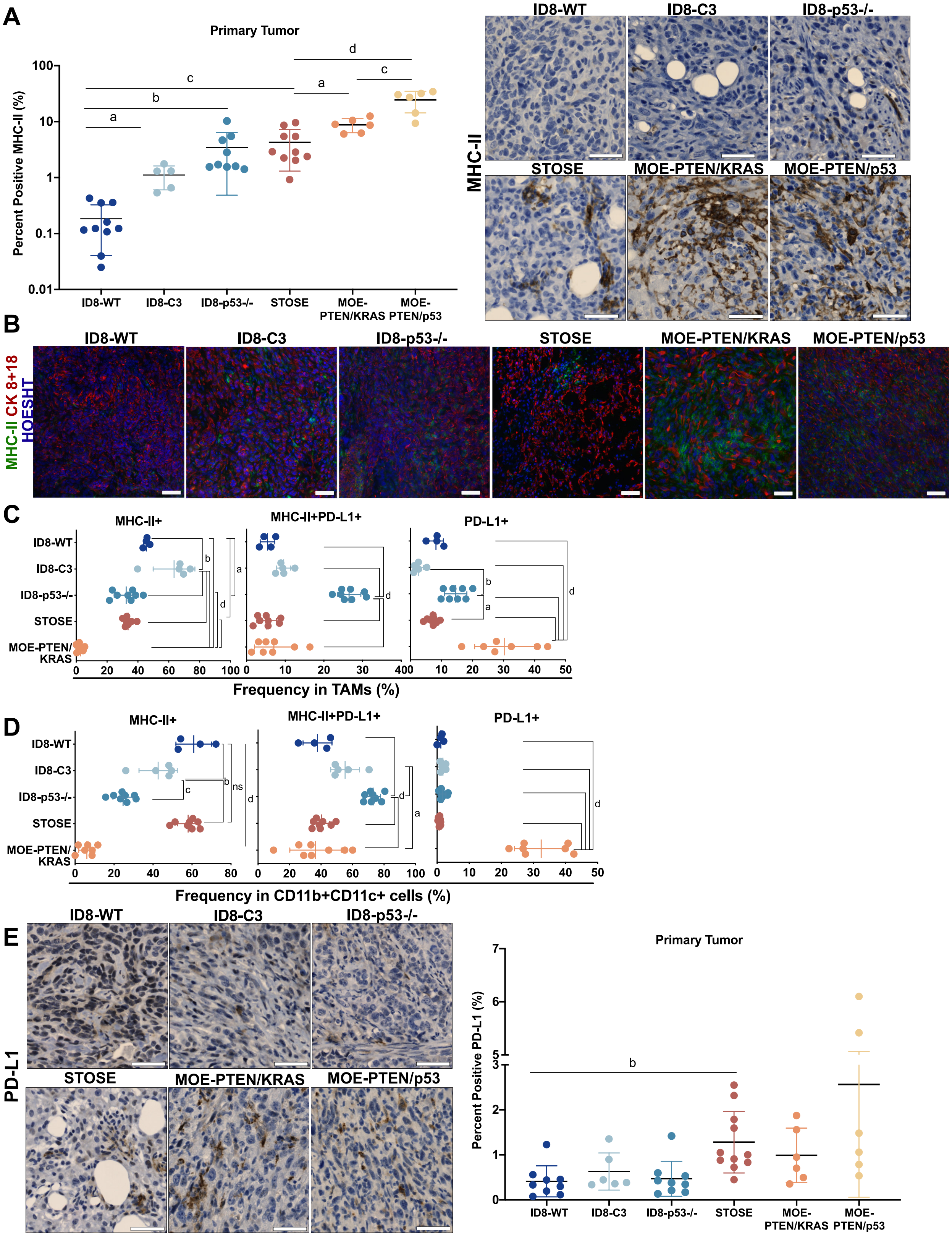
A
Primary Tumor
Percent Positive MHC-II (%)
100
10
1
0.1
0.01
a
b
c
a
d
c
ID8-WT
ID8-C3
ID8-p53-/-
STOSE
MOE-PTEN/KRAS
MOE-PTEN/p53
MHC-II
ID8-WT
ID8-C3
ID8-p53-/-
STOSE
MOE-PTEN/KRAS
MOE-PTEN/p53
B
MHC-II CK 8+18 HOESHT
ID8-WT
ID8-C3
ID8-p53-/-
STOSE
MOE-PTEN/KRAS
MOE-PTEN/p53
C
MHC-II+
MHC-II+PD-L1+
PD-L1+
ID8-WT
ID8-C3
ID8-p53-/-
STOSE
MOE-PTEN/KRAS
b
a
d
d
b
a
d
0
20
40
60
80
100
0
10
20
30
40
0
10
20
30
40
50
Frequency in TAMs (%)
D
MHC-II+
MHC-II+PD-L1+
PD-L1+
ID8-WT
ID8-C3
ID8-p53-/-
STOSE
MOE-PTEN/KRAS
c
b
ns
d
d
a
d
0
20
40
60
80
0
20
40
60
80
100
0
10
20
30
40
50
Frequency in CD11b+CD11c+ cells (%)
E
PD-L1
ID8-WT
ID8-C3
ID8-p53-/-
STOSE
MOE-PTEN/KRAS
MOE-PTEN/p53
Primary Tumor
Percent Positive PD-L1 (%)
7
6
5
3
2
1
0
b
ID8-WT
ID8-C3
ID8-p53-/-
STOSE
MOE-PTEN/KRAS
MOE-PTEN/p53

Figure 14. The TME of FVB/N models is characterized by strong MHC-II expression. (A) Immunohistochemical detection (right panel) and quantification of MHC-II+ cells (left panel) in all tumour models. Sections were counterstained with hematoxylin (blue) and positive cells with DAB (brown). Images are representative of tumours for each model as follows: ID8-WT (n=10), ID8-C3 (n=6), ID8-*p53*$^{-/-}$ (n=9), STOSE (n=10), MOE-PTEN/KRAS (n=6), MOE-PTEN/p53 (n=6) samples. Scale bars = 50µm. Percent positive MHC-II (%) areas of the tumour were quantified using Orbit Image analysis. (B) Immunofluorescence depicting MHC-II (green), Cytokeratin 8+18 (red), and nuclei (Hoechst) on primary tumours. Images are representative of n=3 primary tumours for each model. Scale bars = 50µm. (C-D) MHC-II and PD-L1 expression in (C) TAMs and (D) CD11b+CD11c+ subsets found in the TME, assessed by flow cytometry. Mean values with SEM are shown for each tumour model. Significance was determined by one-way ANOVA with Tukey's post-test comparing all models, ns: not significant; a: $p<0.05$, b: $p<0.01$; c: $p<0.001$; d: $p<0.0001$. (E) Quantification (left) and immunohistochemical detection (right) of PD-L1 expression in all tumour models. Sections were counterstained with hematoxylin (blue) and positive cells with DAB (brown). Images are representative of ID8-WT (n=9), ID8-C3 (n=6), ID8-*p53*$^{-/-}$ (n=9), STOSE (n=12), MOE-PTEN/KRAS (n=6), MOE-PTEN/p53 (n=6) tumours. Scale bars = 50µm. Percent positive PD-L1 (%) areas of the tumour were quantified using Orbit Image analysis. Mean values with SD are shown for each tumour model. Significance was determined by one-way ANOVA within C57BL/6 or FVB/N models with Tukey's post-test or a two-tailed Student's t-test (comparing ID8 and STOSE).

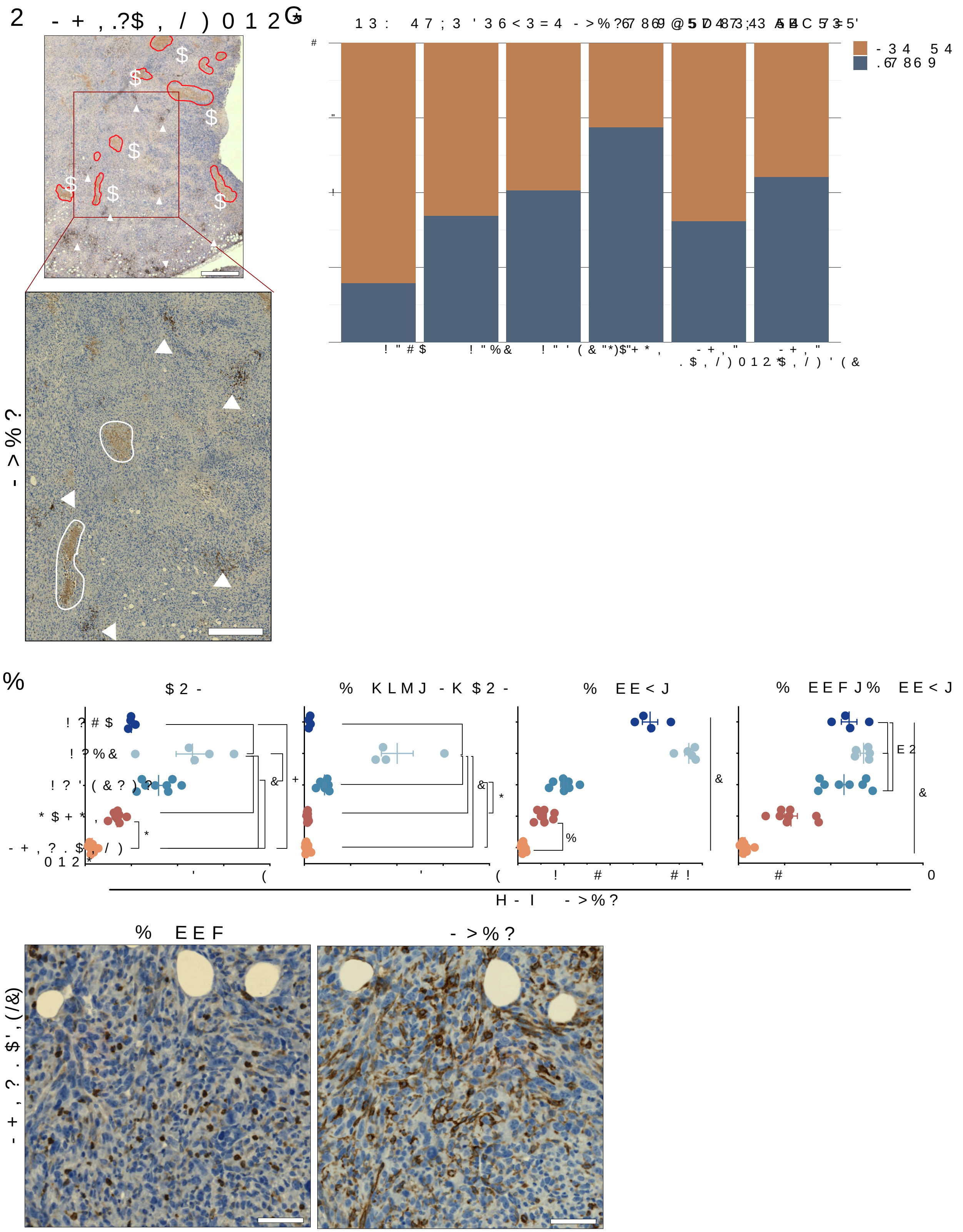
2
- + , .?$, /) 0 1 2
1 3 : 4 7 ; 3 ' 3 6 < 3 = 4 - > % ?
- 3 4 5 4
. 6 7 8 6 9
! " # $
! " % &
- > % ?
%
$ 2 -
% K L M J - K $ 2 -
% E E < J
% E E F J % E E < J
! ? # $
! ? % &
* $ + *
- + , ? . $, /)
0 1 2
H - I - > % ?
% E E F
- > % ?
- + , ? . $' , (/ &)

Figure 15: MHC-II expression in immune and stromal compartments of orthotopic tumours from syngeneic ovarian cancer models. (A) Representative images of IHC for MHC-II staining of MOE-PTEN/KRAS tumours revealing MHC-II+ clusters. Scale bars = 1mm (top panel) and 200µm (bottom panel). White arrowheads in the top panel indicating clusters of MHC-II+ cells are further magnified in the bottom panel. Asterisks (*) indicate outlined necrotic areas deprived of cells with non-specific staining. Sections were counterstained with hematoxylin (blue) and positive cells (brown) were stained with DAB. Scale bars = 50µm. (B) Relative abundance of MHC-II as detected by IHC in primary vs. metastatic tumours. Metastatic tumours were stained and quantified as with primary tumours presented in 6A. ID8-WT (n=10), ID8-C3 (n=5), ID8-*p53*$^{-/-}$ (n=9), STOSE (n=7), MOE-PTEN/KRAS (n=3), MOE-PTEN/p53 (n=5). Significance was determined by Student's t-test, a<0.05. (C) Expression of MHC-II+ in TAMs, CD206+ M2 CD206+ TAMS, CD11c+ and CD11b+CD11c+ cells in primary tumours as assessed by flow cytometry. Mean values with SEM are shown. Significance was determined by one-way ANOVA with Tukey's post-test comparing all models, a: p<0.05, b: p<0.01; c: p<0.001; d: p<0.0001.(D) Representative IHC images of CD11b and MHC-II staining in MOE-PTEN/p53 tumours show MHC-II expression by CD11b negative cells. Images are from serial sections of the same tumour. Images representative of n=6 primary and n=5 metastatic MOE-PTEN/p53 tumours.

We next examined MHC-II and PD-L1 expression in the myeloid populations found most frequently in tumours, TAMs and cDC2s. While MOE-PTEN/KRAS tumours had the lowest frequency of MHC-II+ TAMs and cDC2s, they had the highest frequency (~30%) of PD-L1+ TAMs and cDC2s (**Figure 14C-D**). Interestingly, ID8-*p53*$^{-/-}$ tumours contained the highest frequency of double positive MHC-II and PD-L1 TAMs and cDC2s. MHC-II expression was more pronounced on CD206+ M2 TAMs and DCs derived from the ID8-C3 model, and to a lesser extent from ID8-WT tumours (**Figure 15C**). TAMs and cDC2's in STOSE and ID8-WT were largely MHC-II positive, but had the lowest frequency (**Figure 14C-E**) and expression levels (**Figure 16A**) of PD-L1. Analysis of PD-L1 expression on CD45-negative cells (**Figure 16B**) showed that STOSE tumours had high levels. This was confirmed by IHC, where STOSE and MOE tumours had more PD-L1+ area (**Figure 14E).** STOSE metastases had a significantly lower percent positive PD-L1 expression compared to the primary tumours, while metastases from ID8-derived models had on average ~0.5% positive staining. The STOSE and MOE models had ~1.5% positive staining, but these models also had some metastatic samples with much higher staining of PD-L1, ranging between 5-20% (**Fig 16C**).

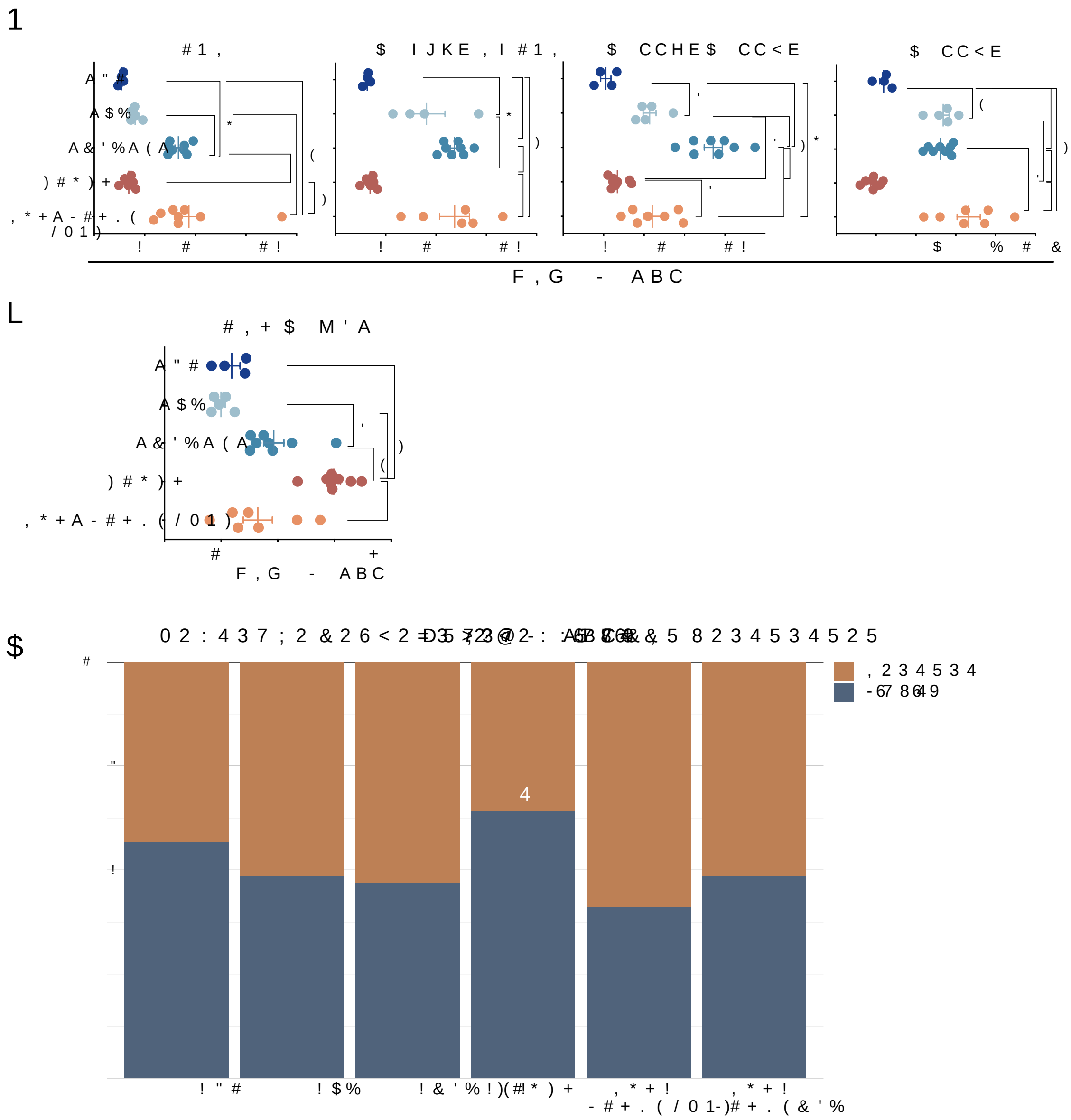

Figure 16: PD-L1 expression in immune and stromal compartments of orthotopic tumours from syngeneic ovarian cancer models. (A) PD-L1 expression assessed by gMFI by flow cytometry in TAMs, M2 CD206+ TAMs, CD11b+CD11c+, and CD11c+ immune subsets found in the TME. Each dot represents a single sample derived from an orthotopic tumour-bearing or control mouse. Cells were analyzed as shown in Figure 8. (B) gMFI of PD-L1 expression on CD45-negative population in the TME. Mean values with SD (A) or SEM (B) are shown for each tumour model. Significance was determined by one-way ANOVA with Tukey's post-test comparing all models, a: p<0.05, b: p<0.01; c: p<0.001; d: p<0.0001. (C) Relative abundance of PD-L1 expression as detected by IHC in primary vs. metastatic tumours. Metastatic tumours were stained and quantified as with primary tumours presented in Figure 6D. Data representative of ID8-WT (n=9), ID8-C3 (n=6), ID8-p53-/- (n=9), STOSE (n=11), MOE-PTEN/KRAS (n=3), MOE-PTEN/p53 (n=5) samples. Significance was determined by Student's t-test, a<0.05.

Taken together, we found that ID8-derived tumours have lost their capability to express MHC-I *in vivo* while STOSE and MOE-PTEN/KRAS-derived models maintained their expression. Moreover, the MOE-PTEN/KRAS model consists of highly immunosuppressive TAMs and cDC2 cells with high PD-L1 expression, unique to this model. This model also has strong MHC-II expression in the tumour niche, similar to the MOE-PTEN/*p53-/-* tumour model.

3.1.6. The immune profile of ascites from MOE-PTEN/KRAS mice mirrors the TME composition

In ovarian cancer, peritoneal ascites adds to tumour burden and plays a major role in influencing therapeutic outcome. We therefore determined the immune profile of the spleen and ascites at the time when orthotopic tumours were collected and compared the frequencies of immune subsets to tumour naïve tissues for each mouse strain. Splenocytes subsets were similar to tumour naive controls (**Fig 17A**) with only MOE-PTEN/KRAS showing different proportions of immune cells compared to FVB/N control spleens. Higher infiltration of CD11b+ cells was found in MOE-PTEN/KRAS (>10% from all leukocytes), and within this population, TAMs were the most prominent (**Figure 17B**).

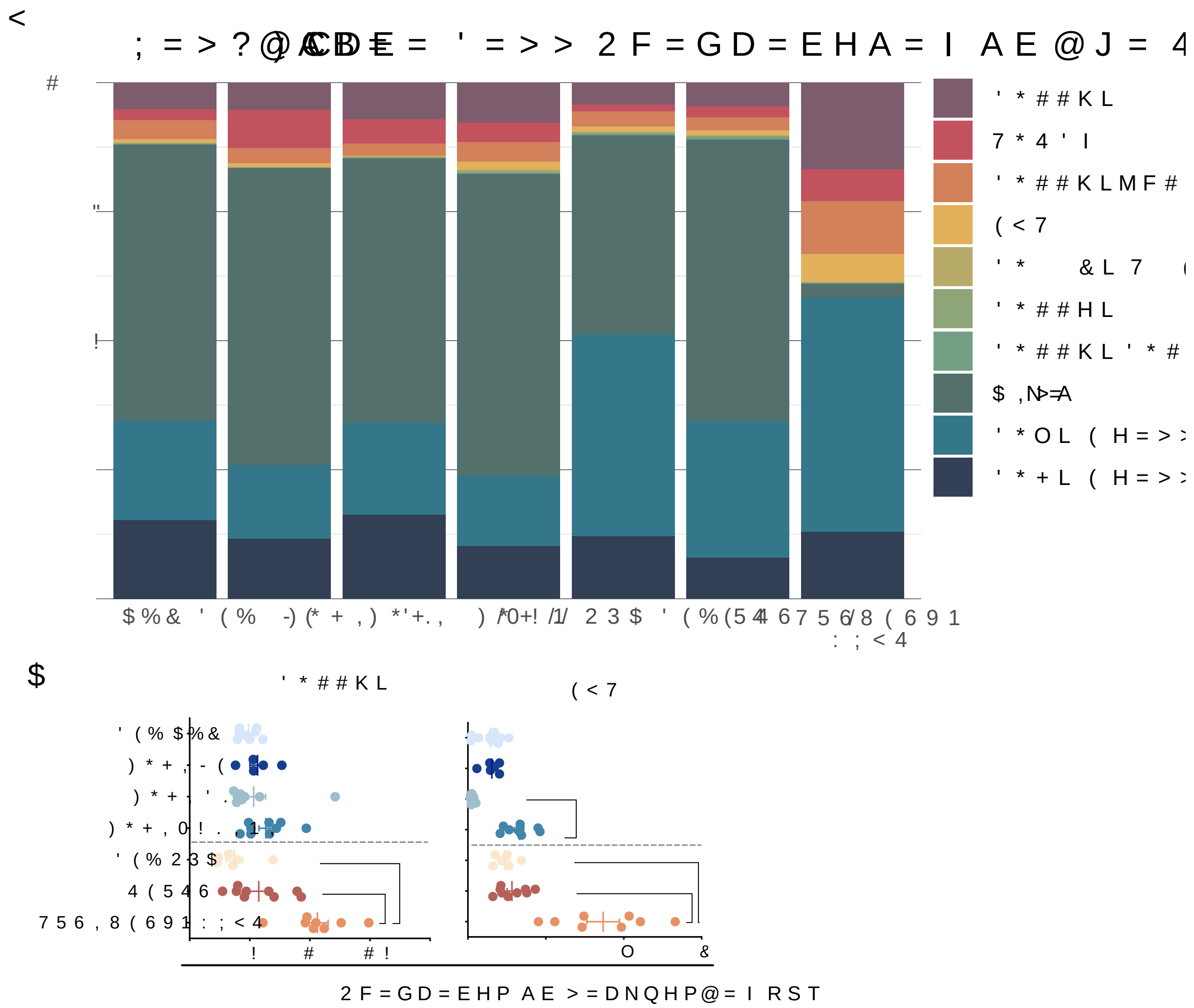

Figure 17: Relative immune cell frequencies found in spleens of ovarian tumour-bearing mice. (A) Stacked-bars figures showing the relative frequencies of several immune populations found in the spleens of tumour-bearing mice, near the endpoint, as assessed by flow cytometry (see Figure 8). Samples from age-matched tumour-naive mice were added as controls for each mouse strain. (B) Frequency of CD11b+ cells and TAMs in the spleens of all models. Each dot represents a single sample derived from an orthotopic tumour-bearing or control mouse. Mean values with SEM are shown. Significance was determined by one-way ANOVA with Tukey's post-test comparing all models, a<0.05, b<0.01. a: p<0.05, b: p<0.01; c: p<0.001.

In the ascites, the immune subsets present in the ID8-C3 model were similar to the C57BL/6 control sample, with a higher proportion of CD4+ T cells, while ID8-WT and ID8-*p53*$^{-/-}$ were more similar (**Figure 18A),** preferentially recruiting MDSCs and CD206+ M2 TAMs (~10 and >20% of all leukocytes, respectively) (**Figure 18B**). Consistent with the results from the tumours, MOE-PTEN/KRAS ascites preferentially attracted more CD4+ T cells (**Figure 18A**) and MDSCs (~10% of all leukocytes) (**Figure 18B**). STOSE ascites also displayed a similar profile to the tumours with more infiltration by CD11b+Gr1- and CD206+ M2 TAMs, representing >40% and 25% of all immune cells in the ascites fluid, respectively, while CD206- TAM proportions were similar between models (**Figure 18B**). Collectively, these findings indicate that the immune profile found in the TME was replicated in the ascites and spleen, with higher frequencies of MDSCs and CD4+ T cells in the MOE-PTEN/KRAS model, and higher TAM infiltration in the STOSE model.

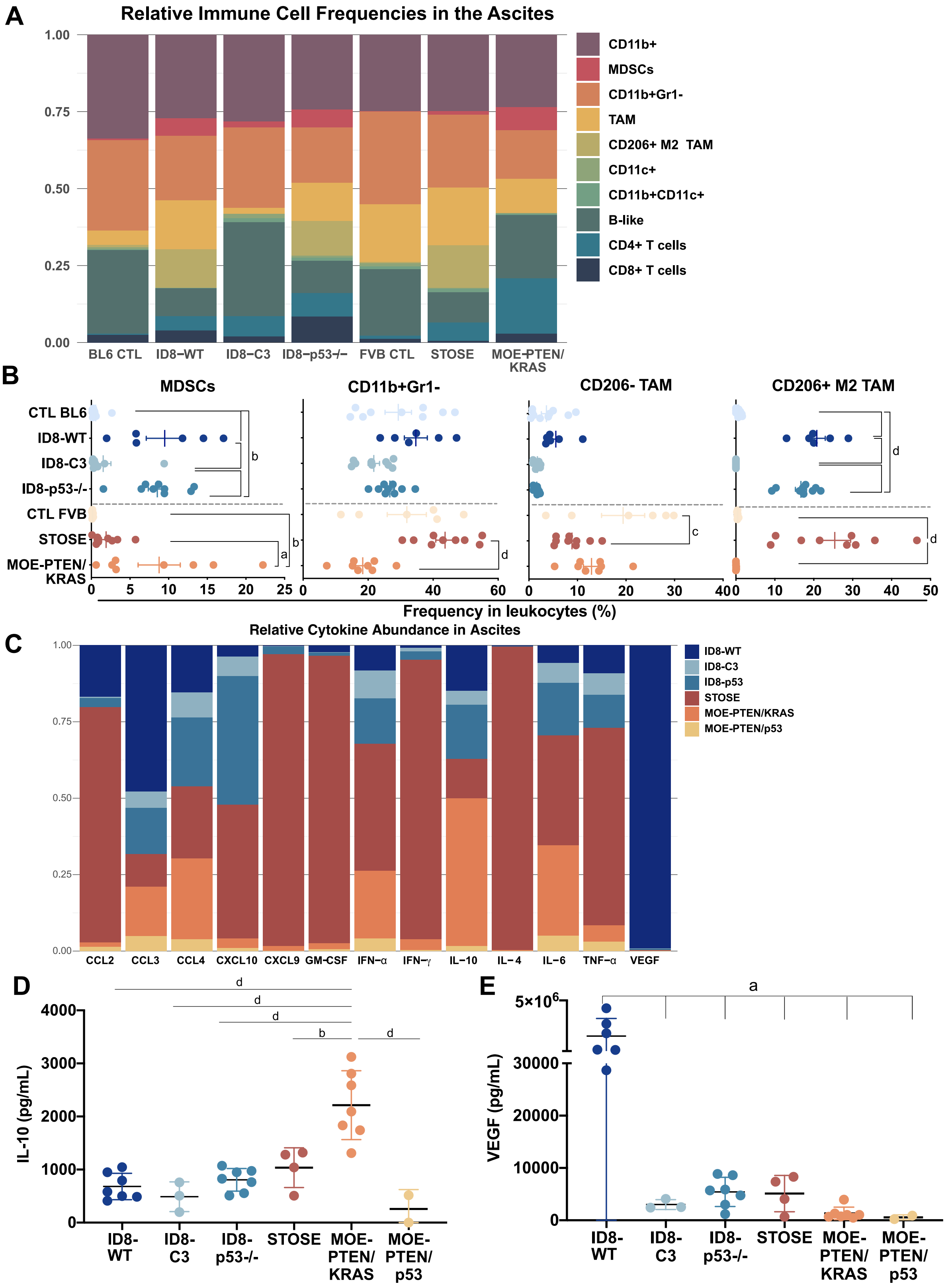
A
Relative Immune Cell Frequencies in the Ascites
1.00
0.75
0.50
0.25
0.00
BL6 CTL
ID8−WT
ID8−C3
ID8−p53−/−
FVB CTL
STOSE
MOE-PTEN/KRAS
CD11b+
MDSCs
CD11b+Gr1-
TAM
CD206+ M2 TAM
CD11c+
CD11b+CD11c+
B-like
CD4+ T cells
CD8+ T cells
B
MDSCs
CD11b+Gr1-
CD206- TAM
CD206+ M2 TAM
CTL BL6
ID8-WT
ID8-C3
ID8-p53-/-
CTL FVB
STOSE
MOE-PTEN/KRAS
a
b
c
d
0 5 10 15 20 25
0 20 40 60
0 10 20 30 40
0 10 20 30 40 50
Frequency in leukocytes (%)
C
Relative Cytokine Abundance in Ascites
1.00
0.75
0.50
0.25
0.00
CCL2
CCL3
CCL4
CXCL10
CXCL9
GM-CSF
IFN−α
IFN−γ
IL−10
IL−4
IL−6
TNF−α
VEGF
ID8-WT
ID8-C3
ID8-p53
STOSE
MOE-PTEN/KRAS
MOE-PTEN/p53
D
IL-10 (pg/mL)
4000
3000
2000
1000
0
d
d
d
b
d
ID8-WT
ID8-C3
ID8-p53-/-
STOSE
MOE-PTEN/KRAS
MOE-PTEN/p53
E
VEGF (pg/mL)
5×10⁶
30000
20000
10000
0
a
ID8-WT
ID8-C3
ID8-p53-/-
STOSE
MOE-PTEN/KRAS
MOE-PTEN/p53

Figure 18: The ascites immune composition and chemo/cytokine network highlights the heterogeneity of the murine orthotopic ovarian cancer models. (A) Stacked-bars figures showing the relative frequencies of several immune populations found in the ascites. (B) Significantly different frequencies of the myeloid-like compartment present in the ascites assessed by flow cytometry. Age-matched tumour-naive C57BL/6 and FVB/N mice were included as controls. Cells were analyzed as shown in Figure 8. Each dot represents a single sample derived from an orthotopic tumour-bearing or control mouse. Mean values with SEM are shown for each tumour model. Significance was determined by one-way ANOVA with Tukey's post-test comparing all models, ns: not significant; a: $p<0.05$, b: $p<0.01$; c: $p<0.001$; d: $p<0.0001$. (C) Stacked-bars figure showing the relative abundance of cytokines and chemokines found in the ascites fluid derived from orthotopic tumour-bearing mice. ID8-WT (n=7), ID8-C3 (n=3), ID8-*p53*$^{-/-}$ (n=7), STOSE (n=4), MOE-PTEN/KRAS (n=7), MOE-PTEN/p53 (n=2). (D) IL-10 and (E) VEGF abundance (pg/ml) in the ascites fluid of each tumour model. Chemo/cytokines were measured by LEGENDplex™ Mouse Cytokine Release Syndrome Panel (13-plex) Multi-Analyte Flow Assay. Each dot represents a single sample derived from the supernatant of ascites from tumour-bearing mice. Mean values with SD are shown for each tumour model. Significance was determined by one-way ANOVA with Tukey's post-test comparing all models, a: $p<0.05$, b: $p<0.01$; d: $p<0.0001$.

We next assessed whether the MHC-II and PD-L1 expression found in TAMs and cDC2s in the ascites reflects their abundance in the tumours. In TAMs (**Figure 19A**), the frequency of MHC-II+ cells was higher only in ID8-C3 ascites while all other models had similar percentages. ID8-*p53*$^{-/-}$ ascites differed significantly by their increased content of MHC-II+PD-L1+ TAMs. We observed more divergence in the proportion of PD-L1+ TAMs with more in ID8-WT, ID8-*p53*$^{-/-}$ and STOSE ascites. MHC-II+ cDC2s were significantly lower in MOE-PTEN/KRAS samples, while being higher in ID8-WT ascites, and PD-L1+ cDC2s were found at highest frequencies in the ID8-*p53*$^{-/-}$ ascites (**Figure 19B**). Lastly, a screening of total PD-L1 expression on myeloid-like cells in the ascites revealed high PD-L1 expression in the TAMs from ID8-*p53*$^{-/-}$ ascites and similarly elevated PD-L1 expression in the cDC2s in ID8-*p53*$^{-/-}$ and MOE-PTEN/KRAS ascites, and to a lesser extent in the CD11c+ population (**Figure 19C**). Analysis of other non-immune (CD45-) cells in the ascites found that, as observed in CD45+ populations, ID8-C3 ascites contained the highest MHC-II expression, in contrast to the MOE-PTEN/KRAS model which poorly expressed MHC-II on CD45- cells (**Figure 19D,** left panel). Similar analysis of PD-L1 in other ascites cells identified an abundance of PD-L1+ cells in both ID8-*p53*$^{-/-}$ and STOSE tumours (**Figure 19D,** right panel). In sum, the main source of PD-L1 expression in the ascitic immune compartment comes from TAMs and cDC2s found mainly in ID8-*p53*$^{-/-}$ and MOE-PTEN/KRAS samples, revealing a more highly immunosuppressive TME.

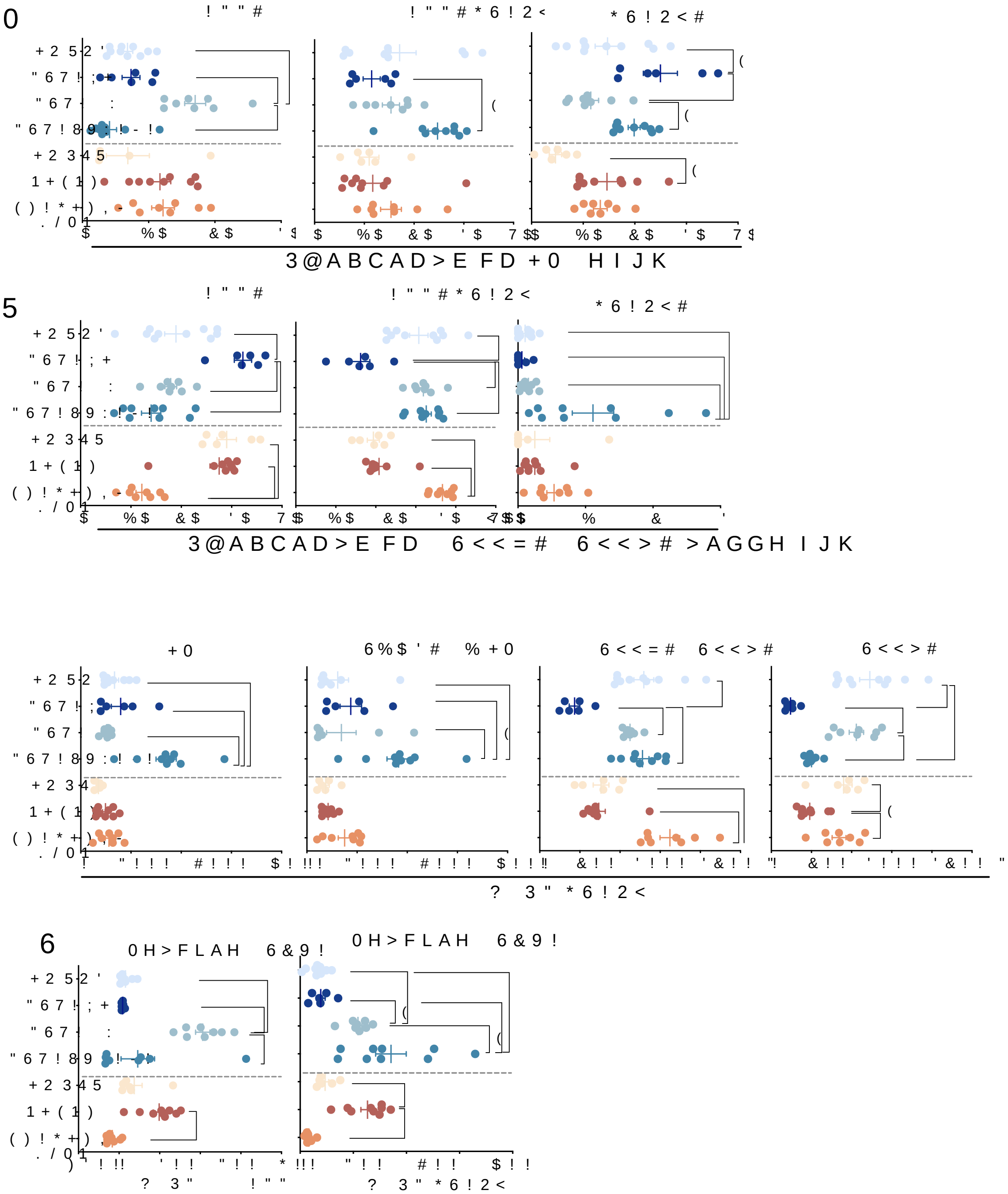

Figure 19: MHC-II and PD-L1 expression in the TME and ascites of ovarian tumour-bearing mice. For ascites analysis, peritoneal derived fluid from age-matched tumour-naive mice were included as controls for each mouse strain. Cells were analyzed as shown in Figure 8 and for each subpopulation, MHC-II or PD-L1 frequency was assessed. Frequency of MHC-II+, MHC-II+PD-L1+, and PD-L1+ (A) TAMs and (B) CD11b+CD11c+ subsets in the ascites fluid. (C) PD-L1 expression assessed by gMFI by flow cytometry in TAMs, M2 CD206+ TAMs, CD11b+CD11c+, and CD11c+ immune subsets in the ascites. Mean values with SEM are shown. Significance was determined by one-way ANOVA with Tukey's post-test comparing all models, a: $p<0.05$, b: $p<0.01$; c: $p<0.001$; d: $p<0.0001$. (D) gMFI of PD-L1 expression on CD45- population in ascites.

Finally, to identify the chemo/cytokines associated with immune cell recruitment, we used multiplexed cytokine assays to determine their abundance in ascites fluid (**Appendix 4**) and plasma (**Appendix 5**). Chemo/cytokines were not found in great abundance in the plasma, with only a few individual samples containing high levels, and no significant differences were observed between the models nor between the tumour-bearing mice and controls (**Fig 20A**). In ascites, 10/13 chemo/cytokines were significantly more abundant in the STOSE samples (**Figure 18C**). Many, such as CCL2, CCL4, CXCL9 and CXCL10, likely contributed to the infiltration and positive feedback signaling of TAMs and MDSCs into the tumours and ascites of this model (Rodriguez et al., 2018). MOE-PTEN/KRAS ascites contained the highest concentration of IL-10, supporting the high prevalence of potentially tolerogenic cDC2s (**Figure 18D**). VEGF was found at highest abundance in the ID8-WT model, likely explaining the poor T cell infiltration and the high ascites accumulation particular to this model (**Figures 18E, 9C, Table 3**) as observed in human ovarian cancers (Rodriguez et al., 2018). ID8-C3 and ID8-*p53*$^{-/-}$ ascites displayed similar levels of chemo/cytokines, but differed from the ID8-WT ascites for IFN-γ and CCL2 production (**Figure 20B-C**), and showed similar trends for TNF-α and IL-6 production (**Appendix 4**). ID8-*p53*$^{-/-}$ ascites fluid contained the highest concentration of CXCL10 among all C57BL/6 models (**Figure 20D**), which potentially can be produced by CD11c+ DCs, enabling a higher recruitment of CD8+ T cells to the ascites (**Figure 18A**). Finally, our main findings were correlated with the scRNA-seq data from ID8-WT and STOSE orthotopic tumours, supporting *Vegfa* being highly expressed in ID8-WT tumours, and *Ccl2* in STOSE tumours (**Figure 21**). Additionally, *Il-18, Tnf, Ptgs2, Cd47, Cxcl1* and *Csf1* were more highly expressed in STOSE tumours, including in the cancer cells, supporting the influence of TAMs in these tumours. Expression of *Ccl4* and *Il1-b* found in immune cells was similar in ID8 and STOSE tumours. Taken together, chemokine/cytokines were profoundly more abundant in STOSE ascites fluid and their abundance correlated with the recruitment of CD206+ M2 TAMs found in the TME and peritoneal cavity of the STOSE model.

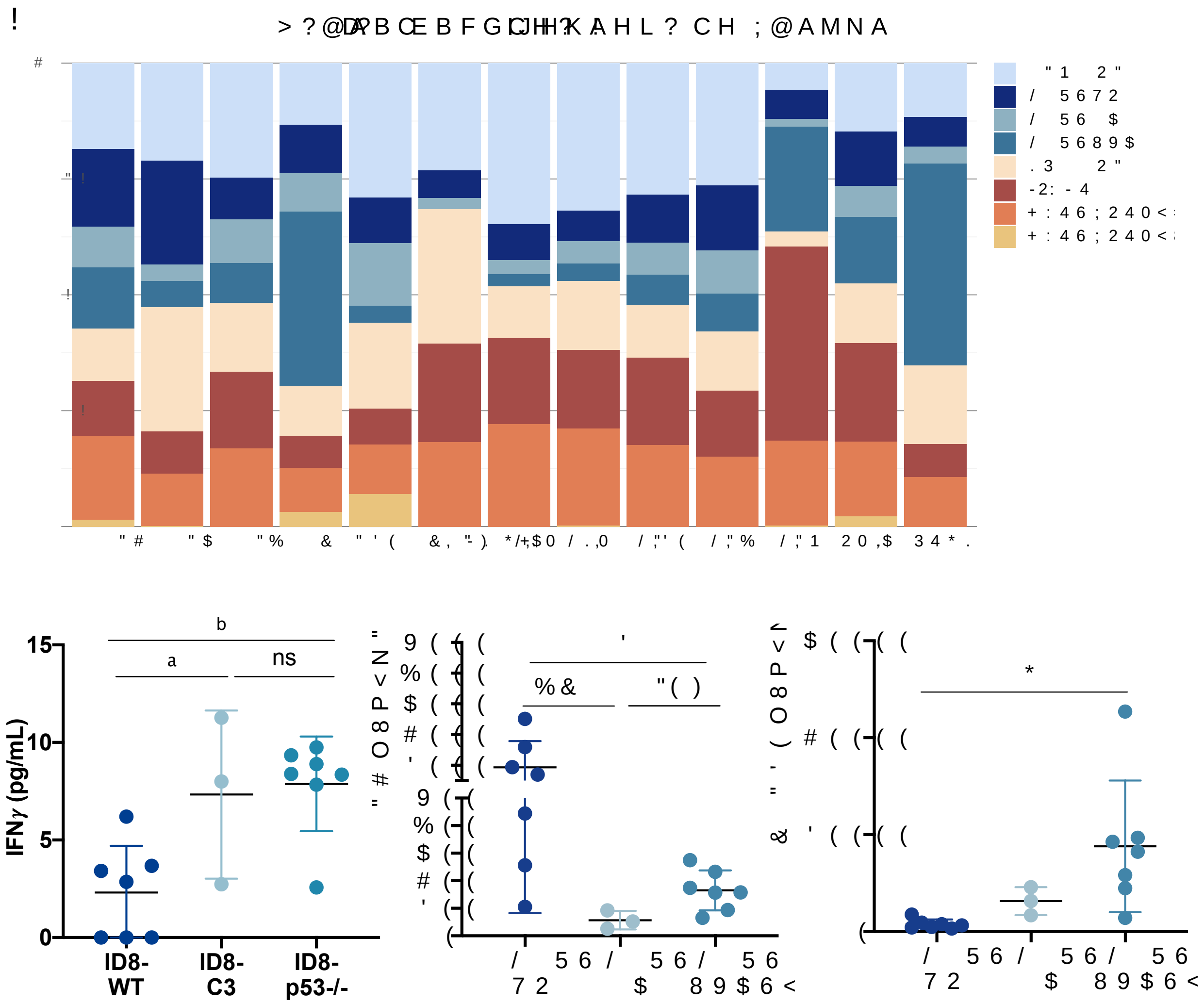

Figure 20: Chemo/cytokine network found in the ascites and plasma of ovarian tumour-bearing mice. (A) Stacked-bars figure showing the relative abundance of cytokines and chemokines in the plasma derived from orthotopic tumour-bearing mice. (B) IFN-γ, (C) CCL2, and (D) CXCL10 in the ascites fluid (pg/ml) of ID8-derived models. Chemo/cytokines were measured by LEGENDplex™ Mouse Cytokine Release Syndrome Panel (13-plex) Multi-Analyte Flow Assay. Each dot represents a single sample derived from ascites fluid (B-D) from tumour-bearing mice. Mean values with SD are shown for each tumour model. Significance was determined by one-way ANOVA with Tukey's post-test, ns: not significant, a: $p<0.05$, b: $p<0.01$.

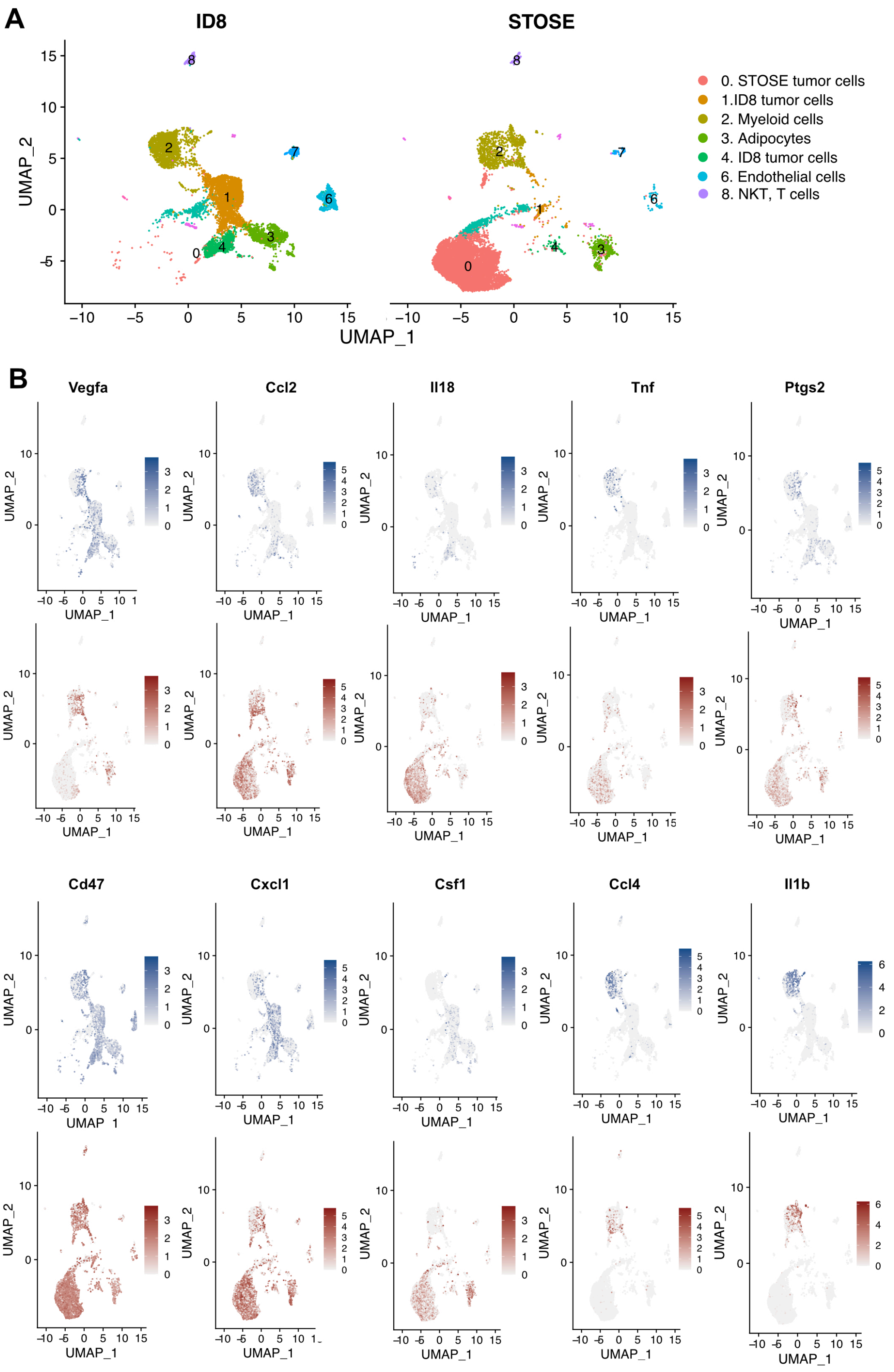
A
ID8
STOSE
UMAP_2
UMAP_1
0. STOSE tumor cells
1.ID8 tumor cells
2. Myeloid cells
3. Adipocytes
4. ID8 tumor cells
6. Endothelial cells
8. NKT, T cells
B
Vegfa
Ccl2
Il18
Tnf
Ptgs2
Cd47
Cxcl1
Csf1
Ccl4
Il1b

Figure 21: Single-cell RNA-sequencing analysis of cytokines/chemokine expression in ID8 and STOSE tumours. (A) Single cell RNA-sequencing UMAP figures depicting cell clusters found in orthotopic ID8-WT (left) and STOSE (right) tumours at endpoint. (B) UMAPs showing expression of *Vegfa, Ccl2, Ccl4, Tnf, Ptgs2, Il18, Il1b, CxCl1, Csf1*, and *Cd47* in ID8-WT (upper panels) and STOSE (lower panels) orthotopic tumours. Heatmap displays the level of expression in cell types (as identified in A) in ID8-WT (blue) and STOSE (red) samples.

3.1.7. Summary

To better model the heterogeneity of human EOC, particularly HGSOC, we assessed MHC-I expression, immunogenicity, immune cell populations, and cytokine profiles of ascites, in 6 syngeneic models of ovarian cancer. This will expand immunotherapy research to include syngeneic model systems from different mouse genetic backgrounds (C57BL/6 and FVB/N), to include a variety of mutations relevant to human disease (*TP53*, *BRCA1*, *BRCA2*, *PTEN*, *KRAS*), and to include both ovarian surface epithelial and fallopian tube derived models. We showed that STOSE and MOE-derived cells express MHC-I *in vitro* and *in vivo*, while ID8-WT and its derivatives do not and are not immunogenic. ID8-WT is the most poorly infiltrated by immune cells, including T cells and myeloid cells. ID8-C3 and ID8-*p53*$^{-/-}$ tumours are most highly infiltrated by T cells, while STOSE and MOE-PTEN/KRAS are infiltrated by CD11b+ myeloid cells. Specifically, STOSE is infiltrated by M2 macrophages while MOE-PTEN/KRAS tumours are infiltrated by CD206- TAMs. This characterization provides a valuable resource for immunotherapy research for EOC and for understanding the role of immunomodulatory factors in EOC tumour progression.

3.2. FGL2 promotes tumour growth by attenuating infiltration of activated anti-tumour Dendritic, Natural Killer and T cells

FGL2 is an immunomodulatory protein associated with tumour progression and poor survival through angiogenesis and immunosuppression in the TME. Using our characterization of the TME of ovarian cancer syngeneic models, and the well-established B16F10 as a model of melanoma, we sought to show the role of FGL2 in tumour progression and survival, and to test a novel immunotherapy (α-FGL2).

3.2.1 Cellular expression of FGL2 and its receptor in tumours

While many previous studies have suggested FGL2 expression by cancer cells will result in a less favourable prognosis (Latha et al., 2019; Qin et al., 2014; Tang et al., 2017; Yan et al., 2015, 2019), we examined publicly available and previously compiled (Cook and Vanderhyden, 2022) scRNA-seq datasets of tumours from patients with melanoma (Jerby-Arnon et al., 2018), ovarian (Geistlinger et al., 2020; Qian et al., 2020), lung (Lambrechts et al., 2018; Qian et al., 2020), breast (Bassez et al., 2021; Qian et al., 2020), and colorectal (Lee et al., 2020; Qian et al., 2020) cancers for expression of FGL2. Remarkably, we found that *FGL2* was expressed predominantly in the macrophage/monocyte and DC populations with minimal expression in the cancer (epithelial) cell populations (**Figures 22** and **23)**. When analyzing expression of the FGL2 receptors, we found that FcγRIIB was primarily expressed by macrophage/monocyte and DC populations as well as B cells (**Figure 24**), and the receptor FcγRIII was primarily expressed in macrophage/monocyte and DC populations as well as NK cells (**Figure 24B**), suggesting FGL2 has autocrine and paracrine activity in the TME.

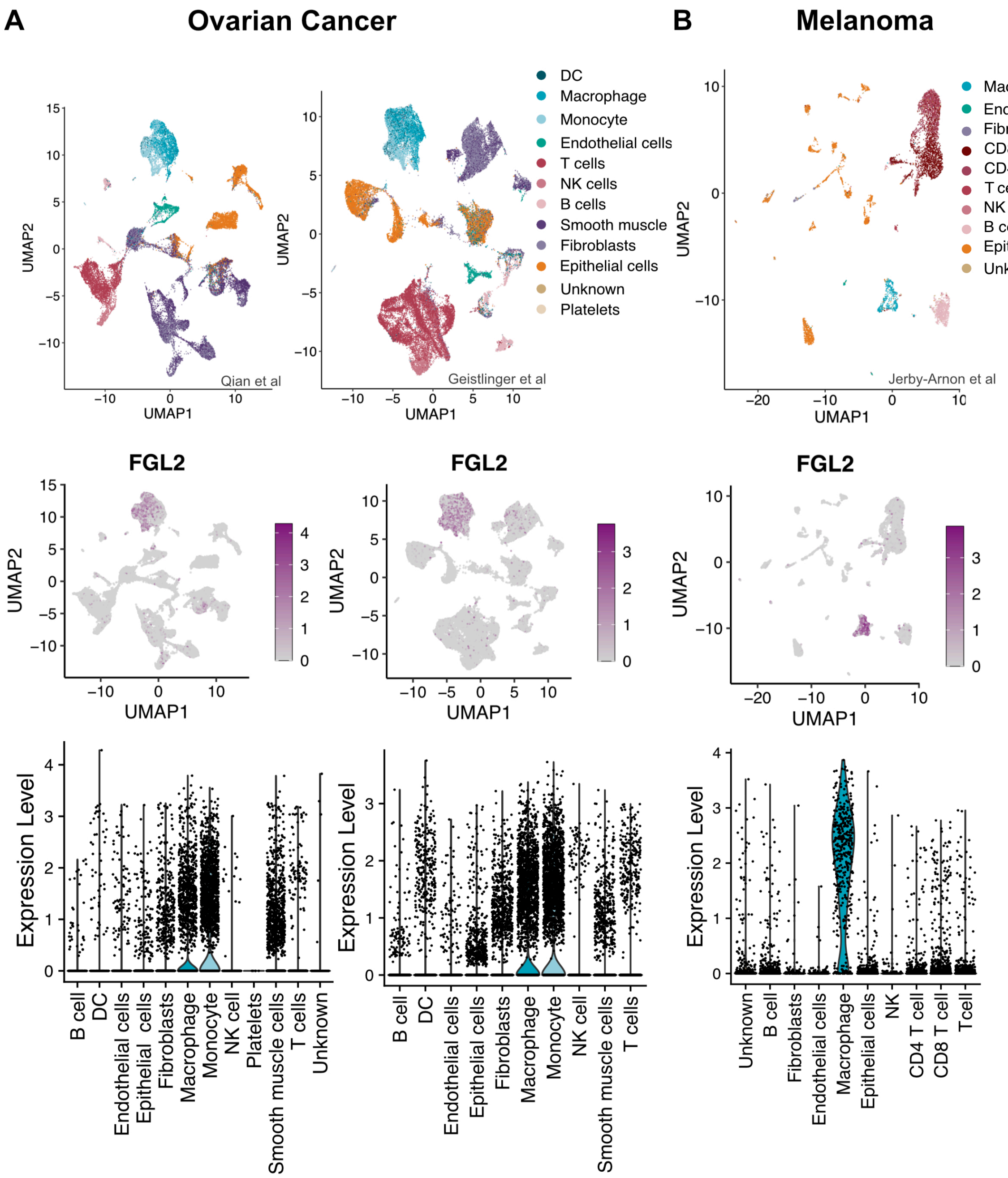

Figure 22. FGL2 is primarily expressed in macrophages of human ovarian cancer and melanoma. (A) scRNA-seq UMAP figures from human ovarian cancer datasets (Left: (Qian et al., 2020, n=5) , Right: (Geistlinger et al., 2020, n=5) depicting cell clusters (top) with accompanying heatmap (middle) and violin plot (bottom) displaying the level of expression of FGL2 in each cell type cluster. **(B)** scRNA-seq UMAP figures from a human melanoma dataset (Jerby-Arnon et al., 2018, n= 33) depicting cell clusters (top) with accompanying heatmap (middle) and violin plot (bottom) displaying the level of expression of FGL2 in each cell type cluster.

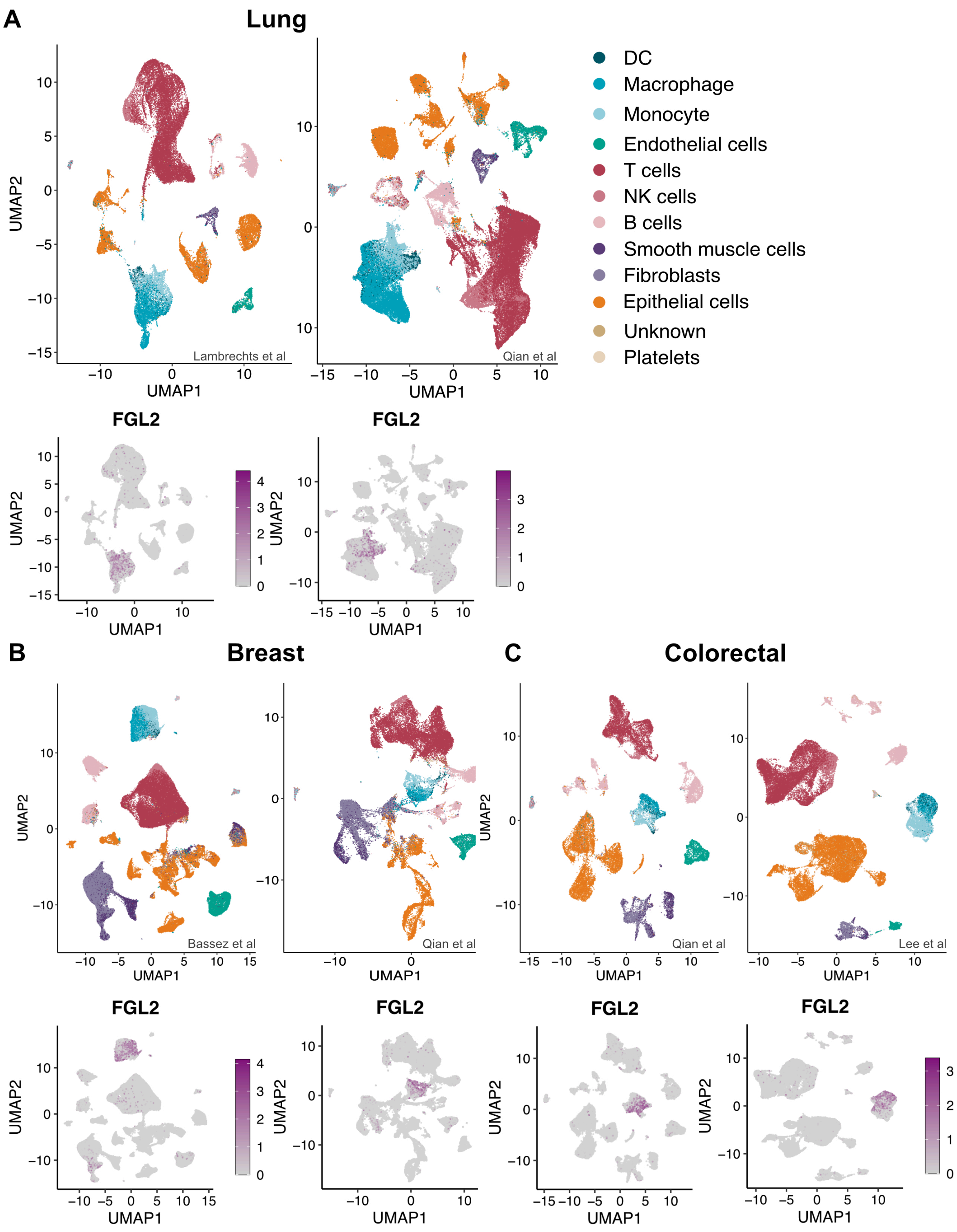

Figure 23. Single-cell RNA sequencing data indicates FGL2 is primarily expressed in macrophages of human lung, breast and colorectal carcinomas. scRNA-seq UMAP figures from human datasets depicting cell clusters with accompanying heatmap displaying the level of expression of FGL2 in each cell type cluster. **(A)** Lung (Left: (Lambrechts et al., 2018, n=9), Right:(Qian et al., 2020, n=24). **(B)** Breast (Left:(Bassez et al., 2021, n=62), Right: (Qian et al., 2020, n=10). **(C)** Colorectal (Left: (Qian et al., 2020, n=11), Right: (Lee et al., 2020, n=25).

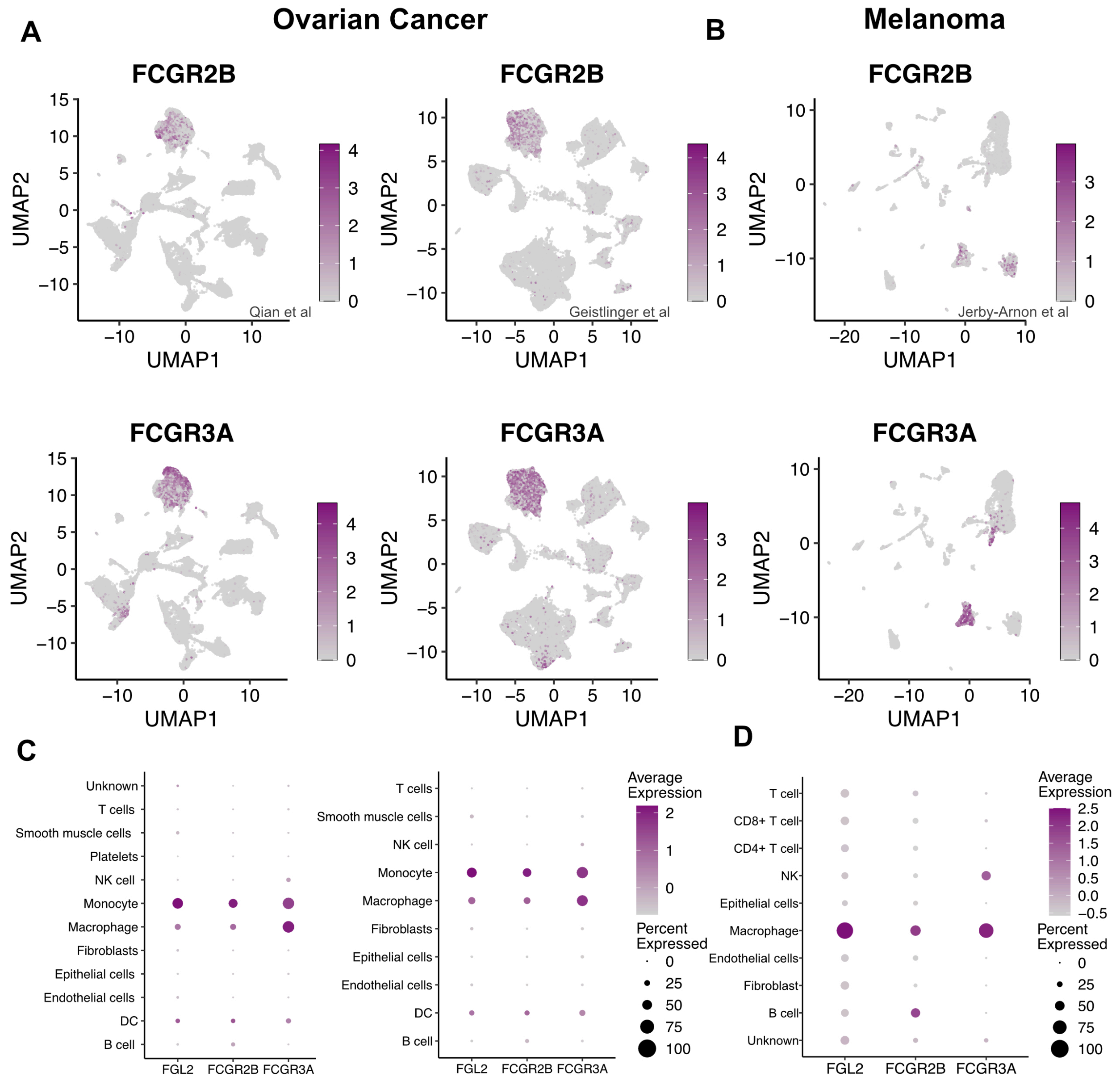

Figure 24. Single-cell RNA sequencing data indicates that FGL2 receptors FcγRIIB and FcγRIII are primarily expressed in macrophages of human ovarian cancer and melanoma. scRNA-seq UMAP figures from human **(A)** ovarian cancer (Left: (Qian et al., 2020, n= 5), Right: (Geistlinger et al., 2020, n=5) datasets and **(B)** human melanoma dataset (Jerby-Arnon et al., 2018, n= 33) depict heatmaps displaying the level of expression of FcγRIIB (top) and FcγRIII (middle) in each cell type cluster. Average expression values of FGL2, FcγRIIB, and FcγRIII in each cell type cluster in **(C)** ovarian cancer (Left: (Qian et al., 2020, n= 5) , Right: (Geistlinger et al., 2020, n=5) datasets and **(D)** human melanoma dataset (Jerby-Arnon et al., 2018, n= 33).

To assess sFGL2 production in ovarian cancer, FGL2 concentrations were quantified in the ascites fluid of patients with ovarian cancer compared with ascites from non-cancer (cirrhotic) patients (**Appendix 6**). FGL2 was abundant in ascites fluid from ovarian cancer patients and at elevated levels when compared to non-cancer ascites (**Figure 25A)**. An assessment of the concentrations of a broad range of cytokines and chemokines revealed that, other than FGL2, only IL-6 was elevated in ovarian cancer ascites compared to non-cancer ascites (**Figure 25B, Figure 25C**). IL-6 is often elevated ovarian cancer ascites, likely due to the fact that ovarian cancer cells in the ascites produce IL-6, and predicts poor prognosis (Giuntoli et al., 2009; Nilsson et al., 2005; Offner et al., 1995). As the results indicate that FGL2 is not expressed by cancer cells in the TME, and FGL2 is associated with immunosuppression in human ovarian cancer, we sought to determine how FGL2 might promote immunosuppression in the TME and how it might influence tumour progression and survival.

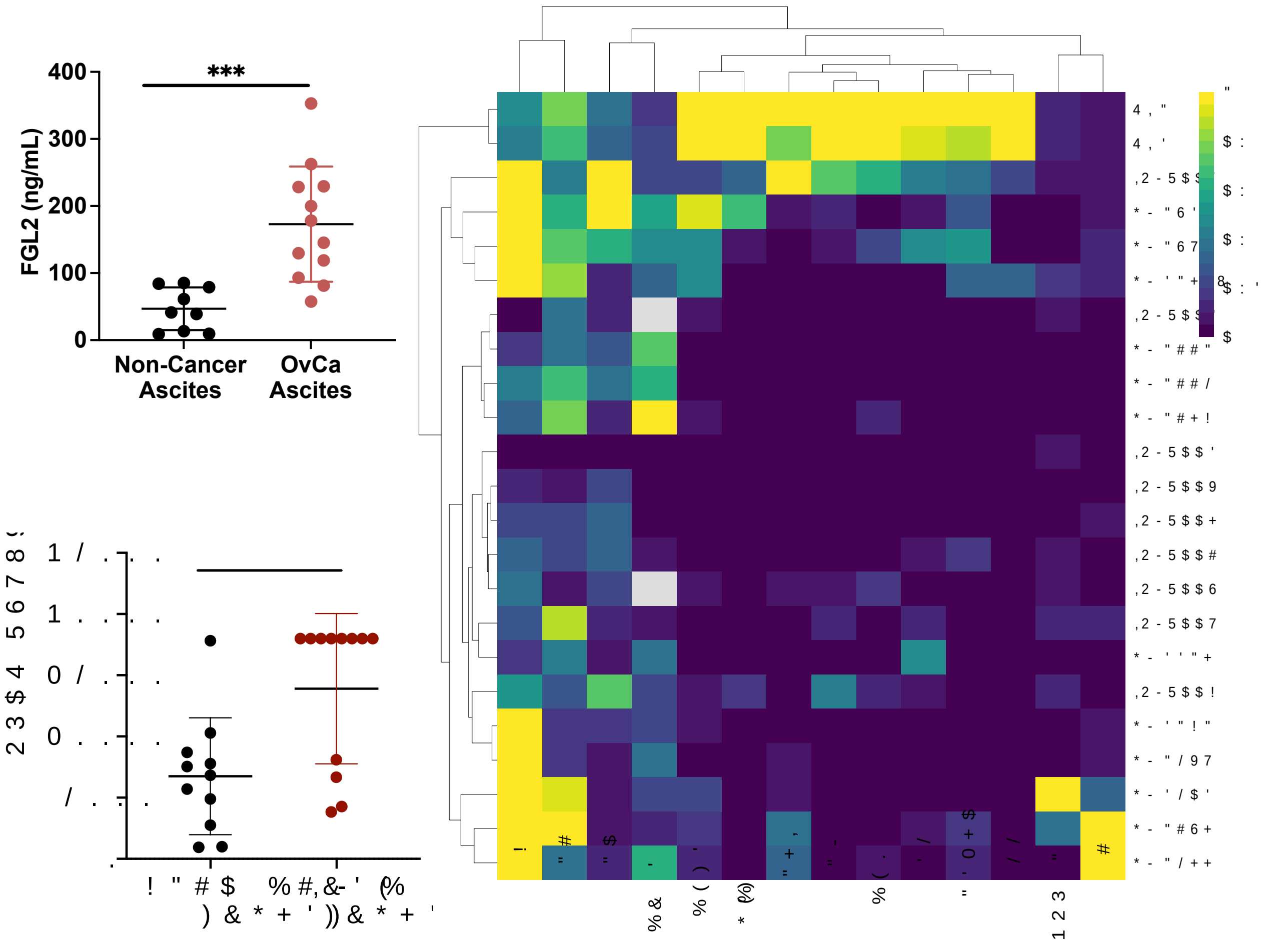

Figure 25. Levels of FGL2 are elevated in human ovarian ascites samples. **(A)** FGL2 concentrations were higher in the ascites fluid from ovarian cancer patients (n=12) compared to non-cancer ascites fluid (n=7) as determined by ELISA. Significance determined by Student's t test. ***p≤ 0.001. **(B)** IL-6 concentrations were higher in the ascites fluid from ovarian cancer patients (n=12) compared to non-cancer ascites fluid (n=7) as determined by LEGENDPlex assay. Significance determined by Student's t test. **p≤ 0.01. **(C)** Clustered heatmap of relative normalized cytokine/chemokine concentrations (min/max normalization for each cytokine/chemokine) and FGL2 concentrations in non-cancer (hA1, hA2 and ACB samples) and ovarian cancer ascites (TB samples).

3.2.2. The absence of FGL2 slows tumour progression and prolongs survival of B16F10 melanoma models

We first sought to determine whether the absence of FGL2 (*Fgl2*$^{-/-}$ mice) relieved immunosuppression and prolonged survival in syngeneic murine tumour models. To specify the role of immune/stromal cell-produced FGL2, we took advantage of *Fgl2* deficient mice and injected them with either ovarian cancer (ID8-*p53*$^{-/-}$*Brca2*$^{-/-}$) or melanoma (B16F10) cells. ID8-*p53*$^{-/-}$*Brca2*$^{-/-}$ and B16F10 cancer cells do not express FGL2 *in vitro* (undetected by qPCR and ELISA, data not shown) nor *in vivo* (**Appendix 7),** mirroring what was found in the tumour cells of human ovarian and melanoma cancers **(Figure 22**). The absence of FGL2 did not prolong survival in i.p. ID8-*p53*$^{-/-}$*Brca2*$^{-/-}$ tumour-bearing mice (**Figure 26A**). However, when we assessed tumour burden at a late timepoint (day 46, immediately prior to the day mice began reaching endpoint) in the orthotopic (i.b.) ID8-*p53*$^{-/-}$*Brca2*$^{-/-}$ model, primary tumour burden was significantly lower in the absence of FGL2 (**Figure 26B**). Additionally, we found a lower accumulated mass of metastatic tumour burden on day 46 for i.b. ID8-*p53*$^{-/-}$*Brca2*$^{-/-}$ tumour-bearing mice (**Figure 26C**), with 4/5 of *Fgl2*^{WT} mice with metastases, but only 1/6 of *Fgl2*$^{-/-}$ mice with metastases. To examine the possibility that genetic modification of the ID8 cell line (deleting *Trp53*, *Brca2*) might affect tumour progression, we similarly assessed survival of an i.p. model of ID8 ovarian cancer, however the absence of FGL2 did not prolong survival in this model either (**Figure 26D**).

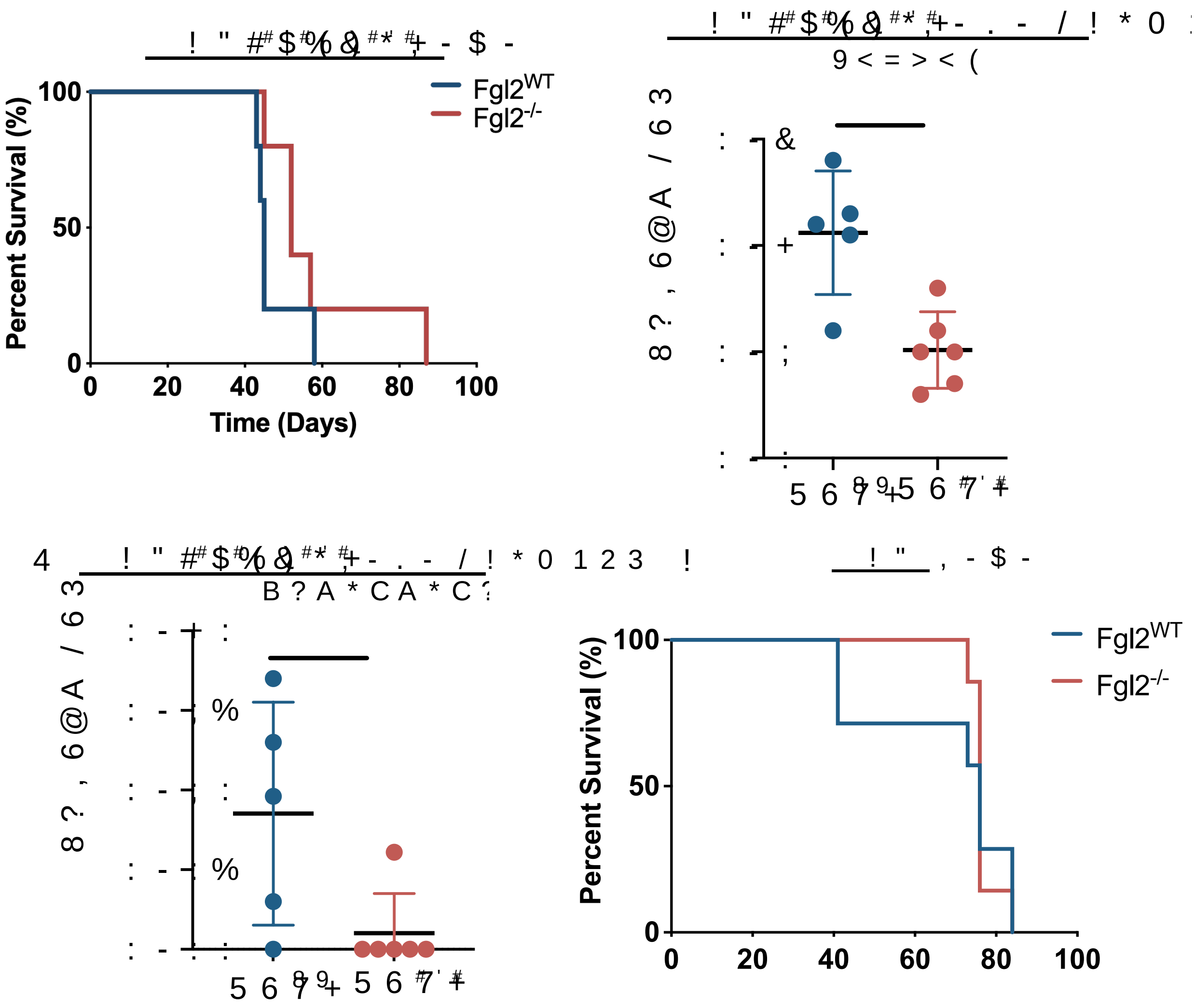

Figure 26. Absence of FGL2 reduces tumour burden in ID8-*p53*$^{-/-}$*Brca2*$^{-/-}$ model. In the ovarian cancer model *Fgl2*^{WT} or *Fgl2*$^{-/-}$ mice received an i.p. injection of ID8-*p53*$^{-/-}$*Brca2*$^{-/-}$ cells (n=6/group) to assess survival **(A)** or an i.b. injection of ID8-*p53*$^{-/-}$*Brca2*$^{-/-}$ cells (n=5-6/group) to collect primary tumours on day 46. While there was no difference on overall survival (Log-Rank test, p=0.2), **(B)** primary and **(C)** metastatic tumour burdens on day 46 were significantly reduced in the *Fgl2*$^{-/-}$ mice. **(D)** *Fgl2*^{WT} or *Fgl2*$^{-/-}$ mice received an i.p. injection of ID8 cells (n=6/group) and were monitored for survival until humane endpoint. No significant difference was observed.

In the melanoma model, the absence of FGL2 significantly prolonged survival of mice injected with B16F10 s.c. (**Figure 27A**) as well as significantly delayed tumour progression (**Figure 27B**). We next sought to determine primary tumour burden at a single timepoint, again immediately prior to endpoint (day 14), for s.c. B16F10 tumour-bearing mice. Primary tumour burden was significantly lower in the absence of FGL2 (**Figure 27C**). To account for potential differences due to location of tumour inoculation, we injected the B16F10 cells i.p. and assessed survival. Similar to the s.c. model, the absence of FGL2 significantly prolonged survival (**Figure 27D**). While the absence of FGL2 did not prolong survival in ID8-*p53*$^{-/-}$*Brca2*$^{-/-}$ tumour-bearing mice, it did reduce tumour burden in these mice at the timepoint prior to endpoint anticipated survival, suggesting an impact on tumour progression. As absence of FGL2 reduced tumour burden in both models, we next sought to determine whether FGL2 normally enhances tumour progression by inducing immune cell changes in the TME.

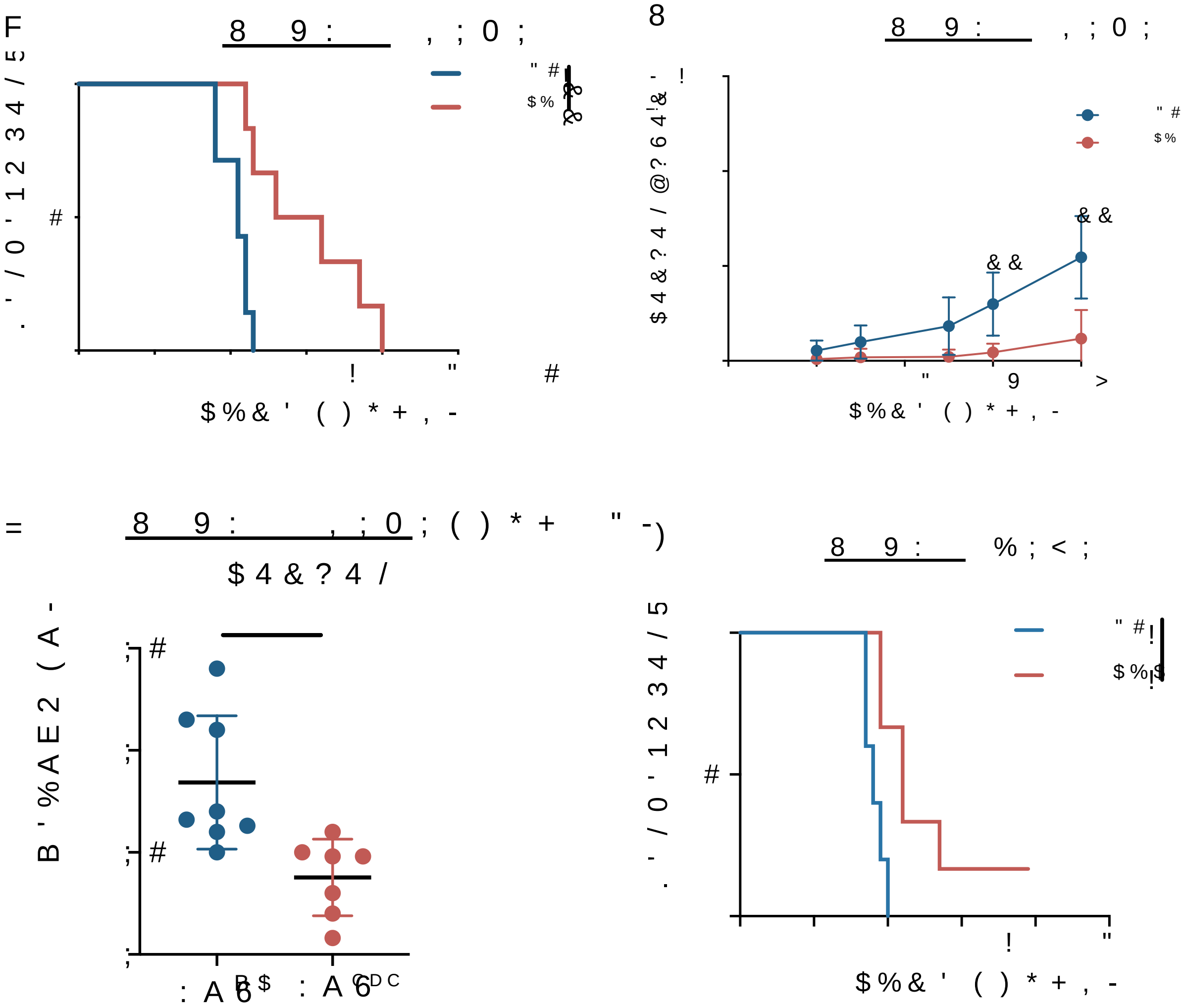

Figure 27. Absence of FGL2 slows tumour progression and prolongs survival of B16F10 melanoma model. In the melanoma model *Fgl2*^{WT} or *Fgl2*$^{-/-}$ mice received a s.c. injection of B16F10 cells (n=6-8/group) to assess for survival with tumours measured approximately every two days using calipers to determine tumour volume (WxWxL), or to collect primary tumours on day 14. **(A).** B16F10 tumour-bearing *Fgl2*$^{-/-}$ mice survived significantly longer (Log-Rank test, $**p \leq 0.01$). **(B)** Tumour volume in *Fgl2*$^{-/-}$ mice was significantly smaller on day 18 and 20. Significance was determined by multiple t tests ($**p \leq 0.01$.) **(C)** Primary tumour burden on day 14 was significantly reduced. Significance determined by Student's t test. $**p \leq 0.01$. Data are representative of 2-3 independent experiments. **(D)** *Fgl2*^{WT} and *Fgl2*$^{-/-}$ mice received an i.p. injection of 0.25 x 10^4 B16F10 cells (n=6/group) and were monitored for survival until humane endpoint. Significance was determined by Log-rank test, $*p \leq 0.05$.

3.2.3. FGL2 is associated with lower expression of NK activation markers and fewer tumour infiltrating NK cells

FGL2 has been associated with immunosuppressive immune cell populations and with diminished activation/maturation of T cells and DCs (Joller et al., 2014; Yan et al., 2015, 2019; Yang et al., 2019; Zhu et al., 2017). Therefore, we characterized immune cell infiltration in B16F10 and ID8-*p53*$^{-/-}$*Brca2*$^{-/-}$ tumours implanted into *Fgl2*$^{-/-}$ mice, to determine if FGL2 favoured tumour progression by inhibiting anti-cancer immunity. We performed flow-cytometric analysis (**Figure 28**) of tumours and spleens collected at day 46 for i.b. ID8-*p53*$^{-/-}$*Brca2*$^{-/-}$ tumour-bearing mice and day 14 for s.c. B16F10 tumour-bearing mice (both timepoints corresponding to a window shortly before mice reach endpoint). First, in *Fgl2*$^{-/-}$ mice we observed a higher infiltration of NK cells in both ID8-*p53*$^{-/-}$*Brca2*$^{-/-}$ (**Figure 29A**) and B16F10 primary tumours (**Figure 29B**). Furthermore, in the absence of FGL2 the frequency of NK cells expressing DNAM-1+ (DNAX accessory molecule, CD226), considered to be more activated and cytotoxic (Martinet et al., 2015), was substantially higher (**Figures 29C** and **29D**). While both tumour-bearing and tumour-naïve *Fgl2*$^{-/-}$ mice had a lower frequency of NK cells in the spleen (**Figure 30 A-C**), a higher frequency of DNAM-1+ NK cells in these mice was not only observed in the tumours, but also in the spleen of tumour-naïve animals (**Figure 30D**). We also observed higher expression of NKG2D and NKG2A (**Figure 30E, F**), suggesting that in the absence of FGL2, NK cells are more activated even in the absence of a pathological challenge. Interestingly, when we probed the basal expression of IFN-γ in resting NK cells, lack of FGL2 resulted in a small but consistent increase in cytokine accumulation (**Figure 30G**), supporting the idea that FGL2 inhibits NK cell activation (Fauriat et al., 2010; Martinet et al., 2015; Weigent et al., 1983; Wensveen et al., 2018). However, higher activation in the absence of FGL2 did not translate to an advantageous response to re-stimulation, as we assessed by stimulating *Fgl2*^{WT} and *Fgl2*$^{-/-}$ splenic NK cells with plate-bound antibodies or chemical activators in CD107 (LAMP1) degranulation, or target cells (YAC1) (**Figure 31 A, B**). In all instances, the cytotoxic response of NK cells was similar in stimulating *Fgl2*^{WT} and *Fgl2*$^{-/-}$ NK cells, which indicates that FGL2 inhibition of NK cell activation can be overcome by acute stimulation, and further suggesting that FGL2 acts as a physiological checkpoint to NK cell activity.

Given the higher activation of NK cells in *Fgl2*$^{-/-}$ mice, we reasoned that the survival advantage in these mice could be due to improved NK cell anti-cancer activity. However, depleting NK cells *in vivo* in a s.c. B16F10 model did not significantly hamper the effect of the absence FGL2 in prolonging survival (**Figure 31C**). The presence of some DX5+ NK cells remaining following depletion may warrant further depletion studies to fully elucidate the role of NK cells *in vivo*. Therefore, while NK cells in the absence of FGL2 have significantly higher NK activation markers by flow cytometry, they do not significantly contribute to prolonged survival or reduced tumour burden in *Fgl2*$^{-/-}$ mice, suggesting that FGL2 had some NK cell-independent effects.

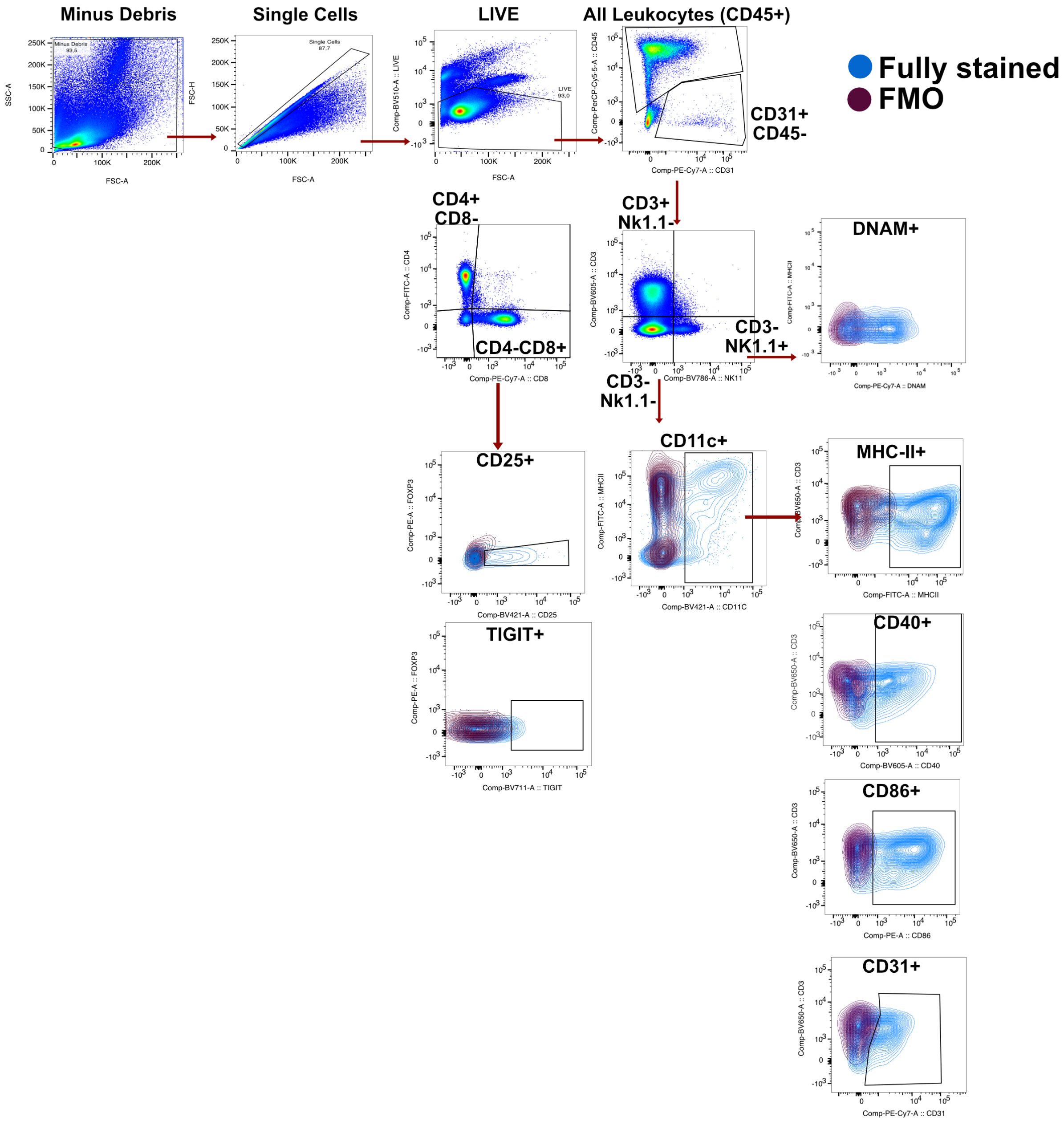

Figure 28. Gating strategy for analysis of flow cytometry data. Gating strategy used to analyze the flow cytometry data from murine tumours and spleens are as follows: cell debris exclusion (Minus Debris), singlet, live/dead exclusion (LIVE), CD45+ (All Leukocytes), NK Cells (CD3-NK1.1+), T cells (CD3+ NK1.1-), CD4+ T cells (CD4+ CD8-), CD8+ T cells (CD4-CD8+), and DCs (CD3- CD11c+). CD25, TIGIT, DNAM-1, MHC-II, CD86, CD40 and CD31 were further used to phenotype immune cell populations. Contour plots show fluorescence minus one (FMOs) for each analyzed marker.

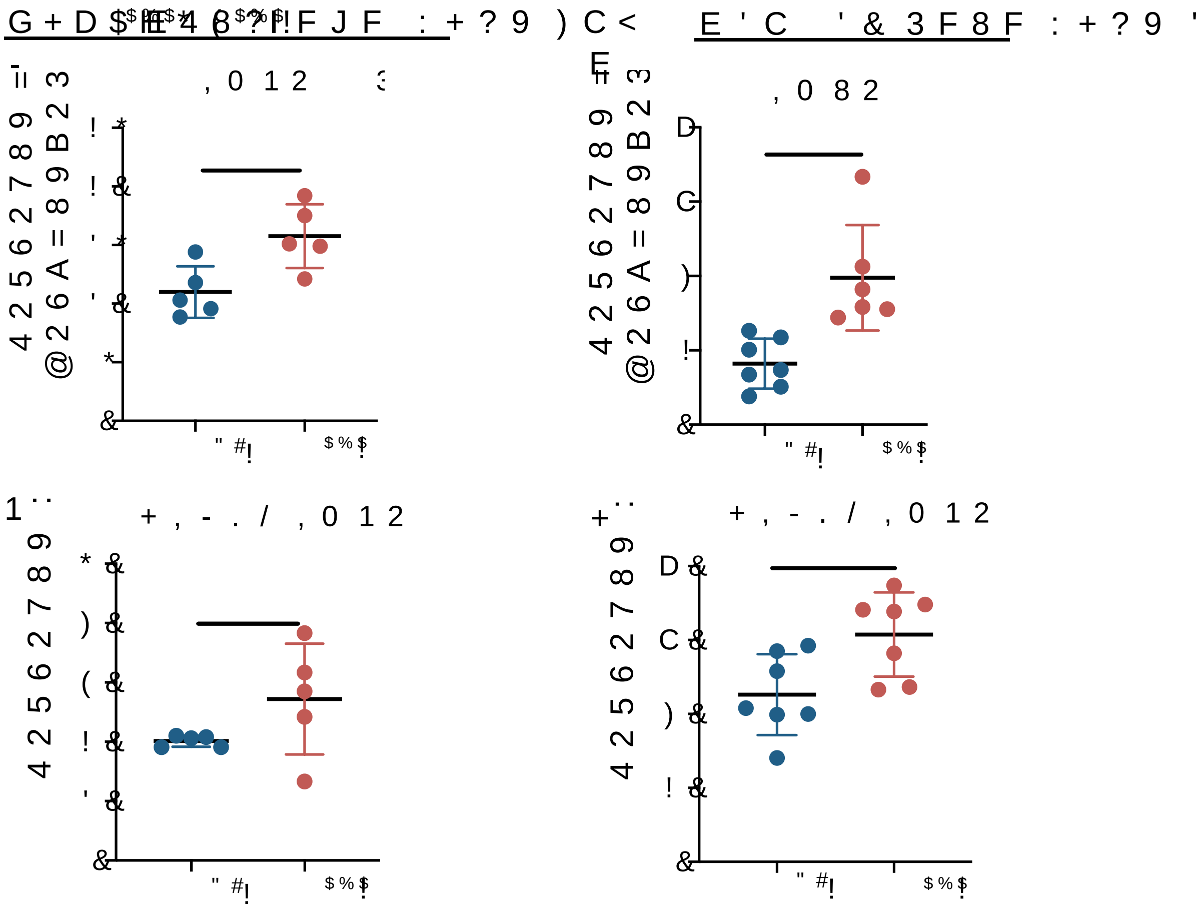

Figure 29. The absence of FGL2 in the tumour microenvironment increases anti-cancer NK cells. *Fgl2*^{WT} and *Fgl2*$^{-/-}$ mice received bilateral i.b. injections of ID8-*p53*$^{-/-}$*Brca2*$^{-/-}$ cells (n=5/group) or s.c. injections of B16F10 cells (n=7/group). Tumours were collected on day 46 or day 14 respectively and assessed by flow cytometry. Absence of FGL2 increased **(A, B)** NK cells and (**C, D)** DNAM-1+ NK cells in ID8-*p53*$^{-/-}$*Brca2*$^{-/-}$ and B16F10 tumours.

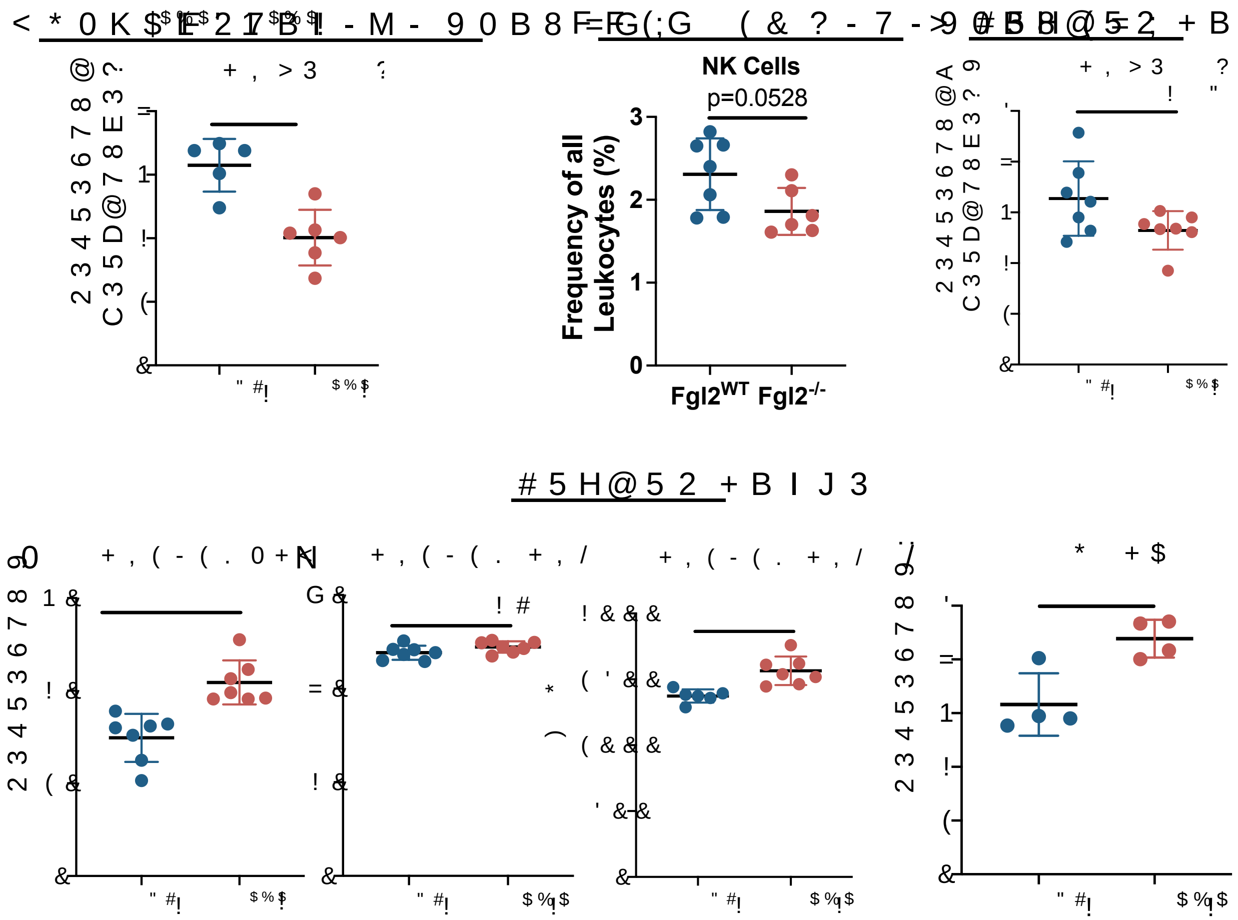

Figure 30. Tumour-naïve *Fgl2$^{-/-}$* NK cells in the spleen have higher NK activation. *Fgl2^{WT}* and *Fgl2$^{-/-}$* mice received bilateral i.b. injections of ID8-*p53$^{-/-}$Brca2$^{-/-}$* cells (n=5/group) or s.c. injections of B16F10 cells (n=7/group) or neither. Spleens were collected on day 46 **(A)** or day 14 **(B)** respectively, as well as from **(C)** tumour-naïve mice (n=3-7 mice/group) and assessed by flow cytometry. Gating strategy: Minus Debris/Singlets/Live Cells/CD45+, NK Cells (NK1.1+CD3-). Spleens of tumour-naïve mice were further assessed by flow cytometry with the absence of FGL2 increasing the frequency of **(D)** DNAM-1+ and **(E)** NKG2A+, **(F)** NKG2D+ expression (gMFI), and **(G)** IFN-γ+ NK cells, Gating strategy: Minus Debris/Singlets/Live Cells/CD45+, NK Cells (NK1.1+CD3-) and DNAM-1+, IFN-γ+, NKG2D+, NKG2A+, NK cells. Significance determined by Student's t test. $*p \leq 0.05$, $**p \leq 0.01$, $***p \leq 0.001$.

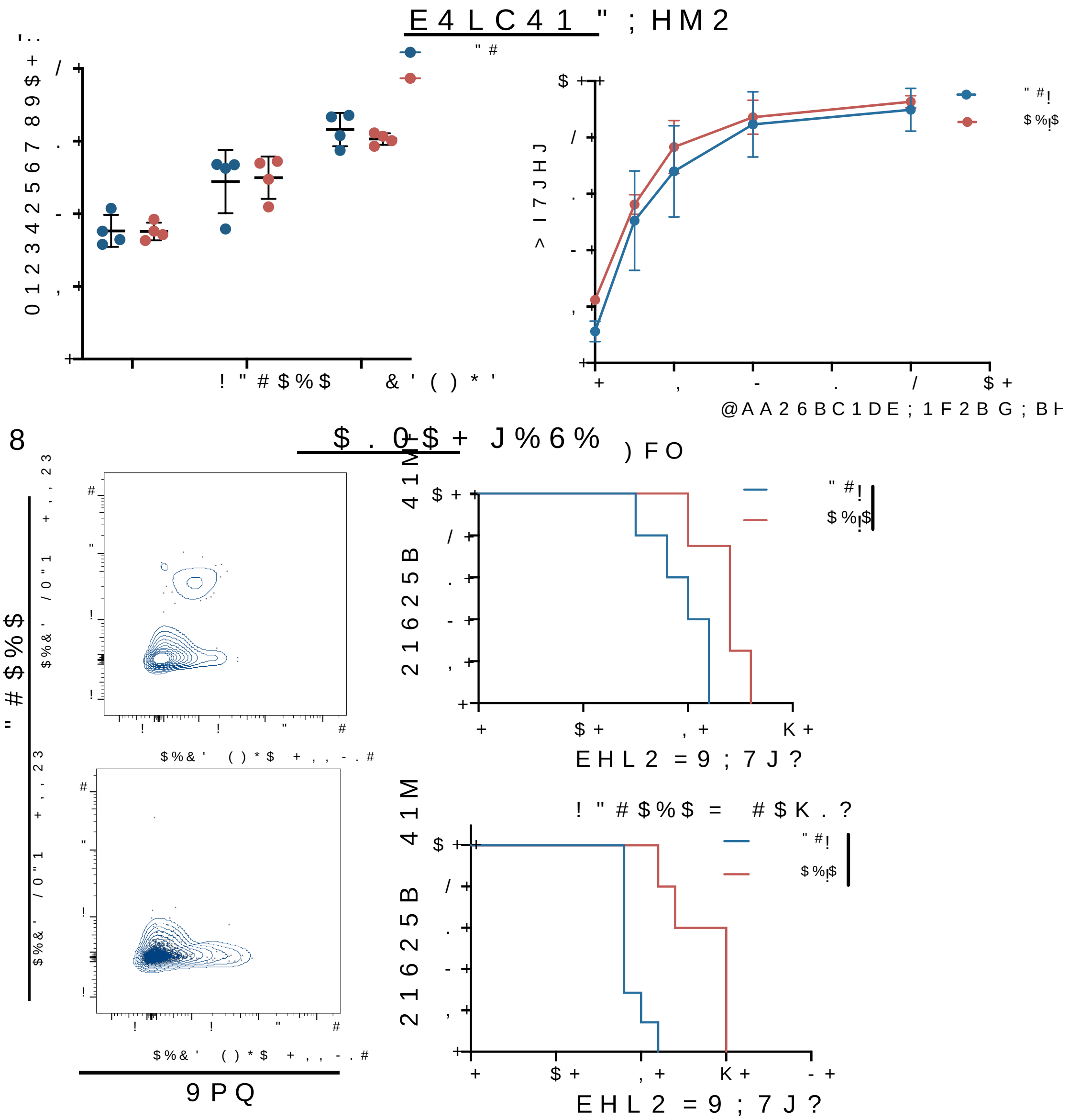

Figure 31. NK cells do not contribute to prolonged survival in *Fgl2*$^{-/-}$ mice. (A) NK cells from *Fgl2*^{WT} and *Fgl2*$^{-/-}$ mice were assessed for degranulation (CD107+ (Alter et al., 2004)) by plate-bound activation with α-NK1.1, non-specific activation by PMA/Ionomycin, or with PBS as an unactivated control. Gating strategy: Minus Debris/Singlets/Live Cells/CD45+/NK Cells (DX5+CD3-) and CD107+ NK cells. **(B)** NK cells from *Fgl2*^{WT} and *Fgl2*$^{-/-}$ mice were assessed for their ability to induce target cell lysis at different ratios of effector: target cell (YAC-1) ratios. Gating strategy: Minus Debris/Singlets/NK Cells (CP450+)/lysed cells (PI+). Significance determined by Student's t test. **(C)** *Fgl2*^{WT} and *Fgl2*$^{-/-}$ mice (n=6mice/group) were treated with 200µg/mouse IgG control antibody or α-NK1.1 (PK136) to deplete NK cells one and two days before tumour injections (B16F10 2x10^{5} cells s.c.) followed by weekly injection of depletion antibodies. Mice were assessed for survival and spleens were collected at endpoint to confirm depletion of NK cells. Gating strategy: Minus Debris/Singlets/Live Cells/CD45+, NK Cells (NK1.1+DX5+CD3-). *Fgl2*$^{-/-}$ mice survived significantly longer in both IgG control and NK depleted groups. Significance determined by Log-Rank test, *p≤ 0.05, **p≤ 0.01.

3.2.4. The absence of FGL2 is associated with more activated dendritic and T cells in the TME

DCs play a key role in the generation of anti-tumoural responses and are key targets of FGL2-mediated immunosuppression (Liu et al., 2008; Yan et al., 2019; Yang et al., 2019). Next, we therefore sought to profile the effect of FGL2 absence on tumour-infiltrating and splenic DCs in B16F10 or ID8-$p53^{-/-}Brca2^{-/-}$ tumours implanted into $Fgl2^{-/-}$ mice. First, we found fewer DCs in ID8-$p53^{-/-}Brca2^{-/-}$ tumours in $Fgl2^{-/-}$ mice (**Figure 32A**), with a strong trend to decreased frequencies of co-stimulatory markers (CD80, CD40) (**Figure 32B**). Interestingly we obtained opposite results in the B16F10 tumours, where we observed a greater frequency of DCs in $Fgl2^{-/-}$ mice (**Figure 32C**). These DCs expressed more co-stimulatory markers (MHC-II+, CD86+, CD40+) and decreased frequency of the co-inhibitory marker CD31 (**Figure 32D**) in $Fgl2^{-/-}$ mice. While no difference was observed in total splenic DC frequencies (**Figure 33A-C**), we observed increased expression of co-stimulatory markers (MHC-II+ CD86+, CD40+) and CD31+ in ID8-$p53^{-/-}Brca2^{-/-}$ tumour-bearing mice (**Figure 33B**), suggesting more antigen presentation in the periphery. No difference was observed in the expression of co-stimulatory markers on splenic DCs (**Figure 33D**) in B16F10 tumour-bearing mice. Profiling DCs in spleens of tumour-naïve mice suggests that $Fgl2^{-/-}$ mice have greater expression of co-stimulatory markers (**Figure 33F**), as previously shown in the literature (Liu et al., 2008). In summary, B16F10 tumours are infiltrated by more DCs and more activated DCs, which are a characteristic of $Fgl2^{-/-}$ mice (Liu et al., 2008), and may contribute to tumour elimination and prolonged survival in this model. This was not the case in the ID8-$p53^{-/-}Brca2^{-/-}$ model, as there were fewer DCs of $Fgl2^{-/-}$ tumours, and higher expression of co-stimulatory molecules was only found in the spleen.

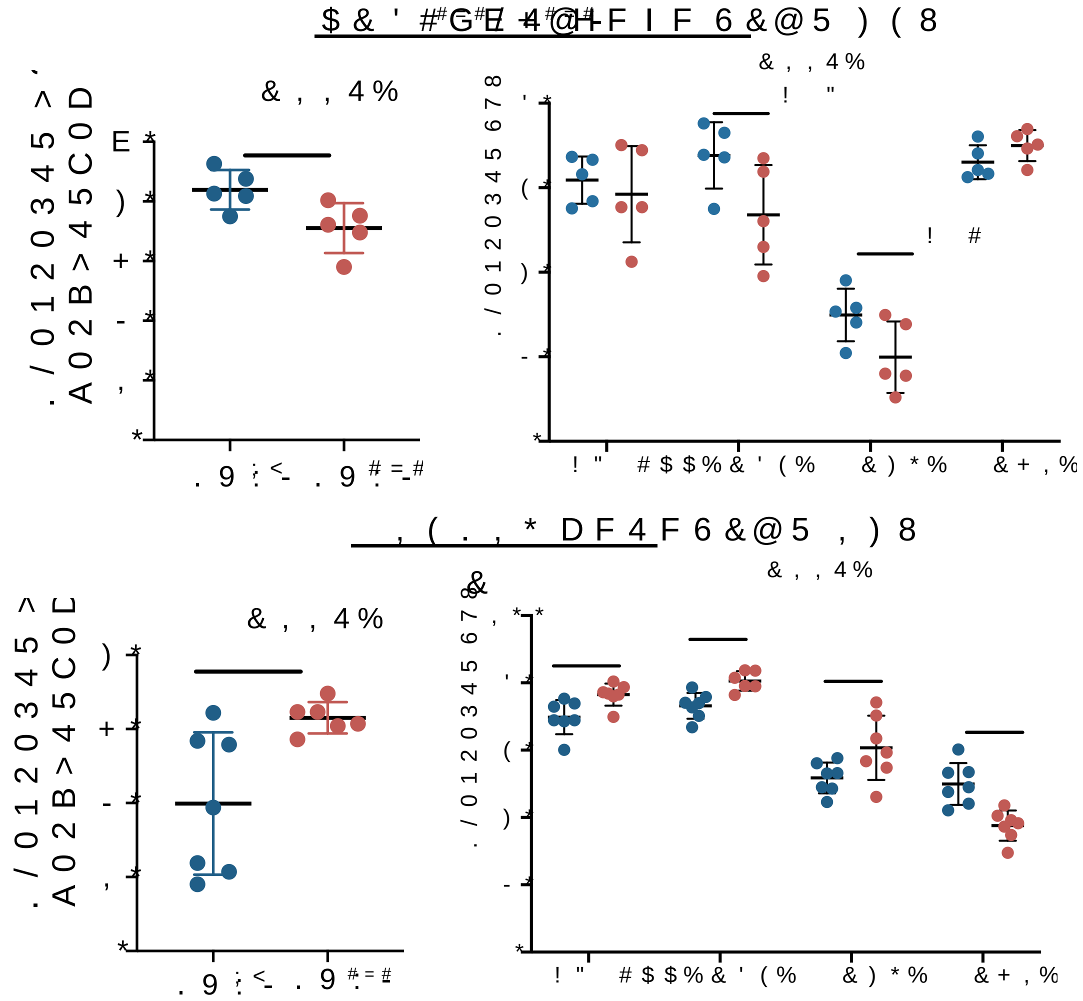

Figure 32: The absence of FGL2 in the tumour microenvironment increases activated DCs in B16F10 tumours. *Fgl2*^{WT} and *Fgl2*$^{-/-}$ mice received bilateral i.b. injection of ID8-*p53*$^{-/-}$*Brca2*$^{-/-}$ cells (n=5/group) or s.c. injection of B16F10 cells (n=7/group). Tumours were collected on day 14 or day 46 respectively and assessed by flow cytometry. (**A**) Absence of FGL2 was associated with fewer DCs in ID8-*p53*$^{-/-}$*Brca2*$^{-/-}$ tumours. **(B)** An assessment of activation/maturation markers showed decreased CD86 and CD40. (**C**) A greater frequency of DCs was observed in B16F10 tumours of *Fgl2*$^{-/-}$ mice. (**D**) Absence of FGL2 was further associated with a greater frequency of MHC-II+, CD86+, and CD40+ DCs in B16F10 tumours. Gating strategy: Minus Debris/Singlets/Live Cells/CD45+/CD3-, followed by: DCs (CD11c+) and MHC-II, CD86, CD40, and CD31 expression. Significance determined by Student's t test; *p≤0.05, **p≤ 0.001.

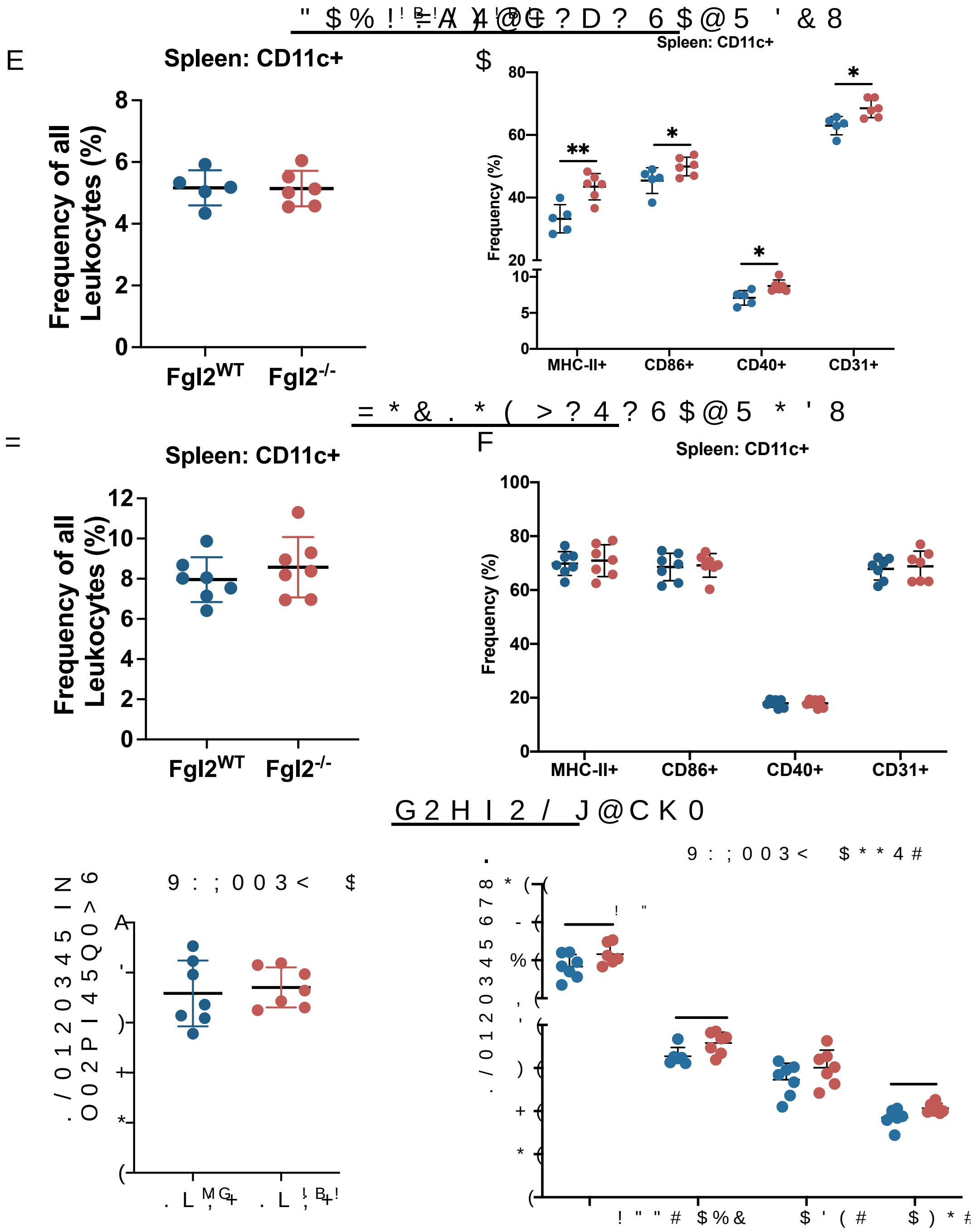

Figure 33: The absence of FGL2 activated splenic DCs in the spleen of ID8-*p53*$^{-/-}$*Brca2*$^{-/-}$ tumour-bearing mice. *Fgl2*^{WT} and *Fgl2*$^{-/-}$ mice received bilateral i.b. injections of ID8-*p53*$^{-/-}$ *Brca2*$^{-/-}$ cells (n=5/group) or s.c. injections of B16F10 cells (n=7/group), or neither. Spleens were collected on day 46 **(A, D)** or day 14 **(B, E)** respectively, as well as from **(C, F)** tumour-naïve mice (n=3-7 mice/group) and DCs were assessed by flow cytometry. **(A-C)** No difference was observed in frequency of splenic DCs. **(D-F)** Absence of FGL2 was further associated with a greater frequency of MHC-II+, CD86+, CD31+, and CD40+ DCs of ID8-*p53*$^{-/-}$*Brca2*$^{-/-}$ tumour-bearing mice and tumour-naïve mice, but not B16F10 mice. Gating strategy: Minus Debris/Singlets/Live Cells/CD45+/CD3-, followed by: DCs (CD11c+) and MHC-II, CD86, CD40, and CD31 expression. Significance determined by Student's t test; $*p \leq 0.05$, $**p \leq 0.001$.

T cells, particularly CD4+ T cells, are a downstream target of FGL2-mediated immunosuppression of DCs (Ai et al., 2018; Bartczak et al., 2016, 2017; Shalev et al., 2008; Wang et al., 2015). Given that DCs have more co-stimulatory molecules, we hypothesized that the absence of FGL2 would correspond to more T cell activation and therefore we next characterized tumour-infiltrating T cells and splenic T cells in B16F10 or ID8-*p53*$^{-/-}$*Brca2*$^{-/-}$ tumours implanted into *Fgl2*^{WT} and *Fgl2*$^{-/-}$ mice. In the absence of FGL2 we observed increased T cells in ID8-*p53*$^{-/-}$*Brca2*$^{-/-}$ tumours (**Figure 34A**) and the CD4+ T cells showed a trend for higher expression of TIGIT (**Figure 34B**). Conversely, we observed decreased T cells in B16F10 tumours implanted in *Fgl2*$^{-/-}$ mice (**Figure 34C**), however the CD4+ T cells were more CD25+ (**Figure 34D)** and TIGIT+ (**Figure 34E),** and CD8+ T cells tended to be more CD25+ (**Figure 34F**), which are markers of activated T cells (Wing et al., 2002; Yu et al., 2009). Finally, no significant difference was observed in MDCSs in either tumour model, although *Fgl2*$^{-/-}$ mice with B16F10 tumours tended to have less infiltration of MDSCs (**Figure 35**). Overall, the absence of FGL2 leads to increased frequency of T cells in ID8-*p53*$^{-/-}$*Brca2*$^{-/-}$ tumours and increased activated tumour-infiltrating T cells in B16F10 tumours.

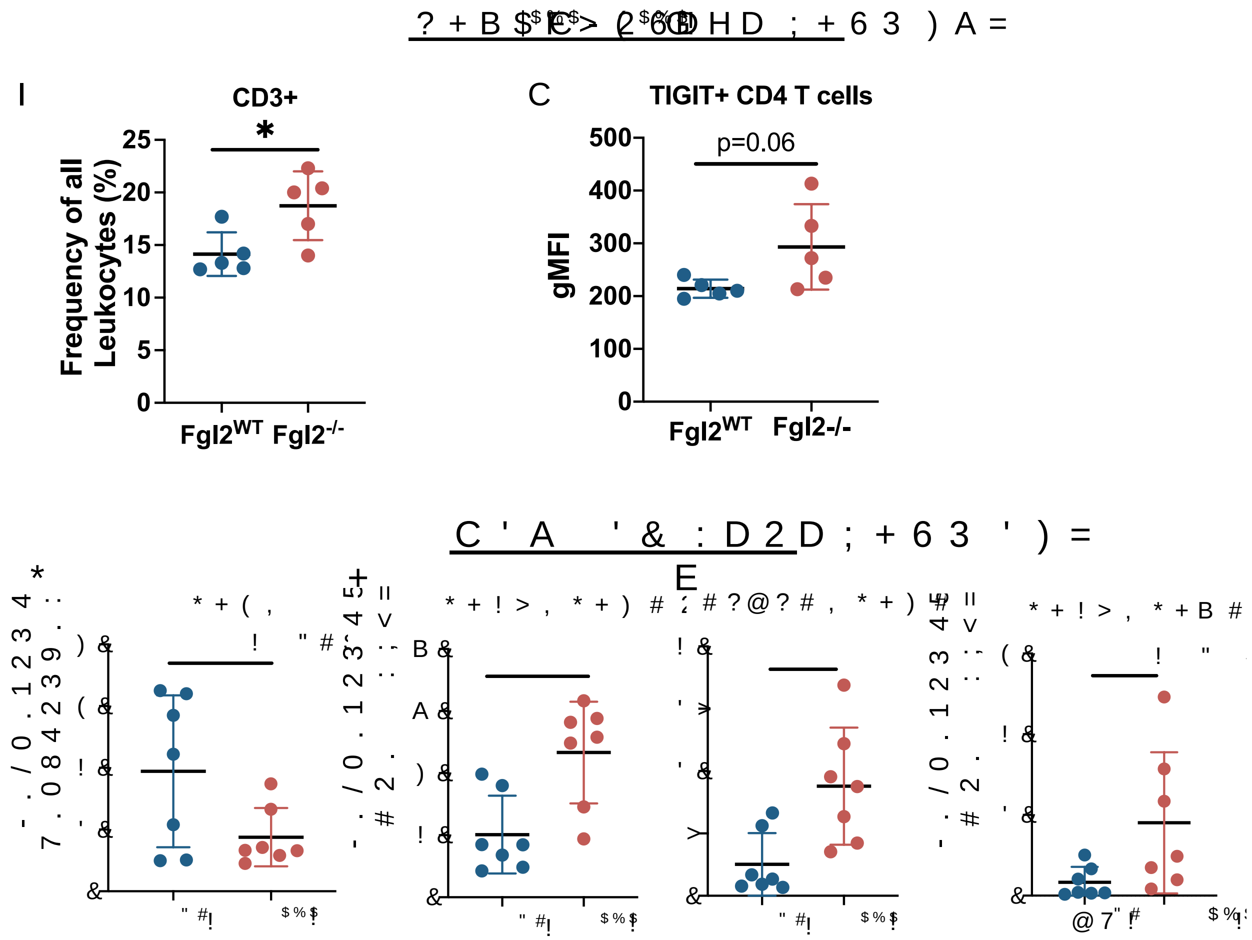

Figure 34: The absence of FGL2 in the tumour microenvironment increased activated T cells in B16F10 tumours. *Fgl2*^{WT} and *Fgl2*$^{-/-}$ mice received bilateral i.b. injection of ID8-*p53*$^{-/-}$*Brca2*$^{-/-}$ cells (n=5/group) or s.c. injection of B16F10 cells (n=7/group). Tumours were collected on day 14 or day 46 respectively and assessed by flow cytometry. Absence of FGL2 increases **(A)** T cells in ID8-*p53*$^{-/-}$*Brca2*$^{-/-}$ tumours and **(B)** CD4+ T cells have a trend for greater expression (gMFI) of TIGIT. Absence of FGL2 in B16F10 tumours **(C)** decreased frequency of T cells but they are more activated with more **(D)** CD4+ CD25+, **(E)** CD4+TIGIT+, and **(F)** CD8+ CD25+ T cells. Gating strategy: Minus Debris/Singlets/Live Cells/CD45+, T cells (NK1.1-CD3+) and CD4/CD8+ CD25+, TIGIT+ markers. Significance determined by Student's t test. *p≤ 0.05, **p≤ 0.01.

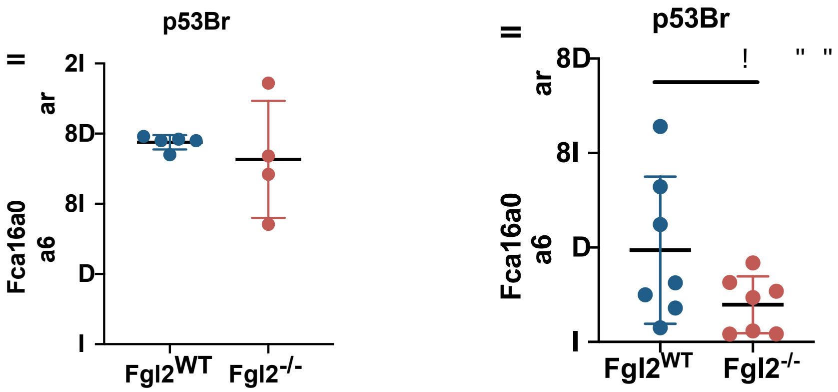

Figure 35. No significant differences observed in tumour infiltrating MDSCs. *Fgl2*^{WT} and *Fgl2*$^{-/-}$ mice received bilateral i.b. injection of ID8-*p53*$^{-/-}$*Brca2*$^{-/-}$ cells (n=5/group) or s.c. injection of B16F10 cells (n=7/group). Tumours were collected on day 14 or day 46 respectively and assessed by flow cytometry. No significant differences were observed in tumour-infiltrating MDSCs in **(A)** ID8-*p53*$^{-/-}$*Brca2*$^{-/-}$ tumours or **(B)** B16F10 tumours. Gating strategy: Minus Debris/Singlets/Live Cells/CD45+, MDSCs (CD3- CD11b+ Gr1+). Significance determined by Student's t test.

3.2.5. FGL2 blockage promotes activated T cells in the TME

Given that the absence of FGL2 prolonged survival in B16F10 tumour-bearing mice, we next sought to therapeutically target FGL2 with a blocking antibody. Although we focused this study on assessing the effects of FGL2 deficiency in the context of sFGL2 action on tumour infiltrating lymphocytes, due to our observations of infiltration of more activated NK cells, T cells and DCs into the tumour, it should be noted that we did observe decreased CD31+ (endothelial) cells in the B16F10 tumours implanted in *Fgl2*$^{-/-}$ mice (**Figure 36A,B**), suggesting the absence of FGL2 also decreased vascularization of the tumour. Decreased vascularization in the TME has previously been attributed to the function of mFGL2 (Liu et al., 2012; Rabizadeh et al., 2015). Therefore, we further sought to distinguish the consequences of targeting both forms of FGL2 using a polyclonal α-FGL2 antibody (Ning et al., 2005) with the effects of an sFGL2-blocking monoclonal antibody (clone 6H12) (Luft et al., 2018) in B16F10 s.c. tumour-bearing mice. Surprisingly, neither the monoclonal nor the polyclonal antibody significantly prolonged survival compared to their appropriate IgG controls (**Figure 36C**), nor did they slow the rate of tumour progression (**Figure 36D**).

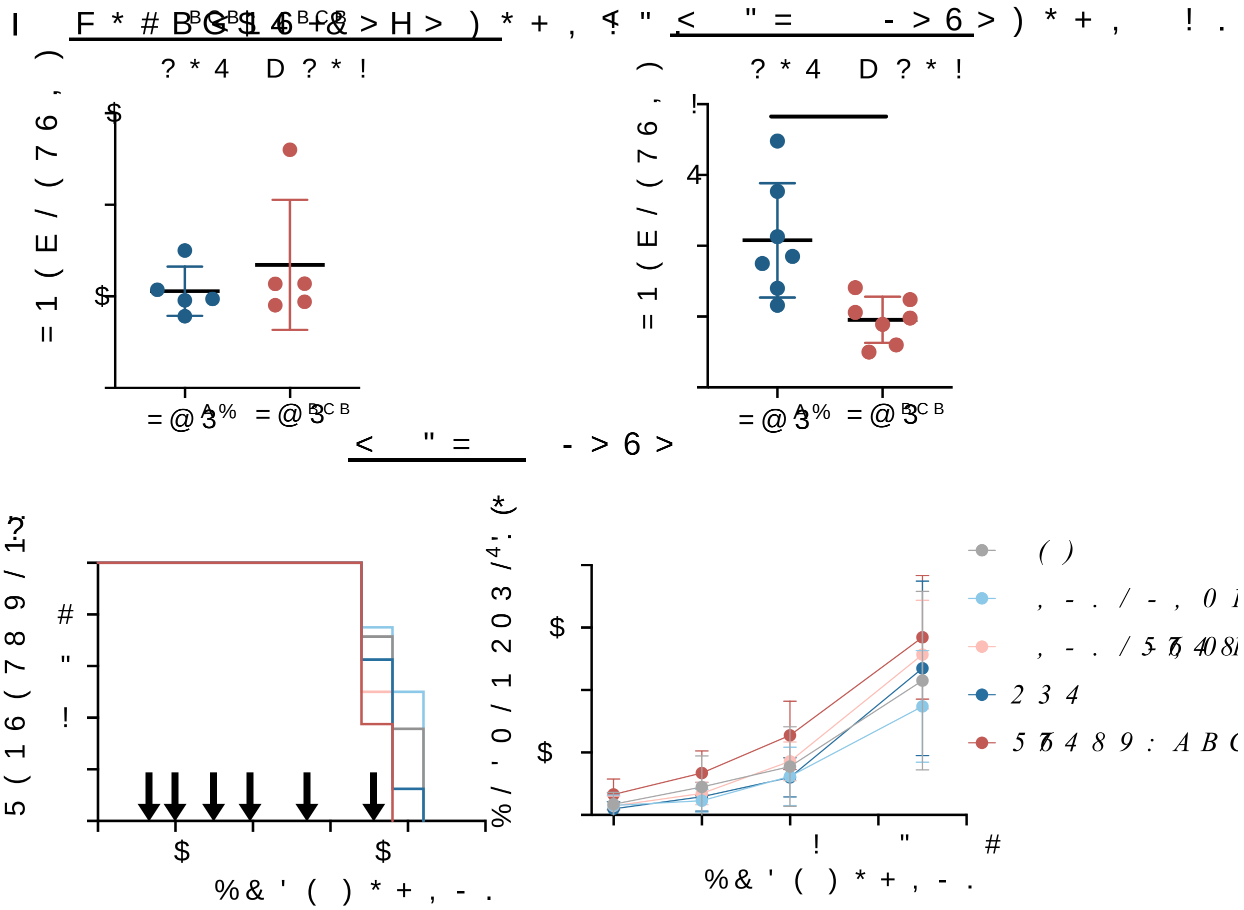

Figure 36. Blocking FGL2 does not slow tumour progression or prolong survival. (A) *Fgl2*^{WT} and *Fgl2*$^{-/-}$ mice received bilateral i.b. injections of ID8-*p53*$^{-/-}$*Brca2*$^{-/-}$ cells (n=5/group) or s.c. injections of B16F10 cells (n=7/group) and the frequency of endothelial cells (CD31+ CD45-) in the tumours was assessed on **(A)** day 46 or **(B)** day 14 respectively. Gating Strategy: Minus Debris/Singlets/Live Cells/CD45-CD31+. Significance determined by Student's t test. $^{**}p \leq 0.01$. Mice were inoculated with $2x10^5$ B16F10 cells s.c. (8 mice/group) and were treated with α-polyclonal FGL2 (100µg/mouse) or α-monoclonal FGL2 (6H12) (150µg/mouse) antibodies starting 3 days after tumour injections (arrows). Injections continued 2x/week. Tumours were measured every two days and mice were assessed for survival. No difference in **(C)** survival or **(D)** tumour progression was observed. Significance was determined by Log-Rank test.

We next used the STOSE ovarian cancer model, as a more immunogenic model (expresses MHC-I) with a greater chance of responding to immunotherapy (Yu et al., 2018), and targeted FGL2 with the monoclonal α-FGL2 (clone 6H12), specifically blocking the sFGL2 form. In this model, we assessed FGL2 levels in the plasma following 7 days of treatment and in the ascites at endpoint by ELISA, demonstrating that the therapeutic antibody successfully targeted sFGL2 (**Figure 37A, 37B**), either decreasing amounts of FGL2 or simply masking the antibody in the ELISA from binding. However, blocking FGL2 did not prolong survival when compared to the appropriate IgG or PBS controls (**Figure 37C)**. Despite the lack of effect on survival, we determined if the antibodies had any effect on the splenic immune cell populations after 7 days of treatment. Similar to what we observed in *Fgl2*$^{-/-}$ mice bearing B16F10 and ID8-*p53*$^{-/-}$*Brca2*$^{-/-}$ tumours, the spleens of STOSE tumour-bearing mice had increased CD25+ (**Figure 37D**) and TIGIT+ (**Figure 37E**) CD4+ T cells, suggesting increased activation of CD4+ T cells when FGL2 activity was blocked. No differences were observed in other immune cell populations in our extensive characterization by flow cytometry.

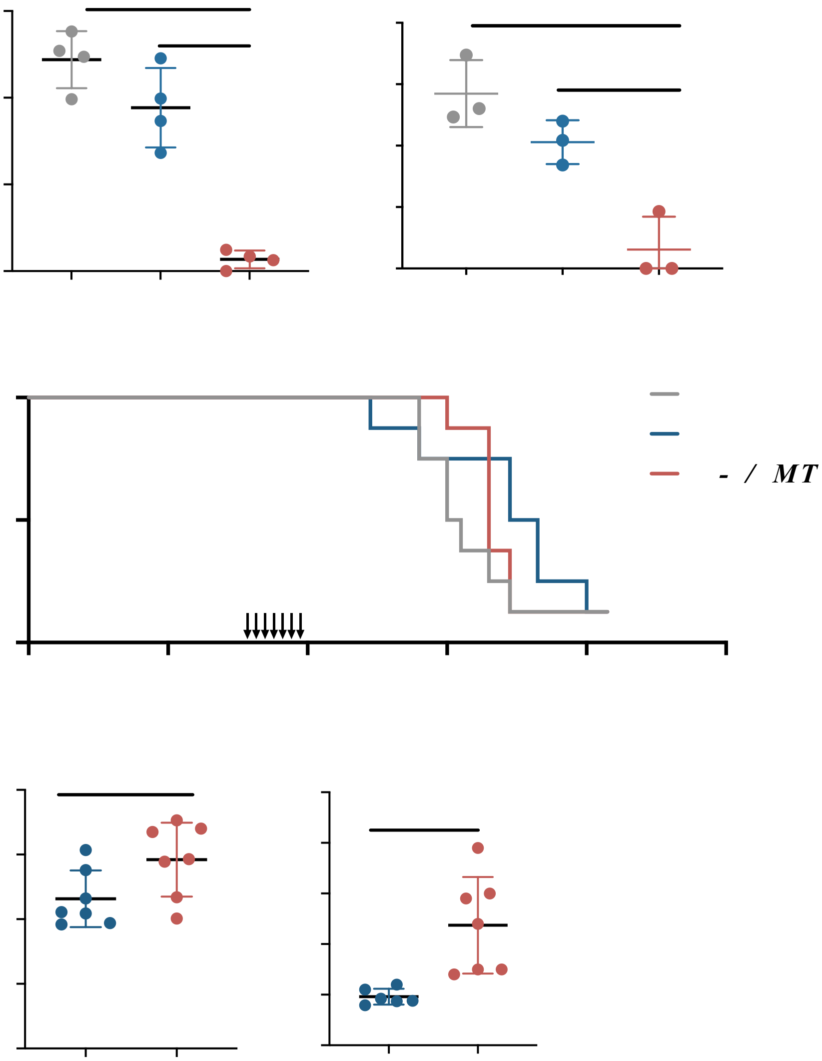

Figure 37: α-mFGL2 treatment of a STOSE model of ovarian cancer increases frequency of activated T cells. FVB/N mice bearing STOSE tumours (31 days post i.p. injection of $5x10^6$ STOSE cells) received 1 daily i.p. injection of PBS, IgG control, or α-FGL2 antibody (150µg/mouse) for 7 days (arrows). Twenty-four hours after the final treatment, 7 mice/group were sacrificed, and spleens were analyzed by flow cytometry. The remaining 8 mice/group were assessed for survival. **(A)** Levels of FGL2, as determined by ELISA, in the ascites at endpoint was significantly lower in α-FGL2 treated mice compared to IgG and PBS treated mice. **(B)** Levels of FGL2 in the plasma following treatment are significantly lower in α-FGL2 treated mice compared to IgG and PBS treated mice. **(C)** No difference was observed in survival. Significance was determined by Log-Rank test. Increased frequencies of activated **(D)** CD25+ and **(E)** TIGIT+ CD4 T cells in the spleen. Gating Strategy: Minus Debris/Singlets/Live Cells/CD45+, CD4+ T cells (NK1.1- CD3+CD4+), CD25+ or TIGIT+. Significance was determined by One-Way ANOVA with Tukey's post-test; *p≤0.05, **p≤ 0.01, ****p<0.0001.

3.2.6. FGL2 knockout and oncolytic virotherapy synergizes to significantly prolong survival

"Cold" tumours present a challenge for immunotherapy success, including low MHC-I expression, lack of TAAs, and/or poor immune cell infiltration into the tumour (Bonaventura et al., 2019). Considering that in the absence of FGL2, DCs in the spleens of ID8-*p53*$^{-/-}$*Brca2*$^{-/-}$ tumour-bearing mice were more activated, but were excluded from the tumour, we therefore combined immunotherapeutic strategies in order to attempt to convert the "cold" tumour [MHC-I low (Figure 5), excluded activated DC] into a "hot" tumour (reviewed in McCloskey et al., 2018; Rodriguez et al., 2018). Oncolytic virotherapy is an immunotherapeutic strategy being used in several clinical trials, and has been shown to turn a "cold" tumour into a "hot" tumour (Bonaventura et al., 2019; Chiocca and Rabkin, 2014; Ribas et al., 2017). OVs selectively infect and kill cancer cells as well as induce immunogenic cell death stimulating immune cell infiltration and activation of antigen presenting cells (DCs and macrophages) (Achard et al., 2018; Stojdl et al., 2003). Therefore, we stimulated immune cell infiltration into the tumour using oncolytic virotherapy (VSV-M51-GFP; Stojdl et al., 2003). ID8-*p53*$^{-/-}$*Brca2*$^{-/-}$ cancer cells were injected i.p., followed by treatment with 1×10^8 pfu of VSV-M51-GFP on days 7, 10, and 13. While neither the absence of FGL2 alone nor the OV alone were able to prolong survival, the combination treatment synergized to prolong survival (Log-Rank test, $^{**}p \leq 0.01$) (**Figure 38A**), with two mice surviving past 150 days, as well as one mouse in the *Fgl2*$^{-/-}$ group that received PBS. Surviving mice were re-challenged with 3×10^6 ID8-*p53*$^{-/-}$*Brca2*$^{-/-}$ cells on day 150, but all reached endpoint as expected (around 55 days post-rechallenge), suggesting no memory response resulted from the combination of *Fgl2*$^{-/-}$ and OV (VSV-M51-GFP) (**Figure 38B**). Overall, we found that blocking FGL2 alone was insufficient to prolong survival as a novel immunotherapy for ovarian cancer. However, when treating a model that was previously unresponsive to the absence of FGL2 with an OV, the combination significantly prolongs survival. This suggests that loss or blockage of FGL2 combined with other immunotherapies may set the stage to enhance response to certain immunotherapies.

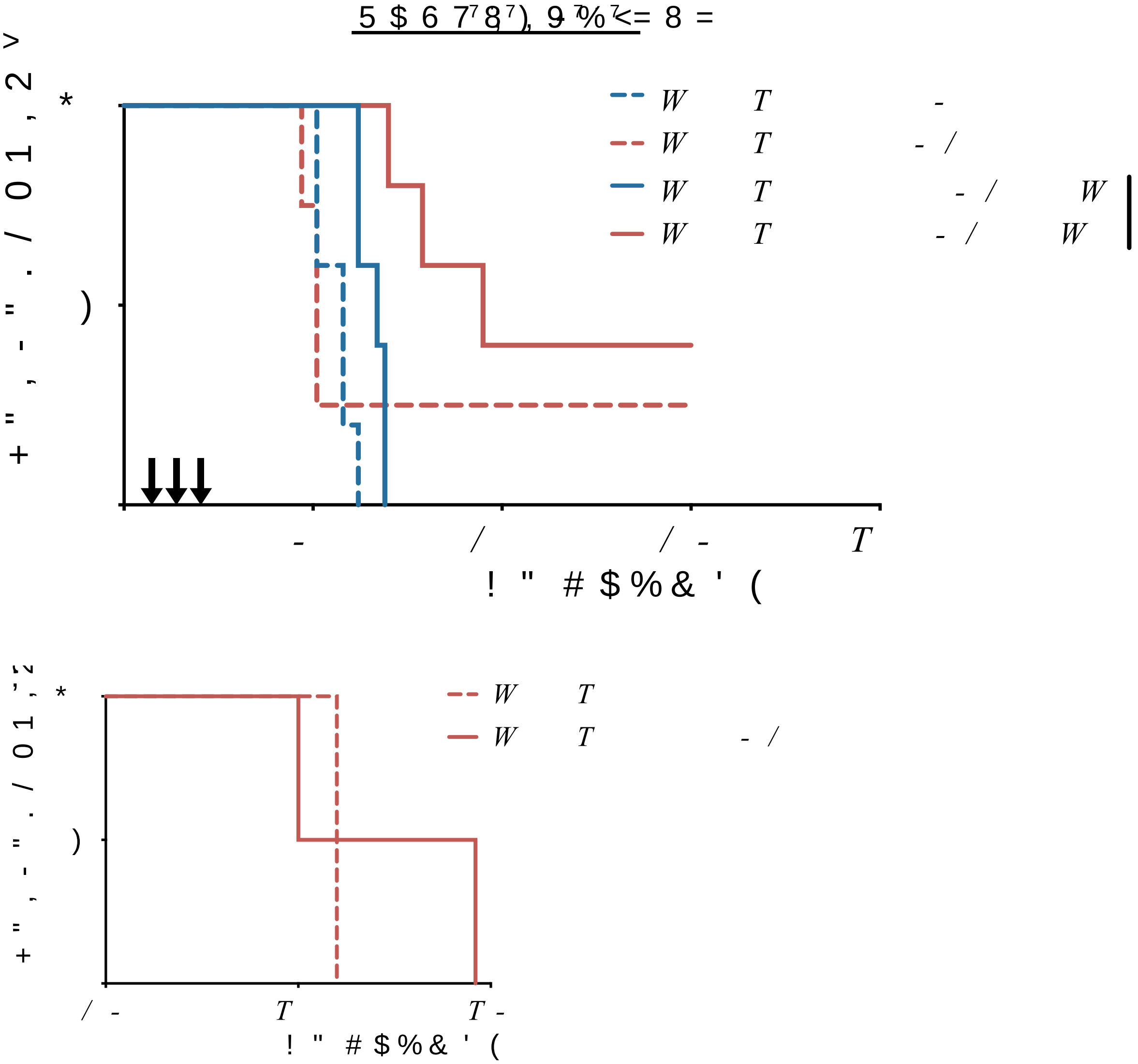

Figure 38. The absence of FGL2 and oncolytic virus treatment synergizes to prolong survival. (A) *Fgl2*^{WT} and *Fgl2*$^{-/-}$ mice received an i.p. injection of ID8-*p53*$^{-/-}$*Brca2*$^{-/-}$ cells followed by VSV-M51-GFP injected i.p. on day 7,10,13 (arrows). *Fgl2*$^{-/-}$ mice + VSV-GFP treatment survived significantly longer than *Fgl2*^{WT} with VSV-M51-GFP treatment (Log-Rank test, $^{**}p \leq 0.01$). **(B)** Surviving mice were re-challenged with 3×10^6 *ID8-p53*$^{-/-}$*Brca2*$^{-/-}$ cells i.p. on day 150 and assessed for survival.

3.2.7. Summary

FGL2 is a mediator of immunosuppression in a number of different settings, including in the TME, leading to tumour progression and poor survival. We showed conclusively for the first time that FGL2 is not expressed in cancer cells in human cancers, based on publicly available scRNA-seq data, but rather is expressed primarily in monocytes/macrophages and DCs. We investigated the role of FGL2 in tumour progression in the B16F10 model of melanoma and ID8-*p53*$^{-/-}$*Brca2*$^{-/-}$ model of ovarian cancer, primarily focusing on the immunosuppressive functions of sFGL2. Tumours in *Fgl2*$^{-/-}$ mice were more infiltrated with DNAM-1+ NK cells in both models, and by activated DCs (CD86+, CD40+) and T cells (CD25+, TIGIT+) in the B16F10 tumours of mice or spleens of ID8-*p53*$^{-/-}$*Brca2*$^{-/-}$ tumour-bearing mice, highlighting the role of FGL2 mediated immunosuppression. The absence of FGL2 prolonged survival in the B16F10 model. Finally, the absence of FGL2 did not prolong survival in ID8-*p53*$^{-/-}$*Brca2*$^{-/-}$ model, but remarkably prolonged survival when combined with OV therapy.

3.3. FGL2 contributes to post-operative immunosuppression and increased metastatic disease

FGL2 is elevated in patient plasma following sepsis (non-sterile tissue injury) (Zhou et al., 2019), and the resulting immunosuppression plays a role in responding inflammation. We hypothesized that FGL2 would be similarly increased following sterile tissue injury (surgical stress) and that FGL2 contributes to the post-operative immunosuppression which leads to increased cancer metastases in a well-established experimental model of surgical stress (Tai et al., 2013, 2018).

3.3.1. Soluble FGL2 is elevated in response to surgical stress

We compared FGL2 levels in plasma of patients prior to surgery (baseline) and one day post-surgery (POD1) with healthy donor samples as a reference. FGL2 levels were significantly increased on POD1, with surgery increasing levels of FGL2 in the blood of 8/10 patients (**Figure 39A, Appendix 8**). PBMCs from 6 colorectal cancer patients at baseline and POD1 previously showed expansion of MDSCs following surgical stress by flow cytometry and this corresponded to expansion of monocytic populations (CD14+ and CD16+), determined from a scRNA-seq dataset (Market, 2020). Querying this data, we found that *FGL2* was expressed in CD14+ and CD16+ monocytes and DCs [subsets 1/3/5 based on novel scRNA-seq classifications (Villani et al., 2017)] **(Figure 39B)**. Expression of *FGL2* was not significantly higher after surgery, although it trended upwards in CD14+ monocytes and DCs, with increased average relative expression in 5/6 patients **(Figure 39C, D)**. However, the abundance of *FGL2*-expressing CD14+/CD16+ monocytes and DCs was significantly increased post-surgery (**Figure 39C, D**), thus suggesting a source for the increase in FGL2 observed in the blood. ADAM17 is a metalloproteinase which has been shown to cleave the membrane-bound form of FGL2 into the secreted form (Zhou et al., 2019). In accordance, querying PBMC scRNA-seq data revealed increased expression of *ADAM17* in 5/6 patients in the same three FGL2-expressing cell clusters (CD14+/CD16+ monocytes and DCs) and increased frequency of the *ADAM17* expressing CD14+ and CD16+ monocytes and DCs (**Figure 40A, B**). Therefore, elevated FGL2 plasma levels following surgical stress is likely the result of cleavage of FGL2 by ADAM17 from an expanded myeloid population (MDSCs).

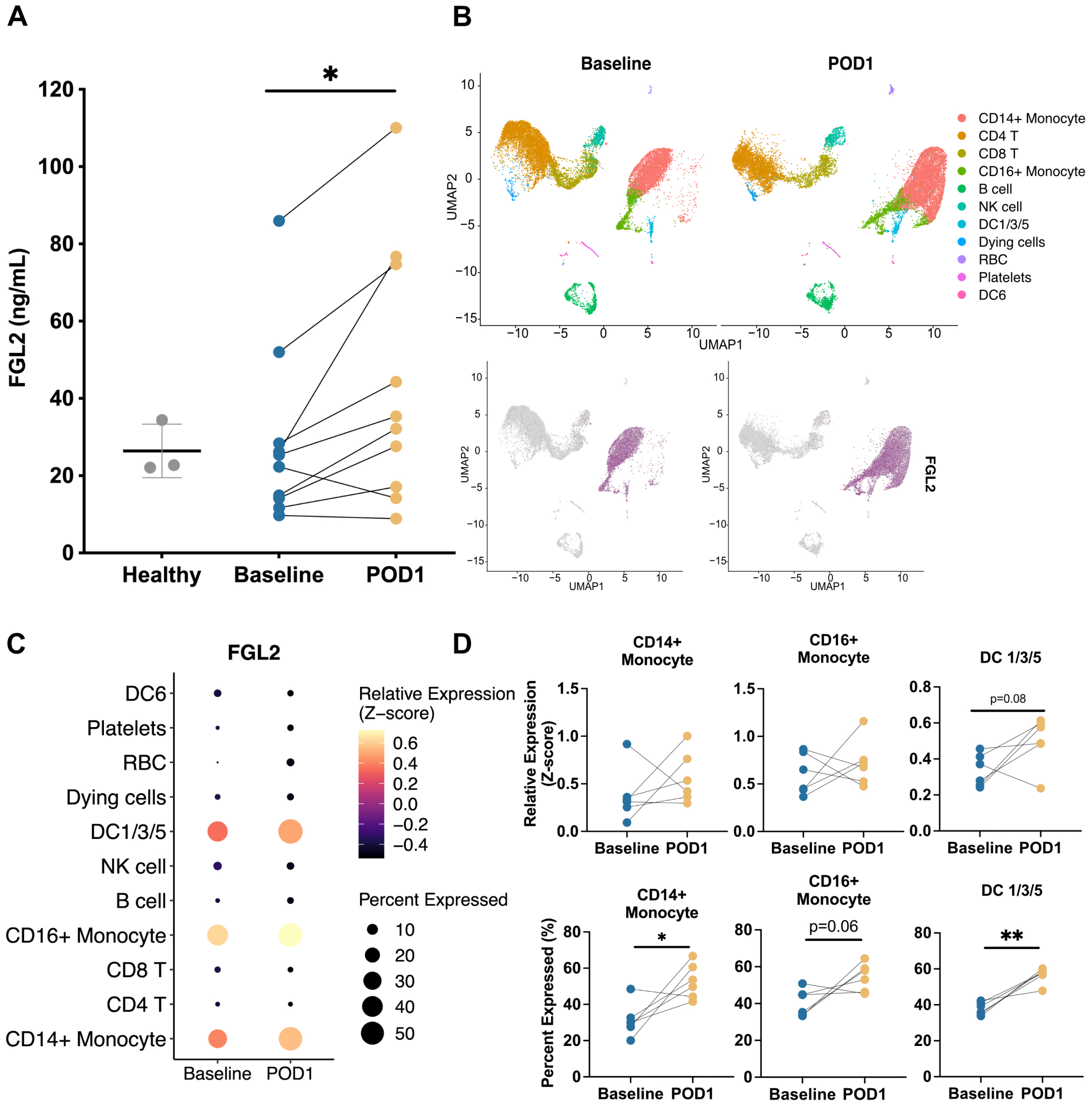

Figure 39. Surgical stress increases FGL2 abundance in plasma. **(A)** FGL2 levels in human plasma was determined by ELISA. Significance was determined by paired t test comparing paired patient samples (baseline vs. POD1). n=10, *p≤ 0.05. **(B)** UMAP embedding of scRNA-seq data from baseline and POD1 PBMC samples (n=6). Each point corresponds to an individual cell (baseline: 15108 cells, POD1: 15665 cells). Datasets depict cell clusters (top) with accompanying heatmap displaying the level of expression of *FGL2* in each cell type cluster (bottom). **(C)** Dot-plot depicting average relative expression level of FGL2 in each cluster from PBMC scRNA-seq data and average frequency of *FGL2*-expressing cells in major cell clusters of PBMC data in paired Baseline vs. POD1 PBMC patient samples (n=6). Colour of dots indicates relative expression and size of dots indicates frequency. **(D)** Relative average expression (top) and percent FGL2 expressing cells (bottom) for each patient (n=6) at baseline and POD1, in *FGL2*-expressing cell clusters (CD14+/CD16+ monocytes and DCs 1/3/5) from PBMC scRNA-seq data. Significance was determined by paired t test comparing paired patient samples (baseline vs. POD1). *$p \leq 0.05$, **$p < 0.01$.

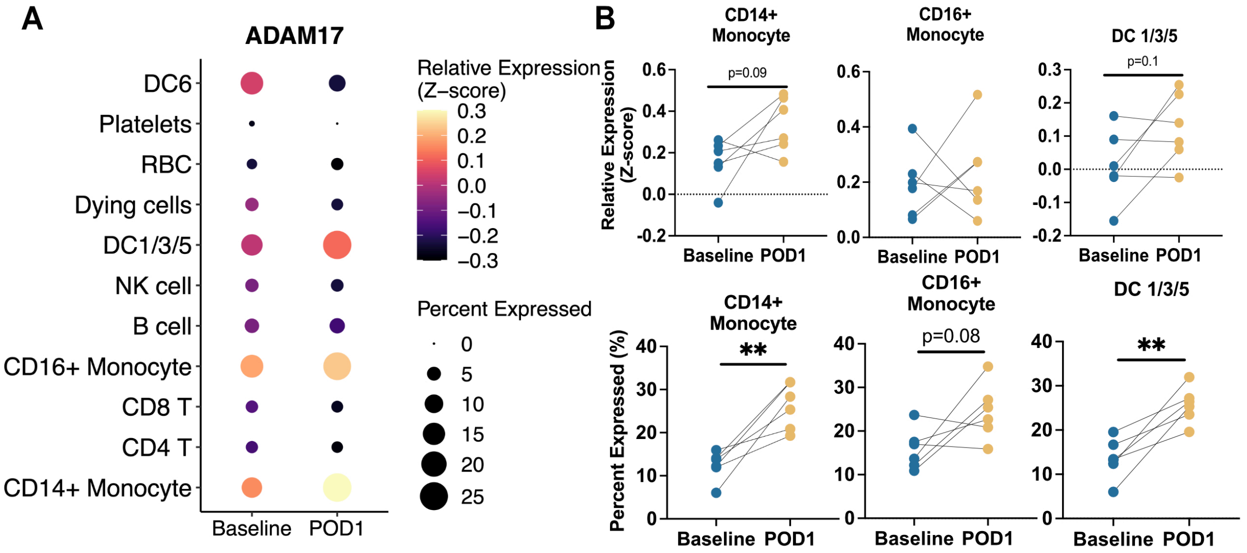

Figure 40. ADAM17 is primarily expressed in surgical stress-induced monocytes (CD14+ and CD16+). (A) Dot-plot depicting average relative expression level of ADAM17 in each cluster from PBMC scRNA-seq data and average frequency of ADAM17 expressing cells in major cell clusters of PBMC data in paired baseline vs. POD1 PBMC patient samples (n=6). **(B)** Relative average expression (top) and percent ADAM17 expressing cells (bottom) for each patient (n=6) at baseline and POD1 in FGL2 expressing cell clusters (CD14+/CD16+ monocytes and DCs 1/3/5) from PBMC scRNA-seq data. Significance was determined by paired t test comparing paired patient samples (baseline vs. POD1). *p≤ 0.05, **p< 0.01.

3.3.2. FGL2 is associated with increased lung metastases following surgical stress

Given that FGL2 plays a role in immunosuppression in a number of other conditions (Ai et al., 2018; Joller et al., 2014; Latha et al., 2019; Liu et al., 2013; Shalev et al., 2008), we sought to investigate the role of FGL2 in contributing to the post-operative immunosuppression which leads to increased cancer metastases (Tai et al., 2013, 2018). We used a well-established experimental model of surgical stress (Seth et al., 2013; Tai et al., 2013, 2018), and applied it to both *Fgl2*^{WT} and *Fgl2*$^{-/-}$ mice. These mice received an i.v. injection of $3x10^5$ B16F10 or B16F10lacZ cells, with some mice undergoing the surgical stress protocol (abdominal laparotomy and left nephrectomy). On POD1, one cohort of mice were sacrificed, and plasma was collected to measure FGL2 by ELISA. Mirroring what we observed in human samples on POD1, *Fgl2*^{WT} mice had higher levels of sFGL2 in the plasma after surgery relative to no surgery (**Figure 41A**). As expected, FGL2 was not present in the plasma of *Fgl2*$^{-/-}$ mice, with or without surgery. Blood was collected from a second cohort of mice 3 days post-surgery (POD3), at which time it was determined that sFGL2 levels in *Fgl2*^{WT} mice which received surgery had returned to no surgery levels (**Figure 41B**).

Previous studies have shown that surgical stress increases lung metastases in mouse models of cancer (Seth et al., 2013; Tai et al., 2013, 2018). To examine the role of FGL2 in this process, *Fgl2*^{WT} and *Fgl2*$^{-/-}$mice received an i.v. injection of $3x10^5$ B16F10lacZ cells on the day of surgery, and lungs were collected 3 days post-surgery and stained with X-gal to quantify lung metastases. To evaluate the longer-term effect of the enhanced FGL2 levels after surgery, lungs were also collected from mice 12-14 days post-surgery. Surgical stress increased the incidence of metastases at both 3 and 12 days post-surgery, but remarkably, *Fgl2*$^{-/-}$ mice did not have this increase in metastases (**Figure 41C, D**). qPCR was performed on RNA extracted from whole lungs collected at 12 days post-surgery (POD12) in order to quantify lung metastatic burden in a more quantitative fashion. Similar to our macroscopic counts of lung metastases, quantifying the melanoma associated genes, TRP2 and GP100 (Sorensen et al., 2014), by qPCR, showed surgical stress increased metastatic burden in *Fgl2*^{WT} mice but not *Fgl2*$^{-/-}$ mice (**Figure 41E, F**). In summary, *Fgl2*$^{-/-}$ mice had significantly fewer metastases following surgery compared to *Fgl2*^{WT} mice and lower expression of melanoma associated genes (TRP2, GP100). Due to the fast progression to endpoint of mice with lung metastases, we were not able to observe differences in survival in mice with or without surgery, however irrespective of surgery, the *Fgl2*$^{-/-}$ mice survived longer (**Figure 42A, B**).

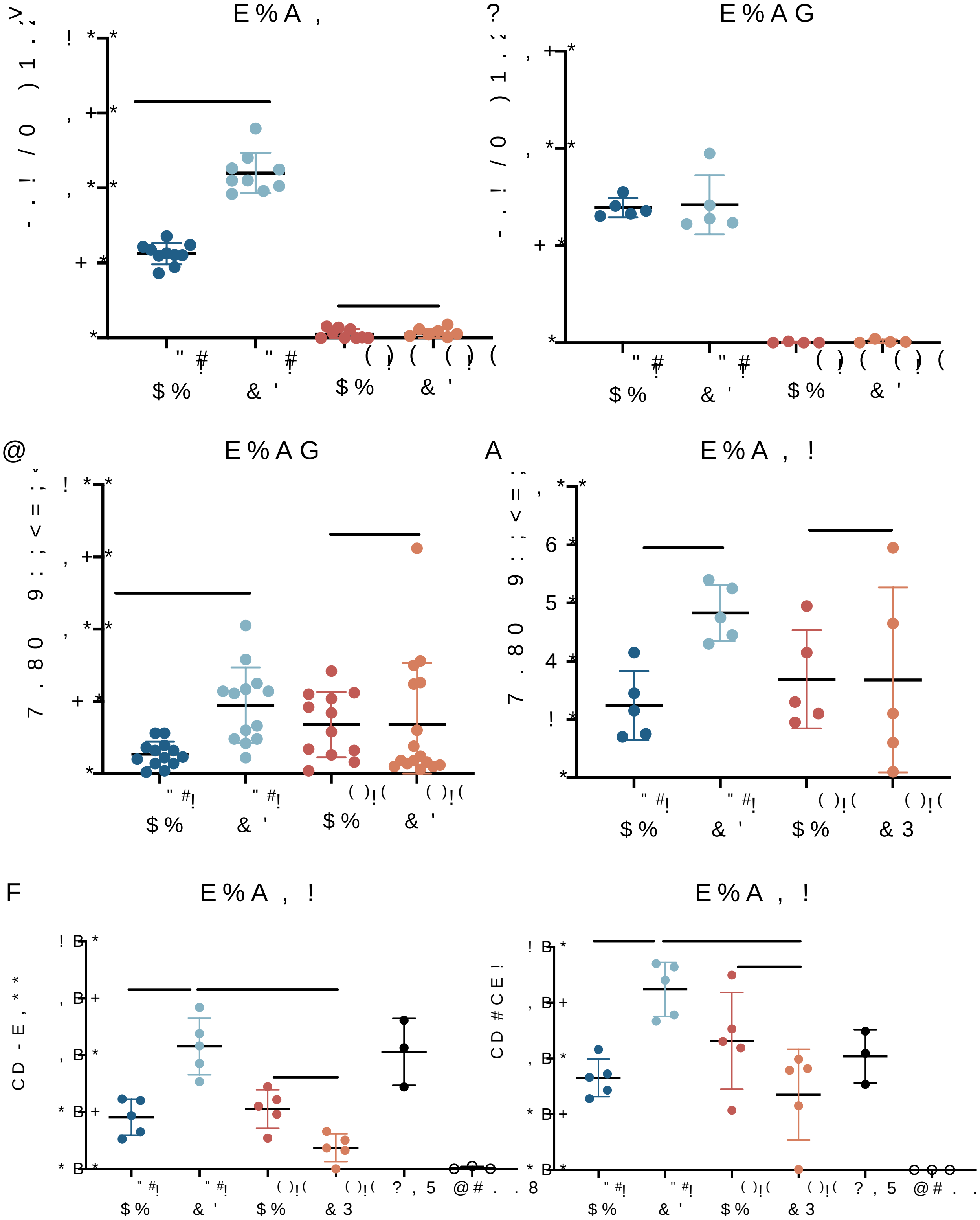
E%A ,
E%AG
?
@
E%AG
A
E%A , !
F
E%A , !
E%A , !
6
5
4
$%
&'
&3
CD - E , * *
CD #CE !
? , 5
@# . . 8

Figure 41: FGL2 is associated with induction of metastases following surgical stress. *Fgl2*^{WT} and *Fgl2*$^{-/-}$ mice received an i.v. injection of 3x10^{5} B16F10 cells followed by surgical stress (abdominal laparotomy and hemi-nephrectomy). **(A)** Levels of FGL2 were assessed in the plasma collected 1 day after surgery and showed increased abundance in *Fgl2*^{WT} mice following surgery relative to untreated mice, but with no detectable FGL2 in *Fgl2*$^{-/-}$ mice. **(B)** Plasma was collected 3 days post-surgery and FGL2 levels assessed by ELISA, showing FGL2 levels had returned to baseline in *Fgl2*^{WT} mice**. (C)** In *Fgl2*^{WT} and *Fgl2*$^{-/-}$ mice which received 3x10^{5} B16F10lacZ cells i.v., with/without surgery, lungs were collected 3 days post-surgery and stained by X-gal before being imaged using a stereomicroscope. Number of metastases is the total from all lobes. Surgery increases lung metastases in *Fgl2*^{WT} but not in *Fgl2*$^{-/-}$ mice. **(D)** Metastases on the surface of the lung were counted on day 12 following cancer cell inoculation and show surgical stress increases metastases in *Fgl2*^{WT} mice but not in *Fgl2*$^{-/-}$ mice. Number of metastases is the total from all lobes. RNA was extracted from whole lungs and expression of melanoma-associated genes **(E)** GP100 and **(F)** TRP2 determined by qPCR confirmed surgical stress does not increase lung metastatic burden in *Fgl2*$^{-/-}$ mice. Relative quantity (RQ) was calculated as fold change over positive control B16F10 cells and normalized to *Ppia* and *36B4*. Control (CTL) lungs were from tumour-naïve mice. Significance was determined by one-way ANOVA, Tukey's post-test, $**p \leq 0.01$, $***p \leq 0.001$, $****p \leq 0.0001$).

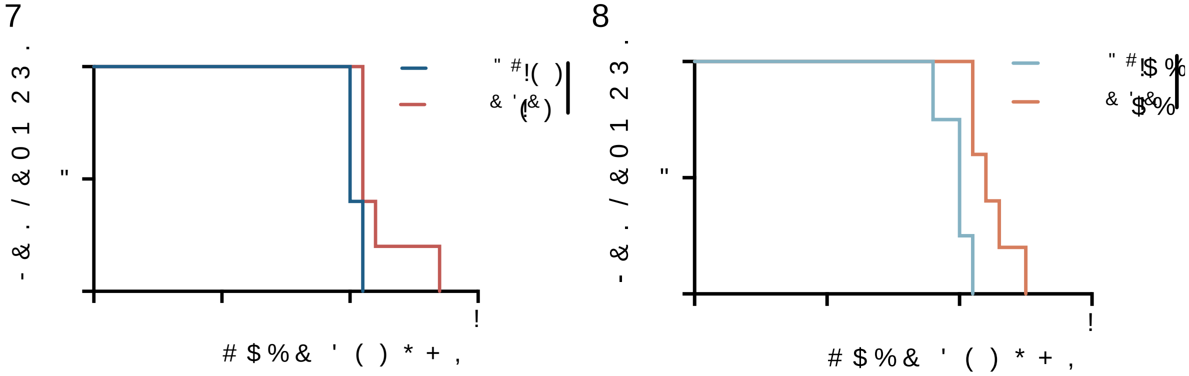

Figure 42. Absence of FGL2 prolongs survival. *Fgl2*^{WT} and *Fgl2*$^{-/-}$ mice received 3x10^5 B16F10 cells i.v. with/without surgery and were assessed for survival until humane endpoint. *Fgl2*$^{-/-}$ mice survived longer, albeit modestly, with no surgery **(A)** or with surgery **(B)**. Significance was determined by Log-rank test, *p≤ 0.05.

3.3.3. FGL2 blockage prevented increase in lung metastases following surgical stress

Given that *Fgl2*$^{-/-}$ mice did not present increased metastatic burden following surgical stress, we treated wild-type mice with an FGL2 blocking antibody to determine if this could prevent metastases. *Fgl2*$^{\mathrm{WT}}$ mice received an i.v. injection of $3\mathrm{x}10^5$ B16F10, followed by induction of surgical stress cells as before. Mice were treated with a control IgG antibody or α-FGL2 antibody 3 days prior and 3 days post-surgery, as well as on the day of surgery. *Fgl2*$^{\mathrm{WT}}$ mice receiving an IgG control antibody showed an increase in incidence of lung metastases following surgical stress; however, blocking FGL2 prevented this increase, keeping the number of metastatic lesions at no-surgery levels (**Figure 43**). These results indicate that surgery increases the abundance of plasma FGL2 in the B16F10 mouse model of surgical stress and that corresponds to a higher incidence of metastases. However, knocking out or blocking FGL2 is sufficient to prevent that post-surgery increase in metastases, suggesting α-FGL2 immunotherapy may have potential as an effective treatment in the post-operative immunosuppressive window in order to reduce metastases and improve outcomes.

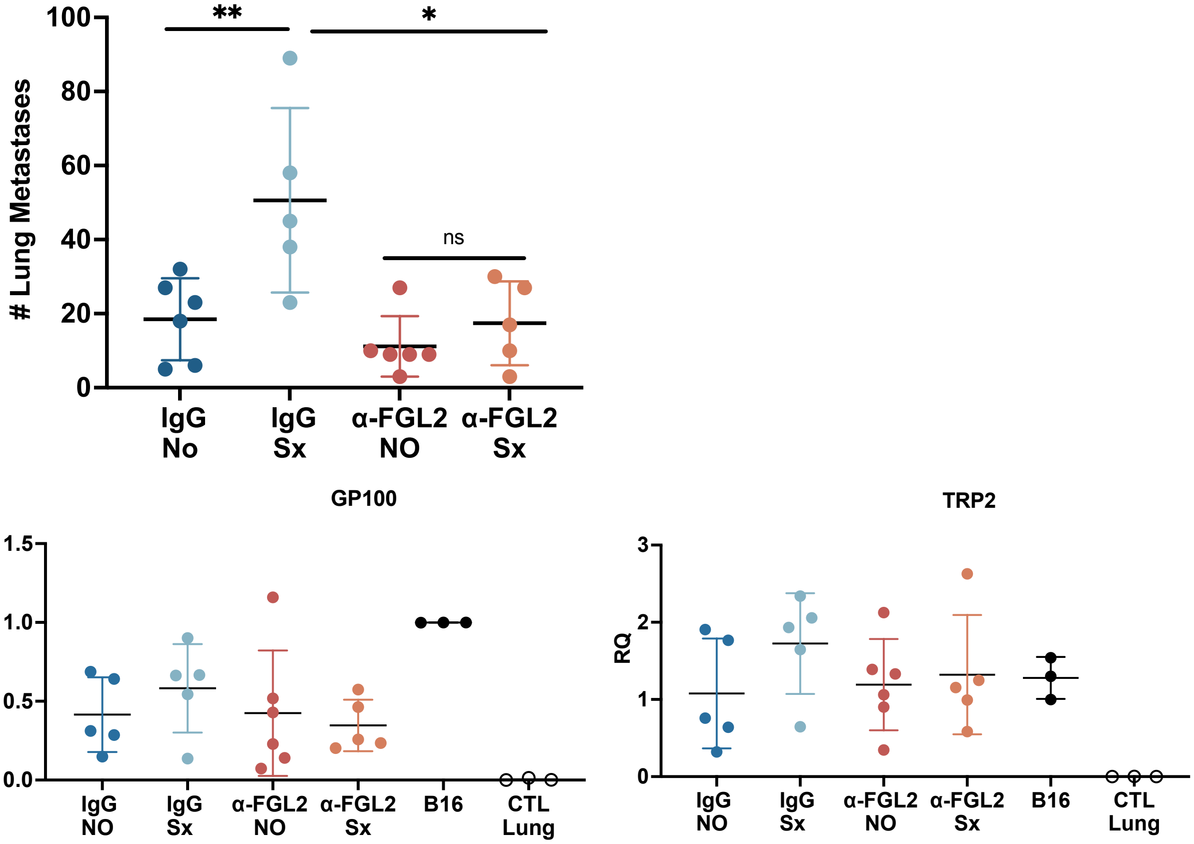

Figure 43. Blocking FGL2 prevents induction of metastases following surgical stress. *Fgl2*$^{\mathrm{WT}}$ mice were treated for 3 days pre- and post-cancer cell injection (3x10^5 B16F10 cells i.v.) and surgery as well as on the day of, with 100µg of IgG or α-FGL2 in 100 µL PBS. **(A)** Blocking FGL2 resulted in blocking of the surgical stress induced metastases. Significance was determined by one-way ANOVA, Tukey's post-test (n=5-6 mice/group). *p≤ 0.05, **p≤ 0.01. Data is representative of 3 independent experiments. Expression of the melanoma-associated genes **(B)** GP100 and **(C)** TRP2 was determined by qPCR, confirming surgical stress does not increase lung metastases in *Fgl2*$^{-/-}$ mice. Relative quantity (RQ) was calculated as fold change over positive control B16F10 cells and normalized to *Ppia* and *36B4*.

3.3.4. Absence of FGL2 does not alter frequency of MDSCs in response to surgical stress

It is well-established that the population of MDSCs are expanded following surgery, an increase that is similarly modeled in the mouse model of surgical stress (Tai et al., 2013, 2018). We next sought to investigate whether FGL2 plays a role in MDSC immunosuppression during the post-operative period. *Fgl2*$^{\mathrm{WT}}$ and *Fgl2*$^{-/-}$ mice received an i.v. injection of B16F10 cells with some mice undergoing the surgical stress protocol. On POD1, one cohort of mice was sacrificed, and spleens were assessed by flow cytometry to characterize immune cell populations via the gating strategy shown in **Figure 44**. We found that PMN-MDSCs ($\mathrm{CD3^{-}CD11b^{+}}$, $\mathrm{Gr^{High}SSC^{Int}/Ly6G^{+}Ly6C^{Low}}$) increased in frequency post-surgery, however this was true for both *Fgl2*$^{\mathrm{WT}}$ and *Fgl2*$^{-/-}$ mice (**Figure 45A**). We did not observe induction of M-MDSCs ($\mathrm{CD3^{-}}$ $\mathrm{CD11b^{+}}$, $\mathrm{Gr^{Low}SSC^{Low}/Ly6G^{-}Ly6C^{+}}$) on POD1, however *Fgl2*$^{-/-}$ mice have higher frequencies of M-MDSCs regardless of surgery status (**Figure 45B**). Similar to human PBMC data, an increase in the frequency of PMN-MDSCs may be responsible for the elevation in FGL2 levels in plasma rather than level of expression in any one cell type. Since knocking out FGL2 did not prevent this increase of MDSCs, we next asked whether these MDSCs may be functionally different. ARG1 is commonly expressed in M-MDSCs and has been identified as a mechanism for post-operative immunosuppression of NK cells by surgery-induced MDSCs (Angka et al., 2022; Tai et al., 2018) by depleting arginine (Gabrilovich and Nagaraj, 2009; Oberlies et al., 2009). However, no induction of ARG1 was observed in PMN-MDSCs (**Figure 45C**) and both frequency of ARG1+ M-MDSCs and expression (gMFI) of ARG1 were similarly increased in M-MDSCS of both *Fgl2*$^{\mathrm{WT}}$ mice and *Fgl2*$^{-/-}$ mice after surgery (**Figure 45D**), suggesting that FGL2 contributes to surgery-induced immunosuppression via another mechanism.

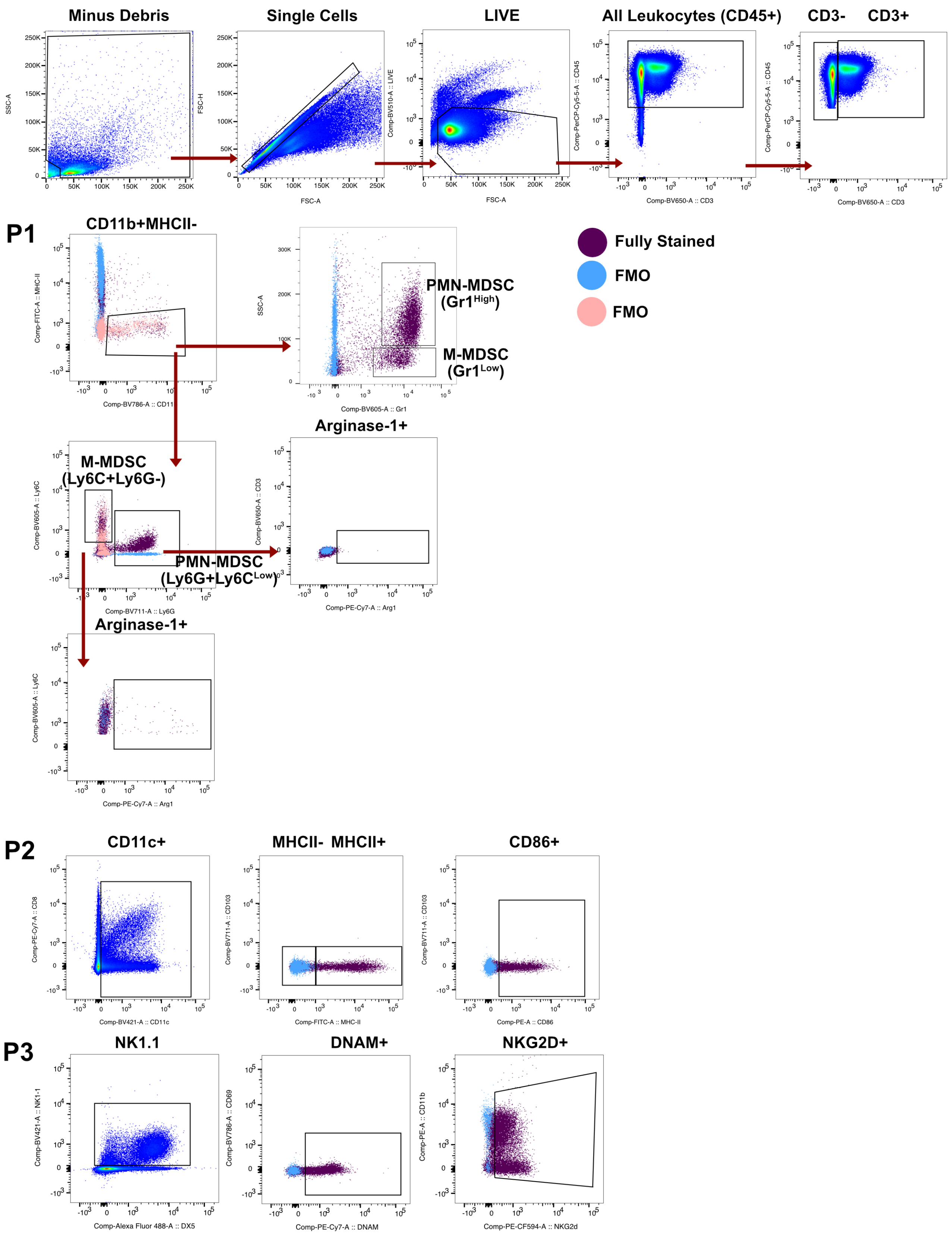

Minus Debris
Single Cells
LIVE
All Leukocytes (CD45+)
CD3-
CD3+
SSC-A
FSC-H
FSC-A
Comp-BV510-A :: LIVE
Comp-PerCP-Cy5-5-A :: CD45
Comp-BV650-A :: CD3
P1
CD11b+MHCII-
Comp-FITC-A :: MHC-II
Comp-BV786-A :: CD11
PMN-MDSC
(Gr1High)
M-MDSC
(Gr1Low)
Comp-BV605-A :: Gr1
Fully Stained
FMO
FMO
M-MDSC
(Ly6C+Ly6G-)
PMN-MDSC
(Ly6G+Ly6CLow)
Comp-BV605-A :: Ly6C
Comp-BV711-A :: Ly6G
Arginase-1+
Comp-BV650-A :: CD3
Comp-PE-Cy7-A :: Arg1
Arginase-1+
Comp-BV605-A :: Ly6C
Comp-PE-Cy7-A :: Arg1
P2
CD11c+
Comp-PE-Cy7-A :: CD8
Comp-BV421-A :: CD11c
MHCII- MHCII+
Comp-BV711-A :: CD103
Comp-FITC-A :: MHC-II
CD86+
Comp-BV711-A :: CD103
Comp-PE-A :: CD86
P3
NK1.1
Comp-BV421-A :: NK1-1
Comp-Alexa Fluor 488-A :: DX5
DNAM+
Comp-BV786-A :: CD69
Comp-PE-Cy7-A :: DNAM
NKG2D+
Comp-PE-A :: CD11b
Comp-PE-CF594-A :: NKG2d

Figure 44. Gating strategy for analysis of flow cytometry data. Gating strategy used to analyze the flow cytometry data from murine tumours and spleens was as follows: cell debris exclusion (minus debris), singlets, live/dead exclusion (LIVE), CD45+ (all leukocytes). **Panel 1 (P1):** CD3-, CD11b+/MHC-II-, PMN-MDSCs (Ly6G+Ly6Clow or Gr1highSScInt) and M-MDSCs (Ly6C+Ly6G- or Gr1Low SScA Low), **Panel 2 (P2):** NK Cells (CD3- NK1.1+), T cells (CD3+ NK1.1-). NKG2D and DNAM-1 were further used to phenotype immune cell populations. **Panel 3 (P3).** DCs (CD3- CD11c+). MHC-II and CD86 were further used to phenotype immune cell populations. Contour plots show fluorescence minus one (FMOs) for each analyzed marker.

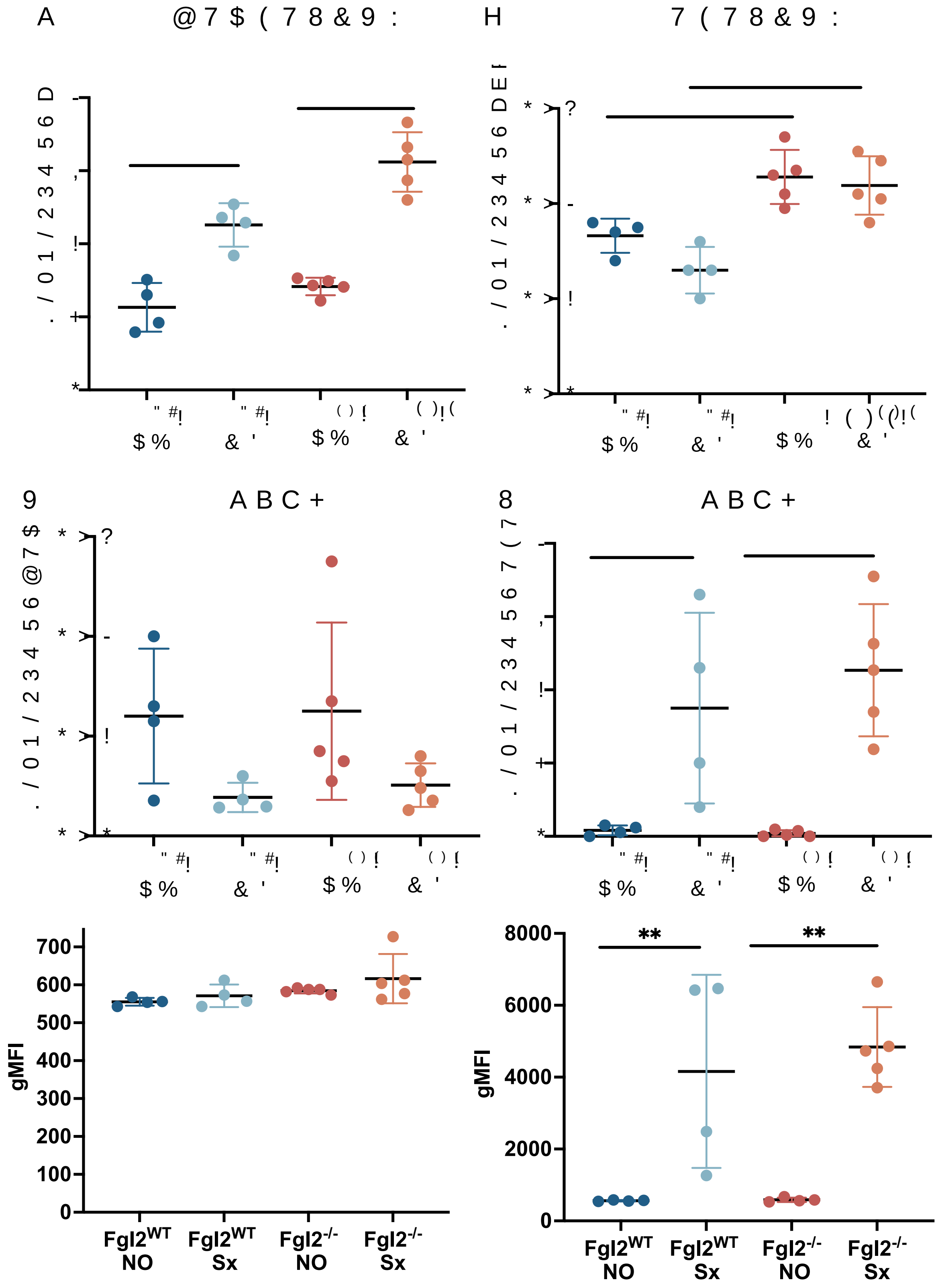
700
600
500
400
300
200
100
0
gMFI
Fgl2WT NO
Fgl2WT Sx
Fgl2-/- NO
Fgl2-/- Sx
8000
6000
4000
2000
0
gMFI
**
**
Fgl2WT NO
Fgl2WT Sx
Fgl2-/- NO
Fgl2-/- Sx

Figure 45. Surgery increases immunosuppressive MDSCs in both *Fgl2*$^{\mathrm{WT}}$ and *Fgl2*$^{-/-}$ mice. *Fgl2*$^{\mathrm{WT}}$ and *Fgl2*$^{-/-}$ mice received 3x10^{5} B16F10 cells i.v, with/without surgery, and flow cytometry was performed on splenic lymphocytes. **(A)** Splenic PMN-MDSCs (SSC$^{\mathrm{hi}}$, CD3^{-} CD11b^{+}Ly6G^{+}Ly6C$^{\mathrm{Low}}$) were expanded post-surgery. **(B)** M-MDSCs (SSC$^{\mathrm{Low}}$, CD3^{-} CD11b^{+}Ly6G^{-}Ly6C^{+}) were observed at a higher frequency in *Fgl2*-/- mice. Frequency (Top) and gMFI (bottom) of ARG1 was unchanged in **(C)** PMN-MDSCs and increased in **(D)** M-MDSCs. Significance was determined by one-way ANOVA, Tukey's post-test (n=4-5 mice/group). *p≤ 0.05, **p≤ 0.01, ***p ≤ 0.001, ****p ≤ 0.0001. Data is representative of 3 independent experiments.

3.3.5. Absence of FGL2 is associated with higher frequency of anti-cancer immune cells

Querying the human PBMC scRNA-seq data to identify possible cellular targets of FGL2, we observed expression of the FGL2 receptors FcγRIIB in CD16+ monocytes and FcγRIII in CD16+ monocytes, NK cells, and DCs (subsets 1/3/5) (**Figure 46A**). We confirmed FcγRIIB/RIII expression in sorted murine NK cells and MDSCs by flow cytometry in *Fgl2*$^{\mathrm{WT}}$ mice (**Figure 46B**). We therefore investigated the role of FGL2 in promoting immunosuppression in MDSCs, DCs, and NK cells. Given that NK cells are a known target of surgery-induced MDSC-mediated immunosuppression (Lu et al., 2020; Mundy-Bosse et al., 2011; Tai et al., 2018; Urakawa et al., 2019; Wang et al., 2017), we first assessed expression of NK activation molecules (DNAM-1 and NKG2D) which we previously showed to be more highly expressed in *Fgl2*$^{-/-}$ mice. Furthermore, markers such as NKG2D have previously been shown to be downregulated in response to surgical stress (Tai et al., 2013). While we did not observe downregulation of DNAM-1 or NKG2D in response to surgical stress, we did observe higher frequency of DNAM-1+ (**Figure 47A**) and NKG2D+ expressing (**Figure 47B**) NK cells in *Fgl2*$^{-/-}$ mice. These results suggest that NK cells from *Fgl2*$^{-/-}$ mice may be more primed to target and eliminate cancer cells (Chan et al., 2010; Martinet et al., 2015) more efficiently than the *Fgl2*$^{\mathrm{WT}}$ mice, even after surgery, as evidenced by their prolonged survival (**Figure 42**).

Given the expression of FGL2 receptors on both NK cells and MDSCS, we next assessed whether FGL2 could act directly on these cell populations. rFGL2 had no effect on NK cytotoxicity/degranulation (**Figure 47C, 47D**). CD155 is a ligand for DNAM-1 on MDSCs (Carlsten et al., 2009) and by incubating MDSCs sorted from bone marrow of tumour/surgery-naïve mice, we found that treatment with rFGL2 increased the percentage of cells expressing CD155 and expression levels of CD155 on CD11b+Gr1+ cells (**Figure 47E**).

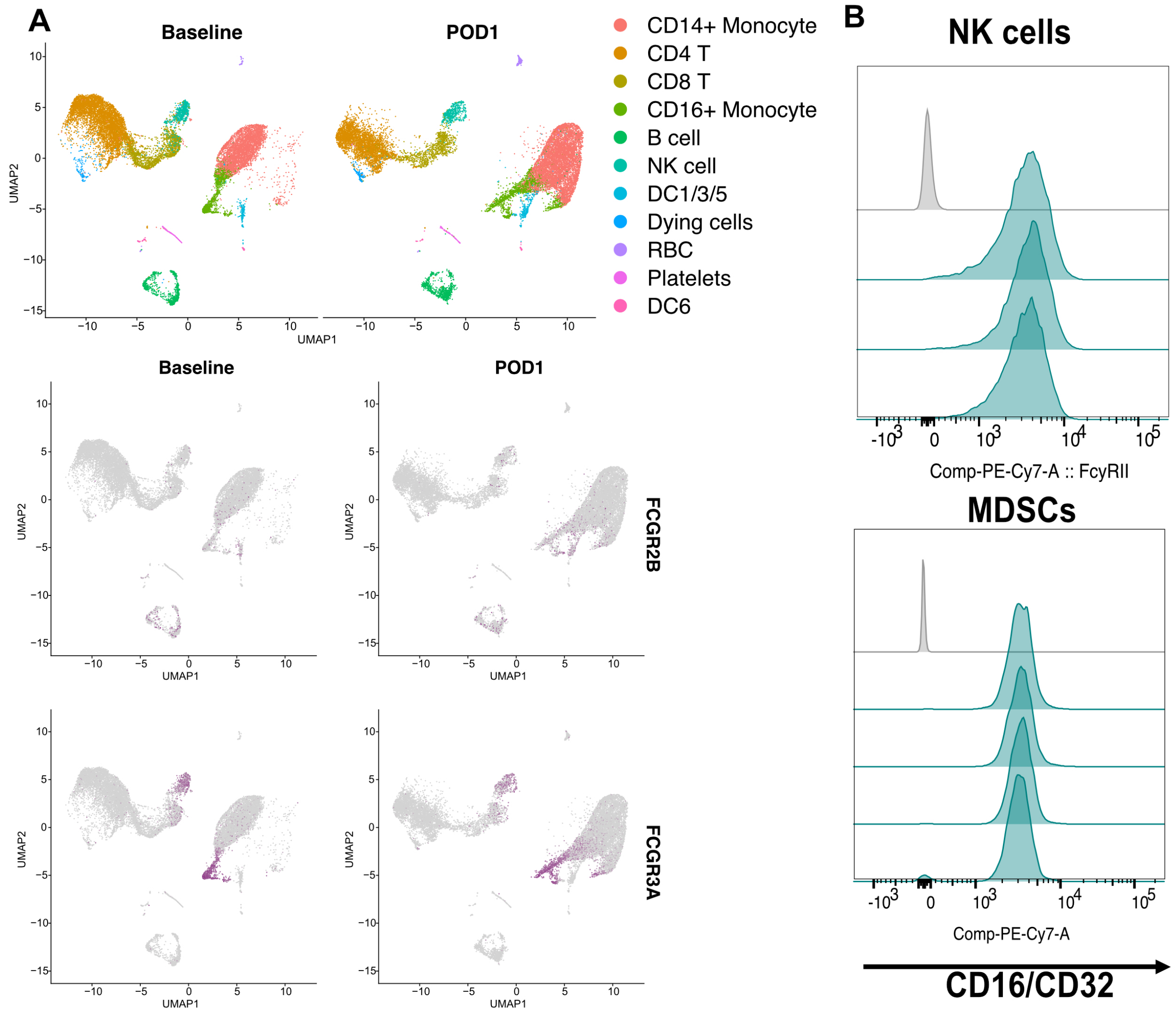

Figure 46. MDSCs, DCs, and NK cells express receptors for FGL2. (A) UMAP figures created from scRNA-seq data using Seurat from paired baseline and POD1 PBMC samples (n=6). Each point corresponds to an individual cell (baseline: 15108 cells, POD1: 15665 cells). Datasets depict cell clusters (top) with accompanying heatmap displaying the level of expression of receptors FcγRIIB (middle) and FcγRIII (bottom) in each cell type cluster. **(B)** NK cells and MDSCs were sorted from murine splenocytes and bone marrow cells respectively and assessed for CD16/CD32 (FcγRIIB/RIII) expression by flow cytometry.

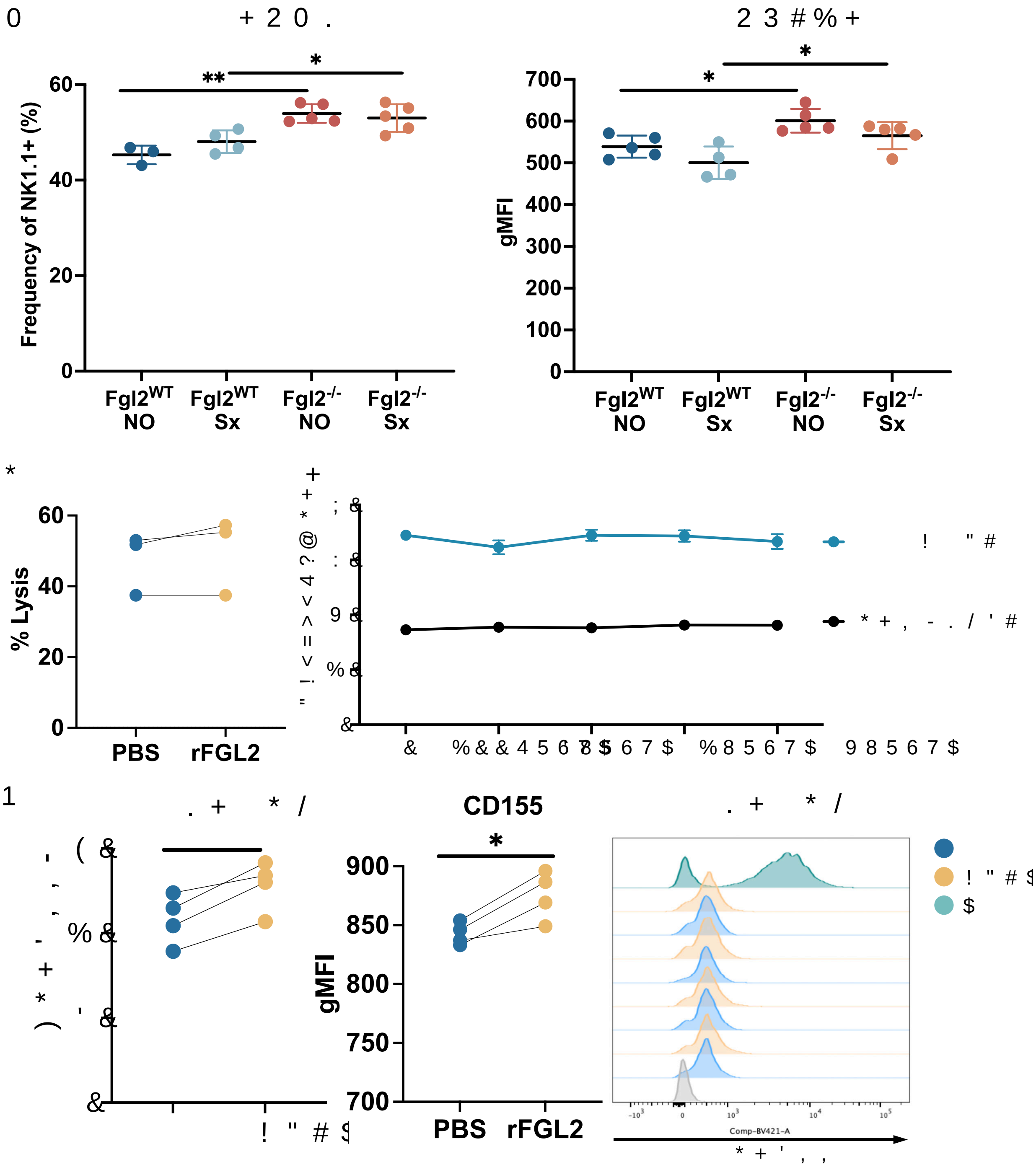

Frequency of NK1.1+ (%)
**
*
Fgl2WT NO
Fgl2WT Sx
Fgl2-/- NO
Fgl2-/- Sx
gMFI
*
*
% Lysis
PBS
rFGL2
CD155
*
gMFI
PBS
rFGL2
Comp-BV421-A

Figure 47. NK cells in *Fgl2*$^{-/-}$ mice are more activated. *Fgl2*^{WT} and *Fgl2*$^{-/-}$ mice received 3x10^{5} B16F10 cells i.v, with/without surgery, and flow cytometry was performed on splenic lymphocytes isolated on POD1. **(A)** *Fgl2*$^{-/-}$ mice have more DNAM-1+ NK cells, with (**B)** a higher expression (gMFI) of NKG2D. **(C)** NK cells from *Fgl2*^{WT} and *Fgl2*$^{-/-}$ mice were assessed for their ability to lyse target cells at 8:1 ratio of effector: target cells (YAC-1), incubated with rFGL2 (or PBS) for 4 hours. Gating strategy: Minus Debris/Singlets/NK Cells (CP450+)/lysed cells (PI+). Significance determined by paired Student's t test (n=3 mice, in duplicate). (**D**) NK cells from *Fgl2*^{WT} and *Fgl2*$^{-/-}$ mice were assessed for degranulation (CD107+ (Alter et al., 2004)) by plate-bound activation with α-NK1.1 or with PBS as an unactivated control, incubated with rFGL2 at the indicated doses for 5 hours (n=1 mouse, in triplicate). Gating strategy: Minus Debris/Singlets/Live Cells/CD45+/NK Cells (NK1.1+CD3-) and CD107+ NK cells. **(E)** Sorted CD11b+Gr1+ MDSCs (n=4 mice, in triplicate) were incubated with rFGL2 for 24 hours and CD155 expression was assessed by cytometry. LPS (1 µg/ml) was added to MDSCs as positive control. Average of triplicate samples is presented, showing increased abundance and expression of CD155 in CD11b+Gr1+ cells. Significance was determined by paired t test. *$p \leq 0.05$, **$p \leq 0.01$. Data is representative of two independent experiments.

Finally, although less commonly studied, DCs have also been shown to be suppressed following surgical stress (Brivio et al., 2000; De et al., 2003; Kawasaki et al., 2006), and are a well-established target of FGL2 (Liu et al., 2008; Shalev et al., 2008; Yang et al., 2019). Interestingly, we found a reduction in DCs following surgery in the *Fgl2*^{WT} mice but not the *Fgl2*$^{-/-}$ mice (**Figure 48A**), further suggesting that anti-cancer immune cells in *Fgl2*$^{-/-}$ mice may be more resistant to suppression. CD86, a target known to be downregulated by FGL2 in DCs (Liu et al., 2008), was significantly lower in *Fgl2*^{WT} mice and higher even after surgery in *Fgl2*$^{-/-}$ mice (**Figure 48A**). Thus, *Fgl2*$^{-/-}$ mice have a population of NK cells with greater expression of effector molecules and a more activated population of DCs after surgery, suggesting that although the frequency of MDSCs increased post-operatively, the anti-cancer immune cells of *Fgl2*$^{-/-}$ mice may be more resistant to immunosuppression and thereby prevent the increase in metastases.

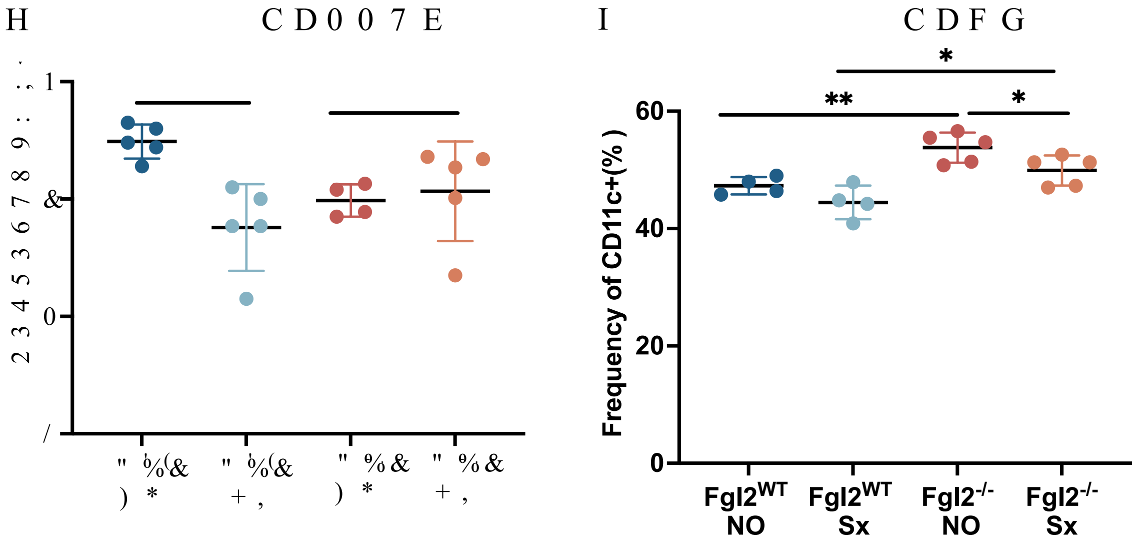

Figure 48. DCs in *Fgl2*$^{-/-}$ mice are more resistant to immunosuppression. *Fgl2*^{WT} and *Fgl2*$^{-/-}$ mice received 3x10^{5} B16F10 cells i.v, with/without surgery, and flow cytometry was performed on splenic lymphocytes isolated on POD1. **(A)** Fewer DCs were observed on POD1 in *Fgl2*^{WT} mice with no difference observed in *Fgl2*$^{-/-}$ mice. **(B)** *Fgl2*$^{-/-}$ mice have a higher frequency of CD86+ DCs. Significance was determined by one-way ANOVA, Tukey's post-test (n=4-5 mice/group). *p≤ 0.05, **p≤ 0.01. Data is representative of 3 independent experiments.

3.3.6. Summary

FGL2 is elevated in human plasma following surgical stress, and is similarly elevated in a mouse model of surgical stress. In this mouse model, we showed that elevated FGL2 is accompanied by an increase in metastases, while there is no increase in surgical stress-induced metastasis in *Fgl2*$^{-/-}$ mice. *Fgl2*$^{-/-}$ mice have increased expression of activated NK markers suggesting *Fgl2*$^{-/-}$ mice are less immunosuppressed and may be more resistant to surgical stress-induced MDSC-mediated NK cell dysfunction. Remarkably, blocking FGL2 with a novel immunotherapy prevented the increase in metastasis normally caused by surgical stress.

Chapter 4. General Discussion

Despite recent advancements with treatment of ovarian cancer, the 5-year survival rate remains low, and the risk of recurrence remains high, highlighting the need to develop novel, more effective treatments. This thesis set out to fully characterize the TME of syngeneic models of ovarian cancer, and to use those models to investigate the role of the immunomodulatory protein FGL2 in ovarian cancer and melanoma progression, as well as in surgical stress induced immunosuppression.

4.1. The tumour immune profile of murine ovarian cancer models: an essential tool for ovarian cancer immunotherapy research

The goal of Chapter 3.1 was to characterize syngeneic models of ovarian cancer, in order to better model the heterogeneity of human EOC, particularly HGSOC. In this study we extensively characterized the immunogenicity and TME at an advanced stage of EOC using models derived from different cells of origin (fallopian tube and ovarian epithelium), harboring mutations relevant to human disease, and from different mouse genetic backgrounds (C57BL/6 and FVB/N). Furthermore, we hoped to be able to attribute the TME characteristics to some of the mutational changes, which may help stratify patients or personalize medicine for human ovarian cancer patients when it comes to referring patients to clinical trials where they may benefit most from the treatment. It is anticipated that this extensive characterization of the tumour immune composition of six syngeneic models of EOC will expand testing of immunotherapies for EOC.

4.1.1. Immunogenicity and MHC-I expression in murine syngeneic models

In the initial characterization, cell lines and tumours from STOSE and MOE cells were found to be positive for MHC-I expression while all ID8-derived models expressed little to none.

This suggests that cancer cells from the STOSE and MOE models could be more capable of presenting TAAs in the TME. Indeed, STOSE and MOE-PTEN/p53-/- were able to induce anti-tumoural protection when used as a cellular vaccine. Therefore, ID8-derived tumours provide researchers with models to investigate treatments capable of overcoming MHC-I loss, associated with poor prognosis in EOC and limited response to immunotherapy in other cancer models (Galluzzi et al., 2018).

4.1.2. The effect of mouse strain on TME

Despite different cellular origin, STOSE and MOE tumours had high expression of MHC-II and PD-L1, which may be a particularity of the FVB/N genetic background, as similar findings on MHC and PD-L1 expression were observed in bladder cancer (Amponsa et al., 2019). Comparison of ID8-WT and STOSE, two unmodified cell lines of similar origin, allowed us to directly assess the impact of mouse strain. There are inherent differences in the immune response reported in these strains, where C57BL/6 mice have a Th1 bias and FVB/N, like BALB/c, have a Th2 bias (Kim et al., 2012; Watanabe et al., 2004). While both ID8-WT and STOSE derive from OSE, their tumours have distinct pathologies, with ID8-WT cells producing small primary tumours and large volumes of bloody ascites, whereas STOSE cells generate large primary tumours and viscous/mucous ascites. Screening of the T cell compartment revealed that ID8-WT and STOSE tumours were poorly infiltrated by T cells, mainly PD-1+. Poor T cell recruitment may be attributed to low CD31+ cells, highlighting the poor vascularization in the TME (Galluzzi et al., 2018). While ID8-WT primary tumours were poorly infiltrated, the metastases were abundant in CD3+ and FOXP3+ cells, and MHC-II+ areas. Chemo/cytokine ascites profiles were also different between the two models, potentially contributing to the recruitment of more CD11b+ cells in STOSE tumours. Analysis of these tumours by scRNA-seq indicated that STOSE tumours are preferentially infiltrated by immunosuppressive myeloid populations, which was confirmed by the abundance of CD206+ M2 TAMs detected by flow cytometry. These M2 TAMs, along with high PD-L1 expression, may trigger high expression of PD-1 and LAG3 on T cells. STOSE tumours appear rich in adipocytes, which could hinder T cell function indirectly by perturbing T cell metabolism or directly through MHC-II expression acting as antigen-presenting cells and causing chronic inflammation (Rodriguez et al., 2018; Song and Deng, 2020). STOSE tumours are a unique, immunogenic, EOC model with a distinct TME that may be informative when testing the response to novel immunotherapies, especially those investigating TAMs.

4.1.3. Effect of TP53 deletion in the ID8-derived tumour model

Recent studies using syngeneic and genetically modified mouse models with HR-deficient DNA repair and P53 mutations have highlighted the heavy immune infiltration suggesting a more immunogenic phenotype (Iyer et al., 2020; McCool et al., 2020; Walton et al., 2016), which is consistent with human disease (Malekzadeh et al., 2021; McCool et al., 2020). However, neither ID8-*p53*$^{-/-}$ nor the derivative cells with *Brca2* deletion were immunogenic as determined by MHC expression and their inability to induce anti-tumoural protection when administered as a cellular vaccine. We observed more T cell infiltration in ID8-p53-/- tumours compared to ID8-WT tumours, but not compared to ID8-C3 tumours. Notably, the tumour immune composition of ID8-WT and ID8-C3 models were often different, perhaps due to clonal selection and/or Cas9 expression, which can modulate innate/adaptive immune responses (Crudele and Chamberlain, 2018; Mehta and Merkel, 2020). The similar immune composition in ID8-*p53*$^{-/-}$ and ID8-C3 tumours, as reported by Walton et al., indicates similar tumour development after i.p. and i.b. injection of cells (Walton et al., 2016). ID8-*p53*$^{-/-}$ tumours were highly infiltrated by T cells, generally lacking expression of the activation markers CD25 and PD-1, but abundant in FOXP3, suggesting the presence of Tregs, which are associated with poor prognosis in human ovarian cancer (Preston et al., 2013). This model also recruited preferentially CD11b+CD11c+ cDC2s which can hamper the anti-tumoural responses by producing high amounts of IL-10 (Li et al., 2008; Wculek et al., 2020). Compared to ID8-C3, this model expressed more inhibitory ligand PD-L1 in macrophages and CD11c+CD11b+ tolerogenic DCs and more pro-tumour CXCL10 in the ascites (Pandey et al., 2021), suggesting a more immunosuppressive TME than the ID8-C3 tumours.

4.1.4. The TME of MOE-KRAS tumours

Given that many HGSOC tumours arise from the fallopian tube, we characterized the MOE-PTEN/KRAS tumours. Like STOSE, MOE-PTEN/KRAS tumours were highly infiltrated by myeloid cells, but these TAMs were primarily CD206 negative. Although both models derive from the FVB/N background, there were clear differences in the TME as a consequence of cell-intrinsic factors (cell type of origin or mutations). MOE-PTEN/KRAS tumours were highly infiltrated by CD4+ T cells, contained high frequencies of LAG3+ CD8+ T cells, and displayed significant expression of MHC-II. Double staining for MHC-II and cytokeratin 8/18 allowed the discrimination of cancer cells from MHC-II+ cells, suggesting other cellular sources of MHC-II expression in this model, such as adipocytes (Song and Deng, 2020) or cancer associated fibroblasts (Kerdidani et al., 2022). In colorectal cancer, *KRAS* mutation suppresses Th1/CTL immunity, reducing IFN-γ and CXCL10 production, therefore decreasing CTL infiltration (Lal et al., 2018). MOE-PTEN/KRAS tumours displayed a shift towards Th2 CD4+ T cells with a high ratio of CD4/CD8 and produced very low amounts of CXCL10 in the ascites fluid. Overall, these tumours were poorly infiltrated by T cells, although we noted specific T cell accumulation in clusters, potentially enabling T cell activating responses. None of the other models had these T cell clusters, suggesting an association with KRAS activation.

4.1.5. PD-L1 expression in the TME of murine ovarian cancer syngeneic models

PD-L1 expression has been detected in 11-60% of HGSOC cases (Varga et al., 2019). In this study all orthotopic tumours expressed PD-L1, but in <3% of the tumour. ID8-p53-/- and MOE-PTEN/KRAS models showed high presence and expression of PD-L1 among the immune cell populations while STOSE showed high PD-L1 expression in non-immune cells. Given low response rates to ICIs for the treatment of ovarian cancer (Hamanishi et al., 2015, 2016b), testing ICIs targeting the PD-1/PD-L1 blockade, alone or in combination with other strategies, in these models may help to stratify those women who may respond to treatment. Studies investigating genetic alterations and response to ICIs have shown that PTEN loss results in resistance to PD-1 blockade in melanoma and uterine leiomyosarcoma (George et al., 2017; Peng et al., 2016). In lung adenocarcinoma, *TP53* and *KRAS* mutations are key factors affecting PD-L1 expression and sensitivity to PD-1 blockade (Dong et al., 2017). Future experiments treating a broad range of existing murine EOC models (Eddie et al., 2015; Iyer et al., 2020; McCool et al., 2020; Walton et al., 2017) with ICI therapy could better elucidate the specific role that these mutations play in response to immunotherapy.

4.1.6. Limitations and future directions

We studied orthotopic tumours, but this approach was limited by the fact that some MOE models (MOE-PTEN/p53 and MOE-PTEN) did not grow well in the intrabursal cavity. For this reason, while we tried to assess the effect of various mutations/deletions on the TME composition, we were often limited by the lack of proper controls. Because the MOE-PTEN^{shRNA} cell line did not grow well after i.b. injection we could not compare the TME in this model to the effect of the *Trp53* mutation in the MOE-PTEN^{shRNA}p53^{R273H} cell line or the KRAS mutation in the MOE-PTEN^{shRNA}KRAS^{G12} cell line. Furthermore, given that the parental MOE cell line is not tumourigenic (Eddie et al., 2015), we could not compare the TME in presence of mutations to the TME of a non-mutated MOE tumour. Although we observed some differences in ID8-C3 and ID8-*p53*$^{-/-}$, we didn't have another pair of tumour models, with or without deletions in *Trp53*, to attribute these differences to *Trp53* deletion, given that the MOE cell line also had *Pten* knockout. Furthermore, while 96% of human HGSOC have alterations in *TP53* (Cancer Genome Atlas Research Network, 2011), only about 25% of these result in a *TP53* deletion (Cole et al., 2016), and the majority represent p53 amplifications or gain of function mutations, which further limits this model to a subset of ovarian cancer patients and restricts our comparison to the MOE cell line. This severely limited our ability to assign TME profiles to a mutation/deletion, but rather to the cell line/tumour model itself.

In this study we characterized the immune cell populations, cytokine expression, MHC expression, and immunogenicity of several syngeneic models, demonstrating that they possess unique TMEs. ID8-C3 and ID8-p53-/- models were more T cell infiltrated compared to the ID8-WT and STOSE, while STOSE and MOE-PTEN/KRAS tumours were heavily infiltrated by TAMs. Finally, the scope of our study did not cover NK, NKT, and B cells, which also play important roles in tumour immunity. Based on our findings, immunotherapeutic approaches can be proposed (Rodriguez et al., 2018) to determine their efficacy in association with the immune characteristics of each model (**Appendix 9**). For example, differences in MHC-I and -II, as well as PD-L1 may suggest which models will respond to ICIs. This comparative analysis provides a solid foundation to understand the shared and distinct features of a set of syngeneic models that have significant potential for future testing of novel immunotherapies for human patients with similar profiles in their TME.

4.2. FGL2 promotes tumour growth by attenuating infiltration of activated anti-tumour Dendritic, Natural Killer and T cells

FGL2 expression in cancer cells is associated with poor survival in a number of different cancers such as colorectal carcinoma (Qin et al., 2014), renal (Tang et al., 2017), glioblastoma multiforme (Latha et al., 2019; Yan et al., 2015, 2019), liver (Liu et al., 2012; Su et al., 2008), and prostate cancer (Rabizadeh et al., 2015), primarily through its prothrombinase function and as a mediator of immunosuppression. Tumour immune cell infiltration, including NK cells, DCs, and T cells, are indicative of better outcome and good prognosis in human cancers (Pagès et al., 2010), including epithelial ovarian (Santoiemma and Powell, 2015; Santoiemma et al., 2016; Zhang et al., 2003) and melanoma (Eggermont et al., 2014; Thomas et al., 2013). As such, some studies have recently suggested that FGL2 is associated with better prognosis in lung (Yuan et al., 2020a), breast (Feng et al., 2020), and gastrointestinal stromal tumour (Pulkka et al., 2022), given FGL2 is expressed in many immune cell types in the TME. By querying scRNA-seq data of many human cancer types, including ovarian, melanoma, lung, breast and colorectal, we have shown that FGL2 is not commonly expressed in cancer cells, but rather multiple cell types in the TME, with predominant expression in monocytes and macrophages. FGL2 levels are higher in ovarian cancer ascites than non-cancer ascites, suggesting FGL2 contributes to the immunosuppressive TME in ovarian cancer. Further, we and others (Yang et al., 2019) showed that FGL2 expression in immune/stromal cells in the TME is associated with poor survival, with larger tumour burden and faster tumour progression, as well as suppression of activation markers on T cells, DCs, and NK cells.

4.2.1. Choosing models used to investigate the role of FGL2 in tumour progression

Based on our laboratory's expertise in ovarian cancer, we first focused on the role of FGL2 in EOC, which has not previously been studied. Given our studies using the B16F10 cells in the surgical stress model and the fact that the role of FGL2 in tumour progression has not been studied in melanoma, we expanded our study to use the B16F10 model to investigate the role of FGL2 in melanoma tumour progression. Furthermore, this gave us the opportunity to compare and contrast the role of immunomodulatory FGL2 in two cancer types, one which generally does not respond to immunotherapy in the clinic (EOC) to one that does (melanoma).

While we did not fully characterize the ID8-*p53*$^{-/-}$*Brca2*$^{-/-}$ cell line in Chapter 3.1, immune infiltration was previously characterized by IHC by Walton et al. (Walton et al., 2016). Tumours derived from this cell line, while not more infiltrated by CD3, CD8, or F480+ cells, was suggested to be more immunogenic by the observation of tertiary lymphoid structures (Walton et al., 2016). HR (*BRCA1*, *BRCA2*) deficiencies in tumours, including ovarian cancer, increases presence of neoantigens or tumour mutational burden (TMB), increases immune infiltration, and better prognosis (Ciombor and Goldberg, 2018; Clarke et al., 2009; Le et al., 2017; Przybytkowski et al., 2020; Strickland et al., 2016). A higher TMB can predict response to immunotherapy such as ICIs, in lung (Rizvi et al., 2015) and melanoma (Snyder et al., 2014). Although *BRCA1* modifications are more common than *BRCA2* (Cancer Genome Atlas Research Network, 2011), because the ID8-

$p53^{-/-}Brca2^{-/-}$ tumours had been partially profiled and suggested to be more immunogenic with the presence of tertiary lymphoid structures, we chose to use the ID8-*$p53^{-/-}Brca2^{-/-}$* cell line as a syngeneic ovarian cancer model in *$Fgl2^{WT}$* and *$Fgl2^{-/-}$* mice instead of the ID8-WT cell line which makes very "cold" tumours. Although it was hypothesized that the ID8-*$p53^{-/-}Brca2^{-/-}$* cell line would be more immunogenic, we showed that it does not express MHC-I *in vitro* or *in vivo* and does not confer protection when used as an irradiated cell vaccine, and as such is a poorly immunogenic cell line. Future studies would be required to determine the TMB of the ID8-*$p53^{-/-}Brca2^{-/-}$* cell line and to determine the presence of immunogenic antigens, as was done for the ID8-WT cell line (Martin et al., 2016).

For treatment with an α-FGL2 antibody we chose to use the syngeneic STOSE model developed in our lab (McCloskey et al., 2014). The STOSE model expressed MHC-I *in vitro* or *in vivo*, was immunogenic (confers protection when used as an irradiated cell vaccine), and thus may be more likely to respond to immunotherapy than the poorly immunogenic ID8-*$p53^{-/-}Brca2^{-/-}$* or the B16F10 melanoma tumour models. Other studies looking at a variety of syngeneic cell lines and response to immunotherapy revealed that MHC-I expression predicts response (Lechner et al., 2013; Mosely et al., 2017). Furthermore, the high infiltration of macrophages in STOSE tumours are CD206+, suggesting M2 polarization. Given the association between FGL2 and M2 macrophage polarization, the STOSE tumour represents an infiltrated and immunosuppressive TME, which may benefit from α-FGL2 immunotherapy treatment. Blocking FGL2 was predicted to inhibit the function of these M2 macrophages, prolonging survival. However, treatment with α-FGL2 antibody did not prolong survival, but did increase the presence of activated T cells in the spleen of α-FGL2 treated mice. Prolonging treatment is likely not necessary to prolong survival, given that we observed blocking of FGL2 in the ascites fluid at endpoint, suggesting a durable response. However, we may consider treating at earlier timepoints. With PD-1 blockade or OV treatment in the ID8 model by other groups, mice were treated much earlier in tumour progression (7-10 days post-tumour inoculation; Gil et al., 2014; Guo et al., 2014; Nounamo et al., 2017). The presence of highly immunosuppressive ascites that accumulates later in disease prevents the effectiveness of treatment, thus treating with α-FGL2 closer to 10-25% of survival rather than the midpoint to predicted survival may show some prolongation in survival. Conversely, we did treat the B16F10 model at earlier timepoints, beginning around day 3 or 10% of survival, but survival was not prolonged in this model either.

Finally, we decided to compare the poorly immunogenic models of ovarian cancer to the commonly used model of B16F10 melanoma (Overwijk and Restifo, 2001). B16F10 has been widely used for pre-clinical testing of immunotherapy such as PD-1/PD-L1 ICIs or OVs (Chen et al., 2015; Lemay et al., 2012; Spranger et al., 2014) which have been translated to FDA approved treatments (Bommareddy et al., 2017; Hargadon et al., 2018). Although B16F10 is still considered poorly immunogenic with low MHC-I expression, the presence of strong antigens (GP100, TRP2) (Johnston et al., 1987) and the short survival make it a compelling model to investigate the role of immunomodulatory sFGL2.

4.2.2. FGL2 and suppression of NK activation markers

We demonstrated for the first time that *Fgl2*$^{-/-}$ mice have more DNAM-1+ NK cells and higher expression of NKG2D+ and NKG2A+ markers (**Figure 49**) and that these DNAM-1+ NK cells are found at higher frequencies in both ovarian (ID8-*p53*$^{-/-}$*Brca2*$^{-/-}$) and melanoma (B16F10) tumours. Ostapchuk et al. (2022) proposed that FGL2 directly contributes to suppression of NK cell cytotoxicity while Yu et al. (2021) suggested *Fgl2* expression in NK cells is associated with a subtype of NK cell with impaired cytotoxicity. In our study, tumour-naïve NK cells were not functionally different between *Fgl2*^{WT} and *Fgl2*$^{-/-}$ mice, using CD107+ degranulation as a readout of NK cell activation and cytotoxicity (Alter et al., 2004), or by direct NK mediated target cell (YAC-1) lysis. NK cells may be functionally different via other pathways such as granzyme production, proliferation, or antibody-dependent cell-mediated cytotoxicity (Vivier et al., 2008) and may be investigated in future studies. However, depleting NK cells *in vivo* did not suggest NK cells were a driving factor to prolong survival in *Fgl2*$^{-/-}$ mice. Therefore, NK cell marker expression may be a downstream consequence of more activated DCs and CD4+ T cells in *Fgl2*$^{-/-}$ mice, producing more IL-15 and IL-2 (de Rham et al., 2007). In one study, FGL2 suppressed MCP-1 secretion from macrophages which in turn lessened NK cell recruitment and IFN-γ production (Fu et al., 2020), suggesting other downstream mechanisms of FGL2 are capable of targeting NK cells and their decreased activation.

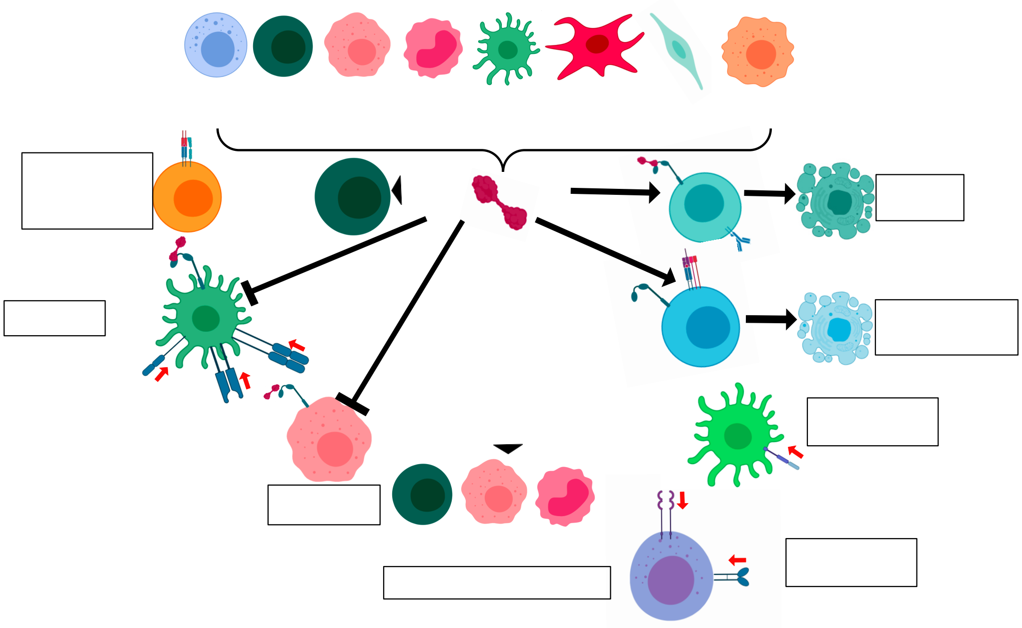

Figure 49. FGL2 is associated with decreased activation of NK cells. FGL2 is expressed in macrophages, T cells (notably Tregs/TIGIT+ Tregs), endothelial cells, cancer associated fibroblasts (CAFs), Natural Killer (NK) cells, Dendritic Cells (DCs), and myeloid-derived suppressor cells (MDSCs). sFGL2 acts directly (solid line) to suppress DC maturation (CD80, CD86, MHC-II downregulation) and macrophage activation. Further contributing to immunosuppression, sFGL2 can directly induce B cell and FCγRllB+CD44^{hi} CD8+ T cell apoptosis. sFGL2 is associated (dotted line) with enhanced Treg suppression of effector T cells, suppression of CD103+CD8α+ DC activation, and with populations of immunosuppressive immune cell populations (Tregs, M2 macrophages, and MDSCs). We show for the first time the association between sFGL2 and suppression of NK cell activation markers.

4.2.3. FGL2 and immunosuppression of DCs and T cells in the TME

Given FGL2's association with immunosuppressive cell populations (M2 macrophages, Tregs, MDSCs) (Joller et al., 2014; Pan et al., 2018; Yan et al., 2015; Zhu et al., 2017) and suppression of DC and T cell activation (Liu et al., 2008; Shalev et al., 2008, 2009; Yang et al., 2019), we further explored these immune cell populations in our two model systems. There were more T cells in the tumours of ID8-*p53*$^{-/-}$*Brca2*$^{-/-}$ mice and more activated T cells and DCs in the B16F10 tumours, similar to findings by Yang et al. (2019), who investigated the effect of FGL2 produced by cells in the TME of hepatocellular carcinoma models. Those authors demonstrated that the suppression of DCs is due to reduced phosphorylation Akt, NF-κB, CREB, and p38 in DCs but not T cells, such that sFGL2 acts directly on DCs which then further suppress CD4+ T cell activation, similar to what has previously been shown by others, although not in the context of the TME (Liu et al., 2008; Shalev et al., 2008, 2009; Yang et al., 2019). Yang et al. (2019) observed a decrease in CD31+ DCs in the absence of FGL2, similar to the decrease in CD31 we observed on DCs in the B16F10 tumours. CD31 acts as a co-inhibitory receptor, where CD31+ DCs are more tolerogenic, suggesting in the absence of FGL2 DCs in B16F10 tumours are more activated (MHC-II+, CD86+, CD40+) and less immunosuppressive (CD31+). Conversely, we also observed increased expression of this immune checkpoint in *Fgl2*$^{-/-}$ tumour-naïve and ID8-*p53*$^{-/-}$ *Brca2*$^{-/-}$ tumour-bearing mice, suggesting a negative feedback mechanism to keep the more activated/pro-inflammatory DCs in check in the absence of FGL2 (Clement et al., 2014). In one study, FcγR engagement led to the downregulation of CD31, which may prompt further studies as to whether sFGL2 is directly acting on DCs through the Fc receptors to downregulate CD31 (Merchand-Reyes et al., 2019).

Knocking out FGL2 or blocking the function of sFGL2 via monoclonal antibody treatment led to increased frequency of or expression of CD25 and TIGIT on CD4+ and CD8+ T cells. Although expression of these markers on CD4+ T cells suggests that the T cell population has become more activated (Wing et al., 2002; Yu et al., 2009), CD25+ or TIGIT+ T cells often represent a more immunosuppressive or regulatory T cell population (Anderson et al., 2016; Joller et al., 2014). In the B16F10 and STOSE models, where blocking FGL2 did not prolong survival, increased presence of TIGIT+ Tregs, which do express high amounts of FGL2 (Joller et al., 2014), may have impeded tumour elimination. Therefore, TIGIT checkpoint blockade in combination with FGL2 blocking antibody therapy may be more successful in prolonging survival (Anderson et al., 2016). Unlike other models which appear to have decreased frequencies of Tregs in the absence of FGL2 (Latha et al., 2019; Yan et al., 2015, 2019), we observed greater frequencies of CD25+, TIGIT+ T cells, suggesting an increased abundance of Tregs. Finally, in our models of melanoma and ovarian cancer, we did not observe differences in the abundance of MDSCs. While this is similar to the outcomes reported for the hepatocellular carcinoma model (Yang et al., 2019), it was different from the increased numbers of MDSC seen in the glioblastoma models where FGL2 is expressed in the cancer cells (Yan et al., 2015) or in Lewis lung carcinoma where FGL2 was produced by the TME (Zhu et al., 2017).

4.2.4. Synergy of FGL2 knockout and oncolytic virotherapy

While FGL2 appears to be involved in numerous common immune pathways in the TME, the response to the absence of FGL2 is clearly model-specific. In this study, only B16F10 tumour-bearing mice had prolonged survival in the absence of FGL2 alone, and the response to FGL2 deficiency is therefore based on cell-intrinsic or other TME-associated characteristics. Although smaller tumour burden was observed at a single timepoint for ID8-*p53*$^{-/-}$*Brca2*$^{-/-}$ tumour-bearing mice, this did not translate to prolonged survival, which may be due to the development of ascites which happens quickly at later stages of tumour progression and drives loss of wellness at endpoint. Both B16F10 and ID8-*p53*$^{-/-}$*Brca2*$^{-/-}$ cell lines express no/low MHC-I and are poorly immunogenic (Lechner et al., 2013; Rodriguez et al., 2022). However, B16F10 cells do express immunogenic antigens such as GP100 or TRP2 (Johnston et al., 1987; Matheoud et al., 2011), whereas the parental ID8-cell line does not express any immunogenic antigens (Martin et al., 2016). Immunogenic antigens present in B16F10 cells may explain why the DCs and T cells in B16F10 tumours are more activated. Given that DCs and T cells were in fact more activated, but only found in the spleen and not the tumour, the ID8-*p53*$^{-/-}$*Brca2*$^{-/-}$ tumours may have differences in physical barriers such as the extracellular matrix or vascularization, or in cytokine/chemokine expression, thereby obstructing immune cell infiltration into the tumour (Winkler et al., 2020). As such, activated DCs in spleens of *Fgl2*$^{-/-}$ mice may not be trafficked into ID8-*p53*$^{-/-}$*Brca2*$^{-/-}$ tumours. Therefore, it is remarkable that a poorly immunogenic cancer model that is unable to respond to a complete knockout in FGL2 was able to survive significantly longer with the addition of an OV to an FGL2-deficient background. This may suggest that the OV stimulated immune cell trafficking and immunogenic cell death in the primary tumours (Achard et al., 2018), allowing the more activated DCs found in the *Fgl2*$^{-/-}$ spleens to traffic to the tumour, thereby prolonging survival. In future studies, depleting DCs, CD4+, or CD8+ T cells in *Fgl2*^{WT} versus *Fgl2*$^{-/-}$ mice will further support the involvement of the adaptive immune system and importance of a strong antigenic response in the role of FGL2 mediated tumour progression.

4.2.5. Future directions

While blocking FGL2 had subtle effects on altering immune cell phenotypes in the TME and did not prolong survival in either the B16F10 or the STOSE models, we showed that the absence of FGL2 can potentially synergize with OV immunotherapy to successfully prolong survival in a model unaffected by the absence of FGL2 alone. In clinical trials to treat ovarian cancer, immune checkpoint inhibitors have had limited success with response rates of 5–20% (Guo et al., 2015b; Hamanishi et al., 2015, 2016a), highlighting the need to develop novel immunotherapeutic strategies. While immune checkpoint blockade in melanoma has had marked success, resistance is still a challenge in the treatment of melanoma (Carlino et al., 2021). Although blocking FGL2 as a monotherapy was unsuccessful in the models studied, we propose that targeting FGL2 in the TME has the potential to be another useful tool to incorporate into combination immunotherapies for treatment of ovarian cancer and melanoma, such as with OVs or TIGIT blockade.

4.3. FGL2 contributes to post-operative immunosuppression and increased metastatic disease

Tissue injury induces first a pro-inflammatory phase followed by a resolving immunosuppressive phase. The resolution phase in the post-operative period involves expansion of MDSCs which suppresses NK cell cytotoxicity. This NK cell dysfunction leads to increased metastasis in mouse models of surgical stress (Seth et al., 2013; Tai et al., 2013, 2018). FGL2 was recently described to be induced during the pro-inflammatory phase during sepsis (non-sterile tissue injury), cleaved from expanded myeloid cells by ADAM17, and is a mediator of immunosuppression (Zhou et al., 2019). In this study, we investigated the role of FGL2 in surgical stress, or sterile tissue injury, highlighting the role of FGL2 in resolving inflammation.

We first show that plasma FGL2 levels were elevated following surgery. Querying previously published and publicly available scRNA-seq data, we found that *FGL2* was expressed in CD14+ and CD16+ monocytes and DCs [subsets 1/3/5 based on novel scRNA-seq classifications (Villani et al., 2017)]. This is in accordance with previous studies which described *FGL2* expression in monocytes/macrophages (Marsden et al., 2003; Ning et al., 2005; Yang et al., 2013; Zhou et al., 2019) and DCs (Yang et al., 2013). While the expression levels of FGL2 were not significantly increased, the frequency of *FGL2* and *ADAM17* expressing cells increased following surgical stress, similar to the expansion of monocyte/macrophage populations observed during sepsis (Zhou et al., 2019) and suggests plasma FGL2 is elevated due to expansion of the FGL2-expressing populations. In our mouse model of surgical stress-induced metastasis, plasma FGL2 was increased following surgery, and the absence of FGL2 prevented the increase in the incidence of metastasis caused by surgical stress. While elevated FGL2 plays a role in resolving inflammation (Zhou et al., 2019), in the case of cancer metastases, the immunosuppression leads to increased metastases, while the absence of FGL2 does not.

4.3.1. FGL2 does not alter expansion of MDSCs following surgical stress

Surgical stress induces MDSCs and leads to suppression of NK cells (Lu et al., 2020; Mundy-Bosse et al., 2011; Tai et al., 2018; Urakawa et al., 2019; Wang et al., 2017). One such mechanism is through elevated expression of ARG-1 (Angka et al., 2022); however. in our model, knocking out FGL2 did not affect the abundance of PMN-MDSCs or expression of ARG-1 following surgery. Many mechanisms of immunosuppression by MDSCs have been described, such as cytokine secretion (IL-10, TGF-β), immune-regulatory mediators such as reactive oxygen species, nitric oxide, PGE2, or expression of immunosuppressive immune checkpoints such as PD-L1 (Bronte et al., 2016). In fact, we showed in this study that FGL2 can augment expression of CD155 on MDSCs. CD155 is a ligand for DNAM-1 and has been shown to downregulate DNAM-1 (Carlsten et al., 2009) on NK cells, and thereby negatively impact NK cytotoxicity. Indeed *Fgl2*$^{-/-}$ mice have higher DNAM-1 expression, even after surgical stress, suggesting these NK cells present a more activated/cytotoxic population (Chan et al., 2010; Martinet et al., 2015). Additionally, CD155 is a ligand for immunosuppressive TIGIT, meaning increased CD155 may cause increased immunosuppression of NK and T cells following surgical stress though the CD155-TIGIT interaction (Anderson et al., 2016). Furthermore, our results revealed that FGL2 is associated with lower expression of the cytotoxic effector molecule NKG2D on NK cells. TGF-β is a potent effector of MDSCs, downregulating NKG2D (Lee et al., 2004) and DNAM-1 (Cluxton et al., 2019) on NK cells, impairing cytotoxicity. Future studies should investigate FGL2's role in TGF-β secretion by MDSCs, as we would hypothesize that FGL2 induced TGF-β, leading to downregulation of NKG2D and DNAM-1. Overall, we observed higher expression of NKG2D and DNAM-1 in NK cells of *Fgl2*$^{-/-}$ mice which may lead to more effective cancer cell surveillance and elimination during the post-operative immunosuppressive window. Further studies are needed to assess the suppression of NK cell cytotoxicity by MDSCs, treated with rFGL2, to determine if FGL2 increases the suppressive function of MDSCs. Additionally, depleting MDSC populations or CD155 blockage following surgical stress in *Fgl2*$^{\mathrm{WT}}$ and *Fgl2*$^{-/-}$ mice could reveal the role of FGL2 and the involvement of these cells in preventing metastases.

4.3.2. Surgical stress induced immunosuppression of dendritic cells

While the majority of studies on surgical stress have focused on MDSC suppression of NK and T cells, there is some evidence that the DC population is also suppressed in a post-operative window (Brivio et al., 2000; De et al., 2003; Kawasaki et al., 2006). In the B16F10 model of surgical stress induced metastasis we observed a lower frequency of DCs in *Fgl2*^{WT} mice after surgery, but no difference in DCs in *Fgl2*$^{-/-}$ mice. Furthermore, we showed that DCs in *Fgl2*$^{-/-}$ mice have more CD86+ DCs compared to *Fgl2*^{WT} following surgery, suggesting they may be more resistant to immunosuppression, and may be more efficient for T cell priming and cancer cell elimination (Liu et al., 2008; Shalev et al., 2008, 2009; Yang et al., 2019). Further studies are needed, such as depleting DC populations following surgical stress in *Fgl2*^{WT} and *Fgl2*$^{-/-}$ mice to show the role of FGL2 and the involvement of these cells in preventing metastases.

4.3.3. Limitations and future directions

Although we focused on the immunosuppressive functions of FGL2, it is important to note that the FGL2 knockout mice will delete the entire FGL2 gene (Shalev et al., 2008), including both the membrane-bound prothrombinase and the secreted immunosuppressive form. Furthermore, the FGL2 blocking antibody used in this study is a polyclonal antibody which will block both forms of FGL2. The membrane-bound prothrombinase function of FGL2 cleaves pro-thrombin to thrombin, independent of other coagulation functions (Chan et al., 2002; Yuwaraj et al., 2001). Importantly, the coagulation cascade triggered by surgical stress contributes to metastases, where thrombin generation leads to activated platelets and fibrin clots, preventing efficient clearance of cancer cells (Seth et al., 2013). Furthermore, thrombin triggers myeloid cell activation (Kaplanski et al., 1997) and infiltration, including monocytes and PMNs, by directly acting as a chemoattractant (Bar-Shavit et al., 1983; Bizios et al., 1986) or by activating endothelial cells and platelets to express P-selectin and stimulate adhesion (Kaplanski et al., 1998; Sugama et al., 1992; Zimmerman et al., 1985). Using scRNA-seq data, we showed that surgery enhances expression of *FGL2* in CD14+ and CD16+ monocytes and DCs and that sFGL2 is induced in plasma post-operatively, however we did not investigate levels of the membrane-bound form specifically. In the case of the non-sterile tissue injury (sepsis) there were temporal shifts in the expression of FGL2, with mFGL2 being cleaved to sFGL2 during the first 24 hours, resulting in decreased mFGL2 but increased sFGL2 (Zhou et al., 2019). Nevertheless, it is important to note that the prothrombinase function of FGL2 may contribute to the fibrin clots by thrombin generation and platelet activation, thus deleting/blocking the membrane-bound form in addition to the secreted form, which may have contributed to blocking the coagulation cascade triggered after surgery, and to fewer metastases after surgical stress. Future studies using the monoclonal α-FGL2 antibody to block the immunosuppressive functions of FGL2 alone may help to differentiate between the role of mFGL2 and sFGL2 in surgical stress.

Given surgery is a first-line treatment strategy for a number of different cancers, including melanoma and ovarian cancer, we first sought to use a well-established model of surgical stress to show the role of FGL2 in post-operative immunosuppression prior to developing more clinically relevant models. Future studies could develop a resection model for ovarian cancer, similar to the 4T1 breast cancer model of surgical stress, for a more clinically relevant model for ovarian cancer surgical stress. Cancer cells could be injected i.b. in *Fgl2*$^{-/-}$ mice and Fgl2^{WT} mice, followed by oophorectomy around halfway to predicted endpoint, allowing for primary tumour growth, but few metastases or ascites. Mice could be assessed for survival or taken at a timepoint prior to endpoint to assess tumour burden and ascites volume. This would allow us to determine if surgical stress similarly induces metastasis in an ovarian cancer model, and what, if any, role FGL2 plays in inducing metastasis. Alternatively, mice could be treated before, on the day of, and after surgical resection to determine if blocking FGL2 as a novel immunotherapy could improve survival following surgical resection, allowing us to more closely model human disease.

While several treatments are being tested in clinical trials to relieve post-operative immunosuppression or the coagulation cascade (Market et al., 2018), there is still work to be done in order to improve outcomes and prevent recurrence following surgical resection, as surgery is one of the most common treatments for many types of cancer. An FGL2 blocking antibody was able to prevent increased metastasis in the B16F10 model of surgical stress when used as a peri-operative treatment. This very positive outcome suggests that α-FGL2 immunotherapy should be investigated further as a potential treatment for the prevention of metastases and recurrence. Knowing ADAM17 is capable of cleaving FGL2 (Zhou et al., 2019), and is similarly induced following surgical stress, targeting ADAM17 with small molecule inhibitors, already in clinical trials (Calligaris et al., 2021), may be an effective alternative strategy to block the secretion of

FGL2 and its role in the post-operative immunosuppressive period and its association with increased metastases.

In this study we showed for the first time the involvement of FGL2 in surgical stress induced metastasis. The absence of FGL2 is associated with NK cells expressing more/higher levels of effector molecules NKG2D and DNAM-1, even during surgical stress induced immunosuppression. Furthermore, we show that DCs are suppressed following surgical stress, but F*gl2*$^{-/-}$ mice are resistant to this suppression with more CD86+ DCs following surgery in these mice. Blocking FGL2 may be an effective immunotherapeutic strategy to relieve immunosuppression of NK cells and DCs, and to prevent metastasis and recurrence.

4.4. Conclusions

This thesis set out to fully characterize the TME of syngeneic models of ovarian cancer, and to test a novel immunotherapy for the treatment of ovarian cancer and melanoma, and for the treatment of surgical stress induced immunosuppression. We assessed MHC-I expression, immunogenicity, immune cell populations, and cytokine profiles of ascites, in 6 syngeneic models of ovarian cancer (Chapter 3.1). This characterization provides a valuable resource for ovarian cancer research, to expand syngeneic model systems for immunotherapy research to include a variety of mutations relevant to human disease (*TP53*, *BRCA1*, *BRCA2*, *PTEN*, *KRAS*) and to include both ovarian surface epithelial and fallopian tube derived models to encompass the heterogeneity of human disease initiation. This study showed for the first time that FGL2 is primarily expressed in macrophages/monocytes in the tumour, with minimal or no expression of FGL2 in the cancer cells. We then described the role of FGL2 expressed from immune/stromal cells of the TME in ovarian cancer disease progression and showed how its deletion can synergize with OV immunotherapy to prolong survival. Furthermore, we showed the importance of model selection for the investigation of immunomodulatory factors by including the B16F10 melanoma model in which the absence of FGL2 prolonged survival (Chapter 3.2). Finally, we showed that elevated FGL2 is associated with increased metastasis in response to surgical stress, and that *Fgl2*$^{-/-}$ immune cells (NK and DCs) may be more resistant to post-operative immunosuppression by being more activated (Chapter 3.3). We report the novel discovery that, in multiple murine cancer models, as well as tumour-naïve mice, *Fgl2*$^{-/-}$ NK cells are more DNAM-1+ and NKG2D+, which suggests that NK cells in *Fgl2*$^{-/-}$ mice may be more activated. These novel findings expand our knowledge of FGL2-mediated immunosuppression which typically focuses on the role of FGL2 in DCs, macrophages, and Tregs, to include NK cells.

References

Achard, C., Surendran, A., Wedge, M.-E., Ungerechts, G., Bell, J., and Ilkow, C.S. (2018). Lighting a fire in the tumor microenvironment using oncolytic immunotherapy. EBioMedicine *31*, 17–24. https://doi.org/10.1016/j.ebiom.2018.04.020.

Ai, G., Yan, W., Yu, H., Xiao, F., Xi, D., Ma, K., Huang, J., Luo, X., Wan, X., and Ning, Q. (2018). Soluble Fgl2 restricts autoimmune hepatitis progression via suppressing Tc17 and conventional CD8+ T cell function. J Gene Med *20*, e3023. https://doi.org/10.1002/jgm.3023.

Alazawi, W., Pirmadjid, N., Lahiri, R., and Bhattacharya, S. (2016). Inflammatory and immune responses to surgery and their clinical impact. Annals of Surgery *264*, 73–80. https://doi.org/10.1097/SLA.0000000000001691.

Alexandrov, L.B., Nik-Zainal, S., Wedge, D.C., Aparicio, S.A.J.R., Behjati, S., Biankin, A.V., Bignell, G.R., Bolli, N., Borg, A., Børresen-Dale, A.-L., et al. (2013). Signatures of mutational processes in human cancer. Nature *500*, 415–421. https://doi.org/10.1038/nature12477.

Alkayyal, A.A., Tai, L.-H., Kennedy, M.A., Souza, C.T. de, Zhang, J., Lefebvre, C., Sahi, S., Ananth, A.A., Mahmoud, A.B., Makrigiannis, A.P., et al. (2017). NK-Cell Recruitment Is Necessary for Eradication of Peritoneal Carcinomatosis with an IL12-Expressing Maraba Virus Cellular Vaccine. Cancer Immunol Res *5*, 211–221. https://doi.org/10.1158/2326-6066.CIR-16-0162.

Alter, G., Malenfant, J.M., and Altfeld, M. (2004). CD107a as a functional marker for the identification of natural killer cell activity. Journal of Immunological Methods *294*, 15–22. https://doi.org/10.1016/j.jim.2004.08.008.

Alwosaibai, K., Abedini, A., Al-Hujaily, E.M., Tang, Y., Garson, K., Collins, O., and Vanderhyden, B.C. (2017). PAX2 maintains the differentiation of mouse oviductal epithelium and inhibits the transition to a stem cell-like state. Oncotarget *8*, 76881–76897. https://doi.org/10.18632/oncotarget.20173.

Amponsa, V.O., Shuman, L., Ellis, J., Wang, E., Walter, V., Owens, R.G., Zaleski, M., Warrick, J.I., Raman, J.D., and DeGraff, D.J. (2019). Carcinogen-induced bladder cancer in the FVB mouse strain is associated with glandular differentiation and increased Cd274/Pdl-1 expression. Am J Clin Exp Urol *7*, 139–152.

Anderson, A.C., Joller, N., and Kuchroo, V.K. (2016). Lag-3, Tim-3, and TIGIT co-inhibitory receptors with specialized functions in immune regulation. Immunity *44*, 989–1004. https://doi.org/10.1016/j.immuni.2016.05.001.

Angka, L., Khan, S.T., Kilgour, M.K., Xu, R., Kennedy, M.A., and Auer, R.C. (2017). Dysfunctional natural killer cells in the aftermath of cancer surgery. Int J Mol Sci *18*. https://doi.org/10.3390/ijms18081787.

Angka, L., Tanese de Souza, C., Baxter, K.E., Khan, S.T., Market, M., Martel, A.B., Tai, L.-H., Kennedy, M.A., Bell, J.C., and Auer, R.C. (2022). Perioperative arginine prevents metastases by accelerating natural killer cell recovery after surgery. Molecular Therapy https://doi.org/10.1016/j.ymthe.2022.05.024.

Bakos, O., Lawson, C., Rouleau, S., and Tai, L.-H. (2018). Combining surgery and immunotherapy: turning an immunosuppressive effect into a therapeutic opportunity. Journal for ImmunoTherapy of Cancer *6*, 86. https://doi.org/10.1186/s40425-018-0398-7.

Banerjee, S., and Kaye, S.B. (2013). New strategies in the treatment of ovarian cancer: current clinical perspectives and future potential. Clin Cancer Res *19*, 961–968. https://doi.org/10.1158/1078-0432.CCR-12-2243.

Bar-Shavit, R., Kahn, A., Fenton, J.W., and Wilner, G.D. (1983). Chemotactic response of monocytes to thrombin. J Cell Biol *96*, 282–285. https://doi.org/10.1083/jcb.96.1.282.

Bartczak, A., Chruscinski, A., Mendicino, M., Liu, H., Zhang, J., He, W., Amir, A.Z., Nguyen, A., Khattar, R., Sadozai, H., et al. (2016). Overexpression of fibrinogen-like protein 2 promotes tolerance in a fully mismatched murine model of heart transplantation. Am. J. Transplant. *16*, 1739–1750. https://doi.org/10.1111/ajt.13696.

Bartczak, A., Zhang, J., Adeyi, O., Amir, A., Grant, D., Gorczynski, R., Selzner, N., Chruscinski, A., and Levy, G.A. (2017). Overexpression of fibrinogen-like protein 2 protects against T cell-induced colitis. World J Gastroenterol *23*, 2673–2684. https://doi.org/10.3748/wjg.v23.i15.2673.

Bassez, A., Vos, H., Van Dyck, L., Floris, G., Arijs, I., Desmedt, C., Boeckx, B., Vanden Bempt, M., Nevelsteen, I., Lambein, K., et al. (2021). A single-cell map of intratumoral changes during anti-PD1 treatment of patients with breast cancer. Nat Med *27*, 820–832. https://doi.org/10.1038/s41591-021-01323-8.

Berek, J.S., and Hacker, N.F. (2015). Berek and Hacker’s gynecologic oncology (Lippincott Williams & Wilkins.).

Bergenfelz, C., and Leandersson, K. (2020). The Generation and Identity of Human Myeloid-Derived Suppressor Cells. Frontiers in Oncology *10*. https://doi.org/10.3389/fonc.2020.00109.

Bézie, S., Picarda, E., Tesson, L., Renaudin, K., Durand, J., Ménoret, S., Mérieau, E., Chiffoleau, E., Guillonneau, C., Caron, L., et al. (2015). Fibrinogen-Like Protein 2/Fibroleukin Induces Long-Term Allograft Survival in a Rat Model through Regulatory B Cells. PLoS One *10*. https://doi.org/10.1371/journal.pone.0119686.

Bezman, N.A., Kim, C.C., Sun, J.C., Min-Oo, G., Hendricks, D.W., Kamimura, Y., Best, J.A., Goldrath, A.W., and Lanier, L.L. (2012). Immgen report: molecular definition of natural killer cell identity and activation. Nat Immunol *13*, 1000–1009. https://doi.org/10.1038/ni.2395.

Bizios, R., Lai, L., Fenton, J.W., and Malik, A.B. (1986). Thrombin-induced chemotaxis and aggregation of neutrophils. J Cell Physiol *128*, 485–490. https://doi.org/10.1002/jcp.1041280318.

du Bois, A., Reuss, A., Pujade-Lauraine, E., Harter, P., Ray-Coquard, I., and Pfisterer, J. (2009). Role of surgical outcome as prognostic factor in advanced epithelial ovarian cancer: A combined exploratory analysis of 3 prospectively randomized phase 3 multicenter trials. Cancer *115*, 1234–1244. https://doi.org/10.1002/cncr.24149.

Bommareddy, P.K., Patel, A., Hossain, S., and Kaufman, H.L. (2017). Talimogene Laherparepvec (T-VEC) and other oncolytic viruses for the treatment of melanoma. Am J Clin Dermatol *18*, 1–15. https://doi.org/10.1007/s40257-016-0238-9.

Bommareddy, P.K., Shettigar, M., and Kaufman, H.L. (2018). Integrating oncolytic viruses in combination cancer immunotherapy. Nature Reviews Immunology *18*, 498. https://doi.org/10.1038/s41577-018-0014-6.

Bonaventura, P., Shekarian, T., Alcazer, V., Valladeau-Guilemond, J., Valsesia-Wittmann, S., Amigorena, S., Caux, C., and Depil, S. (2019). Cold tumors: a therapeutic challenge for immunotherapy. Frontiers in Immunology *10*. https://doi.org/10.3389/fimmu.2019.00168.

Bridle, B.W., Stephenson, K.B., Boudreau, J.E., Koshy, S., Kazdhan, N., Pullenayegum, E., Brunellière, J., Bramson, J.L., Lichty, B.D., and Wan, Y. (2010). Potentiating cancer immunotherapy using an oncolytic virus. Molecular Therapy *18*, 1430–1439. https://doi.org/10.1038/mt.2010.98.

Brivio, F., Gilardi, R., Bucocev, R., Ferrante, R., Rescaldani, R., Vigoré, L., Fumagalli, L., Nespoli, A., and Lissoni, P. (2000). Surgery-induced decline in circulating dendritic cells in operable cancer patients: a possible explanation of postoperative immunosuppression. Hepatogastroenterology *47*, 1337–1339. .

Brivio, F., Fumagalli, L., Lissoni, P., Nardone, A., Nespoli, L., Fattori, L., Denova, M., Chiarelli, M., and Nespoli, A. (2006). Pre-operative immunoprophylaxis with interleukin-2 may improve prognosis in radical surgery for colorectal cancer stage B-C. Anticancer Res *26*, 599–603. .

Bronte, V., Brandau, S., Chen, S.-H., Colombo, M.P., Frey, A.B., Greten, T.F., Mandruzzato, S., Murray, P.J., Ochoa, A., Ostrand-Rosenberg, S., et al. (2016). Recommendations for myeloid-derived suppressor cell nomenclature and characterization standards. Nat Commun *7*, 12150. https://doi.org/10.1038/ncomms12150.

Burger, R.A., Brady, M.F., Bookman, M.A., Fleming, G.F., Monk, B.J., Huang, H., Mannel, R.S., Homesley, H.D., Fowler, J., Greer, B.E., et al. (2011). Incorporation of bevacizumab in the primary treatment of ovarian cancer. New England Journal of Medicine *365*, 2473–2483. https://doi.org/10.1056/NEJMoa1104390.

Callahan, M.J., Nagymanyoki, Z., Bonome, T., Johnson, M.E., Litkouhi, B., Sullivan, E.H., Hirsch, M.S., Matulonis, U.A., Liu, J., Birrer, M.J., et al. (2008). Increased HLA-DMB expression in the tumor epithelium is associated with increased CTL infiltration and improved prognosis in advanced-stage serous ovarian cancer. Clin. Cancer Res. *14*, 7667–7673. https://doi.org/10.1158/1078-0432.CCR-08-0479.

Calligaris, M., Cuffaro, D., Bonelli, S., Spanò, D.P., Rossello, A., Nuti, E., and Scilabra, S.D. (2021). Strategies to Target ADAM17 in Disease: From its Discovery to the iRhom Revolution. Molecules *26*, 944. https://doi.org/10.3390/molecules26040944.

Canadian Cancer Society (2019a). Survival statistics for ovarian cancer.

Canadian Cancer Society (2019b). Canadian Cancer Statistics Advisory Committee. Canadian Cancer Statistics 2019.

Canadian Cancer Society (2019c). Survival statistics for melanoma skin cancer.

Cancer Genome Atlas Research Network (2011). Integrated genomic analyses of ovarian carcinoma. Nature *474*, 609–615. https://doi.org/10.1038/nature10166.

Cao, J., Gong, J., Li, X., Hu, Z., Xu, Y., Shi, H., Li, D., Liu, G., Jie, Y., Hu, B., et al. (2021). Unsupervised hierarchical clustering identifies immune gene subtypes in gastric cancer. Front Pharmacol *12*, 692454. https://doi.org/10.3389/fphar.2021.692454.

Carlino, M.S., Larkin, J., and Long, G.V. (2021). Immune checkpoint inhibitors in melanoma. The Lancet *398*, 1002–1014. https://doi.org/10.1016/S0140-6736(21)01206-X.

Carlsten, M., Norell, H., Bryceson, Y.T., Poschke, I., Schedvins, K., Ljunggren, H.-G., Kiessling, R., and Malmberg, K.-J. (2009). Primary Human tumor cells expressing CD155 impair tumor targeting by down-regulating DNAM-1 on NK cells. The Journal of Immunology *183*, 4921–4930. https://doi.org/10.4049/jimmunol.0901226.

Chalmers, Z.R., Connelly, C.F., Fabrizio, D., Gay, L., Ali, S.M., Ennis, R., Schrock, A., Campbell, B., Shlien, A., Chmielecki, J., et al. (2017). Analysis of 100,000 human cancer genomes reveals the landscape of tumor mutational burden. Genome Medicine *9*, 34. https://doi.org/10.1186/s13073-017-0424-2.

Chan, C.J., Andrews, D.M., McLaughlin, N.M., Yagita, H., Gilfillan, S., Colonna, M., and Smyth, M.J. (2010). DNAM-1/CD155 interactions promote cytokine and NK cell-mediated suppression of poorly immunogenic melanoma metastases. J Immunol *184*, 902–911. https://doi.org/10.4049/jimmunol.0903225.

Chan, C.W.Y., Chan, M.W.C., Liu, M., Fung, L., Cole, E.H., Leibowitz, J.L., Marsden, P.A., Clark, D.A., and Levy, G.A. (2002). Kinetic analysis of a unique direct prothrombinase, fgl2, and identification of a serine residue critical for the prothrombinase activity. J. Immunol. *168*, 5170–5177. https://doi.org/10.4049/jimmunol.168.10.5170.

Chan, C.W.Y., Kay, L.S., Khadaroo, R.G., Chan, M.W.C., Lakatoo, S., Young, K.J., Zhang, L., Gorczynski, R.M., Cattral, M., Rotstein, O., et al. (2003). Soluble fibrinogen-like protein 2/fibroleukin exhibits immunosuppressive properties: suppressing t cell proliferation and inhibiting maturation of bone marrow-derived dendritic cells. The Journal of Immunology *170*, 4036–4044. https://doi.org/10.4049/jimmunol.170.8.4036.

Chen, D.S., and Mellman, I. (2017). Elements of cancer immunity and the cancer-immune set point. Nature *541*, 321–330. https://doi.org/10.1038/nature21349.

Chen, S., Lee, L.-F., Fisher, T.S., Jessen, B., Elliott, M., Evering, W., Logronio, K., Tu, G.H., Tsaparikos, K., Li, X., et al. (2015). Combination of 4-1BB agonist and PD-1 antagonist promotes antitumor effector/memory CD8 T cells in a poorly immunogenic tumor model. Cancer Immunology Research *3*, 149–160. https://doi.org/10.1158/2326-6066.CIR-14-0118.

Chiocca, E., and Rabkin, S. (2014). Oncolytic viruses and their application to cancer immunotherapy. Cancer Immunol Res *2*, 295–300. https://doi.org/10.1158/2326-6066.CIR-14-0015.

Cho, B., Choi, I., Lee, E.M., Hurh, S., Lee, B.C., and Ahn, C. (2018). Up-regulation of fibrinogen-like protein 2 in porcine endothelial cells by xenogeneic CD40 signal. Anim Cells Syst (Seoul) *22*, 92–99. https://doi.org/10.1080/19768354.2018.1433718.

Chruscinski, A., Rojas-Luengas, V., Moshkelgosha, S., Issachar, A., Luo, J., Yowanto, H., Lilly, L., Smith, R., Renner, E., Zhang, J., et al. (2021). Evaluation of a gene expression biomarker to identify operationally tolerant liver transplant recipients: the LITMUS trial. Clin Exp Immunol *207*, 123–139. https://doi.org/10.1093/cei/uxab011.

Ciombor, K.K., and Goldberg, R.M. (2018). Hypermutated Tumors and Immune Checkpoint Inhibition. Drugs *78*, 155–162. https://doi.org/10.1007/s40265-018-0863-0.

Clark, D.A., Ding, J.W., Chaouat, G., Coulam, C.B., August, C., and Levy, G.A. (1999). The emerging role of immunoregulation of fibrinogen-related procoagulant Fgl2 in the success or spontaneous abortion of early pregnancy in mice and humans. Am. J. Reprod. Immunol. *42*, 37–43. https://doi.org/10.1111/j.1600-0897.1999.tb00463.x.

Clark, D.A., Ding, J.W., Yu, G., Levy, G.A., and Gorczynski, R.M. (2001). Fgl2 prothrombinase expression in mouse trophoblast and decidua triggers abortion but may be countered by OX-2. Mol. Hum. Reprod. *7*, 185–194. https://doi.org/10.1093/molehr/7.2.185.

Clarke, B., Tinker, A.V., Lee, C.-H., Subramanian, S., van de Rijn, M., Turbin, D., Kalloger, S., Han, G., Ceballos, K., Cadungog, M.G., et al. (2009). Intraepithelial T cells and prognosis in ovarian carcinoma: novel associations with stage, tumor type, and BRCA1 loss. Mod. Pathol. *22*, 393–402. https://doi.org/10.1038/modpathol.2008.191.

Clement, M., Fornasa, G., Guedj, K., Ben Mkaddem, S., Gaston, A.-T., Khallou-Laschet, J., Morvan, M., Nicoletti, A., and Caligiuri, G. (2014). CD31 is a key coinhibitory receptor in the development of immunogenic dendritic cells. Proc Natl Acad Sci U S A *111*, E1101–E1110. https://doi.org/10.1073/pnas.1314505111.

Cluxton, C.D., Spillane, C., O'Toole, S.A., Sheils, O., Gardiner, C.M., and O'Leary, J.J. (2019). Suppression of Natural Killer cell NKG2D and CD226 anti-tumour cascades by platelet cloaked cancer cells: Implications for the metastatic cascade. PLOS ONE *14*, e0211538. https://doi.org/10.1371/journal.pone.0211538.

Coffey, J.C., Wang, J.H., Smith, M.J.F., Bouchier-Hayes, D., Cotter, T.G., and Redmond, H.P. (2003). Excisional surgery for cancer cure: therapy at a cost. The Lancet Oncology *4*, 760–768. https://doi.org/10.1016/S1470-2045(03)01282-8.

Cole, A.J., Dwight, T., Gill, A.J., Dickson, K.-A., Zhu, Y., Clarkson, A., Gard, G.B., Maidens, J., Valmadre, S., Clifton-Bligh, R., et al. (2016). Assessing mutant p53 in primary high-grade serous ovarian cancer using immunohistochemistry and massively parallel sequencing. Scientific Reports *6*, 1–12. https://doi.org/10.1038/srep26191.

Cook, D.P., and Vanderhyden, B.C. (2022). Transcriptional census of epithelial-mesenchymal plasticity in cancer. Sci Adv *8*, eabi7640. https://doi.org/10.1126/sciadv.abi7640.

Cortez, A.J., Tudrej, P., Kujawa, K.A., and Lisowska, K.M. (2018). Advances in ovarian cancer therapy. Cancer Chemother. Pharmacol. *81*, 17–38. https://doi.org/10.1007/s00280-017-3501-8.

Coscia, F., Watters, K.M., Curtis, M., Eckert, M.A., Chiang, C.Y., Tyanova, S., Montag, A., Lastra, R.R., Lengyel, E., and Mann, M. (2016). Integrative proteomic profiling of ovarian cancer cell lines reveals precursor cell associated proteins and functional status. Nature Communications *7*, 1–14. https://doi.org/10.1038/ncomms12645.

Couto, G.K., Segatto, N.V., Oliveira, T.L., Seixas, F.K., Schachtschneider, K.M., and Collares, T. (2019). The melding of drug screening platforms for melanoma. Frontiers in Oncology *9*. https://doi.org/10.3389/fonc.2019.00512.

Crudele, J.M., and Chamberlain, J.S. (2018). Cas9 immunity creates challenges for CRISPR gene editing therapies. Nat Commun *9*, 3497. https://doi.org/10.1038/s41467-018-05843-9.

Curiel, T.J., Coukos, G., Zou, L., Alvarez, X., Cheng, P., Mottram, P., Evdemon-Hogan, M., Conejo-Garcia, J.R., Zhang, L., Burow, M., et al. (2004). Specific recruitment of regulatory T cells in ovarian carcinoma fosters immune privilege and predicts reduced survival. Nat. Med. *10*, 942–949. https://doi.org/10.1038/nm1093.

Curti, B.D., and Faries, M.B. (2021). Recent advances in the treatment of melanoma. New England Journal of Medicine *384*, 2229–2240. https://doi.org/10.1056/NEJMra2034861.

De, A.K., Laudanski, K., and Miller-Graziano, C.L. (2003). Failure of monocytes of trauma patients to convert to immature dendritic cells is related to preferential macrophage-colony-stimulating factor-driven macrophage differentiation. The Journal of Immunology *170*, 6355–6362. https://doi.org/10.4049/jimmunol.170.12.6355.

Ding, J.W., Ning, Q., Liu, M.F., Lai, A., Leibowitz, J., Peltekian, K.M., Cole, E.H., Fung, L.S., Holloway, C., Marsden, P.A., et al. (1997). Fulminant hepatic failure in murine hepatitis virus strain 3 infection: tissue-specific expression of a novel fgl2 prothrombinase. J. Virol. *71*, 9223–9230. https://doi.org/10.1128/JVI.71.12.9223-9230.1997.

Ding, J.W., Ning, Q., Liu, M.F., Lai, A., Peltekian, K., Fung, L., Holloway, C., Yeger, H., Phillips, M.J., and Levy, G.A. (1998). Expression of the fgl2 and its protein product (prothrombinase) in tissues during murine hepatitis virus strain-3 (MHV-3) infection. Adv. Exp. Med. Biol. *440*, 609–618. https://doi.org/10.1007/978-1-4615-5331-1_79.

Dong, Z.-Y., Zhong, W.-Z., Zhang, X.-C., Su, J., Xie, Z., Liu, S.-Y., Tu, H.-Y., Chen, H.-J., Sun, Y.-L., Zhou, Q., et al. (2017). Potential predictive value of TP53 and KRAS mutation status for response to PD-1 blockade immunotherapy in lung adenocarcinoma. Clin Cancer Res *23*, 3012–3024. https://doi.org/10.1158/1078-0432.CCR-16-2554.

Ducie, J., Dao, F., Considine, M., Olvera, N., Shaw, P.A., Kurman, R.J., Shih, I.-M., Soslow, R.A., Cope, L., and Levine, D.A. (2017). Molecular analysis of high-grade serous ovarian carcinoma with and without associated serous tubal intra-epithelial carcinoma. Nature Communications *8*, 1–9. https://doi.org/10.1038/s41467-017-01217-9.

Dummer, R., Hoeller, C., Gruter, I.P., and Michielin, O. (2017). Combining talimogene laherparepvec with immunotherapies in melanoma and other solid tumors. Cancer Immunol. Immunother. *66*, 683–695. https://doi.org/10.1007/s00262-017-1967-1.

Duraiswamy, J., Freeman, G.J., and Coukos, G. (2013). Therapeutic PD-1 Pathway Blockade Augments with Other Modalities of Immunotherapy T-Cell Function to Prevent Immune Decline in Ovarian Cancer. Cancer Res *73*, 6900–6912. https://doi.org/10.1158/0008-5472.CAN-13-1550.

Eddie, S.L., Quartuccio, S.M., hAinmhire, E.Ó., Moyle-Heyrman, G., Lantvit, D.D., Wei, J.-J., Vanderhyden, B.C., and Burdette, J.E. (2015). Tumorigenesis and peritoneal colonization from fallopian tube epithelium. Oncotarget *6*, 20500–20512. https://doi.org/10.18632/oncotarget.3985.

Eggermont, A., Robert, C., Soria, J.C., and Zitvogel, L. (2014). Harnessing the immune system to provide long-term survival in patients with melanoma and other solid tumors. Oncoimmunology *3*, e27560. https://doi.org/10.4161/onci.27560.

Eisenkop, S.M., Spirtos, N.M., Friedman, R.L., Lin, W.-C.M., Pisani, A.L., and Perticucci, S. (2003). Relative influences of tumor volume before surgery and the cytoreductive outcome on survival for patients with advanced ovarian cancer: a prospective study. Gynecol Oncol *90*, 390–396. https://doi.org/10.1016/s0090-8258(03)00278-6.

El-Mesery, M., El-Mowafy, M., Elgaml, A., Youssef, L.F., and Abed, S.Y. (2017). Correlation of Serum Soluble Fibrinogen-Like Protein 2 with Soluble FAS Ligand and Interferon Gamma in Egyptian Hepatitis C Virus-Infected Patients and Hepatocellular Carcinoma Patients. J. Interferon Cytokine Res. *37*, 342–347. https://doi.org/10.1089/jir.2016.0128.

van Elsas, A., Hurwitz, A.A., and Allison, J.P. (1999). Combination immunotherapy of b16 melanoma using anti–cytotoxic t lymphocyte–associated antigen 4 (ctla-4) and granulocyte/macrophage colony-stimulating factor (gm-csf)-producing vaccines induces rejection of subcutaneous and metastatic tumors accompanied by autoimmune depigmentation. Journal of Experimental Medicine *190*, 355–366. https://doi.org/10.1084/jem.190.3.355.

Endsley, M.P., Moyle-Heyrman, G., Karthikeyan, S., Lantvit, D.D., Davis, D.A., Wei, J.-J., and Burdette, J.E. (2015). Spontaneous transformation of murine oviductal epithelial cells: a model system to investigate the onset of fallopian-derived tumors. Front Oncol *5*. https://doi.org/10.3389/fonc.2015.00154.

Faries, M.B., Cochran, A.J., Elashoff, R.M., and Thompson, J.F. (2015). Multicenter Selective Lymphadenectomy Trial-I confirms the central role of sentinel node biopsy in contemporary melanoma management: response to "No survival benefit for patients with melanoma undergoing sentinel lymph node biopsy: critical appraisal of the Multicenter Selective Lymphadenectomy Trial-I final report." Br J Dermatol *172*, 571–573. https://doi.org/10.1111/bjd.13676.

Fauriat, C., Long, E.O., Ljunggren, H.-G., and Bryceson, Y.T. (2010). Regulation of human NK-cell cytokine and chemokine production by target cell recognition. Blood *115*, 2167–2176. https://doi.org/10.1182/blood-2009-08-238469.

Feng, Y., Guo, C., Wang, H., Zhao, L., Wang, W., Wang, T., Feng, Y., Yuan, K., and Huang, G. (2020). Fibrinogen-like protein 2 (fgl2) is a novel biomarker for clinical prediction of human breast cancer. Med Sci Monit *26*. https://doi.org/10.12659/MSM.923531.

Foerster, K., Helmy, A., Zhu, Y., Khattar, R., Adeyi, O.A., Wong, K.M., Shalev, I., Clark, D.A., Wong, P.-Y., Heathcote, E.J., et al. (2010). The novel immunoregulatory molecule FGL2: a potential biomarker for severity of chronic hepatitis C virus infection. J. Hepatol. *53*, 608–615. https://doi.org/10.1016/j.jhep.2010.04.020.

Foley, O.W., Rauh-Hain, J.A., and del Carmen, M.G. (2013). Recurrent epithelial ovarian cancer: an update on treatment. Oncology (Williston Park, N.Y.) *27*, 288–294, 298.

Fu, Y., Ding, Y., Wang, Q., Zhu, F., Tan, Y., Lu, X., Guo, B., Zhang, Q., Cao, Y., Liu, T., et al. (2020). Blood-stage malaria parasites manipulate host innate immune responses through the induction of sFGL2. Sci Adv *6*. https://doi.org/10.1126/sciadv.aay9269.

Fullerton, J.N., and Gilroy, D.W. (2016). Resolution of inflammation: a new therapeutic frontier. Nat Rev Drug Discov *15*, 551–567. https://doi.org/10.1038/nrd.2016.39.

Gabrilovich, D.I., and Nagaraj, S. (2009). Myeloid-derived suppressor cells as regulators of the immune system. Nat. Rev. Immunol. *9*, 162–174. https://doi.org/10.1038/nri2506.

Galluzzi, L., Chan, T.A., Kroemer, G., Wolchok, J.D., and López-Soto, A. (2018). The hallmarks of successful anticancer immunotherapy. Science Translational Medicine *10*. https://doi.org/10.1126/scitranslmed.aat7807.

Garrido, F., and Aptsiauri, N. (2019). Cancer immune escape: MHC expression in primary tumours versus metastases. Immunology *158*, 255–266. https://doi.org/10.1111/imm.13114.

Geistlinger, L., Oh, S., Ramos, M., Schiffer, L., LaRue, R.S., Henzler, C.M., Munro, S.A., Daughters, C., Nelson, A.C., Winterhoff, B.J., et al. (2020). Multiomic analysis of subtype evolution and heterogeneity in high-grade serous ovarian carcinoma. Cancer Research *80*, 4335–4345. https://doi.org/10.1158/0008-5472.CAN-20-0521.

George, S., Miao, D., Demetri, G.D., Adeegbe, D., Rodig, S.J., Shukla, S., Lipschitz, M., Amin-Mansour, A., Raut, C.P., Carter, S.L., et al. (2017). Loss of PTEN Is associated with resistance to anti-pd-1 checkpoint blockade therapy in metastatic uterine leiomyosarcoma. Immunity *46*, 197–204. https://doi.org/10.1016/j.immuni.2017.02.001.

Ghaedi, M., Shen, Z.Y., Orangi, M., Martinez-Gonzalez, I., Wei, L., Lu, X., Das, A., Heravi-Moussavi, A., Marra, M.A., Bhandoola, A., et al. (2019). Single-cell analysis of RORα tracer mouse lung reveals ILC progenitors and effector ILC2 subsets. J Exp Med *217*, jem.20182293. https://doi.org/10.1084/jem.20182293.

Ghanekar, A., Mendicino, M., Liu, H., He, W., Liu, M., Zhong, R., Phillips, M.J., Levy, G.A., and Grant, D.R. (2004). Endothelial Induction of fgl2 Contributes to Thrombosis during Acute Vascular Xenograft Rejection. The Journal of Immunology *172*, 5693–5701. https://doi.org/10.4049/jimmunol.172.9.5693.

Gil, M., Komorowski, M.P., Seshadri, M., Rokita, H., McGray, A.J.R., Opyrchal, M., Odunsi, K.O., and Kozbor, D. (2014). CXCL12/CXCR4 blockade by oncolytic virotherapy inhibits ovarian cancer growth by decreasing immunosuppression and targeting cancer initiating cells. J Immunol *193*, 5327–5337. https://doi.org/10.4049/jimmunol.1400201.

Giuntoli, R.L., Webb, T.J., Zoso, A., Rogers, O., Diaz-Montes, T.P., Bristow, R.E., and Oelke, M. (2009). Ovarian cancer-associated ascites demonstrates altered immune environment: implications for antitumor immunity. Anticancer Res. *29*, 2875–2884. .

Glasner, A., Avraham, R., Rosenne, E., Benish, M., Zmora, O., Shemer, S., Meiboom, H., and Ben-Eliyahu, S. (2010). Improving survival rates in two models of spontaneous postoperative metastasis in mice by combined administration of a β-adrenergic antagonist and a cyclooxygenase-2 inhibitor. The Journal of Immunology *184*, 2449–2457. https://doi.org/10.4049/jimmunol.0903301.

Goldfarb, Y., Sorski, L., Benish, M., Levi, B., Melamed, R., and Ben-Eliyahu, S. (2011). Improving postoperative immune status and resistance to cancer metastasis: a combined perioperative approach of immunostimulation and prevention of excessive surgical stress responses. Ann Surg *253*, 798–810. https://doi.org/10.1097/SLA.0b013e318211d7b5.

Guo, S., Yang, C., Diao, B., Huang, X., Jin, M., Chen, L., Yan, W., Ning, Q., Zheng, L., Wu, Y., et al. (2015a). The NLRP3 inflammasome and IL-1β accelerate immunologically mediated pathology in experimental viral fulminant hepatitis. PLoS Pathog. *11*, e1005155. https://doi.org/10.1371/journal.ppat.1005155.

Guo, Z., Wang, X., Cheng, D., Xia, Z., Luan, M., and Zhang, S. (2014). PD-1 blockade and OX40 triggering synergistically protects against tumor growth in a murine model of ovarian cancer. PLoS One *9*. https://doi.org/10.1371/journal.pone.0089350.

Guo, Z., Wang, H., Meng, F., Li, J., and Zhang, S. (2015b). Combined Trabectedin and anti-PD1 antibody produces a synergistic antitumor effect in a murine model of ovarian cancer. J Transl Med *13*, 247. https://doi.org/10.1186/s12967-015-0613-y.

Hagemann, T., Wilson, J., Burke, F., Kulbe, H., Li, N.F., Plüddemann, A., Charles, K., Gordon, S., and Balkwill, F.R. (2006). Ovarian cancer cells polarize macrophages toward a tumor-associated phenotype. J. Immunol. *176*, 5023–5032. .

Hamanishi, J., Mandai, M., Ikeda, T., Minami, M., Kawaguchi, A., Murayama, T., Kanai, M., Mori, Y., Matsumoto, S., Chikuma, S., et al. (2015). Safety and antitumor activity of anti-PD-1 Antibody, Nivolumab, in patients with platinum-resistant ovarian cancer. J. Clin. Oncol. *33*, 4015–4022. https://doi.org/10.1200/JCO.2015.62.3397.

Hamanishi, J., Mandai, M., and Konishi, I. (2016a). Immune checkpoint inhibition in ovarian cancer. Int Immunol *28*, 339–348. https://doi.org/10.1093/intimm/dxw020.

Hamanishi, J., Mandai, M., Matsumura, N., Abiko, K., Baba, T., and Konishi, I. (2016b). PD-1/PD-L1 blockade in cancer treatment: perspectives and issues. Int. J. Clin. Oncol. *21*, 462–473. https://doi.org/10.1007/s10147-016-0959-z.

Han, M., Yan, W., Huang, Y., Yao, H., Wang, Z., Xi, D., Li, W., Zhou, Y., Hou, J., Luo, X., et al. (2008a). The nucleocapsid protein of SARS-CoV induces transcription of hfgl2 prothrombinase gene dependent on C/EBP alpha. J. Biochem. *144*, 51–62. https://doi.org/10.1093/jb/mvn042.

Han, M., Yan, W., Guo, W., Xi, D., Zhou, Y., Li, W., Gao, S., Liu, M., Levy, G., Luo, X., et al. (2008b). Hepatitis B virus-induced hFGL2 transcription is dependent on c-Ets-2 and MAPK signal pathway. J. Biol. Chem. *283*, 32715–32729. https://doi.org/10.1074/jbc.M806769200.

Hao, J., Yan, F., Zhang, Y., Triplett, A., Zhang, Y., Schultz, D.A., Sun, Y., Zeng, J., Silverstein, K.A.T., Zheng, Q., et al. (2018). Expression of Adipocyte/Macrophage Fatty Acid-Binding Protein in Tumor-Associated Macrophages Promotes Breast Cancer Progression. Cancer Res *78*, 2343–2355. https://doi.org/10.1158/0008-5472.CAN-17-2465.

Hao, Y., Hao, S., Andersen-Nissen, E., Mauck, W.M., Zheng, S., Butler, A., Lee, M.J., Wilk, A.J., Darby, C., Zager, M., et al. (2021). Integrated analysis of multimodal single-cell data. Cell *184*, 3573-3587.e29. https://doi.org/10.1016/j.cell.2021.04.048.

Hargadon, K.M., Johnson, C.E., and Williams, C.J. (2018). Immune checkpoint blockade therapy for cancer: An overview of FDA-approved immune checkpoint inhibitors. Int. Immunopharmacol. *62*, 29–39. https://doi.org/10.1016/j.intimp.2018.06.001.

Hou, X.-X., Wang, X.-Q., Zhou, W.-J., and Li, D.-J. (2021). Regulatory T cells induce polarization of pro-repair macrophages by secreting sFGL2 into the endometriotic milieu. Commun Biol *4*, 499. https://doi.org/10.1038/s42003-021-02018-z.

Iyer, S., Zhang, S., Yucel, S., Horn, H., Smith, S.G., Reinhardt, F., Hoefsmit, E., Assatova, B., Casado, J., Meinsohn, M.-C., et al. (2020). Genetically Defined Syngeneic Mouse Models of Ovarian Cancer as Tools for the Discovery of Combination Immunotherapy. Cancer Discov https://doi.org/10.1158/2159-8290.CD-20-0818.

Jablonski, K.A., Amici, S.A., Webb, L.M., Ruiz-Rosado, J. de D., Popovich, P.G., Partida-Sanchez, S., and Guerau-de-Arellano, M. (2015). Novel Markers to Delineate Murine M1 and M2 Macrophages. PLOS ONE *10*, e0145342. https://doi.org/10.1371/journal.pone.0145342.

Jerby-Arnon, L., Shah, P., Cuoco, M.S., Rodman, C., Su, M.-J., Melms, J.C., Leeson, R., Kanodia, A., Mei, S., Lin, J.-R., et al. (2018). A cancer cell program promotes T cell exclusion and resistance to checkpoint blockade. Cell *175*, 984-997.e24. https://doi.org/10.1016/j.cell.2018.09.006.

Johnston, D., Schachne, J.P., and Bystryn, J.C. (1987). Identification of immunogenic B16 melanoma-associated antigens. J Biol Response Mod *6*, 108–120.

Joller, N., Lozano, E., Burkett, P.R., Patel, B., Xiao, S., Zhu, C., Xia, J., Tan, T.G., Sefik, E., Yajnik, V., et al. (2014). Treg cells expressing the co-inhibitory molecule TIGIT selectively inhibit pro-inflammatory Th1 and Th17 cell responses. Immunity *40*, 569–581. https://doi.org/10.1016/j.immuni.2014.02.012.

Kamran, N., Takai, Y., Miyoshi, J., Biswas, S.K., Wong, J.S.B., and Gasser, S. (2013). Toll-like receptor ligands induce expression of the costimulatory molecule CD155 on antigen-presenting cells. PLoS One *8*, e54406. https://doi.org/10.1371/journal.pone.0054406.

Kaplanski, G., Fabrigoule, M., Boulay, V., Dinarello, C.A., Bongrand, P., Kaplanski, S., and Farnarier, C. (1997). Thrombin induces endothelial type II activation in vitro: IL-1 and TNF-alpha-independent IL-8 secretion and E-selectin expression. J Immunol *158*, 5435–5441.

.Kaplanski, G., Marin, V., Fabrigoule, M., Boulay, V., Benoliel, A.-M., Bongrand, P., Kaplanski, S., and Farnarier, C. (1998). Thrombin-activated human endothelial cells support monocyte adhesion in vitro following expression of Intercellular Adhesion Molecule-1 (ICAM-1; CD54) and Vascular Cell Adhesion Molecule-1 (VCAM-1; CD106). Blood *92*, 1259–1267. https://doi.org/10.1182/blood.V92.4.1259.

Kawasaki, T., Fujimi, S., Lederer, J.A., Hubbard, W.J., Choudhry, M.A., Schwacha, M.G., Bland, K.I., and Chaudry, I.H. (2006). Trauma-hemorrhage induces depressed splenic dendritic cell functions in mice. J Immunol *177*, 4514–4520. https://doi.org/10.4049/jimmunol.177.7.4514.

Kerdidani, D., Aerakis, E., Verrou, K.-M., Angelidis, I., Douka, K., Maniou, M.-A., Stamoulis, P., Goudevenou, K., Prados, A., Tzaferis, C., et al. (2022). Lung tumor MHCII immunity depends on in situ antigen presentation by fibroblasts. Journal of Experimental Medicine *219*, e20210815. https://doi.org/10.1084/jem.20210815.

Kiessling, R., Klein, E., and Wigzell, H. (1975). „Natural” killer cells in the mouse. I. Cytotoxic cells with specificity for mouse Moloney leukemia cells. Specificity and distribution according to genotype. European Journal of Immunology *5*, 112–117. https://doi.org/10.1002/eji.1830050208.

Kim, E.-M., Bae, Y.M., Choi, M.-H., and Hong, S.-T. (2012). Cyst formation, increased anti-inflammatory cytokines and expression of chemokines support for Clonorchis sinensis infection in FVB mice. Parasitol Int *61*, 124–129. https://doi.org/10.1016/j.parint.2011.07.001.

Kirstein, J.M., Graham, K.C., Mackenzie, L.T., Johnston, D.E., Martin, L.J., Tuck, A.B., MacDonald, I.C., and Chambers, A.F. (2009). Effect of anti-fibrinolytic therapy on experimental melanoma metastasis. Clin. Exp. Metastasis *26*, 121–131. https://doi.org/10.1007/s10585-008-9221-z.

Konecny, G.E., and Kristeleit, R.S. (2016). PARP inhibitors for *BRCA1/2*-mutated and sporadic ovarian cancer: current practice and future directions. British Journal of Cancer *115*, 1157–1173. https://doi.org/10.1038/bjc.2016.311.

Koyama, T., Hall, L.R., Haser, W.G., Tonegawa, S., and Saito, H. (1987). Structure of a cytotoxic T-lymphocyte-specific gene shows a strong homology to fibrinogen beta and gamma chains. Proc. Natl. Acad. Sci. U.S.A. *84*, 1609–1613. https://doi.org/doi: 10.1073/pnas.84.6.1609.

Kreuzinger, C., Geroldinger, A., Smeets, D., Braicu, E.I., Sehouli, J., Koller, J., Wolf, A., Darb-Esfahani, S., Joehrens, K., Vergote, I., et al. (2017). A complex network of tumor microenvironment in human high-grade serous ovarian cancer. Clin. Cancer Res. *23*, 7621–7632. https://doi.org/10.1158/1078-0432.CCR-17-1159.

Kroeger, D.R., Milne, K., and Nelson, B.H. (2016). Tumor-Infiltrating plasma cells are associated with tertiary lymphoid structures, cytolytic t-cell responses, and superior prognosis in ovarian cancer. Clin Cancer Res *22*, 3005–3015. https://doi.org/10.1158/1078-0432.CCR-15-2762.

Lal, N., White, B.S., Goussous, G., Pickles, O., Mason, M.J., Beggs, A.D., Taniere, P., Willcox, B.E., Guinney, J., and Middleton, G.W. (2018). KRAS mutation and Consensus Molecular Subtypes 2 and 3 are independently associated with reduced immune infiltration and reactivity in colorectal cancer. Clin Cancer Res *24*, 224–233. https://doi.org/10.1158/1078-0432.CCR-17-1090.

Lambrechts, D., Wauters, E., Boeckx, B., Aibar, S., Nittner, D., Burton, O., Bassez, A., Decaluwé, H., Pircher, A., Van den Eynde, K., et al. (2018). Phenotype molding of stromal cells in the lung tumor microenvironment. Nat Med *24*, 1277–1289. https://doi.org/10.1038/s41591-018-0096-5.

Lan, C., Huang, X., Lin, S., Huang, H., Cai, Q., Wan, T., Lu, J., and Liu, J. (2013). Expression of M2-polarized macrophages is associated with poor prognosis for advanced epithelial ovarian cancer. Technol. Cancer Res. Treat. *12*, 259–267. https://doi.org/10.7785/tcrt.2012.500312.

Latha, K., Yan, J., Yang, Y., Gressot, L.V., Kong, L.-Y., Manyam, G., Ezhilarasan, R., Wang, Q., Sulman, E.P., Eric Davis, R., et al. (2019). The Role of Fibrinogen-Like Protein 2 on Immunosuppression and Malignant Progression in Glioma. J Natl Cancer Inst *111*, 292–300. https://doi.org/10.1093/jnci/djy107.

Lawrenson, K., Fonseca, M.A.S., Liu, A.Y., Segato Dezem, F., Lee, J.M., Lin, X., Corona, R.I., Abbasi, F., Vavra, K.C., Dinh, H.Q., et al. (2019). A study of high-grade serous ovarian cancer origins implicates the SOX18 transcription factor in tumor development. Cell Rep *29*, 3726-3735.e4. https://doi.org/10.1016/j.celrep.2019.10.122.

Le, D.T., Durham, J.N., Smith, K.N., Wang, H., Bartlett, B.R., Aulakh, L.K., Lu, S., Kemberling, H., Wilt, C., Luber, B.S., et al. (2017). Mismatch-repair deficiency predicts response of solid tumors to PD-1 blockade. Science *357*, 409–413. https://doi.org/10.1126/science.aan6733.

Lechner, M.G., Karimi, S.S., Barry-Holson, K., Angell, T.E., Murphy, K.A., Church, C.H., Ohlfest, J.R., Hu, P., and Epstein, A.L. (2013). Immunogenicity of murine solid tumor models as a defining feature of in vivo behavior and response to immunotherapy. J Immunother *36*, 477–489. https://doi.org/10.1097/01.cji.0000436722.46675.4a.

Lee, H.-O., Hong, Y., Etlioglu, H.E., Cho, Y.B., Pomella, V., Van den Bosch, B., Vanhecke, J., Verbandt, S., Hong, H., Min, J.-W., et al. (2020). Lineage-dependent gene expression programs influence the immune landscape of colorectal cancer. Nat Genet *52*, 594–603. https://doi.org/10.1038/s41588-020-0636-z.

Lee, J.-C., Lee, K.-M., Kim, D.-W., and Heo, D.S. (2004). Elevated TGF-beta1 secretion and down-modulation of NKG2D underlies impaired NK cytotoxicity in cancer patients. J Immunol *172*, 7335–7340. https://doi.org/10.4049/jimmunol.172.12.7335.

Lee, N., Zakka, L.R., Mihm, M.C., and Schatton, T. (2016). Tumour-infiltrating lymphocytes in melanoma prognosis and cancer immunotherapy. Pathology *48*, 177–187. https://doi.org/10.1016/j.pathol.2015.12.006.

Lemay, C.G., Rintoul, J.L., Kus, A., Paterson, J.M., Garcia, V., Falls, T.J., Ferreira, L., Bridle, B.W., Conrad, D.P., Tang, V.A., et al. (2012). Harnessing oncolytic virus-mediated antitumor immunity in an infected cell vaccine. Molecular Therapy *20*, 1791–1799. https://doi.org/10.1038/mt.2012.128.

Levy, G.A., Liu, M., Ding, J., Yuwaraj, S., Leibowitz, J., Marsden, P.A., Ning, Q., Kovalinka, A., and Phillips, M.J. (2000). Molecular and functional analysis of the human prothrombinase gene (HFGL2) and its role in viral hepatitis. Am J Pathol *156*, 1217–1225. https://doi.org/doi: 10.1016/S0002-9440(10)64992-9.

Li, A., Herbst, R.H., Canner, D., Schenkel, J.M., Smith, O.C., Kim, J.Y., Hillman, M., Bhutkar, A., Cuoco, M.S., Rappazzo, C.G., et al. (2019). IL-33 signaling alters regulatory t cell diversity in support of tumor development. Cell Reports *29*, 2998-3008.e8. https://doi.org/10.1016/j.celrep.2019.10.120.

Li, C., Fung, L.S., Chung, S., Crow, A., Myers-Mason, N., Phillips, M.J., Leibowitz, J.L., Cole, E., Ottaway, C.A., and Levy, G. (1992). Monoclonal antiprothrombinase (3D4.3) prevents mortality from murine hepatitis virus (MHV-3) infection. J Exp Med *176*, 689–697. https://doi.org/10.1084/jem.176.3.689.

Li, H., Zhang, G.-X., Chen, Y., Xu, H., Fitzgerald, D.C., Zhao, Z., and Rostami, A. (2008). CD11c+ CD11b+ dendritic cells play an important role in intravenous tolerance and the suppression of experimental autoimmune encephalomyelitis. J Immunol *181*, 2483–2493. https://doi.org/10.4049/jimmunol.181.4.2483.

Li, T., Chen, R.-R., Gong, H.-P., Wang, B.-F., Wu, X.-X., Chen, Y.-Q., and Huang, Z.-M. (2020). FGL2 regulates IKK/NF-κB signaling in intestinal epithelial cells and lamina propria dendritic cells to attenuate dextran sulfate sodium-induced colitis. Mol. Immunol. *117*, 84–93. https://doi.org/10.1016/j.molimm.2019.11.001.

Li, W., Wang, H., Wang, J., LV, F., Zhu, X., and Wang, Z. (2012). Ovarian metastases resection from extragenital primary sites: outcome and prognostic factor analysis of 147 patients. BMC Cancer *12*, 278. https://doi.org/10.1186/1471-2407-12-278.

Li, W.-Z., Wang, J., Long, R., Su, G.-H., Bukhory, D.-K., Dai, J., Jin, N., Huang, S.-Y., Jia, P., Li, T., et al. (2014). Novel antibody against a glutamic acid-rich human fibrinogen-like protein 2-derived peptide near Ser91 Inhibits hfgl2 prothrombinase activity. PLoS One *9*. https://doi.org/10.1371/journal.pone.0094551.

Li, W.-Z., Yang, Y., Liu, K., Long, R., Jin, N., Huang, S.-Y., You, Y., Dai, J., Fan, C., Wang, J., et al. (2018). FGL2 prothrombinase contributes to the early stage of coronary microvascular obstruction through a fibrin-dependent pathway. International Journal of Cardiology https://doi.org/10.1016/j.ijcard.2018.09.051.

Li, X.L., Ménoret, S., Bezie, S., Caron, L., Chabannes, D., Hill, M., Halary, F., Angin, M., Heslan, M., Usal, C., et al. (2010). Mechanism and localization of CD8 regulatory T Cells in a heart transplant model of tolerance. The Journal of Immunology *185*, 823–833. https://doi.org/10.4049/jimmunol.1000120.

Lichty, B.D., Breitbach, C.J., Stojdl, D.F., and Bell, J.C. (2014). Going viral with cancer immunotherapy. Nat. Rev. Cancer *14*, 559–567. https://doi.org/10.1038/nrc3770.

Lin, H., Chen, R., Jiang, X., Wu, X., Huang, X., Dong, X., Yang, X., Lin, X., Chen, X., Chen, X., et al. (2017). Elevated fibrinogen-like protein 2 in TNBS-induced colitis mice: Association with Th17 and regulatory T cells. Mol Med Rep *16*, 3445–3454. https://doi.org/10.3892/mmr.2017.7005.

Liu, B.-Q., Bao, Z.-Y., Zhu, J.-Y., and Liu, H. (2021). Fibrinogen-like protein 2 promotes the accumulation of myeloid-derived suppressor cells in the hepatocellular carcinoma tumor microenvironment. Oncol Lett *21*, 47. https://doi.org/10.3892/ol.2020.12308.

Liu, H., Shalev, I., Manuel, J., He, W., Leung, E., Crookshank, J., Liu, M.F., Diao, J., Cattral, M., Clark, D.A., et al. (2008). The FGL2-FcgammaRIIB pathway: a novel mechanism leading to immunosuppression. Eur. J. Immunol. *38*, 3114–3126. https://doi.org/10.1002/eji.200838338.

Liu, H., Yang, P.S., Zhu, T., Manuel, J., Zhang, J., He, W., Shalev, I., Zhang, L., Cybulsky, M.I., Grant, D.R., et al. (2013). Characterization of fibrinogen-like protein 2 (FGL2): monomeric

FGL2 has enhanced immunosuppressive activity in comparison to oligomeric FGL2. Int. J. Biochem. Cell Biol. *45*, 408–418. https://doi.org/10.1016/j.biocel.2012.10.014.

Liu, M., Leibowitz, J.L., Clark, D.A., Mendicino, M., Ning, Q., Ding, J.W., D'Abreo, C., Fung, L., Marsden, P.A., and Levy, G.A. (2003). Gene transcription of fgl2 in endothelial cells is controlled by Ets-1 and Oct-1 and requires the presence of both Sp1 and Sp3. Eur. J. Biochem. *270*, 2274–2286. https://doi.org/10.1046/j.1432-1033.2003.03595.x.

Liu, M., Mendicino, M., Ning, Q., Ghanekar, A., He, W., McGilvray, I., Shalev, I., Pivato, D., Clark, D.A., Phillips, M.J., et al. (2006). Cytokine-induced hepatic apoptosis is dependent on FGL2/fibroleukin: the role of Sp1/Sp3 and STAT1/PU.1 composite cis elements. J. Immunol. *176*, 7028–7038. https://doi.org/10.4049/jimmunol.176.11.7028.

Liu, X., Chu, Y., Wang, D., Weng, Y., and Jia, Z. (2019). MAPK-mediated upregulation of fibrinogen-like protein 2 promotes proliferation, migration, and invasion of colorectal cancer cells. Cell Biology International *43*, 1483–1491. https://doi.org/10.1002/cbin.11198.

Liu, Y., Xu, L., Zeng, Q., Wang, J., Wang, M., Xi, D., Wang, X., Yang, D., Luo, X., and Ning, Q. (2012). Downregulation of FGL2/prothrombinase delays HCCLM6 xenograft tumour growth and decreases tumour angiogenesis. Liver Int. *32*, 1585–1595. https://doi.org/10.1111/j.1478-3231.2012.02865.x.

Lo, C.S., Sanii, S., Kroeger, D.R., Milne, K., Talhouk, A., Chiu, D.S., Rahimi, K., Shaw, P.A., Clarke, B.A., and Nelson, B.H. (2017). Neoadjuvant chemotherapy of ovarian cancer results in three patterns of tumor-infiltrating lymphocyte response with distinct implications for immunotherapy. Clin. Cancer Res. *23*, 925–934. https://doi.org/10.1158/1078-0432.CCR-16-1433.

Lu, Z., Zou, J., Li, S., Topper, M.J., Tao, Y., Zhang, H., Jiao, X., Xie, W., Kong, X., Vaz, M., et al. (2020). Epigenetic therapy inhibits metastases by disrupting premetastatic niches. Nature *579*, 284–290. https://doi.org/10.1038/s41586-020-2054-x.

Luft, O., Khattar, R., Farrokhi, K., Ferri, D., Yavorska, N., Zhang, J., Sadozai, H., Adeyi, O., Chruscinski, A., Levy, G.A., et al. (2018). Inhibition of the Fibrinogen-Like Protein 2:Fcγ RIIB/RIII immunosuppressive pathway enhances antiviral T-cell and B-cell responses leading to clearance of lymphocytic choriomeningitis virus clone 13. Immunology *154*, 476–489. https://doi.org/10.1111/imm.12897.

Makarenkova, V.P., Bansal, V., Matta, B.M., Perez, L.A., and Ochoa, J.B. (2006). CD11b+/Gr-1+ myeloid suppressor cells cause T cell dysfunction after traumatic stress. J Immunol *176*, 2085–2094. https://doi.org/10.4049/jimmunol.176.4.2085.

Malekzadeh, P., Pasetto, A., Robbins, P.F., Parkhurst, M.R., Paria, B.C., Jia, L., Gartner, J.J., Hill, V., Yu, Z., Restifo, N.P., et al. (2021). Neoantigen screening identifies broad *TP53* mutant immunogenicity in patients with epithelial cancers. J Clin Invest *129*. https://doi.org/10.1172/JCI123791.

Marazzi, S., Blum, S., Hartmann, R., Gundersen, D., Schreyer, M., Argraves, S., Fliedner, V. von, Pytela, R., and Rüegg, C. (1998). Characterization of human fibroleukin, a fibrinogen-like protein secreted by T lymphocytes. The Journal of Immunology *161*, 138–147.

Market, M. (2020). TGFβ causes postoperative natural killer cell paralysis through mTOR inhibition. University of Ottawa.

Market, M., Baxter, K.E., Angka, L., Kennedy, M.A., and Auer, R.C. (2018). The Potential for cancer immunotherapy in targeting surgery-induced natural killer cell dysfunction. Cancers (Basel) *11*. https://doi.org/10.3390/cancers11010002.

Marsden, P.A., Ning, Q., Fung, L.S., Luo, X., Chen, Y., Mendicino, M., Ghanekar, A., Scott, J.A., Miller, T., Chan, C.W.Y., et al. (2003). The Fgl2/fibroleukin prothrombinase contributes to immunologically mediated thrombosis in experimental and human viral hepatitis. J. Clin. Invest. *112*, 58–66. https://doi.org/10.1172/JCI18114.

Martin, S.D., Brown, S.D., Wick, D.A., Nielsen, J.S., Kroeger, D.R., Twumasi-Boateng, K., Holt, R.A., and Nelson, B.H. (2016). Low mutation burden in ovarian cancer may limit the utility of neoantigen-targeted vaccines. PLoS ONE *11*, e0155189. https://doi.org/10.1371/journal.pone.0155189.

Martinet, L., Ferrari De Andrade, L., Guillerey, C., Lee, J.S., Liu, J., Souza-Fonseca-Guimaraes, F., Hutchinson, D.S., Kolesnik, T.B., Nicholson, S.E., Huntington, N.D., et al. (2015). DNAM-1 expression marks an alternative program of NK cell maturation. Cell Reports *11*, 85–97. https://doi.org/10.1016/j.celrep.2015.03.006.

Matheoud, D., Baey, C., Vimeux, L., Tempez, A., Valente, M., Louche, P., Bon, A.L., Hosmalin, A., and Feuillet, V. (2011). Dendritic cells crosspresent antigens from live B16 cells more efficiently than from apoptotic cells and protect from melanoma in a therapeutic model. PLOS ONE *6*, e19104. https://doi.org/10.1371/journal.pone.0019104.

Matsushita, N., Ghazizadeh, M., Konishi, H., and Araki, T. (2003). Association of ovarian tumor epithelium coexpressing HLA-DR and CA-125 antigens with tumor infiltrating cytotoxic T lymphocytes. J Nippon Med Sch *70*, 40–44. https://doi.org/10.1272/jnms.70.40.

McCloskey, C.W., Goldberg, R.L., Carter, L.E., Gamwell, L.F., Al-Hujaily, E.M., Collins, O., Macdonald, E.A., Garson, K., Daneshmand, M., Carmona, E., et al. (2014). A new spontaneously transformed syngeneic model of high-grade serous ovarian cancer with a tumor-initiating cell population. Front Oncol *4*, 53. https://doi.org/10.3389/fonc.2014.00053.

McCloskey, C.W., Rodriguez, G.M., Galpin, K.J.C., and Vanderhyden, B.C. (2018). Ovarian cancer immunotherapy: preclinical models and emerging therapeutics. Cancers (Basel) *10*. https://doi.org/10.3390/cancers10080244.

McCool, K.W., Freeman, Z.T., Zhai, Y., Wu, R., Hu, K., Liu, C.-J., Tomlins, S.A., Fearon, E.R., Magnuson, B., Kuick, R., et al. (2020). Murine Oviductal high-grade serous carcinomas mirror the genomic alterations, gene expression profiles, and immune microenvironment of their human counterparts. Cancer Res *80*, 877–889. https://doi.org/10.1158/0008-5472.CAN-19-2558.

McGranahan, N., Furness, A.J.S., Rosenthal, R., Ramskov, S., Lyngaa, R., Saini, S.K., Jamal-Hanjani, M., Wilson, G.A., Birkbak, N.J., Hiley, C.T., et al. (2016). Clonal neoantigens elicit T cell immunoreactivity and sensitivity to immune checkpoint blockade. Science *351*, 1463–1469. https://doi.org/10.1126/science.aaf1490.

Mehta, A., and Merkel, O.M. (2020). Immunogenicity of Cas9 Protein. J Pharm Sci *109*, 62–67. https://doi.org/10.1016/j.xphs.2019.10.003.

Melnyk, M.C., Shalev, I., Zhang, J., Bartczak, A., Gorczynski, R.M., Selzner, N., Inman, R., Marsden, P.A., Phillips, M.J., Clark, D.A., et al. (2011). The prothrombinase activity of FGL2 contributes to the pathogenesis of experimental arthritis. Scand. J. Rheumatol. *40*, 269–278. https://doi.org/10.3109/03009742.2010.536163.

Mendicino, M., Liu, M., Ghanekar, A., He, W., Koscik, C., Shalev, I., Javadi, M., Turnbull, J., Chen, W., Fung, L., et al. (2005). Targeted deletion of Fgl-2/fibroleukin in the donor modulates immunologic response and acute vascular rejection in cardiac xenografts. Circulation *112*, 248–256. https://doi.org/10.1161/CIRCULATIONAHA.105.534271.

Merchand-Reyes, G., Robledo-Avila, F.H., Buteyn, N.J., Gautam, S., Santhanam, R., Fatehchand, K., Mo, X., Partida-Sanchez, S., Butchar, J.P., and Tridandapani, S. (2019). CD31 acts as a checkpoint molecule and is modulated by FcγR-mediated signaling in monocytes. J Immunol *203*, 3216–3224. https://doi.org/10.4049/jimmunol.1900059.

Mittal, D., Gubin, M.M., Schreiber, R.D., and Smyth, M.J. (2014). New insights into cancer immunoediting and its three component phases--elimination, equilibrium and escape. Curr. Opin. Immunol. *27*, 16–25. https://doi.org/10.1016/j.coi.2014.01.004.

Morris, A.B., Farley, C.R., Pinelli, D.F., Adams, L.E., Cragg, M.S., Boss, J.M., Scharer, C.D., Fribourg, M., Cravedi, P., Heeger, P.S., et al. (2020). Signaling through the inhibitory Fc receptor FcγRIIB induces CD8+ T cell apoptosis to limit t cell immunity. Immunity *52*, 136-150.e6. https://doi.org/10.1016/j.immuni.2019.12.006.

Mosely, S.I.S., Prime, J.E., Sainson, R.C.A., Koopmann, J.-O., Wang, D.Y.Q., Greenawalt, D.M., Ahdesmaki, M.J., Leyland, R., Mullins, S., Pacelli, L., et al. (2017). Rational selection of syngeneic preclinical tumor models for immunotherapeutic drug discovery. Cancer Immunology Research *5*, 29–41. https://doi.org/10.1158/2326-6066.CIR-16-0114.

Mundy-Bosse, B.L., Thornton, L.M., Yang, H.-C., Andersen, B.L., and Carson, W.E. (2011). Psychological stress is associated with altered levels of myeloid-derived suppressor cells in breast cancer patients. Cell Immunol *270*, 80–87. https://doi.org/10.1016/j.cellimm.2011.04.003.

Nilsson, M.B., Langley, R.R., and Fidler, I.J. (2005). Interleukin-6, Secreted by human ovarian carcinoma cells, is a potent proangiogenic cytokine. Cancer Res *65*, 10794–10800. https://doi.org/10.1158/0008-5472.CAN-05-0623.

Ning, Q., Sun, Y., Han, M., Zhang, L., Zhu, C., Zhang, W., Guo, H., Li, J., Yan, W., Gong, F., et al. (2005). Role of fibrinogen-like protein 2 prothrombinase/fibroleukin in experimental and human allograft rejection. J. Immunol. *174*, 7403–7411. https://doi.org/10.4049/jimmunol.174.11.7403.

Nounamo, B., Liem, J., Cannon, M., and Liu, J. (2017). Myxoma virus optimizes cisplatin for the treatment of ovarian cancer in vitro and in a syngeneic murine dissemination model. Mol Ther Oncolytics *6*, 90–99. https://doi.org/10.1016/j.omto.2017.08.002.

Oberlies, J., Watzl, C., Giese, T., Luckner, C., Kropf, P., Müller, I., Ho, A.D., and Munder, M. (2009). Regulation of NK cell function by human granulocyte arginase. J Immunol *182*, 5259–5267. https://doi.org/10.4049/jimmunol.0803523.

Offner, F.A., Obrist, P., Stadlmann, S., Feichtinger, H., Klingler, P., Herold, M., Zwierzina, H., Hittmair, A., Mikuz, G., and Abendstein, B. (1995). IL-6 secretion by human peritoneal mesothelial and ovarian cancer cells. Cytokine *7*, 542–547. https://doi.org/10.1006/cyto.1995.0073.

Olson, G.E., Winfrey, V.P., NagDas, S.K., and Melner, M.H. (2004). Region-specific Expression and Secretion of the Fibrinogen-related Protein, fgl2, by Epithelial Cells of the Hamster Epididymis and Its Role in Disposal of Defective Spermatozoa. J. Biol. Chem. *279*, 51266–51274. https://doi.org/10.1074/jbc.M410485200.

Ostapchuk, Y.O., Perfilyeva, Y.V., Kali, A., Tleulieva, R., Yurikova, O.Y., Stanbekova, G.E., Karalnik, B.V., and Belyaev, N.N. (2022). Fc receptor is involved in NK cell functional anergy induced by Miapaca2 tumor cell line. Immunol Invest *51*, 138–153. https://doi.org/10.1080/08820139.2020.1813757.

Overwijk, W.W., and Restifo, N.P. (2001). B16 as a mouse model for human melanoma. Curr Protoc Immunol *CHAPTER*, Unit-20.1. https://doi.org/10.1002/0471142735.im2001s39.

Pagès, F., Galon, J., Dieu-Nosjean, M.-C., Tartour, E., Sautès-Fridman, C., and Fridman, W.-H. (2010). Immune infiltration in human tumors: a prognostic factor that should not be ignored. Oncogene *29*, 1093–1102. https://doi.org/10.1038/onc.2009.416.

Pan, G., Zhao, Z., Tang, C., Ding, L., Li, Z., Zheng, D., Zong, L., and Wu, Z. (2018). Soluble fibrinogen-like protein 2 ameliorates acute rejection of liver transplantation in rat via inducing Kupffer cells M2 polarization. Cancer Med https://doi.org/10.1002/cam4.1528.

Pandey, V., Fleming-Martinez, A., Bastea, L., Doeppler, H.R., Eisenhauer, J., Le, T., Edenfield, B., and Storz, P. (2021). CXCL10/CXCR3 signaling contributes to an inflammatory microenvironment and its blockade enhances progression of murine pancreatic precancerous lesions. ELife *10*, e60646. https://doi.org/10.7554/eLife.60646.

Parr, R.L., Fung, L., Reneker, J., Myers-Mason, N., Leibowitz, J.L., and Levy, G. (1995). Association of mouse fibrinogen-like protein with murine hepatitis virus-induced prothrombinase activity. J. Virol. *69*, 5033–5038. https://doi.org/10.1128/JVI.69.8.5033-5038.1995.

Peng, W., Chen, J.Q., Liu, C., Malu, S., Creasy, C., Tetzlaff, M.T., Xu, C., McKenzie, J.A., Zhang, C., Liang, X., et al. (2016). Loss of PTEN Promotes resistance to T cell-mediated immunotherapy. Cancer Discov *6*, 202–216. https://doi.org/10.1158/2159-8290.CD-15-0283.

Preston, C.C., Maurer, M.J., Oberg, A.L., Visscher, D.W., Kalli, K.R., Hartmann, L.C., Goode, E.L., and Knutson, K.L. (2013). The ratios of CD8+ T cells to CD4+CD25+ FOXP3+ and FOXP3- T cells correlate with poor clinical outcome in human serous ovarian cancer. PLoS ONE *8*, e80063. https://doi.org/10.1371/journal.pone.0080063.

Przybytkowski, E., Davis, T., Hosny, A., Eismann, J., Matulonis, U.A., Wulf, G.M., and Nabavi, S. (2020). An immune-centric exploration of BRCA1 and BRCA2 germline mutation related breast and ovarian cancers. BMC Cancer *20*, 197. https://doi.org/10.1186/s12885-020-6605-1.

Pulkka, O.-P., Viisanen, L., Tynninen, O., Laaksonen, M., Reichardt, P., Reichardt, A., Eriksson, M., Hall, K.S., Wardelmann, E., Nilsson, B., et al. (2022). Fibrinogen-like protein 2 in gastrointestinal stromal tumour. Journal of Cellular and Molecular Medicine *26*, 1083–1094. https://doi.org/10.1111/jcmm.17163.

Qian, J., Olbrecht, S., Boeckx, B., Vos, H., Laoui, D., Etlioglu, E., Wauters, E., Pomella, V., Verbandt, S., Busschaert, P., et al. (2020). A pan-cancer blueprint of the heterogeneous tumor microenvironment revealed by single-cell profiling. Cell Res *30*, 745–762. https://doi.org/10.1038/s41422-020-0355-0.

Qin, W.-Z., Li, Q.-L., Chen, W.-F., Xu, M.-D., Zhang, Y.-Q., Zhong, Y.-S., Ma, L.-L., Hu, J.-W., Cai, M.-Y., He, M.-J., et al. (2014). Overexpression of fibrinogen-like protein 2 induces epithelial-to-mesenchymal transition and promotes tumor progression in colorectal carcinoma. Med. Oncol. *31*, 181. https://doi.org/10.1007/s12032-014-0181-7.

Rabizadeh, E., Cherny, I., Lederfein, D., Sherman, S., Binkovsky, N., Rosenblat, Y., and Inbal, A. (2015). The cell-membrane prothrombinase, fibrinogen-like protein 2, promotes angiogenesis and tumor development. Thromb. Res. *136*, 118–124. https://doi.org/10.1016/j.thromres.2014.11.023.

Rehman, H., Silk, A.W., Kane, M.P., and Kaufman, H.L. (2016). Into the clinic: Talimogene laherparepvec (T-VEC), a first-in-class intratumoral oncolytic viral therapy. J Immunother Cancer *4*, 53. https://doi.org/10.1186/s40425-016-0158-5.

de Rham, C., Ferrari-Lacraz, S., Jendly, S., Schneiter, G., Dayer, J.-M., and Villard, J. (2007). The proinflammatory cytokines IL-2, IL-15 and IL-21 modulate the repertoire of mature human natural killer cell receptors. Arthritis Research & Therapy *9*, R125. https://doi.org/10.1186/ar2336.

Ribas, A., Dummer, R., Puzanov, I., VanderWalde, A., Andtbacka, R.H.I., Michielin, O., Olszanski, A.J., Malvehy, J., Cebon, J., Fernandez, E., et al. (2017). Oncolytic virotherapy promotes intratumoral T cell infiltration and improves anti-PD-1 immunotherapy. Cell *170*, 1109-1119.e10. https://doi.org/10.1016/j.cell.2017.08.027.

Ricca, J.M., Oseledchyk, A., Walther, T., Liu, C., Mangarin, L., Merghoub, T., Wolchok, J.D., and Zamarin, D. (2018). Pre-existing immunity to oncolytic virus potentiates its immunotherapeutic efficacy. Molecular Therapy *26*, 1008–1019. https://doi.org/10.1016/j.ymthe.2018.01.019.

Rizvi, N.A., Hellmann, M.D., Snyder, A., Kvistborg, P., Makarov, V., Havel, J.J., Lee, W., Yuan, J., Wong, P., Ho, T.S., et al. (2015). Mutational landscape determines sensitivity to PD-1 blockade in non–small cell lung cancer. Science *348*, 124–128. https://doi.org/10.1126/science.aaa1348.

Roby, K.F., Taylor, C.C., Sweetwood, J.P., Cheng, Y., Pace, J.L., Tawfik, O., Persons, D.L., Smith, P.G., and Terranova, P.F. (2000). Development of a syngeneic mouse model for events related to ovarian cancer. Carcinogenesis *21*, 585–591. https://doi.org/10.1093/carcin/21.4.585.

Rodriguez, G.M., Galpin, K.J.C., McCloskey, C.W., and Vanderhyden, B.C. (2018). The Tumor microenvironment of epithelial ovarian cancer and its influence on response to immunotherapy. Cancers (Basel) *10*. https://doi.org/10.3390/cancers10080242.

Rodriguez, G.M., Galpin, K.J.C., Cook, D.P., Yakubovich, E., Maranda, V., Macdonald, E.A., Wilson-Sanchez, J., Thomas, A.L., Burdette, J.E., and Vanderhyden, B.C. (2022). The Tumor immune profile of murine ovarian cancer models: an essential tool for ovarian cancer immunotherapy research. Cancer Research Communications *2*, 417–433. https://doi.org/10.1158/2767-9764.CRC-22-0017.

Rüegg, C., and Pytela, R. (1995). Sequence of a human transcript expressed in T-lymphocytes and encoding a fibrinogen-like protein. Gene *160*, 257–262. https://doi.org/10.1016/0378-1119(95)00240-7.

Santoiemma, P.P., and Powell, D.J. (2015). Tumor infiltrating lymphocytes in ovarian cancer. Cancer Biol. Ther. *16*, 807–820. https://doi.org/10.1080/15384047.2015.1040960.

Santoiemma, P.P., Reyes, C., Wang, L.-P., McLane, M.W., Feldman, M.D., Tanyi, J.L., and Powell, D.J. (2016). Systematic evaluation of multiple immune markers reveals prognostic factors in ovarian cancer. Gynecol. Oncol. *143*, 120–127. https://doi.org/10.1016/j.ygyno.2016.07.105.

Sato, E., Olson, S.H., Ahn, J., Bundy, B., Nishikawa, H., Qian, F., Jungbluth, A.A., Frosina, D., Gnjatic, S., Ambrosone, C., et al. (2005). Intraepithelial CD8+ tumor-infiltrating lymphocytes and a high CD8+/regulatory T cell ratio are associated with favorable prognosis in ovarian cancer. PNAS *102*, 18538–18543. https://doi.org/10.1073/pnas.0509182102.

Schatton, T., Scolyer, R.A., Thompson, J.F., and Mihm, M.C. (2014). Tumor-infiltrating lymphocytes and their significance in melanoma prognosis. Methods Mol Biol *1102*, 287–324. https://doi.org/10.1007/978-1-62703-727-3_16.

Schreiber, R.D., Old, L.J., and Smyth, M.J. (2011). Cancer immunoediting: integrating immunity's roles in cancer suppression and promotion. Science *331*, 1565–1570. https://doi.org/10.1126/science.1203486.

Seth, R., Tai, L.-H., Falls, T., de Souza, C.T., Bell, J.C., Carrier, M., Atkins, H., Boushey, R., and Auer, R.A. (2013). Surgical stress promotes the development of cancer metastases by a coagulation-dependent mechanism involving natural killer cells in a murine model. Ann. Surg. *258*, 158–168. https://doi.org/10.1097/SLA.0b013e31826fcbdb.

Shalev, I., Liu, H., Koscik, C., Bartczak, A., Javadi, M., Wong, K.M., Maknojia, A., He, W., Liu, M.F., Diao, J., et al. (2008). Targeted deletion of fgl2 leads to impaired regulatory T cell activity and development of autoimmune glomerulonephritis. J. Immunol. *180*, 249–260. https://doi.org/10.4049/jimmunol.180.1.249.

Shalev, I., Wong, K.M., Foerster, K., Zhu, Y., Chan, C., Maknojia, A., Zhang, J., Ma, X.-Z., Yang, X.C., Gao, J.F., et al. (2009). The novel CD4+CD25+ regulatory T cell effector molecule fibrinogen-like protein 2 contributes to the outcome of murine fulminant viral hepatitis. Hepatology *49*, 387–397. https://doi.org/10.1002/hep.22684.

Snyder, A., Makarov, V., Merghoub, T., Yuan, J., Zaretsky, J.M., Desrichard, A., Walsh, L.A., Postow, M.A., Wong, P., Ho, T.S., et al. (2014). Genetic basis for clinical response to ctla-4 blockade in melanoma. New England Journal of Medicine *371*, 2189–2199. https://doi.org/10.1056/NEJMoa1406498.

Song, J., and Deng, T. (2020). The adipocyte and adaptive immunity. Frontiers in Immunology *11*, 3052. https://doi.org/10.3389/fimmu.2020.593058.

Song, Z., Wang, Y., Du, Y., Zhang, Z., and Yuan, Y. (2020). Identification of integrative molecular and clinical profiles of Fibrinogen-like protein 2 in gliomas using 1323 samples. Int Immunopharmacol *88*, 106894. https://doi.org/10.1016/j.intimp.2020.106894.

Sorensen, M.R., Pedersen, S.R., Lindkvist, A., Christensen, J.P., and Thomsen, A.R. (2014). Quantification of B16 melanoma cells in lungs using triplex q-pcr - a new approach to evaluate melanoma cell metastasis and tumor control. PLOS ONE *9*, e87831. https://doi.org/10.1371/journal.pone.0087831.

Sosman, J.A., Moon, J., Tuthill, R.J., Warneke, J.A., Vetto, J.T., Redman, B.G., Liu, P.Y., Unger, J.M., Flaherty, L.E., and Sondak, V.K. (2011). A Phase II trial of complete resection for stage iv melanoma: results of southwest oncology group (SWOG) Clinical Trial S9430. Cancer *117*, 4740–4706. https://doi.org/10.1002/cncr.26111.

Spranger, S., Koblish, H.K., Horton, B., Scherle, P.A., Newton, R., and Gajewski, T.F. (2014). Mechanism of tumor rejection with doublets of CTLA-4, PD-1/PD-L1, or IDO blockade involves restored IL-2 production and proliferation of CD8+ T cells directly within the tumor microenvironment. Journal for ImmunoTherapy of Cancer *2*, 3. https://doi.org/10.1186/2051-1426-2-3.

Stojdl, D.F., Lichty, B.D., tenOever, B.R., Paterson, J.M., Power, A.T., Knowles, S., Marius, R., Reynard, J., Poliquin, L., Atkins, H., et al. (2003). VSV strains with defects in their ability to shutdown innate immunity are potent systemic anti-cancer agents. Cancer Cell *4*, 263–275. https://doi.org/10.1016/S1535-6108(03)00241-1.

Strickland, K.C., Howitt, B.E., Shukla, S.A., Rodig, S., Ritterhouse, L.L., Liu, J.F., Garber, J.E., Chowdhury, D., Wu, C.J., D'Andrea, A.D., et al. (2016). Association and prognostic significance of BRCA1/2-mutation status with neoantigen load, number of tumor-infiltrating lymphocytes and expression of PD-1/PD-L1 in high grade serous ovarian cancer. Oncotarget *7*, 13587–13598. https://doi.org/10.18632/oncotarget.7277.

Su, K., Chen, F., Yan, W.-M., Zeng, Q.-L., Xu, L., Xi, D., Pi, B., Luo, X.-P., and Ning, Q. (2008). Fibrinogen-like protein 2/fibroleukin prothrombinase contributes to tumor hypercoagulability via IL-2 and IFN-gamma. World J. Gastroenterol. *14*, 5980–5989. https://doi.org/0.3748/wjg.14.5980.

Sugama, Y., Tiruppathi, C., offakidevi, K., Andersen, T.T., Fenton, J.W., and Malik, A.B. (1992). Thrombin-induced expression of endothelial P-selectin and intercellular adhesion molecule-1: a mechanism for stabilizing neutrophil adhesion. J Cell Biol *119*, 935–944. https://doi.org/10.1083/jcb.119.4.935.

Sun, Y., Xi, D., Ding, W., Wang, F., Zhou, H., and Ning, Q. (2014). Soluble FGL2, a novel effector molecule of activated hepatic stellate cells, regulates T-cell function in cirrhotic patients with hepatocellular carcinoma. Hepatol Int *8*, 567–575. https://doi.org/10.1007/s12072-014-9568-y.

Sungnak, W., Wagner, A., Kowalczyk, M.S., Bod, L., Kye, Y.-C., Sage, P.T., Sharpe, A.H., Sobel, R.A., Quintana, F.J., Rozenblatt-Rosen, O., et al. (2020). TFR-derived Fibrinogen-like Protein 2 regulates production of autoantibodies and induction of systemic autoimmunity. J Immunol *205*, 3247–3262. https://doi.org/10.4049/jimmunol.2000748.

Swart, M., Verbrugge, I., and Beltman, J.B. (2016). Combination approaches with immune-checkpoint blockade in cancer therapy. Front Oncol *6*. https://doi.org/10.3389/fonc.2016.00233.

Tai, L.-H., de Souza, C.T., Bélanger, S., Ly, L., Alkayyal, A.A., Zhang, J., Rintoul, J.L., Ananth, A.A., Lam, T., Breitbach, C.J., et al. (2013). Preventing postoperative metastatic disease by inhibiting surgery-induced dysfunction in natural killer cells. Cancer Res. *73*, 97–107. https://doi.org/10.1158/0008-5472.CAN-12-1993.

Tai, L.-H., Alkayyal, A.A., Leslie, A.L., Sahi, S., Bennett, S., Souza, C.T. de, Baxter, K., Angka, L., Xu, R., Kennedy, M.A., et al. (2018). Phosphodiesterase-5 inhibition reduces postoperative metastatic disease by targeting surgery-induced myeloid derived suppressor cell-dependent inhibition of Natural Killer cell cytotoxicity. OncoImmunology *7*, e1431082. https://doi.org/10.1080/2162402X.2018.1431082.

Tanda, E.T., Vanni, I., Boutros, A., Andreotti, V., Bruno, W., Ghiorzo, P., and Spagnolo, F. (2020). Current state of target treatment in braf mutated melanoma. Frontiers in Molecular Biosciences *7*. https://doi.org/10.3389/fmolb.2020.00154.

Tang, M., Cao, X., Li, P., Zhang, K., Li, Y., Zheng, Q., Li, G., Chen, J., Xu, G., and Zhang, K. (2017). Increased expression of Fibrinogen-Like Protein 2 is associated with poor prognosis in patients with clear cell renal cell carcinoma. Scientific Reports *7*, 12676. https://doi.org/10.1038/s41598-017-13149-x.

Tewari, K.S., Burger, R.A., Enserro, D., Norquist, B.M., Swisher, E.M., Brady, M.F., Bookman, M.A., Fleming, G.F., Huang, H., Homesley, H.D., et al. (2019). Final overall survival of a randomized trial of bevacizumab for primary treatment of ovarian cancer. JCO *37*, 2317–2328. https://doi.org/10.1200/JCO.19.01009.

Thomas, E.D., Meza-Perez, S., Bevis, K.S., Randall, T.D., Gillespie, G.Y., Langford, C., and Alvarez, R.D. (2016). IL-12 Expressing oncolytic herpes simplex virus promotes anti-tumor activity and immunologic control of metastatic ovarian cancer in mice. J Ovarian Res *9*. https://doi.org/10.1186/s13048-016-0282-3.

Thomas, N.E., Busam, K.J., From, L., Kricker, A., Armstrong, B.K., Anton-Culver, H., Gruber, S.B., Gallagher, R.P., Zanetti, R., Rosso, S., et al. (2013). Tumor-infiltrating lymphocyte grade in primary melanomas is independently associated with melanoma-specific survival in the population-based genes, environment and melanoma study. J Clin Oncol *31*, 4252–4259. https://doi.org/10.1200/JCO.2013.51.3002.

Tsuchiya, Y., Sawada, S., Yoshioka, I., Ohashi, Y., Matsuo, M., Harimaya, Y., Tsukada, K., and Saiki, I. (2003). Increased surgical stress promotes tumor metastasis. Surgery *133*, 547–555. https://doi.org/10.1067/msy.2003.141.

Tumilasci, V.F., Olière, S., Nguyên, T.L.-A., Shamy, A., Bell, J., and Hiscott, J. (2008). Targeting the apoptotic pathway with BCL-2 inhibitors sensitizes primary chronic lymphocytic leukemia cells to vesicular stomatitis virus-induced oncolysis. J Virol *82*, 8487–8499. https://doi.org/10.1128/JVI.00851-08.

Tyzzer, E.E. (1913). Factors in the production and growth of tumor metastases. J Med Res *28*, 309-332.1. .

Urakawa, S., Yamasaki, M., Goto, K., Haruna, M., Hirata, M., Morimoto-Okazawa, A., Kawashima, A., Iwahori, K., Makino, T., Kurokawa, Y., et al. (2019). Peri-operative monocyte count is a marker of poor prognosis in gastric cancer: increased monocytes are a characteristic of myeloid-derived suppressor cells. Cancer Immunol Immunother *68*, 1341–1350. https://doi.org/10.1007/s00262-019-02366-0.

Urbanellis, P., Shyu, W., Khattar, R., Wang, J., Zakharova, A., He, W., Sadozai, H., Amir, A.Z., Shalev, I., Phillips, M.J., et al. (2015). The regulatory T cell effector molecule fibrinogen-like protein 2 is necessary for the development of rapamycin-induced tolerance to fully MHC-mismatched murine cardiac allografts. Immunology *144*, 91–106. https://doi.org/10.1111/imm.12354.

Van Allen, E.M., Miao, D., Schilling, B., Shukla, S.A., Blank, C., Zimmer, L., Sucker, A., Hillen, U., Foppen, M.H.G., Goldinger, S.M., et al. (2015). Genomic correlates of response to CTLA-4 blockade in metastatic melanoma. Science *350*, 207–211. https://doi.org/10.1126/science.aad0095.

Van Tong, H., Van Ba, N., Hoan, N.X., Binh, M.T., Quyen, D.T., Son, H.A., Van Luong, H., Quyet, D., Meyer, C.G., Song, L.H., et al. (2018). Soluble fibrinogen-like protein 2 levels in patients with hepatitis B virus-related liver diseases. BMC Infect Dis *18*. https://doi.org/10.1186/s12879-018-3473-2.

Varga, A., Piha-Paul, S., Ott, P.A., Mehnert, J.M., Berton-Rigaud, D., Morosky, A., Yang, P., Ruman, J., and Matei, D. (2019). Pembrolizumab in patients with programmed death ligand 1–positive advanced ovarian cancer: Analysis of KEYNOTE-028. Gynecologic Oncology *152*, 243–250. https://doi.org/10.1016/j.ygyno.2018.11.017.

Villani, A.-C., Satija, R., Reynolds, G., Sarkizova, S., Shekhar, K., Fletcher, J., Griesbeck, M., Butler, A., Zheng, S., Lazo, S., et al. (2017). Single-cell RNA-seq reveals new types of human blood dendritic cells, monocytes, and progenitors. Science *356*, eaah4573. https://doi.org/10.1126/science.aah4573.

Vivier, E., Tomasello, E., Baratin, M., Walzer, T., and Ugolini, S. (2008). Functions of natural killer cells. Nat Immunol *9*, 503–510. https://doi.org/10.1038/ni1582.

van Vloten, J.P., Santry, L.A., McAusland, T.M., Karimi, K., McFadden, G., Petrik, J.J., Wootton, S.K., and Bridle, B.W. (2019). Quantifying antigen-specific t cell responses when using antigen-agnostic immunotherapies. Mol Ther Methods Clin Dev *13*, 154–166. https://doi.org/10.1016/j.omtm.2019.01.012.

Walton, J., Blagih, J., Ennis, D., Leung, E., Dowson, S., Farquharson, M., Tookman, L.A., Orange, C., Athineos, D., Mason, S., et al. (2016). CRISPR/Cas9-Mediated Trp53 and Brca2 knockout to generate improved murine models of ovarian high-grade serous carcinoma. Cancer Res *76*, 6118–6129. https://doi.org/10.1158/0008-5472.CAN-16-1272.

Walton, J.B., Farquharson, M., Mason, S., Port, J., Kruspig, B., Dowson, S., Stevenson, D., Murphy, D., Matzuk, M., Kim, J., et al. (2017). CRISPR/Cas9-derived models of ovarian high grade serous carcinoma targeting Brca1, Pten and Nf1, and correlation with platinum sensitivity. Sci Rep *7*. https://doi.org/10.1038/s41598-017-17119-1.

Wang, J., Vuitton, D.A., Müller, N., Hemphill, A., Spiliotis, M., Blagosklonov, O., Grandgirard, D., Leib, S.L., Shalev, I., Levy, G., et al. (2015). Deletion of Fibrinogen-like Protein 2 (FGL-2), a Novel CD4+ CD25+ Treg Effector Molecule, Leads to Improved Control of Echinococcus multilocularis Infection in Mice. PLoS Negl Trop Dis *9*, e0003755. https://doi.org/10.1371/journal.pntd.0003755.

Wang, J., Yang, L., Yu, L., Wang, Y.-Y., Chen, R., Qian, J., Hong, Z.-P., and Su, X.-S. (2017). Surgery-induced monocytic myeloid-derived suppressor cells expand regulatory T cells in lung cancer. Oncotarget *8*, 17050–17058. https://doi.org/10.18632/oncotarget.14991.

Wang, M., Liu, J., Xi, D., Luo, X., and Ning, Q. (2016). Adenovirus-mediated artificial microRNA against human fibrinogen like protein 2 inhibits hepatocellular carcinoma growth. J Gene Med *18*, 102–111. https://doi.org/10.1002/jgm.2883.

Wang, Y., Yan, K., Lin, J., Li, J., and Bi, J. (2021). Macrophage M2 co-expression factors correlate with the immune microenvironment and predict outcome of renal clear cell carcinoma. Front Genet *12*, 615655. https://doi.org/10.3389/fgene.2021.615655.

Watanabe, H., Numata, K., Ito, T., Takagi, K., and Matsukawa, A. (2004). Innate immune response in Th1- and Th2-dominant mouse strains. Shock *22*, 460–466. https://doi.org/10.1097/01.shk.0000142249.08135.e9.

Wculek, S.K., Cueto, F.J., Mujal, A.M., Melero, I., Krummel, M.F., and Sancho, D. (2020). Dendritic cells in cancer immunology and immunotherapy. Nat Rev Immunol *20*, 7–24. https://doi.org/10.1038/s41577-019-0210-z.

Wei, H., Zhao, L., Li, W., Fan, K., Qian, W., Hou, S., Wang, H., Dai, M., Hellstrom, I., Hellstrom, K.E., et al. (2013). Combinatorial PD-1 blockade and CD137 activation has therapeutic efficacy in murine cancer models and synergizes with cisplatin. PLoS ONE *8*, e84927. https://doi.org/10.1371/journal.pone.0084927.

Weigent, D.A., Stanton, G.J., and Johnson, H.M. (1983). Interleukin 2 enhances natural killer cell activity through induction of gamma interferon. Infect Immun *41*, 992–997. .

Wensveen, F.M., Jelenčić, V., and Polić, B. (2018). NKG2D: A master regulator of immune cell responsiveness. Frontiers in Immunology *9*. https://doi.org/10.3389/fimmu.2018.00441.

Wing, K., Ekmark, A., Karlsson, H., Rudin, A., and Suri-Payer, E. (2002). Characterization of human CD25+ CD4+ T cells in thymus, cord and adult blood. Immunology *106*, 190–199. https://doi.org/10.1046/j.1365-2567.2002.01412.x.

Winkler, J., Abisoye-Ogunniyan, A., Metcalf, K.J., and Werb, Z. (2020). Concepts of extracellular matrix remodelling in tumour progression and metastasis. Nat Commun *11*, 5120. https://doi.org/10.1038/s41467-020-18794-x.

Wu, S., Li, M., Xu, F., Li, G., Han, B., He, X., Li, S., He, Q., Lai, X., Zhou, S., et al. (2020). Fibrinogen-like protein 2 deficiency aggravates renal fibrosis by facilitating macrophage polarization. Biomedicine & Pharmacotherapy *130*, 110468. https://doi.org/10.1016/j.biopha.2020.110468.

Xie, L., Ichimaru, N., Morita, M., Chen, J., Zhu, P., Wang, J., Urbanellis, P., Shalev, I., Nagao, S., Sugioka, A., et al. (2012). Identification of a novel biomarker gene set with sensitivity and specificity for distinguishing between allograft rejection and tolerance. Liver Transpl. *18*, 444–454. https://doi.org/10.1002/lt.22480.

Yan, J., Kong, L.-Y., Hu, J., Gabrusiewicz, K., Dibra, D., Xia, X., Heimberger, A.B., and Li, S. (2015). FGL2 as a multimodality regulator of tumor-mediated immune suppression and therapeutic target in gliomas. J. Natl. Cancer Inst. *107*. https://doi.org/10.1093/jnci/djv137.

Yan, J., Zhao, Q., Gabrusiewicz, K., Kong, L.-Y., Xia, X., Wang, J., Ott, M., Xu, J., Davis, R.E., Huo, L., et al. (2019). FGL2 promotes tumor progression in the CNS by suppressing CD103 + dendritic cell differentiation. Nature Communications *10*, 448. https://doi.org/10.1038/s41467-018-08271-x.

Yan, J., Zhao, Q., Wang, J., Tian, X., Wang, J., Xia, X., Ott, M., Rao, G., Heimberger, A.B., and Li, S. (2021). FGL2-wired macrophages secrete CXCL7 to regulate the stem-like functionality of glioma cells. Cancer Lett *506*, 83–94. https://doi.org/10.1016/j.canlet.2021.02.021.

Yang, C., Chen, Y., Guo, G., Li, H., Cao, D., Xu, H., Guo, S., Fei, L., Yan, W., Ning, Q., et al. (2013). Expression of B and T lymphocyte attenuator (BTLA) in macrophages contributes to the fulminant hepatitis caused by murine hepatitis virus strain-3. Gut *62*, 1204–1213. https://doi.org/10.1136/gutjnl-2012-302239.

Yang, M., Zhang, Z., Chen, J., Xu, M., Huang, J., Wang, M., Li, W., Wan, X., Yuen, M.-F., Luo, X., et al. (2019). Soluble fibrinogen-like protein 2 promotes the growth of hepatocellular carcinoma via attenuating dendritic cell-mediated cytotoxic T cell activity. Journal of Experimental & Clinical Cancer Research *38*, 351. https://doi.org/10.1186/s13046-019-1326-5.

Yang, R., Cai, Z., Zhang, Y., Yutzy, W.H., Roby, K.F., and Roden, R.B.S. (2006). CD80 in immune suppression by mouse ovarian carcinoma-associated Gr-1+CD11b+ myeloid cells. Cancer Res. *66*, 6807–6815. https://doi.org/10.1158/0008-5472.CAN-05-3755.

Ye, X., Ding, J., Chen, Y., and Dong, J. (2017). Adenovirus-mediated artificial microRNA targeting fibrinogen-like protein 2 attenuates the severity of acute pancreatitis in mice. Biosci. Rep. https://doi.org/10.1042/BSR20170964.

Yu, J.W., Bhattacharya, S., Yanamandra, N., Kilian, D., Shi, H., Yadavilli, S., Katlinskaya, Y., Kaczynski, H., Conner, M., Benson, W., et al. (2018). Tumor-immune profiling of murine syngeneic tumor models as a framework to guide mechanistic studies and predict therapy response in distinct tumor microenvironments. PLoS One *13*. https://doi.org/10.1371/journal.pone.0206223.

Yu, M., Su, Z., Huang, X., and Wang, X. (2021). Single-Cell sequencing reveals the novel role of Ezh2 in NK cell maturation and function. Frontiers in Immunology *12*.

Yu, X., Harden, K., Gonzalez, L.C., Francesco, M., Chiang, E., Irving, B., Tom, I., Ivelja, S., Refino, C.J., Clark, H., et al. (2009). The surface protein TIGIT suppresses T cell activation by promoting the generation of mature immunoregulatory dendritic cells. Nat Immunol *10*, 48–57. https://doi.org/10.1038/ni.1674.

Yu, Y.-R.A., O'Koren, E.G., Hotten, D.F., Kan, M.J., Kopin, D., Nelson, E.R., Que, L., and Gunn, M.D. (2016). A Protocol for the Comprehensive Flow Cytometric Analysis of Immune Cells in Normal and Inflamed Murine Non-Lymphoid Tissues. PLOS ONE *11*, e0150606. https://doi.org/10.1371/journal.pone.0150606.

Yuan, B., Huang, S., Gong, S., Wang, F., Lin, L., Su, T., Sheng, H., Shi, H., Ma, K., and Yang, Z. (2016). Programmed death (PD)-1 attenuates macrophage activation and brain inflammation via regulation of fibrinogen-like protein 2 (Fgl-2) after intracerebral hemorrhage in mice. Immunol. Lett. *179*, 114–121. https://doi.org/10.1016/j.imlet.2016.10.001.

Yuan, K., Feng, Y., Wang, H., Zhao, L., Wang, W., Wang, T., Feng, Y., Huang, G., and Xu, A. (2020a). FGL2 is positively correlated with enhanced antitumor responses mediated by T cells in lung adenocarcinoma. PeerJ *8*. https://doi.org/10.7717/peerj.8654.

Yuan, X., Li, Y., Zhang, A.Z., Jiang, C.H., Li, F.P., Xie, Y.F., Li, J.F., Liang, W.H., Zhang, H.J., Liu, C.X., et al. (2020b). Tumor-associated macrophage polarization promotes the progression of esophageal carcinoma. Aging (Albany NY) *13*, 2049–2072. https://doi.org/10.18632/aging.202201.

Yuwaraj, S., Ding, J., Liu, M., Marsden, P.A., and Levy, G.A. (2001). Genomic characterization, localization, and functional expression of fgl2, the human gene encoding fibroleukin: a novel human procoagulant. Genomics *71*, 330–338. https://doi.org/10.1006/geno.2000.6444.

Zacchigna, S., Martinelli, V., Moimas, S., Colliva, A., Anzini, M., Nordio, A., Costa, A., Rehman, M., Vodret, S., Pierro, C., et al. (2018). Paracrine effect of regulatory T cells promotes cardiomyocyte proliferation during pregnancy and after myocardial infarction. Nat Commun *9*, 2432. https://doi.org/10.1038/s41467-018-04908-z.

Zeng, M., Li, Q., Chen, J., Huang, W., Liu, J., Wang, C., Huang, M., Li, H., Zhou, S., Xie, M., et al. (2022). The Fgl2 interaction with Tyrobp promotes the proliferation of cutaneous squamous cell carcinoma by regulating ERK-dependent autophagy. Int J Med Sci *19*, 195–204. https://doi.org/10.7150/ijms.66929.

Zhan, D., Zhang, C., Long, W., Wei, L., Jin, S., Du, C., Li, Z., Guo, S., Huang, L., Ning, Q., et al. (2021). Intrauterine inflammation induced white matter injury protection by fibrinogen-like protein 2 deficiency in perinatal mice. Pediatr Res *89*, 1706–1714. https://doi.org/10.1038/s41390-020-01211-w.

Zhang, J., Huang, D., Saw, P.E., and Song, E. (2022). Turning cold tumors hot: from molecular mechanisms to clinical applications. Trends in Immunology *43*, 523–545. https://doi.org/10.1016/j.it.2022.04.010.

Zhang, L., Conejo-Garcia, J.R., Katsaros, D., Gimotty, P.A., Massobrio, M., Regnani, G., Makrigiannakis, A., Gray, H., Schlienger, K., Liebman, M.N., et al. (2003). Intratumoral T cells, recurrence, and survival in epithelial ovarian cancer. New England Journal of Medicine *348*, 203–213. https://doi.org/10.1056/NEJMoa020177.

Zhang, X., Ma, J., Li, H., Zhou, L., Liu, Z., Lyu, S., He, Q., and Li, X. (2021). Overexpression of fibrinogen-like protein 2 alleviates acute rejection in rat models of liver transplantation. Ann Transl Med *9*, 408. https://doi.org/10.21037/atm-20-7881.

Zhao, Z., Yang, C., Wang, L., Li, L., Zhao, T., Hu, L., Rong, R., Xu, M., and Zhu, T. (2014). The regulatory T cell effector soluble fibrinogen-like protein 2 induces tubular epithelial cell apoptosis in renal transplantation. Exp Biol Med (Maywood) *239*, 193–201. https://doi.org/10.1177/1535370213514921.

Zheng, Z., Yu, Y., Potla, R., Wu, Y., and Wu, H. (2018). Fibrinogen-like protein-2 causes deterioration in cardiac function in experimental autoimmune myocarditis rats through regulation of programmed death-1 and inflammatory cytokines. Immunology *153*, 246–252. https://doi.org/10.1111/imm.12837.

Zhou, Y., Lei, J., Xie, Q., Wu, L., Jin, S., Guo, B., Wang, X., Yan, G., Zhang, Q., Zhao, H., et al. (2019). Fibrinogen-like protein 2 controls sepsis catabasis by interacting with resolvin Dp5. Science Advances *5*, eaax0629. https://doi.org/10.1126/sciadv.aax0629.

Zhu, C.-L., Yan, W.-M., Zhu, F., Zhu, Y.-F., Xi, D., Tian, D.-Y., Levy, G., Luo, X.-P., and Ning, Q. (2005). Fibrinogen-like protein 2 fibroleukin expression and its correlation with disease progression in murine hepatitis virus type 3-induced fulminant hepatitis and in patients with severe viral hepatitis B. World J. Gastroenterol. *11*, 6936–6940. https://doi.org/10.3748/wjg.v11.i44.6936.

Zhu, Y., Zhang, L., Zha, H., Yang, F., Hu, C., Chen, L., Guo, B., and Zhu, B. (2017). Stroma-derived Fibrinogen-like Protein 2 activates cancer-associated fibroblasts to promote tumor growth in lung cancer. Int. J. Biol. Sci. *13*, 804–814. https://doi.org/10.7150/ijbs.19398.

Zhu, Y., Zhou, J., Feng, Y., Chen, L., Zhang, L., Yang, F., Zha, H., Wang, X., Han, X., Shu, C., et al. (2018). Control of intestinal inflammation, colitis-associated tumorigenesis, and macrophage polarization by fibrinogen-like protein 2. Front Immunol *9*, 87. https://doi.org/10.3389/fimmu.2018.00087.

Zilionis, R., Engblom, C., Pfirschke, C., Savova, V., Zemmour, D., Saatcioglu, H.D., Krishnan, I., Maroni, G., Meyerovitz, C.V., Kerwin, C.M., et al. (2019). Single-cell transcriptomics of human and mouse lung cancers reveals conserved myeloid populations across individuals and species. Immunity *50*, 1317-1334.e10. https://doi.org/10.1016/j.immuni.2019.03.009.

Zimmerman, G.A., McIntyre, T.M., and Prescott, S.M. (1985). Thrombin stimulates the adherence of neutrophils to human endothelial cells in vitro. J Clin Invest *76*, 2235–2246. https://doi.org/10.1172/JCI112232.

Appendix

Appendix 1. Role of mFGL2 and sFGL2 in tumour progression

Cancer Type	mFGL2/ sFGL2	Role of FGL2	Reference
Various (colon, esophageal, gastric, breast, lung, cervix)	mFGL2	• FGL2 colocalized with fibrin deposition in a variety of tumours • FGL2 induced by tumour related cytokines (IFN-γ and IL-2) in macrophage/endothelial cell lines contributes to coagulation	(Su et al., 2008)
HCC	mFGL2	• FGL2 colocalizes with fibrin deposition in HCC tumours • Elevated FGL2 in HCC cell lines is associated with lower coagulation time while knockdown of FGL2 is associated with decreased proliferation • The knockout of FGL2 in HCC cell line xenograft tumours decreased tumour progression and tumour volume, and decreased tumour vessel density	(Liu et al., 2012)
CRC	mFGL2	• FGL2 is highly expressed in tumour tissue compared to peritumour tissue in CRC patients. • High FGL2 is correlated with poor overall survival • Knockdown of FGL2 in CRC cell lines decreased proliferation, made cells more epithelial *in vitro* and decreased tumour growth and microvessel density (CD31 IHC staining) *in vivo*	(Qin et al., 2014)
HCC	sFGL2	• sFGL2 is elevated in plasma of patients with liver cirrhosis and hepatocellular carcinoma • sFGL2 produced by hepatic stem cells may suppress CD8+ T cell proliferation and activation (IFN-γ)	(Sun et al., 2014)
Prostate	mFGL2	• FGL2 silencing in PC-3 xenografts in immunodeficient (SCID) mice decreased tumour growth and vessel density (VWF IHC staining) • Silencing FGL2 is thought to decrease tumour angiogenesis through downregulated ERK1/2 phosphorylation	(Rabizadeh et al., 2015)
GBM	sFGL2	• High FGL2 mRNA expression in GBM TCGA data associated with poorer survival and correlates with immunosuppressive markers (*PD-1, PD-L1, CTLA-4, CD39, BTLA, LAG3, TGF-β1,* and *IL-10*) • FGL2 is elevated in glioblastoma cell lines and tumours compared to low grade glioma	(Yan et al., 2015)

		• FGL2 expression in syngeneic DBT tumours led to larger tumour volumes and faster tumour progression, this phenomenon was absent in tumours implanted in immunodeficient (NSG) mice attributing the function of sFGL2 through greater proportions of immunosuppressive immune cell populations in the tumours (PD-1+ leukocytes, CD39+ Tregs, CD11b+GR1+ MDSCs, and F4/80+CD206+ M2 macrophages). • Treating with α-FGL2 antibody improved survival and reduced proportions of immunosuppressive immune cell populations in the tumour (Tregs, M2 Macrophages and MDSCs)	
HCC	mFGL2	• Knockdown of FGL2 reduced proliferation of LM6 HCC cells *in vitro* • miRNA knockdown of FGL2 in HCC xenografts delivered via intratumoural Adenovirus injection reduced tumour growth • Tumours with miRNA knockdown of FGL2 had less fibrin deposition and lower microvessel density (CD31 IHC staining)	(Wang et al., 2016)
NSCLC	sFGL2	• Lewis Lung Cancer (LLC) tumours in $\mathit{Fgl2}^{-/-}$ mice had slower tumour progression compared to $\mathit{Fgl2}^{WT}$ mice and tumours had lower proportions of MDSCs (CD11b+Gr1+) and increased DCs (CD11c+MHC-II+) • sFGL2 produced by immune cells in the TME leads to activated CAFs and enhanced CXCL12 recruitment of MDSCs in the tumours • FGL2, CAF markers (FAP, PDGFRα) and MDSC (CD33, IL-10, CD14) markers correlate in TCGA data from the NSCLC tumours in suggesting FGL2 enhances immunosuppression to promote tumour progression	(Zhu et al., 2017)
ccRCC	mFGL2	• FGL2 is elevated in ccRCC tumour tissues compared to peritumoural tissue and high FGL2 expression is associated with poor survival • Knocking down FGL2 in ccRCC cell line (786-O) reduced cell viability and ERK1/2 and JNK phosphorylation	(Tang et al., 2017)
HCC	sFGL2	• Elevated serum levels of sFGL2 in patients with HCC	(Van Tong et al., 2018).
CRC	mFGL2	• FGL2 expression is higher in CRC tissues and cell lines compared to non-CRC • MAPK signalling (p38, ERK) is associated with FGL2 greater expression • FGL2 KD reduces proliferation, migration and invasion of CRC cell lines	(Liu et al., 2019)
GBM	sFGL2	• High grade glioma's have higher expression of FGL2 compared to low grade glioma's and is associated with poor survival • sFGL2 induced high grade glioma in mice with PDGFB/Ntv-a low grade gliomas and had greater recruitment of Tregs (CD4+ FOXP3+) and M2	(Latha et al., 2019)

		macrophages while treating with an α-FGL2 antibody prolonged survival and reduced Treg populations in the tumour • Knocking out FGL2 in GL261 tumour reduced tumour formation	
HCC	sFGL2	• FGL2 knockout or α-FGL2 treated mice had reduced tumour growth and greater proportions of activated CD8, CD4 T cells, DCs but fewer Tregs in tumours • sFGL2 inhibits Akt and p38 signalling preventing DC maturation, shown by lower levels of MHC-II+, CD40, CD80, CD86, CD83, and CD31 on CD11c+ (DCs) *in vitro*. • sFGL2 promotes HCC growth by inhibiting DC maturation and activation of CD4 and CD8 T cells.	(Yang et al., 2019)
GBM	sFGL2	• Glioma stem cells express FGL2 • Syngeneic GBM (GL261) in *Fgl2*$^{-/-}$ mice or FGL2 knockout of syngeneic LLC or astrocytoma (DBT) survive longer where enhanced tumour clearance in the absence of FGL2 is dependent on CD8 T cells • FGL2 knockout tumours and dLNs have a larger population of migratory CD103^{+} DCs capable of cross-presenting antigen and activating CD8+ T cells. • sFGL2 blocks GM-GSF activation of CD103+ expression through inhibition of JAK/STAT and TRAF6 signalling pathways. • *Decreased FGL2* levels and increased *GM-CSF* levels in mRNA expression data from GBM patients in the TCGA had a longer median OS	(Yan et al., 2019)
Lung Adeno carcinoma	NA	• FGL2 expression greater in lung adenocarcinoma tissue, correlates with more immune cell infiltration, and better outcomes	(Yuan et al., 2020a)
Esophageal	sFGL2	• High FGL2 expression correlates with poor survival and correlates with more immune cell infiltration (M2 macrophages) based on gene correlation within TCGA data • FGL2 expressed by M2 macrophages, promotes immunosuppressive TME (TCGA gene correlation)	(Yuan et al., 2020b)
GMB	NA	• FGL2 expression higher in GBM tissue, associated with mesenchymal subtype • High FGL2 associated with poor survival • High FGL2 associated with immune cell infiltration, PD-1/PD-L1/PD-L2, CD39 expression	(Song et al., 2020)
Breast	NA	• FGL2 expression is lower in tumour tissue compared to normal tissue	(Feng et al., 2020)

		• High FGL2 associated with better prognosis and is positively correlated with immune cell infiltration (B cells, CD4/CD8+ T cells, macrophages and DCs)	
HCC	sFGL2	• Overexpressing FGL2 in HCC cells leads to larger tumour growth which is attributed to more MDSCs found in the tumour and spleen.	(Liu et al., 2021)
GBM	sFGL2	• FGL2 secreted from glioma stem cells binds FcγRllB on monocytes, inducing CXCL7 which recruits glioma stem cells and promotes proliferation and stem-like transition	(Yan et al., 2021)
Gastric	NA	• FGL2 highly expressed in Subtype 3 of gastric cancer which has best prognosis and high prevalence of immune cells (CD4/CD8+ T cells, DCs, NK cells, Macrophages)	(Cao et al., 2021)
Gastrointestinal stromal	NA	• FGL2 associated with better recurrence free survival	(Pulkka et al., 2022)
Prostate	sFGL2	• FGL2 containing media from prostate cancer cells, decreases IFN-γ expression and CD107 degranulation in NK cells.	(Ostapchuk et al., 2022)
CSCC	mFGL2	• Higher expression in CSCC tumours • FGL2 in cancer cells promotes proliferation *in vitro* and tumour growth *in vivo* • FGL2 regulates ERK-dependent autophagy	(Zeng et al., 2022)

Appendix 2: Hallmark gene list for ID8 and STOSE cancer cells

	ID8	STOSE
1	Rdh10	Sulf1
3	Hspd1	Cfh
4	Hspe1	Prdx6
8	Ier5	Creg1
9	Atf3	Wt1
10	Hspa5	Prnp
11	Tnfaip6	Lrrn4
15	Tm4sf1	Cst12
18	F3	Slpi
19	Dnaja1	Ptgis
21	Cd52	Pmepa1
22	Errfi1	Rpl39
23	Fosl2	Xist
24	Jchain	Rpl22l1
27	Hspb1	Ecm1
29	Hsph1	Vcam1
30	Gm20186	Pnrc1
31	Igkc	Prdx1
37	Fxyd3	Rspo1
40	Bag3	Nbl1
41	Sbno2	Akr1b3
43	Phlda1	Cald1
44	Tspan8	1810058I24Rik
45	Star	Tmem176b
51	Mt1	Tmem176a
53	Rgcc	Mgst1
54	Hspa8	Rps9
55	Csrnp1	Ifitm3
57	Tm4sf5	Ctsd
58	Vmp1	Psap
59	Krt19	Bicc1
63	Timp2	Col6a1
64	Klf6	Hal
66	Rhob	Cd63
67	Ifrd1	Hmox1
70	Hsp90aa1	Ncam1
72	Ighm	Cryab
74	Pkhd1l1	Ppib
75	Trib1	Gsta4
76	Myc	Eef1a1
77	Lgals2	Trf

79	Maff	Rpl23
80	Krt7	Krt14
81	Krt8	Slc9a3r1
87	Pim1	Akr1c18
88	H2-K1	Gas1
89	Hspa1b	Zfp36l1
90	Ier3	Ifi27l2a
93	Cystm1	Rpl37
95	Chka	Ndrg1
100	Dusp5	Rpl8
101		Pfdn5
102		Atp5g2
103		Msln
104		Fau
105		Zfand5
106		Il33

Appendix 2: M0/M1/M2 gene-sets.

First 50 genes, complete list of genes presented in supplemental Table 5 (Rodriguez et al., 2022)

M0	M1	M2
Lifr	Cxcl9	Retnla
Ighm	Il12b	Flt1
Ccr3	Slfn1	Arg1
Rad51ap1	Ms4a4c	Mgl2
Cdca7	Ptges	Tmem26
Shcbp1	Cd38	Rnase2a
Cenpi	Susd2	Egr2
Slc40a1	Zfp811	Tmem26
E2f8	Cxcl10	Egr2
P2ry1	Ppfia3	Ube2c
Slc13a3	Nos2	Mrc1
BB163080	Slco3a1	Gask1b
Slc9a9	Pstpip2	Chil3
Cacna1b	Hdc	Irf4
Cd5l	Ptges	Il1rl1
Stmn1	Gbp6	Socs2
Pcp4l1	Mcemp1	Olfm1
Cryba4	U90926	Il31ra
Sncaip	Rsad2	Ptgs1
Rad51ap1	Ifit1bl1	Pparg
Slc40a1	Cd200	Il31ra
Slc46a3	Epb41l3	Lat
Armc3	Ccrl2	Atp6v0d2
Fcrls	Plpp1	F3
Rab3il1	Dgat2	Rbp4
Dlgap5	Cd69	Ccnb2
Cdc25c	Irf7	Ptgs1
Tmem176b	Acsl1	Ryr1
Cep55	Gpr18	Gask1b
Gas6	Cx3cr1	Pole
Sult1a1	Smpdl3b	Rnase6
Cd28	Mx1	Wwc1
Rrm2	Clec4e	Mcf2l
Tmem176a	F11r	Atp6v0d2
Stmn1	Calhm6	Matk
Ccnd1	Ifi213	S100a4
Rasgrp3	AY512915	Npas2
Abcb1b	Hcar2	Clec7a
Cdca3	Ms4a6b	E2f7
Ccnd1	Tnf	Nuf2
Slc9a9	Iigp1	Dclk1
Rrm2	Ddx60	Clec4b1
Uhrf1	Oas3	Itgb3
Rgs2	Irak3	Flt1
Efr3b	Procr	Esco2
Rgs2	Cmpk2	Ankrd55
Rnf150	Dgat2	Kif23
Slc13a3	4930518F22Rik	Pclaf
Smagp	Nfkbiz	Ccl17
Mcm5	Ifi209	Pdcd1lg2
Rgs18	Herc6	Rras2

Appendix 4: Average and standard deviation of concentrations of cytokines and chemokines in the ascites of syngeneic mouse models of ovarian cancer at endpoint.

Cytokine/ Chemokine (pg/mL)	ID8-WT (n=7)	ID8-C3 (n=3)	ID8-Tp53-/- F3 (n=7)	STOSE (n=4)	MOE-PTEN^{shRNA} KRAS^{G12V} (n=7)	MOE-PTEN^{shRNA} p53^{R273H} (n=2)
IFN-γ	2.31 ± 2.40	7.33 ± 4.31	7.88 ± 2.43	454.08 ± 475.13	10.13 ± 6.72	3.24 ± 4.58
IL-10	681 ± 247.74	488.35 ± 280.06	807.34 ± 213.35	1036.61± 374.44	2213.45 ± 648.34	258.26 ± 365.23
CCL4	27.51 ± 13.54	34.42 ± 15.66	40.07 ± 17.07	73.7 ± 27.15	47.28 ± 10.31	23.76 ± 33.59
IFN-α	3.45 ± 3.79	8.99 ± 8.78	6.28 ± 3.41	30.59 ± 14.44	9.31 ± 5.83	6 ± 8.48
CXCL9	5.44 ± 9.91	11.7 ± 20.26	53.35 ± 37.65	3744.98 ± 3947.50	34.44 ± 38.70	6.21 ± 8.78
CXCL10	756.07 ± 491.13	3143.28 ± 1447.90	8799.47 ± 6790.58	1.60E+04 ± 6912.75	648.26 ± 354.62	741.5 ± 824.06
TNF-α	36.44 ± 20.02	66.37± 52.49	43.42 ± 10.02	451.78 ± 346.65	21.3 ± 6.12	43.72 ± 43.81
IL-6	170.47± 103.66	439 ± 127.49	497.06 ± 415.81	1836.16 ± 1682.97	858.57 ± 257.21	513.48 ± 181.79
VEGF	1.31E+06 ± 1.66E+06	3006.03 ± 932.23	5427.64 ± 2783.62	5108.65 ± 3471.08	1322.53 ± 1182.76	562.78 ± 463.18
IL-4	1.31± 2.45	0 ± 0.00	0.63 ± 1.13	827.87 ± 798.96	1.27 ± 0.94	1.47 ± 2.08
CCL3	53.46 ± 100.10	14.13 ± 6.63	16.85 ± 6.64	21.04 ± 40.88	17.96 ± 7.17	19.41 ± 53.46
CCL2	935.58 ± 852.90	56.88 ± 33.32	164.97 ± 72.69	7512.37 ± 7086.16	78.28 ± 55.28	257.1 ± 935.58
GM-CSF	23.8 ± 30.21	2.83 ± 4.9	10.63 ± 7.35	1726.23 ± 1698.54	21.21 ± 10.64	19.21 ± 23.8

Appendix 5: Average and standard deviation of concentrations of cytokines and chemokines in the plasma of syngeneic mouse models of ovarian cancer collected near endpoint.

Cytokine/ Chemokine (pg/mL)	ID8-WT (n=5)	ID8-C3 (n=5)	ID8-Tp53-/-F3 (n=5)	C57BL/6 control (n=9)	STOSE (n=5)	MOE-PTEN^{shRNA}/ KRAS^{G12V} (n=5)	MOE-PTEN^{shRNA}/ p53^{R273H} (n=2)	FVB/N control (n=6)
IFN-γ	14.56 ±11.56	10.56 ±3.08	8.04 ± 3.42	38.60 ± 43.99	36.99 ± 24.43	45.75 ± 47.96	1.43 ± 2.02	27.11± 33.36
IL-10	549.2± 422.09	358.31± 190.39	340.97 ± 199.04	827.07 ± 758.69	995.93 ± 485.89	924.07 ± 804.72	0.00 ± 0.00	495.5 ± 461.68
CCL4	61.53± 41.50	64.43 ± 20.26	58.65 ± 33.53	93.70 ± 56.44	113.52 ± 30.49	114.89 ± 58.52	0.00 ± 0.00	83.97 ± 36.31
IFN-a	17.35± 14.40	6.62 ± 5.59	5.85 ± 4.16	42.87 ± 53.24	41.41 ± 35.36	49.05 ± 60.04	0.00 ± 0.00	20.61 ± 34.52
CXCL9	22.42± 21.46	30.22 ± 12.06	8.34 ± 7.80	36.24 ± 26.22	17.54 ± 13.83	24.06 ± 15.42	39.87 ± 37.56	34.64 ± 34.76
CXCL10	605.19±263.48	471.04 ± 255.06	2144.39 ± 2558.09	418.80 ± 157.65	388.95 ± 200.63	542.58 ± 83.55	456.30 ± 37.48	510.50 ± 237.01
TNF-α	16.67± 12.28	9.40 ± 2.93	20.27 ± 18.74	11.60 ± 8.46	30.08 ± 15.77	22.89 ± 12.27	7.69 ± 0.06	15.17 ± 9.48
IL-6	14.35± 10.88	3.92 ± 2.50	51.99 ± 84.20	7.45 ± 4.27	96.51 ± 115.80	42.07 ± 42.30	1.72 ± 0.39	6.03 ± 4.84
VEGF	6.45± 4.78	3.67 ± 2.25	43.40 ± 88.96	6.44 ± 5.44	7.22 ± 3.86	10.70 ± 5.61	0.00 ± 0.00	14.03 ± 17.14
IL-4	5.18± 2.37	3.43 ± 0.99	3.05 ± 1.29	5.39 ± 4.10	5.24 ± 2.71	5.57 ± 3.99	0.00 ± 0.00	3.90 ± 2.85
CCL3	91.46±133.93	14.23 ± 7.62	22.70 ± 13.63	47.15 ± 43.88	36.81 ± 26.80	45.99 ± 46.77	1.38 ± 1.96	90.59 ± 127.97
CCL2	209.6± 117.16	110.17 ± 47.38	164.83 ± 185.35	128.92 ±78.93	148.99 ± 36.89	225.98 ± 116.76	48.38 ± 30.90	116.11 ± 54.66
GM-CSF	11.22± 19.89	4.61 ± 6.32	0.00 ± 0.00	23.90 ± 23.03	39.68 ± 23.57	34.03 ± 37.28	0.00 ± 0.00	44.91 ± 34.14

Appendix 6: Non-cancer and ovarian cancer ascites patient characteristics

	Study ID	Date enrolled	Diagnosis	M/F/O
Non-cancer ascites (Protocol #: 20210799-01H)	ACB-002	09-Feb-22	Non cirrhotic portal hypertension (idiopathic)	F
	ACB-003	11-Feb-22	Alcohol cirrhosis	M
	ACB-004	14-Feb-22	Likely alcohol decompensated cirrhosis	F
	ACB-005	28-Feb-22	Alcohol cirrhosis	M
	ACB-006	02-Mar-22	Alcohol cirrhosis	F
	ACB-007	04-Mar-22	Nonalcoholic Steatohepatitis (NASH)	F
	ACB-008	04-Mar-22	Cirrhosis due to congestive hepatopathy	F
	hA1	NA	Cirrhosis	Unknown
	hA2	NA	Cirrhosis	Unknown
Ovarian Cancer Ascites (Protocol #: 1999540-01H)	2191	Mar.10.17	High Grade Serous	F
	2261	Jul.24.18	High Grade Serous	F
	2219	Sept.28.17	High Grade Serous	F
	2166b	Mar.2.17	High Grade Serous	F
	2158	Aprl.8.16	High Grade Serous	F
	1947	Jan.14.09	High Grade Serous	F
	2172a	Jul.8.16	High Grade Serous	F
	1927	April.4.07	High Grade Serous	F
	1413	June.21.06	High Grade Serous	F
	1940	July.2.08	High Grade Serous	F
	1359	Sept.24.04	High Grade Serous	F
	2301	Feb.6.20	High Grade Serous	F
	2272	Nov.16.18	High Grade Serous	F
	2161	May.3.16	High Grade Serous	F
	2217	Aug.20.17	High Grade Serous	F
	2170a	Jan.16.16	High Grade Serous	F
	2166	June.2.16	High Grade Serous	F
	2141	Dec.17.15	High Grade Serous	F
	2162	May.6.16	High Grade Serous	F
	2302	Feb.13.20	High Grade Serous	F
	2177	Aug.12.16	High Grade Serous	F
	2221	Sept.28.17	High Grade Serous	F

Appendix 7: ID8-*p53*$^{-/-}$*Brca2*$^{-/-}$ and B16F10 cancer cells do not express FGL2 *in vivo.*

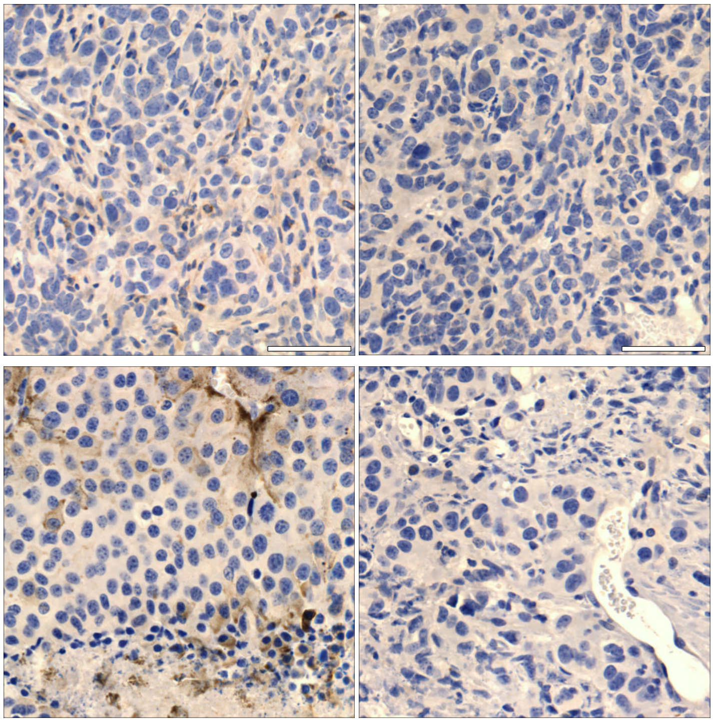

IHC detection of FGL2 expressing endothelial and immune cells in B16F10 and ID8-*p53*$^{-/-}$ *Brca2*$^{-/-}$ tumours in *Fgl2*^{WT} and *Fgl2*$^{-/-}$ mice. Sections were counterstained with hematoxylin (blue) and positive cells (brown) were stained with DAB. Images are representative of each tumour model. Scale bars, = 50 µm.

Appendix 8. Patient characteristics and plasma FGL2 levels at baseline and POD1.

Patient ID	Sex	Age	Cancer Type	FGL2 (ng/mL)	
				Baseline	POD1
489	M	18	Non cancer	14.19175	27.62542
536	M	61	Thymoma	26.17614	76.73356
490	F	75	Non cancer	9.732441	8.896321
550	M	60	Parotid gland	25.39576	35.37347
534	M	72	Thigh sarcoma	14.91639	32.14047
548	M	66	Prostate	22.32999	14.19175
508	F	30	Myxoid liposarcoma	85.98662	110.0669
562	M	70	Lung	28.4058	44.29208
540	M	50	Renal	51.98439	74.72687
539	M	61	Lung and prostate	11.68339	17.14604

Appendix 9: Key features of syngeneic models of ovarian cancer

Murine tumour model	Key features of the TME	Proposed immunotherapy (Rodriguez et al., 2018)
1. ID8-WT	Coldest tumour on the C57BL6 background. Higher production of VEGF and CCL3 in the ascites fluid.	Immunogenic cell death inducers, oncolytic virotherapy
2. ID8-C3	Necessary control for ID8 mutants, as Cas9 expression influences immune infiltration profile.	Immunogenic cell death inducers, oncolytic virotherapy
3. ID8-p53-/-	P53 depletion influences myeloid recruitment.	Immunogenic cell death inducers, TLR agonists, IDO inhibitors
4. STOSE	Higher content of M2-like macrophages. Tumours with high adipocyte content. Higher concentration of CCL2, CXCL9, GM-CSF, IFN-γ, IL-4 and TNF-α in the ascites fluid.	Macrophages reprogramming agents (Trabectedin)
5. MOE-PTEN/KRAS	Immune profile similar to ID8-WT. Tumours harbor T cell clusters. Lack of recruitment of M2-like macrophages. High PD-L1 expression on the myeloid compartment. High concentration of IL-10 in the ascites fluid.	Cell therapy transfer, ICI
6. MOE-PTEN/p53	Higher MHC-II expression in the TME.	Oncolytic virotherapy, Infected cell vaccine (deliver MHC-II dependent Ag to increase CD4+ T cell responses)